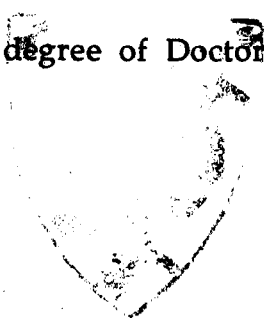


NEUTRON DIFFRACTION AND MOLECULAR DYNAMICS
STUDIES OF FLUID HALOCARBONS

Thesis submitted in accordance with the
requirements of the University of Liverpool
for the degree of Doctor in Philosophy



Christopher David Hall

To my parents

PREFACE

In 1988, when this work was initiated, only one project was foreseen; a supercritical solubility study by High Pressure Nuclear Magnetic Resonance Spectroscopy (HPNMR). In the year-long period while the apparatus necessary for this experiment was engineered, I read countless research papers and repaired a supercritical fluid chromatography instrument for ICI, Runcorn. When the HPNMR equipment duly arrived, various technical problems and time limitations on the spectrometer (which was shared with eight other people) led me to other research.

The opportunity arose for me to perform a series of neutron diffraction experiments at the Rutherford Appleton Laboratories (RAL) in Oxfordshire. In the weeks following those experiments, any time that I was unable to perform HPNMR experiments was spent in perfecting the data analysis routine for the diffraction results.

It was our intention to analyse the neutron diffraction results in more detail by comparing them with Molecular Dynamics (MD) computer simulations. A package for such a simulation was available from the SERC, and ICI acquired a copy. In the summer of 1990, while I was busy analysing the neutron diffraction data, an American student working at ICI as a summer fellow scrutinised the simulation programme and modified it for our objectives. In the winter of 1990, I began my research into MD simulations. The results were very promising and a further set of neutron diffraction experiments were performed at the RAL, followed by the respective MD simulations.

In the meantime, still facing problems with the HPNMR experiment, the method was changed slightly to see if this had any effect. The results from this were also disappointing, the experiment was abandoned, and all the remaining time was devoted to MD simulations.

ABSTRACT

The aim of this thesis was to study the structure of fluid halocarbons using the complementary techniques of neutron diffraction and Molecular Dynamics (MD) computer simulation.

The neutron diffractometers used to study the fluids at the Rutherford Appleton Laboratories were the Liquid and Amorphous Diffractometer (LAD) and the Small Angle Neutron Diffractometer for Amorphous and Liquids Samples (SANDALS). The halocarbons successfully studied were dichlorodifluoromethane, protonated- and deuterated-chlorodifluoromethane, chlorotrifluoromethane, bromotrifluoromethane and fluoroform all at a temperature of 153 K. After detailed data reduction had been performed on the diffraction results using the ATLAS computer package, a pair distribution function (pdf) was given for each fluid. From the pdfs, the intramolecular atomic separations and bond angles of the molecules were derived. In the intermolecular regions of the pdfs for dichlorodifluoromethane and fluoroform there were some very interesting features. The first intermolecular peak in the pdf of fluid dichlorodifluoromethane had a shoulder indicative of preferential orientation and the fluoroform pdf had a peak centred at 2.5 Å due to a close H...F interaction (again indicating the presence of preferential orientation).

MD computer simulations, using Lennard-Jones potentials to model intermolecular forces, were run for each of the six fluids successfully diffracted. The simulations were run until the total energy of the simulated fluid matched that expected at 153 K, and the pdfs given in the diffraction experiments were compared with those derived from MD computer simulations. The comparison for dichlorodifluoromethane and fluoroform was excellent, and consequently the most probable orientations of molecules in the two liquids were derived in detail. Dichlorodifluoromethane molecules align in a 'straddle' conformation with a preference for close chlorine contacts. Fluoroform molecules align, not in a rocket conformation as was first thought following the diffraction results, but in a skewed 'straddle' conformation with a preponderance for close H...F interactions.

ACKNOWLEDGEMENTS

Most of all I would like to thank my family, especially my mom and dad, without whose love and financial help this thesis would not have been possible.

I must also heartily thank Jon Iggo for his help with the NMR, and Kathy Johnson for her tireless support during my time at Liverpool University.

ICI thankfully contributed, mainly in the guise of Andy Burgess, not only much needed financial assistance but also experiments to do when all else failed. Other ICI employees whose help and friendship was inestimable include Christine Temple, Kevin Jackson, Bob Page, Barry Johnson, Lee Griffiths and Neil Winterton.

A special mention to Spencer Howells and Alan Soper at the Rutherford Appleton Laboratory.

To Jack Dutton, a wonderful workman - MILLE GRAZIE. Also on the technical side at Liverpool, thanks are extended to Charlie, Bert and Pete.

For their proof-reading, my friends Chris and Jenny were invaluable. Finally, thanks go to John Temple and the others in the tea-room square.

This work was funded by the SERC in collaboration with ICI Chemicals and Polymers.

This thesis has been prepared using Word and ChemDraw on a Macintosh Classic.

CONTENTS

CHAPTER ONE

PAGES 39-41 HAVE BEEN REMOVED FROM AND PAGE 24a HAS BEEN ADDED TO THIS CHAPTER.

1.1	Introduction.....	1
1.2	Neutron Diffraction and Molecular Dynamics.....	2
1.3	The Pair Distribution Function	3
1.4	Intermolecular Forces.....	5
1.4.1	Two Monatomic Molecules.....	5
1.4.2	Many-Bodied Systems.....	7
1.4.3	Molecular Systems.....	9
1.5	The Makeup of Two-Body Intermolecular forces.....	11
1.5.1	The Attractive Energy, ϕ_A	11
1.5.1(a)	Permanent Dipole - Permanent Dipole (or Electrostatic) Attraction Energy, ϕ_P	11
1.5.1(b)	Induction Energy, ϕ_i	13
1.5.1(c)	London or Dispersion Energy, ϕ_L	14
1.5.2	The Resultant Attractive Energy.....	15
1.5.3	The Repulsive Energy, ϕ_R	16
1.5.4	The Resultant Potential.....	18
1.5.5	The Potentials for Liquid Halocarbons.....	19
1.6	A Review of Recent Literature.....	21
1.6.1	General Results	21
1.6.2	Argon - A Monatomic Fluid	24
1.6.3	Trichloromethane (CHCl_3).....	25
1.6.4	Dichloromethane (CH_2Cl_2).....	26
1.6.5	Tetrachloromethane (CCl_4).....	27
1.6.6	Other Comparative Studies of Polyatomic Molecules.....	28
1.6.7	Water.....	29

1.7	Building Better Potentials.....	31
1.8	Summary.....	34
	REFERENCES	35

CHAPTER TWO

PAGE 62 HAS BEEN REMOVED FROM THIS CHAPTER.

2.1	Introduction.....	42
2.2	Historical Background	42
2.3	The Neutron.....	44
2.4	Scattering and Structure.....	46
2.4.1	Elastic and Inelastic Scattering	46
2.4.2	Coherent and Incoherent Scattering.....	47
2.4.3	Other Scattering Events.....	49
2.5	The Pulsed Time-of-Flight Experiment and the Elastic Scattering.....	49
2.6	Scattering Theory.....	53
2.6.1	Relating $S(Q)$ to the $DCS(Q)$, $d\sigma/d\Omega$	54
2.6.2	Intramolecular and Intermolecular Form Factors	56
2.7	Ideal Scattering Systems	57
2.7.1	Scattering from a Single Particle.....	57
2.7.2	Scattering from a Monatomic Ideal Gas.....	57
2.7.3	Scattering from a Polyatomic Ideal Gas.....	57
2.7.4	Scattering from Polyatomic Ideal Solids and Liquids	59
2.8	The Time-of-Flight (TOF) Neutron Diffraction Equipment.....	61
2.8.1	The Neutron Source	61
2.8.2	The Moderator.....	64
2.8.3	The Collimator	64
2.8.4	The Target Sample.....	65

2.8.5	The Detectors	66
2.8.5(a)	The Incident and Transmission Monitors	66
2.8.5(b)	The Scattered Neutron Detectors	66
2.8.6	The Data Storage System	70
2.8.7	The Data Analysis Package	70
2.9	Deriving the Structure of Liquids using Neutron Diffraction.....	70
2.10	The Basis of the Data Analysis.....	73
2.10.1	Dividing out the incident spectrum.....	75
2.10.2	Removing the Background	76
2.10.3	Attenuation and Multiple Scattering Corrections, and Normalisation.....	77
2.10.4	Inelastic, Recoil and Self-scattering Corrections	78
2.10.6	Merging the Data	79
2.10.7	Fourier Transformation	80
2.11	The LAD Experiments	80
2.11.1	The Experimental Components	80
2.11.2	Dichlorodifluoromethane	81
2.11.2.1	Experimental.....	81
2.11.2.2	Data Reduction.....	82
2.11.2.3	Results and discussion.....	92
2.11.3	Chlorodifluoromethane, CHClF_2 , and Fluoroform, CHF_3	93
2.11.3.1	Experimental.....	93
2.11.3.2	Data Reduction.....	94
2.11.3.3	Results and Discussion.....	95
2.12	The SANDALS experiments.....	101
2.12.1	Experimental Components.....	101
2.12.2	Chlorotrifluoromethane and Bromotrifluoromethane	102

2.12.2.1	Experimental.....	102
2.12.2.2	Data Reduction.....	103
2.12.2.3	Results and Discussion.....	106
2.12.3	Deuterated-Chlorodifluoromethane.....	114
2.12.3.1	Experimental and Data Analysis	114
2.12.3.2	Results and Discussion.....	114
2.12.4	Deuterated-fluoroform and Trichlorofluoromethane.....	118
2.13	Concluding Remarks	119
2.14	Future Work.....	119
REFERENCES	120

CHAPTER THREE

3.1	Introduction.....	124
3.2	The Motivation for Simulation	125
3.3	MDMPOL; Liquid Molecules in a Box.....	126
3.3.1	Potential Energy	126
3.3.1.1	The LJ Potential Equation	127
3.3.1.2	The Long-Range Electrostatic-Charge Contribution to the Potential Equation.....	129
3.3.2	Kinetic Energy.....	129
3.3.2.1	Linear Motion.....	131
3.3.2.2	Rotational Motion.....	133
3.3.3	Conventions	133
3.3.4	Data Input.....	135
3.3.5	Setting up the Molecules in the Box.....	136
3.3.6	Equilibration	137
3.3.7	The Simulation of Liquids.....	137
3.3.8	Checking the Results.....	137

3.3.9	The Pair Distribution Function	138
3.3.10	Manipulating and Plotting the Pdf	139
3.3.10.1	Normalisation of the Pdfs.....	139
3.3.10.2	Calculating Neutron Weighted Pdfs	140
3.3.10.3	Plotting the Simulated Pdfs.....	142
3.3.10.4	Plotting the Experimental Results	142
3.3.10.5	Overlaying Pdfs	142
3.3.10.6	Integrating Regions of the Pdf.....	142
3.4	Experimental.....	144
3.4.1	Dichloromethane.....	144
3.4.2	Dichlorodifluoromethane	145
3.4.2.1	Input Parameters.....	145
3.4.2.2	The Simulations	147
3.4.2.3	Thermodynamic Comparisons.....	148
3.4.2.4	The Total and Neutron-Weighted Pair Distribution Functions.....	150
3.4.2.5	The Individual Pair Distribution Functions and their Integration.....	153
3.4.2.6	Discussion of the Structure	158
3.4.3	Fluoroform.....	161
3.4.3.1	Input Parameters.....	161
3.4.3.2	The Final Simulation	164
3.4.3.3	The Total and Neutron-Weighted Pair Distribution Functions.....	164
3.4.3.4	The Individual Pair Distribution Functions and their Integration.....	168
3.4.3.5	The Discussion of the Structure	172
3.4.4	Chlorodifluoromethane and Deuterated-Chloro- difluoromethane.....	174

3.4.4.1	Input Parameters.....	174
3.4.4.2	The Total and Neutron-Weighted Pair Distribution Functions.....	176
3.4.4.3	Discussion of the Structure.....	178
3.4.5	The Other Simulations.....	181
3.4.5.1	Input Parameters.....	181
3.4.5.2	Thermodynamic Comparisons.....	182
3.4.5.3	The Total and Neutron-Weighted Pair Distribution Functions.....	183
3.4.5.3	Discussion of the Structure.....	184
3.5	Conclusion.....	187
	REFERENCES.....	189

"Four times under our educational rules, the human pack is shuffled and cut - at eleven plus, sixteen plus, eighteen-plus and twenty-plus - and happy is he who comes top of the deck on each occasion, but especially the last. This is called Finals, the very name of which implies that nothing of importance can happen after it. The British postgraduate student is a lonely, forlorn soul, uncertain of what he's doing or whom he's trying to please - you may recognise him by the glazed look in his eyes"

DAVID LODGE in *Changing Places*

THE STRUCTURE OF FLUID HALOCARBONS:
A STUDY BY NEUTRON DIFFRACTION
AND MOLECULAR DYNAMICS

CHAPTER ONE
LIQUIDS AND LIQUID STRUCTURE

1.1 Introduction

In this chapter some of the different methods of deriving liquid structure are described and compared.

The general structure of liquids, (and that of glasses and other amorphous solids), is compared with that of crystalline solids or gases in figure 1.1. Liquid structure is characterised by a degree of local molecular ordering, but a lack of long range order compared with crystalline solids whose structure is periodic. Liquids and their properties are described in an excellent book by Temperley and Trevena [1].

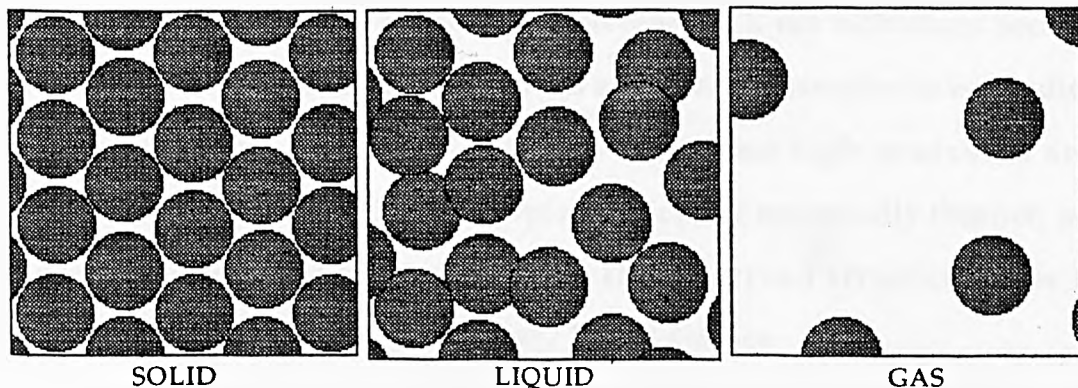


Figure 1.1 The general structure of crystalline solid, liquid and gas

The techniques used to derive liquid structure that are of interest in this study are Neutron Diffraction (Chapter 2) and Molecular Dynamics Simulation (Chapter 3). They both describe the structure in terms of the pair (or radial) distribution function, $g(R)$, which describes the probability

of finding an atom at a distance R from another at the origin. Figure 1.2 shows generalised examples of $g(R)$ for crystalline solid, liquid and gas.

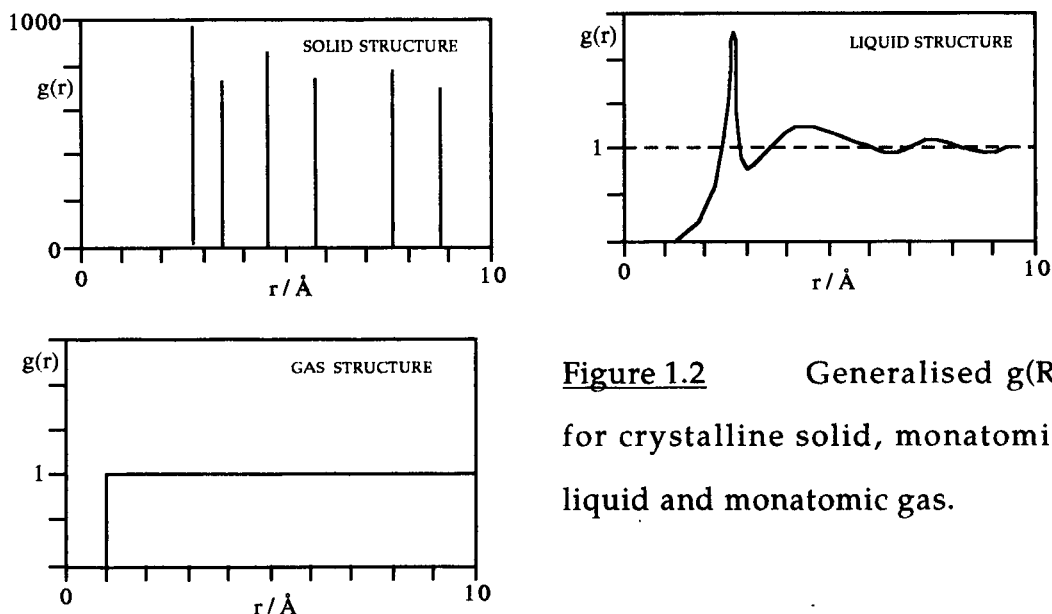


Figure 1.2 Generalised $g(R)$ for crystalline solid, monatomic liquid and monatomic gas.

1.2 Neutron Diffraction and Molecular Dynamics

One of the uses of neutron diffraction is in deriving the structure of liquids. It is used for this purpose in preference to X-ray diffraction because low absorption coefficients for neutrons allow larger samples to be studied in strongly built containers that can withstand high pressures and high/low temperatures. X-ray samples, which are necessarily thinner, are more likely to show uncertainties in their derived structures due to contamination by foreign atoms at the liquid surface.

Molecular dynamics is a computer technique that uses models of the potential between the atoms of molecules, and their motion under that potential, to simulate liquid structure. Other simulation techniques include oiled-ball-bearings-on-tray models, ball-bearings-in-balloon models, and Monte Carlo simulations. They are all described in Temperley and Trevena [1].

1.3 The Pair Distribution Function

The pair distribution function, or $g(R)$, is a probability function describing the positions of atoms in fluids with respect to each other and normalised to ideal gas structure.

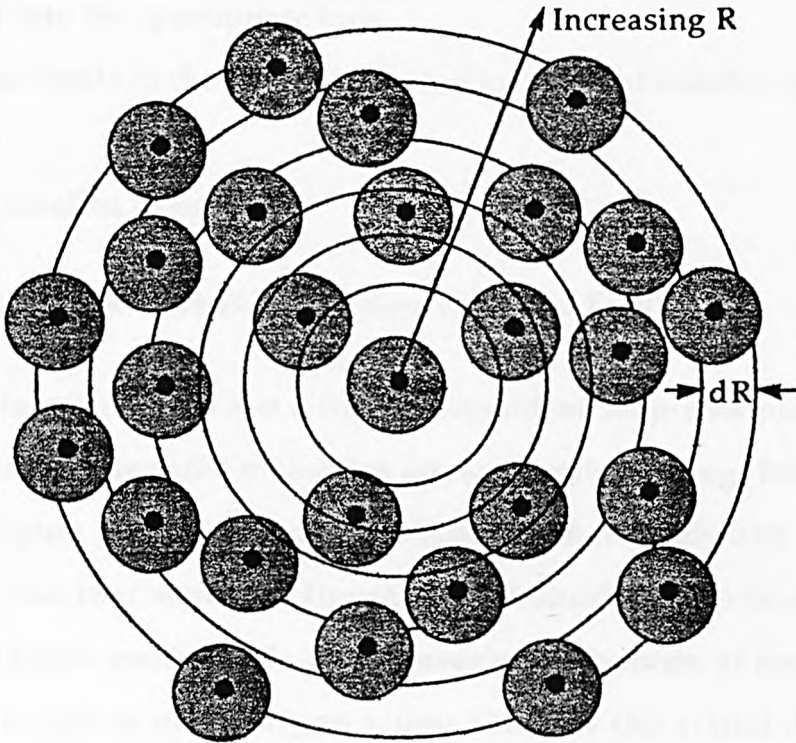


Figure 1.3 The distribution of liquid argon atoms in two dimensions.

Consider the simple case of argon atoms in the liquid phase at any one instant. Figure 1.3 shows the distribution of the argon atoms in two dimensions for simplicity; the description of $g(R)$ given below is for a three dimensional system. $g(R)$ is derived from this distribution in five steps:

- (i) one of the atoms is arbitrarily chosen and spheres of radius R are drawn around it in very small equal increments of dR (the binwidth of a histogram),

- (ii) the number of atoms, $n(R)$, within the shells between each sphere (of thickness dr) is counted and placed in the histogram bins,
- (iii) $n(R)$ is divided through by the atomic number density, ρ , and the volume of the shell, $4\pi R^2 dR$,
- (iv) steps (i)-(iii) are repeated for all the other atoms adding the results into the appropriate bins,
- (v) the totals in the bins are divided by the total number of atoms, N .

This is equivalent to using,

$$g(R) = \langle n(R) \rangle / 4\pi\rho R^2 dR, \text{ where } \langle n(R) \rangle = \sum n(R) / N. \quad (1.1)$$

For liquids, $g(R)$ versus R is a time-independent snap-shot picture of the liquid structure since the molecules are constantly moving. For the argon atoms in figure 1.3, choosing a small value of dR (roughly 0.05 \AA) the $g(R)$ will look like that shown in figure 1.2. At short R , $g(R)$ is zero due to repulsive forces (section 1.5). It increases to a maximum at roughly twice the atomic radius of the argon atoms ($2R_{Ar}$) – the actual distance is dependent upon the density of the liquid - then $g(R)$ oscillates more weakly around unity. The $g(R) = 1$ value is significant in that for an ideal gas $g(R)$ is unity for all values of R . If $g(R) > 1$, the probability of finding an argon atom at a distance R from another atom in the liquid is greater than would be found for randomly arranged ideal gas atoms. That the $g(R)$ damps quickly to unity after the first (nearest-neighbour) maximum indicates the lack of long-range structure in liquids. $g(R)$ is explained in further detail in Chapter Two.

1.4 Intermolecular Forces

The intermolecular structure of liquids is defined by the intermolecular forces between the atoms of the molecules that make up the liquids. The very nature of the condensed state depends upon these forces and van-der-Waals' showed that without attractive forces the condensed state could not even exist [2]. The low compressibility of liquids and solids compared with gases is dependent upon the repulsive forces between their molecules. In this section these forces are introduced and the potential models used to represent condensed matter behaviour are described.

1.4.1 Two Monatomic Molecules

If there are two monatomic molecules (e.g., argon) infinitely separated in a system, the energy of that system, $E_S(\infty)$, is the sum of the energies of the individual atoms, E_1+E_2 , because the molecules do not interact. For monatomic molecules the major contribution to E_1 and E_2 is translational kinetic energy.

If the molecules are brought closer to each other there will be an interaction, U , between them that is dependent upon the distance, R , they are apart. The system energy, $E_S(R)$ is now $E_1+E_2+U(R)$. $U(R)$ is said to be the potential energy between the two molecules and is also called the pair potential. It can be thought of as the work required to bring the two molecules together from infinity to a distance of R .

If $F(R)$ is the force acting between the two molecules, which are separated by a distance, R , then

$$U(R) = \int_R^{\infty} F(R) dR \quad (1.2)$$

$F(R)$ is by convention positive when repulsive and negative when attractive.

The general form of $U(R)$ and $F(R)$ is shown in figure 1.4.

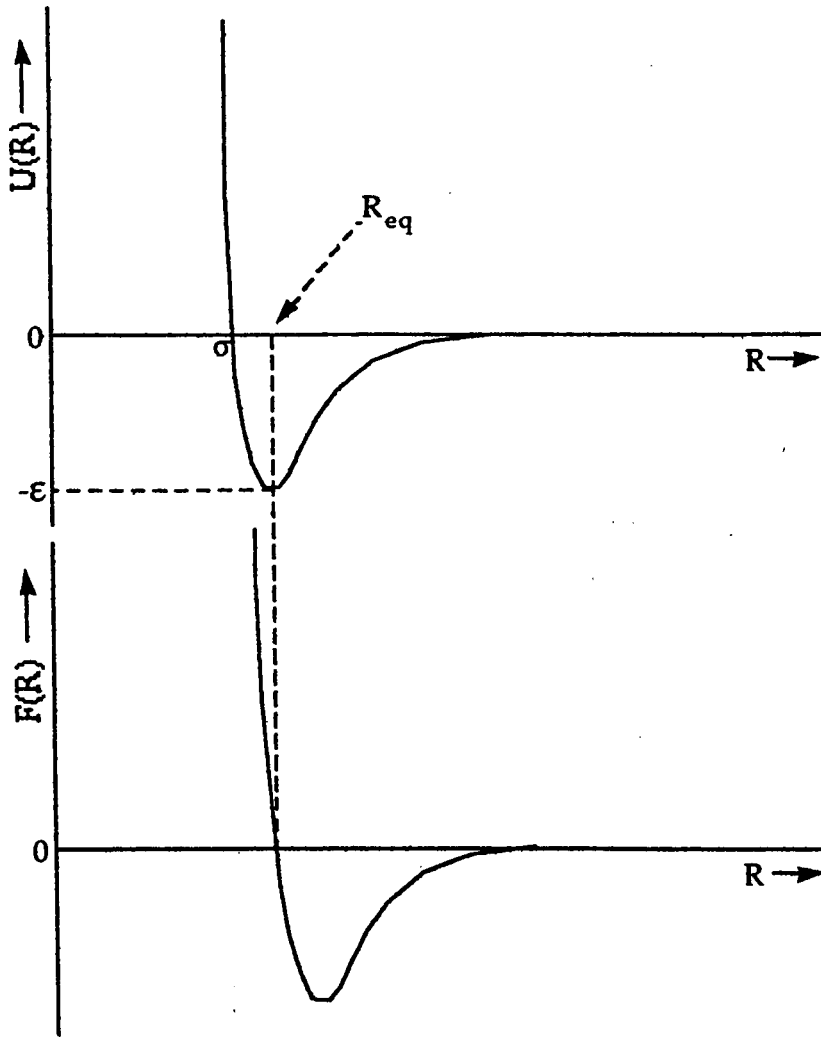


Figure 1.4 The general form of $U(R)$ and $F(R)$

In both cases, there is a repulsive wall at short range and an attractive tail at long range. If two monatomic molecules are at the separation, R_{eq} , the potential energy, $U(R)$, is a minimum ($-\epsilon$) and the force acting between the two molecules, $F(R)$ is zero. R_{eq} is the favoured distance between two molecules and thus the repulsive and attractive forces between the two are in equilibrium. ϵ is known as the well depth. $U(R) = 0$ when the molecules

are separated by σ (this is roughly equal to the sum of the atomic radii of the interacting molecules).

1.4.2 Many-Bodied Systems

For a system of N monatomic molecules the form of $U(R)$ is more complicated. The system energy is the sum of the kinetic energies ($\sum E_N$) of all the molecules plus the sum of all the potential energies between all the atoms of the system. That is,

$$E_s(R) = \sum E_N + \sum\sum v_2(R_i, R_j) + \sum\sum\sum v_3(R_i, R_j, R_k) + \dots, \quad (1.3)$$

where $v_2(R_i, R_j)$ is the potential energy due to two-body interactions, $v_3(R_i, R_j, R_k)$ is the three-body term, etc.

Equation (1.3) may also be written

$$E_s(R) = \sum E_N + U(R_i, R_j, R_k, \dots). \quad (1.4)$$

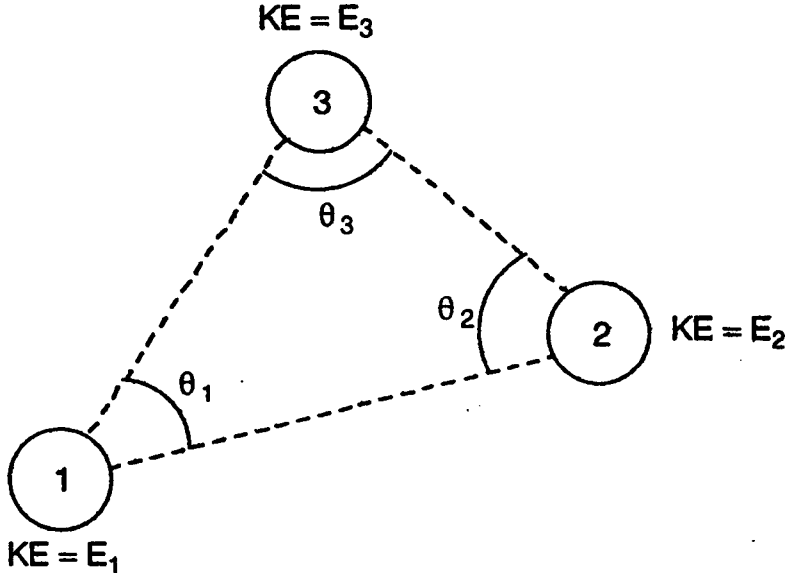
Consider as an example of the higher order terms of this equation, the three argon atoms in figure 1.5. The potential $U(R_{12}, R_{23}, R_{31})$, where R_{xy} is the distance between atom x and atom y , is not simply the sum of all the pairwise potentials $U(R_{12}) + U(R_{23}) + U(R_{31})$ - there is an extra term $u(R_{12}, R_{23}, R_{31})$ to be added which arises due to the non-additivity of the potential i.e.,

$$E_s(R) = \sum E_N + U(R_{12}) + U(R_{23}) + U(R_{31}) + u(R_{12}, R_{23}, R_{31}). \quad (1.5)$$

$u(R_{12}, R_{23}, R_{31})$ may be written [3] as

$$u(R_{12}, R_{23}, R_{31}) = v(R_{12}, R_{23}, R_{31})^{-3} (3 \cos \theta_1 \cos \theta_2 \cos \theta_3 + 1), \quad (1.6)$$

where $\theta_1, \theta_2, \theta_3$ are the angles of the triangle formed by the atoms, and v is the three body coefficient, which for argon is 7.3982×10^{-11} erg \AA^9 ($1 \text{ J} = 10^7$ erg).



$$E_s = E_1 + E_2 + E_3 + U(R_{12}) + U(R_{23}) + U(R_{13}) + u(R_{12}, R_{23}, R_{13})$$

Figure 1.5 Three body interactions and non-additivity

Generally, the terms of order higher than three are small enough to ignore [4]. The three-body effects are large enough to affect the form of the potential and for simplicity the two-body potential is slightly modified to include a component representing the average three-body effects in the two-body potential. This potential is called the 'effective' two-body potential:

$$E_s(R) = \sum E_N + \sum \sum v_2^{\text{eff}}(R_i, R_j). \tag{1.7}$$

The three body term contributes about 10% of the total interaction energy in liquid argon.

1.4.3 Molecular Systems

If we consider a system of N molecules such as Cl_2 or CCl_2F_2 , the system is further complicated in that

- (i) the intermolecular-effective-pair potential between every atom on every molecule must be considered,
- (ii) the molecules are free to rotate (energy = RE),
- (iii) the atoms in the molecule freely vibrate (energy = VE).

The most complete description of the interactions in a molecular liquid is given by a $g(R)$ dependent upon both the distance and orientation of the molecules, $g(R_i, R_j, w_i, w_j)$. An anisotropic potential that considers the orientation of the molecules will best describe such a system. However, due to the number of variables involved, neither $g(R_i, R_j, w_i, w_j)$ nor the corresponding anisotropic potential are simple functions to calculate. The most popular alternative (the one used in this study) is one that ignores orientational effects and considers $g(R)$ only in terms of the distance that the atoms in the liquid are apart, $g(R_{ij})$.

Consider as an example the two diatomic molecules shown below in figure 1.6.

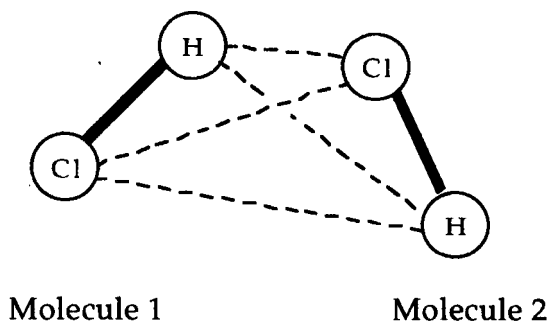


Figure 1.6 The four pairwise interactions for a HCl molecule

There are 4 atom-atom pairwise intermolecular interactions which make up the total pair distribution function, $g(\mathbf{R})$,

$$g(\mathbf{R}) = g_{\text{HH}}(R_{\text{HH}}) + 2g_{\text{HCl}}(R_{\text{HCl}}) + g_{\text{ClCl}}(R_{\text{ClCl}}). \quad (1.8)$$

The subscripts in g_{ab} show that this is a partial pair distribution function for the atoms a and b ; the subscripts in R_{ab} are often missed out. Equation (1.8) is more complicated for neutron diffraction pair distribution functions because the scattering lengths of the atoms in the liquid influence the proportion of the individual $g_{ab}(\mathbf{R})$ which make up the total. Other functions that describe the pair distribution of liquids are described in the review by Andreani *et al.* [5].

The energy of a molecular system, ignoring orientational effects, is

$$E_s(\mathbf{R}) = \sum \text{TE} + \sum \text{RE} + \sum \text{VE} + \sum \sum v_{ab}(R_{ab}), \quad (1.9)$$

where, TE is the translational kinetic energy, R_{ab} is shorthand for $R_{ia}-R_{jb}$, and $U(\mathbf{R}) = \sum \sum v_{ab}(R_{ab})$, the effective pair potential.

The simulations of such liquids are usually simplified by holding the intramolecular structure rigid at the average intramolecular separation so that the simulation does not have to calculate vibrational or internal-rotational energies. There are, however, simulation routines now appearing on the CCP5 library which allow internal degrees of freedom. This is especially important when deriving the structure of liquids such as C_2F_6 whose structure may be dependent on the rotation of the C–C bond.

For a molecule such as CCl_2F_2 there are 25 two-body potentials to consider (as will be seen in Chapter 3). However, the general potential shown in equation (1.9) still holds.

1.5 The Makeup of Two-Body Intermolecular forces

The intermolecular pair potential can be split in two parts

$$U(R) = \phi_A + \phi_R, \quad (1.10)$$

where ϕ_A is the attractive part and ϕ_R the repulsive part.

1.5.1 The Attractive Energy, ϕ_A

The attractive energy (for non-ionic molecules) has three contributions

- (a) interaction between two permanent dipoles, ϕ_p ,
- (b) interaction between an induced dipole in one molecule and the permanent dipole of another, ϕ_i ,
- (c) interaction between instantaneous dipoles or London attraction, ϕ_L .

1.5.1(a) Permanent Dipole - Permanent Dipole (or Electrostatic) Attraction Energy, ϕ_p .

This is the type of interaction that occurs in polar molecules containing a permanent electric dipole and examples are shown in figure 1.7 for the simple two-dimensional case of two diatomic molecules.

The two molecules can be orientated at any angle to each other, and the strength of the electrostatic force between them is related to both orientation and separation. The electrostatic energy would average to zero if each of the orientations had an equal probability. However, attractive orientations (where partial positive charges face partial negative ones, figures 1.7(a,b)) are more favourable than repulsive ones (figures 1.7(c,d)). Attractive alignments are the lower energy orientations and thus they are

more probable. The average energy of the electrostatic interactions is an attractive one proportional to $-1/R^6$ and is given by [7]

$$\phi_p = -2(P_1P_2/4\pi\epsilon_0)^2(1/R)^6(1/3kT) + \dots, \quad (1.11)$$

where P_1 and P_2 are the dipole moments, ϵ_0 is the permittivity of free space and k is the Boltzmann constant.

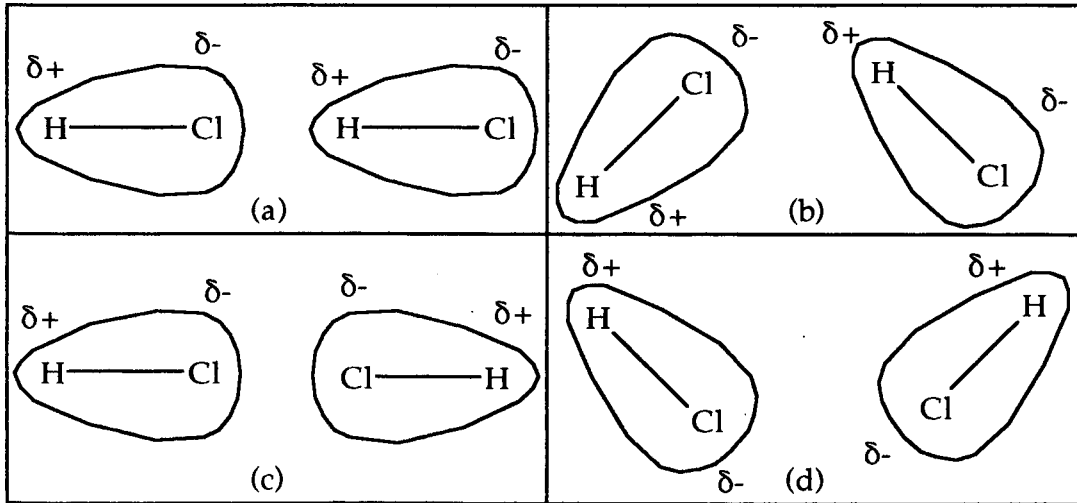


Figure 1.7 The electrostatic interactions of H-Cl; (a), (b) are attractive, (c), (d) are repulsive

ϕ_p decreases as temperature increases. This is because thermal motion is randomising and thus thermal agitation destroys the mutual orientation effects of two dipoles.

From equation (1.11) the magnitude of the potential depends upon the size of the dipole moments. HF and H₂O molecules have very large dipole moments and are said to form 'hydrogen bonds'. The effect of hydrogen bonding is reflected in the high enthalpy of vaporisation of these liquids.

Note that, although the energy depends upon the orientations of the molecules and the distance between them, equation (1.11) depends

only upon the distance between the molecules. This is due to the Boltzmann averaging of all the different orientations of the dipoles; this introduces the temperature dependence into the potential equation.

Higher terms in equation (1.11), as signified by are due to other permanent interactions such as dipole-quadrupole and quadrupole-quadrupole. These all contribute to the electrostatic energy to varying extents. For example, carbon dioxide contains a permanent quadrupole (figure 1.8). The quadrupole can be considered as two dipoles back-to-back.

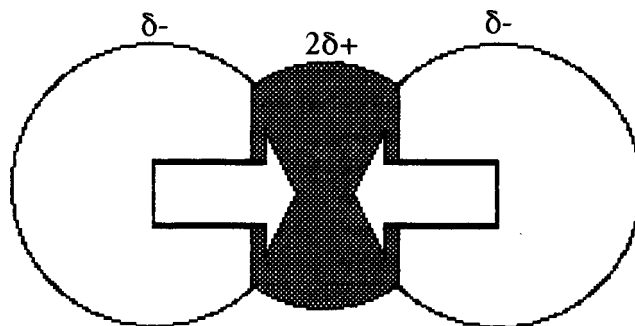


Figure 1.8 CO₂ as an example of a quadrupole

1.5.1(b) Induction Energy, ϕ_i

The induction energy arises when (i) a molecule containing a permanent dipole is in the vicinity of a similar molecule, and (ii) a molecule containing a permanent dipole is in the vicinity of a non-polar molecule. The permanent dipole of the polar molecule induces a dipole in a nearby molecule. This is a mutual effect for two permanent dipoles. In the other case, the nearby permanent dipole causes a distortion of the electrons in the non-polar molecule. The non-polar molecule is consequently attracted to the permanent dipole. The average energy of this is again proportional to $-1/R^6$ and is given by

$$\phi_i = -\alpha_1(P_2/4\pi\epsilon_0)^2 (1/R)^6 + \dots, \tag{1.12}$$

for polar-non-polar interactions, and by

$$\phi_i = -2\alpha_1(P_2/4\pi\epsilon_0)^2 (1/R)^6 + \dots, \tag{1.13}$$

for polar-polar interactions.

In equations (1.12) and (1.13), α_1 is the polarisability of the molecule whose electric field is being distorted by the permanent dipole and P_2 is the dipole moment of the inducing molecule.

There is no temperature dependence for this potential; the induced moment is always parallel to the field [6]. This is a simplistic treatment of the induction energy since it ignores all higher-order multipole effects.

1.5.1(c) London or Dispersion Energy, ϕ_L

Dispersion (or London) forces are the only ones present in all molecular systems. Molecules that are thought of as non-polar such as Ar or CCl_4 (although the latter contains a permanent octopole (figure 1.9)) are still attracted to one another due to these forces.

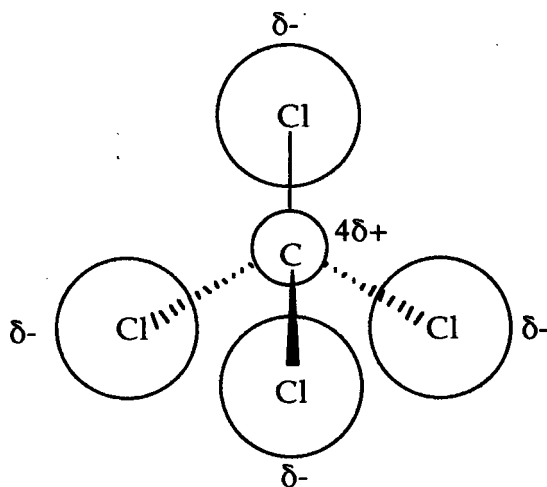


Figure 1.10 CCl_4 as an example of an octopole.

London forces exist due to instantaneous dipole moments arising in the electron clouds of atoms on molecules. The dipole averages to zero over a period of time but nevertheless exists in an instant. This instantaneous dipole induces a similar dipole in a neighbouring atom on another molecule, leading to an attraction between them. The quantum mechanical treatment of this is explained in references [1, 7] but ϕ_L has been calculated to be proportional to $-1/R^6$ (and related to the polarisability of the atoms in the molecule). This is a simplistic picture of the actual potential because in addition to the instantaneous dipole-dipole energy, there are instantaneous dipole-quadrupole interactions, quadrupole-quadrupole interactions, etc. The dispersion energy is more fully written as $C_6/R^6+C_8/R^8+C_{10}/R^{10}+\dots$. The value of C_6 (equation (1.14)) has been approximated by London from an oscillator model (see reference [7] for a detailed account of the derivation) but it is more accurately obtained from quantum mechanical perturbation theory [7].

$$C_6 = -\left(\frac{3}{2}\right) \left(\frac{I_1 I_2}{I_1 + I_2}\right) \frac{\alpha_1 \alpha_2}{(4\pi\epsilon_0)^2}, \quad (1.14)$$

where I_1 and I_2 are ionization energies.

C_8, C_{10} and the higher order terms are not readily obtained from theory.

1.5.2 The Resultant Attractive Energy

The total attractive energy is given by equation (1.15)

$$\phi_A = \phi_p + \phi_i + \phi_L. \quad (1.15)$$

In this simplistic treatment, all the separate components of ϕ_A are related to $-1/R^6$. Hence we can write

$$\phi_A = -A/R^6, \quad (1.16)$$

where A is dependent upon the types of molecules that constitute the liquid.

For example, the attractive potential energy between two HCl molecules (ignoring higher-order multipole/quantum effects) is given by

$$\phi_A = -(1/4\pi\epsilon_0)^2 \{(2P^4/3kT) + (2P^2\alpha) + (3\alpha^2I/4)\}(1/R)^6. \quad (1.17)$$

ϕ_L nearly always makes the largest contribution to ϕ_A even in polar molecules. An exception to this is water, which is a small very highly polar molecule. In non-polar molecules ϕ_L is the only contribution, and is often referred to as the van-der-Waals interaction energy. The induction energy is always the smallest contribution. There may or may not be a temperature dependence of the potential - this depends upon the molecules making up the liquid. For HCl the magnitude of the potential will depend upon the temperature because it contains a permanent dipole. For Ar, which is held together only by van-der-Waals' forces, there is no temperature dependence inherent in the potential.

1.5.3 The Repulsive Energy, ϕ_R

The repulsive energy arises when two molecules approach each other very closely so that their electron clouds overlap. It is a consequence of the Pauli exclusion principle: *No more than two electrons may occupy any given orbital, and if two do occupy one orbital, their spins must be antiparallel.* Consider as an example the two helium atoms approaching each other in figure 1.10. Their 1s orbitals are completely filled with two

electrons apiece. When the orbitals overlap three or four electrons attempt to occupy the space reserved for only two electrons, and there is a mutual repulsion of the helium atoms.

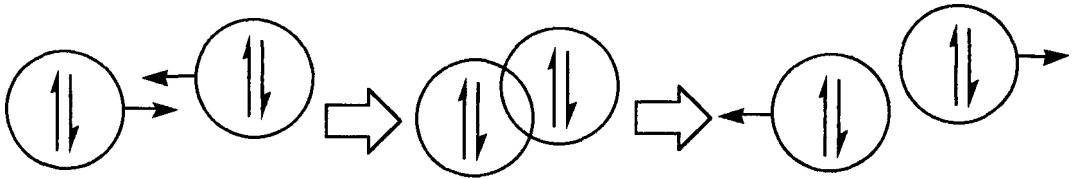


Figure 1.10 Repulsion of He atoms due to the Pauli principle

This is not the case when two hydrogen atoms approach each other. The two 1s orbitals are half filled and a reaction between the two atoms may take place when the distance between them is sufficiently small (figure 1.11).

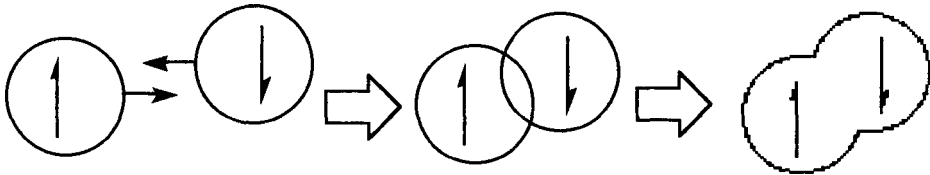


Figure 1.11 The reaction between two H atoms

The form of the repulsive potential is difficult to derive even for simple systems. It can, however be approximated to

$$\phi_R = B/R^n, \tag{1.18}$$

where B and n are constants.

An exponential form of the potential, known as the exp(-6) potential can also be used instead [7].

1.5.4 The Resultant Potential

Putting the attractive and repulsive potentials together in equation (1.10) we get

$$U(R) = B/R^n - A/R^6 \quad (1.19)$$

From this, in 1931, Lennard-Jones derived the **Lennard-Jones** [8] or **LJ 12-6** potential function,

$$U(R) = 4\epsilon[(\sigma/R)^{12} - (\sigma/R)^6], \quad (1.20)$$

where $A=4\epsilon^6$, $B=4\epsilon^{12}$, and $\sigma=R_{eq}/2^{1/6}$.

This function has been used in this study to perform the Molecular Dynamics calculations.

The LJ potential (which has a form similar to that shown in figure 1.4) was the one used in this study because it is the simplest differentiable potential to give meaningful simulations. In simpler computer simulations, a potential that ignores the attractive part of the potential, the hard-sphere model, is used. The molecules are considered to act like billiard balls in that they are deflected away from one another when they interact at a distance σ as shown in figure 1.12.

There are other pair-potential models (some more realistic than the LJ 12-6, some less so) which can be used to model liquid structure computationally and these are neatly explained in Appendix 1 of reference [7]. Further description of the mechanics of the simulations using the LJ model, including the long range correction added to produce better comparison with experimental data, is given in Chapter 3. The most modern potentials used in simulations are described in section 1.7.

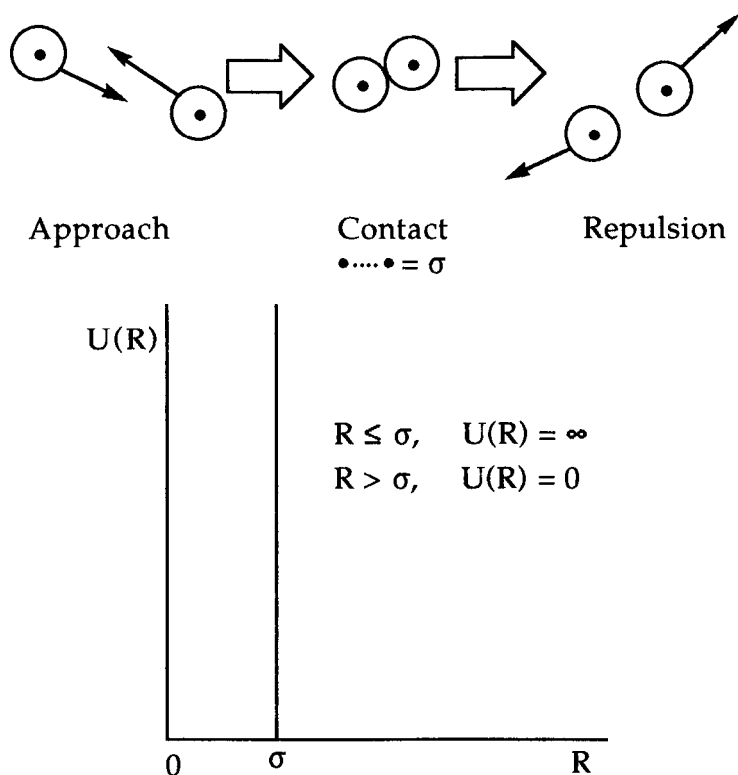


Figure 1.12 The hard-sphere potential. σ is roughly equal to the sum of the van-der-Waals radii of the interacting atoms

1.5.5 The Potentials for Liquid Halocarbons

The molecules studied in this thesis were dichlorodifluoromethane (CCl_2F_2), chlorodifluoromethane (CHClF_2), chlorotrifluoromethane (CClF_3), trichlorofluoromethane (CCl_3F), fluoroform (CHF_3) and bromotrifluoromethane (CBrF_3).

The gross attractive potential of a halocarbon is dependent upon the dipole moment, the polarisability and the ionisation energy of the molecule as shown in equation (1.17), which is also applicable to the fluorocarbons. These parameters are shown in table 1.1 for the halocarbons of interest in this study. Table 1.2 shows the gross contributions of the electrostatic, induction and dispersion parts to the molecular attractive energy at 153 K, the temperature chosen for the neutron diffraction

experiments in this study. These values give an idea of the magnitude of the contributions to the potential. For, example, the electrostatic interaction plays a far more important role in the attraction of two CHF₃ molecules than in the attraction between two CCl₂F₂ molecules.

Molecule	Dipole Moment, P/ D [43]	Polarisability, $\alpha/ \text{\AA}^3$	Ionisation Energy, I/ eV
CClF ₃	0.50 ± 1%	5.59 [43]	12.91 ± 0.03 [43]
CBrF ₃	0.65 ± 5%	9.75 [44]	11.89 [43]
CHF ₃	1.65 ± 0.1%	2.80 [45]	14.8 [46]
CHClF ₂	1.42 ± 2%	5.91 [43]	12.45 ± 0.05 [43]
CCl ₃ F	0.45 ± 5%	8.24 [45]	11.77 ± 0.02 [43]
CCl ₂ F ₂	0.51 ± 5%	7.81 [43]	12.31 ± 0.05 [43]

Table 1.1 The dipole moment, polarisability, and ionisation energy of selected halocarbons

Molecule	Electrostatic Energy $-\phi_p R^6/ J \text{\AA}^6$	Induction Energy $-\phi_i R^6/ J \text{\AA}^6$	Dispersion Energy $-\phi_L R^6/ J \text{\AA}^6$
CClF ₃	1.97 x 10 ⁻¹⁹	2.80 x 10 ⁻¹⁹	4.85 x 10 ⁻¹⁷
CBrF ₃	5.64 x 10 ⁻¹⁹	8.24 x 10 ⁻¹⁹	1.36 x 10 ⁻¹⁶
CHF ₃	2.34 x 10 ⁻¹⁷	1.53 x 10 ⁻¹⁸	1.39 x 10 ⁻¹⁷
CHClF ₂	1.28 x 10 ⁻¹⁷	2.38 x 10 ⁻¹⁸	5.23 x 10 ⁻¹⁷
CCl ₃ F	1.30 x 10 ⁻¹⁹	3.34 x 10 ⁻¹⁹	9.60 x 10 ⁻¹⁷
CCl ₂ F ₂	2.14 x 10 ⁻¹⁹	4.06 x 10 ⁻¹⁹	9.00 x 10 ⁻¹⁷

Table 1.2 The contributions to the attractive energy of the electrostatic, induction, and dispersion parts at 153 K.

The potential used in the simulation work in this study was the LJ (12-6) potential which considers each atom separately, rather than modelling the molecule as a single entity. Better sophistication still might be achieved by modifying the potential depending on the type of atom involved. The repulsive part for fluorine or hydrogen could be made harder by using a value of n greater than 12 (possibly as high as 30 or 40) or by modelling it as a hard sphere. The repulsive part for bromine could be made softer by using a value of n less than 12. However, this would increase the computation time which would be warranted only when the 12-6 potential could not model the diffraction results effectively.

1.6 A Review of Recent Literature

There has been a whole host of work looking at liquid structure and dynamics, and reviews have been written by Andreani *et al.* [5], Evans [9], and Evans and Evans [10]. However, only a minority of this experimental work involving liquids has been using neutron diffraction, so there are few comparative studies of neutron diffraction and molecular dynamics. This section is devoted to outlining some of the comparative studies starting from simple monatomic systems. First some of general comments are listed.

1.6.1 General Results

There are some general results that apply to all simulations and these are listed below:

(i) "one of the factors influencing, and sometimes dominating, the structure of a liquid is simply the geometrical problem of stacking together a lot of hard spheres" [11]. Even if liquid molecules are modelled as hard spheres (figure 1.12) with no attractive interactions some structure is still apparent. The attractive well of the LJ potential is a necessary part of any more accurate model of liquid structure; it modifies the hard sphere model "by gathering and trapping particles into each other's vicinity" [11].

(ii) results of structural investigations show that on a local level, a significantly-orientated structure exists in liquids [10] but according to Bossis *et al.* [12], even in intensely dipolar molecules, medium-range correlations disappear at roughly 10 Å.

(iii) in some MD simulations an effective Coulomb partial charge-partial charge interaction ($z_1 z_2 / 4\pi\epsilon_0 R_{ij}$, where z_1 and z_2 are the effective partial-charges on the interacting atoms) term is added to the LJ potential to account for 'ionic' long-range interactions [13]. The Coulomb interaction is described by 'fictitious' partial-point charges distributed on the interaction sites in a quasi-realistic way in order reproduce known multipole moments [13]. Any difference between the results from the potentials with and without charges reflects the sensitivity of the electrodynamic parts of the pair potential [10].

(iv) in a neutron diffraction experiment a time-averaged 'picture' of how close fluid molecules approach one another is given. This is generally given as

- (a) a total structure factor, $S(Q)$ in reciprocal space,
- (b) an intermolecular structure factor, $D_M(Q)$ in reciprocal space,
- (c) a pair distribution function, $g(R)$ in real space,
- (d) an intermolecular pair distribution function, $d(R)$ in real space.

1.6.2 Argon - A Monatomic Fluid

Argon is one of the 'simplest' of all substances to study. It is a spherically symmetrical atomic liquid with no permanent dipole moment, whose atoms are held together solely by London forces. Amongst the most accurate estimates of the effective-pair potential between two atoms of argon are the Maitland-Smith (BBMS) [14] and Barker-Fisher-Watts (BFW) [15] potentials. They combine a wide variety of experimental data (molecular-beam-spectroscopy, second virial coefficients, solid state properties) with a theoretical calculation of long-range order to provide a potential that is consistent with gas-phase transport coefficients. The LJ 12-6 potential, which is widely used in liquid simulation studies, is a reasonably good model for argon only if the values of ϵ and σ are carefully chosen ($\sigma = 3.405 \text{ \AA}$, $\epsilon/k = 125.2 \text{ K}$ [16]). These values, however, are not the ones that would apply to an isolated pair of argon atoms, especially since they include a correction for three-body effects. The LJ potential for argon is compared with the BBMS potential in figure 1.13.

In 1973, Yarnell *et al.* [17] performed a very careful neutron diffraction study of liquid argon near its triple point. They found excellent agreement between their experimental $S(Q)$ and one given by a LJ effective-pair potential molecular dynamics simulation, as can be seen in figure 1.14. They also compared their experimental $g(R)$ with both a LJ molecular dynamics simulation and one obtained from a Monte Carlo calculation based on the BFW potential [15]. They found excellent agreement again between experiment and simulation and the two simulations were almost indistinguishable. This shows that the effective LJ potential is a useful tool in describing liquid structure. It is interesting to

show that the simulated $S(Q)$ obtained using the LJ potential (figure 1.15) is better than that obtained using the hard sphere potential (figure 1.16).

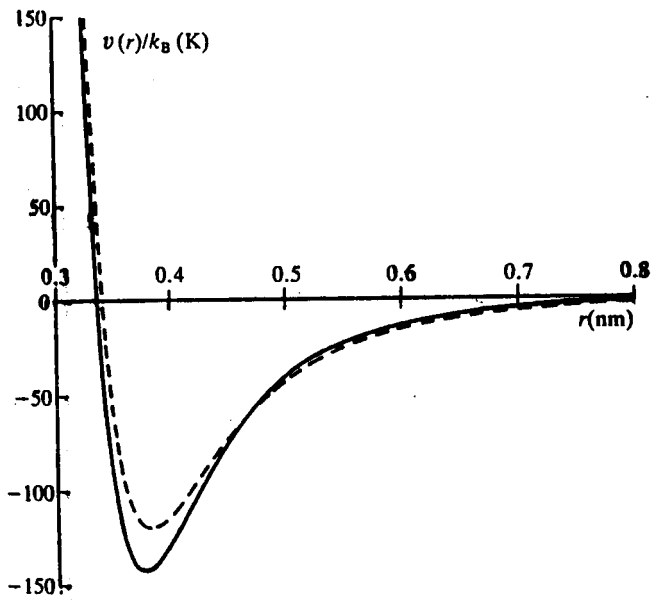


Figure 1.14 A comparison of the BBMS (solid line) and LJ (dashed line) pair-potentials for argon. The BFW potential is numerically very similar to the BBMS potential [13]

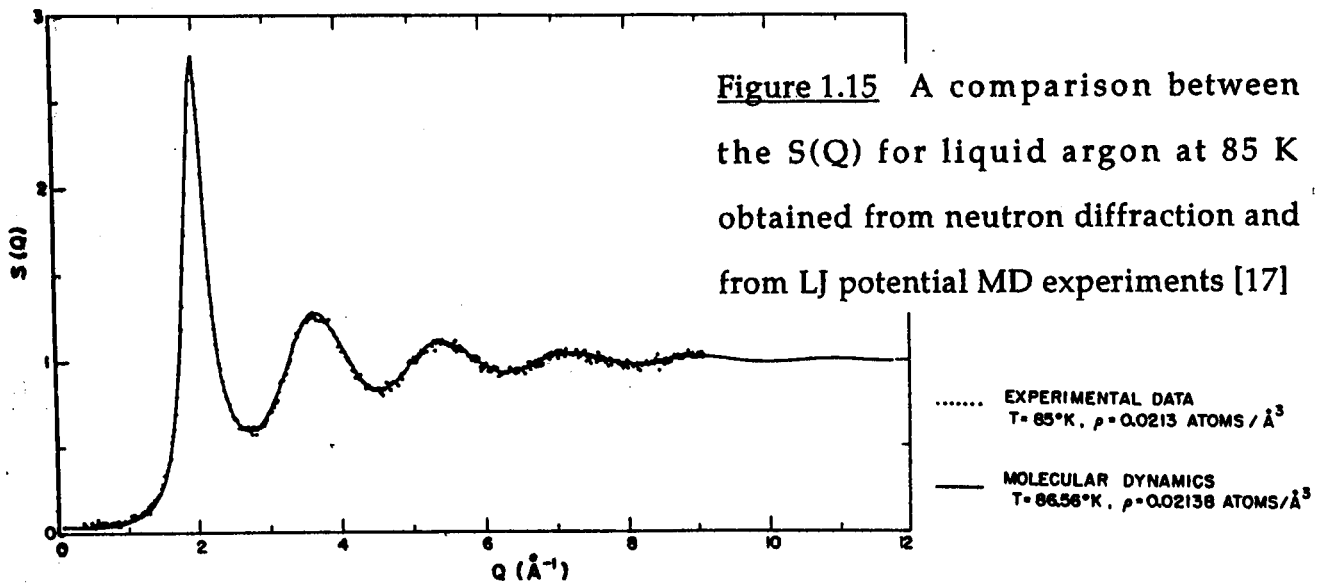


Figure 1.15 A comparison between the $S(Q)$ for liquid argon at 85 K obtained from neutron diffraction and from LJ potential MD experiments [17]

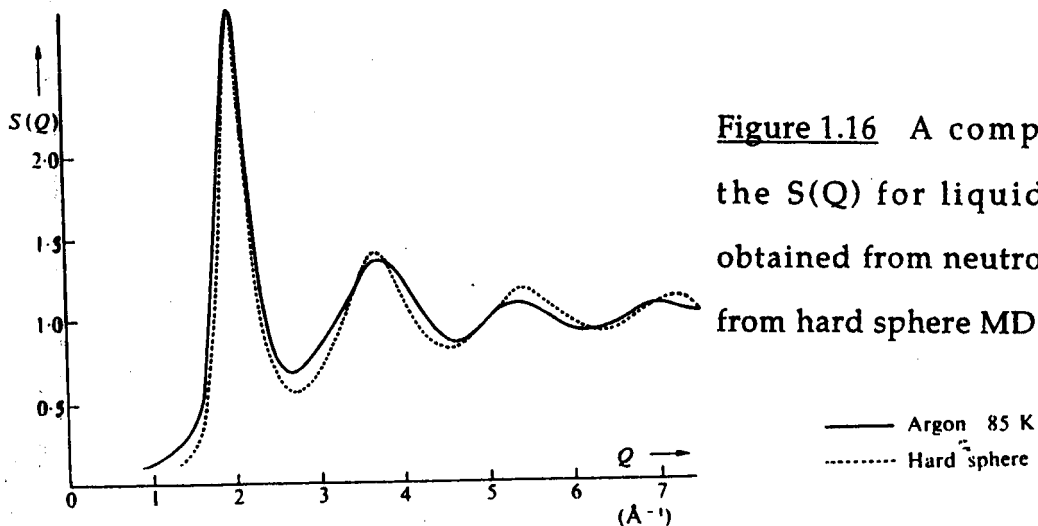


Figure 1.16 A comparison between the $S(Q)$ for liquid argon at 85 K obtained from neutron diffraction and from hard sphere MD experiments [18]

1.6.3 Trichloromethane (CHCl_3)

Trichloromethane, a tetrahedral molecule, is one of the most widely studied liquids. There are over 100 papers published on its structure and dynamics.

Evans [9] compared his computer simulation of liquid trichloromethane, using a partial-Coulomb-charge-modified LJ potential, with the individual pair distribution functions (g_{CC} , g_{ClCl} , and the sum of the g_{ClH} and g_{CCl} pdfs) derived from a number of neutron diffraction studies [19-25]. The compounds studied were CHCl_3 (natural abundance) and a variety of different isotopically labelled molecules (CDCl_3 , $\text{CD}^{35}\text{Cl}_3$, $\text{CD}^{37}\text{Cl}_3$). The pair distribution functions were similar but detailed agreement was not obtained. He associated this with:

- (i) diffraction data can only give a one-dimensional quantity $g(R)$ which is an average of the angular dependence of a number of quantities [i.e., $g(R)$ describes the structure in terms of the distance atoms are away from each other rather than their orientation to one another],
- (ii) modern instrumental precision is only roughly 1% which is barely adequate; when coupled with data reduction problems and systematic errors, disagreement is inevitable. In fact, even different experiments performed on the same liquid sometimes disagree. It is important that both experiments and data reduction are accurately performed to minimise these errors.

He summarised his work with the comment "The data survey and simulation both point to the need for a coordinated effort at obtaining more accurate and wider ranging data, and to develop and improve currently available theoretical and data-reduction methods".

1.6.4 Dichloromethane (CH_2Cl_2)

Kneller and Geiger studied dichloromethane in 1989 [21]. They compared the MD simulations of two potentials (exp-6 and LJ) with the neutron diffraction results of Jung *et al.* [27].

Both of the potentials used in the MD simulations reproduced the diffraction results quite well for all isotopic mixtures of dichloromethane. There were a few dissimilarities that were attributed to problems in the data reduction especially with the inelasticity corrections. They were confident enough, however, to consider their two potentials, which gave similar results, to be good models of the structure of CH_2Cl_2 .

1.6.5 Tetrachloromethane (CCl_4)

The structure of CCl_4 seems to have caused researchers problems over the years [28]; even the dependence of the structure upon the long-range electrostatic term (the octopole-octopole interactions) is in question. Gubbins [29] said that the structure of CCl_4 depends upon these interactions, whereas the other groups [28,30-32] said that there is no such dependence.

Egelstaff *et al.* [30] believed the local structure of CCl_4 could be explained by the so-called APOLLO, or ROCKET, (figure 1.16(a)) conformation.

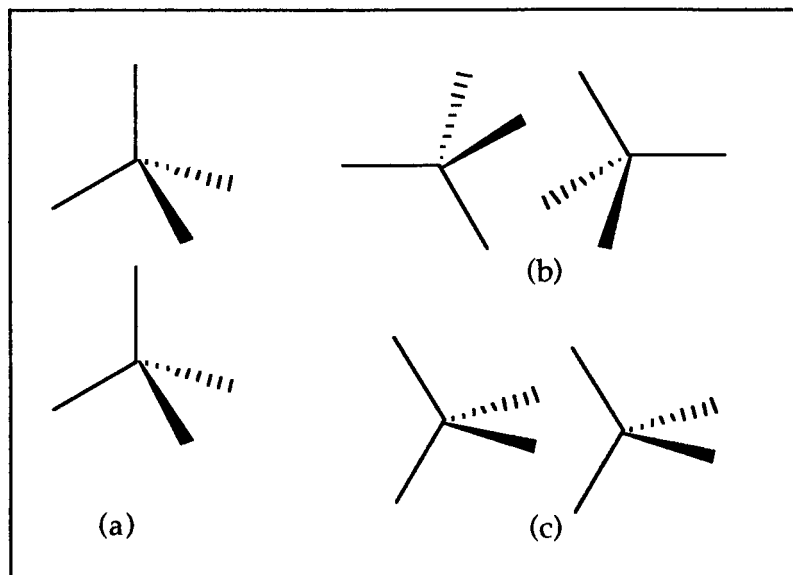


Figure 1.16 Proposed structures of tetrachloromethane (a) APOLLO structure [30], (b) INTERLOCKING structure [31], (c) STRADDLE structure.

Using a technique called RISM analysis (which will not be discussed here), Lowden and Chandler [31] described the local ordering in terms of the INTERLOCKING structure shown in figure 1.16(b). McDonald *et al.* [32] proposed, on the basis of their LJ model, that the conformation shown in figure 1.16(c), which in this thesis, will be referred to as the STRADDLE conformation, is the most important. McDonald *et al.* felt that the Apollo conformation was also important but discounted the existence of the interlocking conformation of Lowden and Chandler. The RISM and LJ analyses give similar results and both give good agreement with experimental data. The differences in the proposed structures is one of interpretation. I am inclined to agree with McDonald *et al.*'s [32] conclusions. A more thorough quantitative analysis of the computer data, including integrations of the peaks in the individual $g(R)$, would be helpful in a clearer derivation of the structure.

1.6.6 Other Comparative Studies of Polyatomic Molecules

H. J. Böhm *et al.* studied a variety of different liquids using Molecular Dynamics simulations [33, 34]. They were able to compare some of their simulation results with the intermolecular structure factors given from diffraction studies. The liquids studied were; chloromethane, CH_3Cl (they found only fair comparison at best), acetonitrile, CH_3CN , carbon dioxide CO_2 and carbon disulphide CS_2 (all three gave good agreement, although peak heights were generally underestimated), dichloromethane CH_2Cl_2 (good agreement except for the height of the first peak and its shoulder - they were unable to account for this discrepancy) and trichloromethane CHCl_3 (excellent agreement for natural-Cl abundance CDCl_3 , slight agreement for CHCl_3 and CD^{35}Cl , but no agreement at all for CD^{37}Cl - attributed to experimental problems when using ^{37}Cl).

The most recent analysis of a quasi-tetrahedral molecule was for acetonitrile, CH_3CN [35]. Ohba and Ikawa performed two LJ-type simulations; one including fractional charges (LJ+FC), the other excluding them (LJ). The large gas phase dipole moment of CH_3CN indicated that a dipole-dipole interaction could be important to the local structure in the liquid. Ohba and Ikawa attempted to discover the extent that the dipole-dipole interaction had on the structure. They calculated a centre-of-mass $g(\text{R})$ for the charged and non-charged potentials, which surprisingly gave essentially the same results. A comparison with X-ray experimental results was excellent for both simulations. However, further analysis showed that the angular correlations for the centres of mass were completely different; the LJ+FC simulation showed significant angular correlations between the centres of mass, whereas the LJ simulation showed none. The paper gives no interpretation of the orientational structures which ensue from such

differences, and does not show the total $g(R)$ or the individual $g(R)$ for this compound. The differences between the two simulations would have been shown equally well by comparing the individual $g(R)$; if angular correlations determined the structure of CH_3CN , the differences would appear in the $g_{\text{NH}}(R)$.

1.6.7 Water

The most important liquid for study is water and, typically, water is one of the most difficult compounds to study using diffraction techniques. Hydrogen is almost 'invisible' to X-rays, and ^1H has a high inelastic and incoherent scattering behaviour with neutrons, coupled with a negative scattering length. Heavy water (D_2O) is generally accepted as an effective replacement for H_2O . It does have different chemical and physiological behaviour but its averaged structure, 'visible' by neutron diffraction, is believed to be a useful model for the structure of H_2O . Although incoherent scattering from D_2O is moderate, the problem of inelasticity is a factor in D_2O studies and Placzek corrections (which are not trivial for H_2O or D_2O - about 20% at 10 \AA^{-1} [36]) need to be performed with some care. Even the bond distances and angles have been difficult to derive with any degree of accuracy due to the uncertainty in the data reduction.

Page *et al.* [36] limited their diffraction analysis to $Q < 10 \text{ \AA}^{-1}$ in their 1971 study of D_2O at $22 \text{ }^\circ\text{C}$. They attempted to model the derived structure factor, $S(Q)$ but had little success. Their study involved estimating the form factors for; an uncorrelated model, three correlated (the icy, the watery and the clathrate) H-bonded models and a correlated non-H-bonded model. They attempted to relate these to the diffraction data, but found no similarities.

Powles (1981) [37] took the diffraction data of Walford *et al.* [38] and reinterpreted it with a better data-reduction technique to give new estimates of the O-D ($0.983 \pm 0.008 \text{ \AA}$) and D-D ($1.55 \pm 0.02 \text{ \AA}$) atomic separations. Although he did not perform any MD simulations of the water structure, his results are worth noting. He wanted to discover whether the structure of water was similar to that of ice I (the simplest solid phase in water), or closer to that in the gas, by relating the bond distances he had derived from Walford *et al.*'s diffraction data with those previously given for ice I. He was unable to give any firm conclusions as to the structure of water due to the inconsistency of other diffraction studies:

"If we accept the value 1.01 \AA for [the O-D bond distance of] Ice I then we conclude that the D_2O molecules in liquid heavy water are much more like vapour molecules [where the bond distance is shorter implying the H-bonding is weaker] and so the intermolecular interactions are much weaker than they are in Ice I. As some would put it, they form fewer or weaker hydrogen bonds.

If we accept the value 0.983 \AA for ice I (as some would have it) then we say that the bond length observed in the liquid is nearer to that of ice than to that in the vapour.....In this case greater experimental accuracy and better theoretical corrections are required before we can assess the importance of intermolecular interactions in the condensed phases on the O-D distance in particular and on the molecular structure in general."

His remarks accurately sum up the problems of relating experimental data to the structure of fluids.

In 1987, Teleman *et al.* [39], reported their molecular dynamics simulation work on water but failed to compare their data with diffraction

studies, which is unfortunate since their model incorporated intramolecular flexibility into one of their LJ-type simulations.

1.7 Building Better Potentials

The search for a better potential is similar to that for a better equation of state. We can link the hard sphere potential to the ideal gas equation and the LJ potential to the van-der-Waals equation of state. We would ultimately like a 'realistic' potential that can perform a number of functions:

- (i) model solid, liquid and gas structure
- (ii) model solid, liquid and gas dynamics
- (iii) predict phase changes
- (iv) accurately reflect thermodynamic behaviour

Obviously, the potential and the equation of state of a fluid are inextricably linked; the structure and dynamics of a fluid, influenced by the potential between the molecules in a system, is reflected in the equation of state, i.e. the macroscopic properties depend upon microscopic behaviour. The phase changes, solid-liquid and liquid-gas, depend upon the nature of the potential of the system. Consider argon; its liquid range is only 3 K due to the weak attractive forces binding the molecules together. Its low melting point (87 K) is also a consequence of this. Conversely, the only reason solid and liquid argon form is due to the existence of the London forces. Water, on the other hand, has a liquid range that extend from 273 to 373 K. The molecules of H₂O are associated by the formation of hydrogen bonds; the attractive forces in water are strong.

In order to build better potentials our models must be able to realistically reproduce experimental data. Just as the van-der-Waals

equation of state collapses near the critical point, the LJ potential gives poor results when modelling highly associative or highly anisotropic liquids.

Sarah Price and others have attempted to build better potentials. A recent paper by Price was called "Is the isotropic atom-atom model potential adequate?" [40]. Using the highly accurate argon potential as a starting point, she attempted to map out the shortcomings of the LJ (and related) potentials and to address them in a systematic way.

The Barker-Pompe or Barker-Fisher-Watts (BFW) potential for Ar is

$$U(R)/\epsilon = \exp[\alpha(1-R/R_{eqm})]\sum A_i(R/R_{eqm}-1)^i + \sum C_{2j+6}/(\delta+(R/R_{eqm})^{2j+6}). \quad (1.22)$$

The second summation is the attractive part and considers the higher order effects up to four-body interactions (C_{10}). δ is a small non-physical parameter (~ 0.01) and α is a parameter which measures the steepness of the repulsive potential energy ($\sim 14-15$). The first term models the repulsive wall. The form of the repulsive wall can be manipulated to fit the experimental data via the disposable form parameters, A_i .

The equation can account for a wide range of properties but it is complicated; there are 13 adjustable parameters - and this is a simple system. Diatomics are the next simplest systems. The LJ-type potentials may not be good models of the system for many reasons:

- (i) long range electrostatic interactions are not well modelled by point charges,
- (ii) induction energy is highly non-additive and 'effective' potentials are often imprecise,
- (iii) the LJ potential ignores the effects of orientation, known as anisotropy, on the molecules in the liquid.

To address these points, Price chose Cl_2 as her example. In LJ potentials the long range interactions of Cl_2 are modelled using a point quadrupole; that is, a negative charge on each Cl atom and a doubly positive charge at the centre of the molecule. The LJ potential considers only the dipole-dipole interactions between these point charges. They are proportional to $1/R^3$. Using an *ab initio* technique for mapping the electron density of Cl_2 , Price showed that this is an inaccurate model. Electron density builds up at the lone pairs of the Cl atoms and a refined model of the charge distribution is a point charge on each Cl atom plus a quadrupole and dipole on each atom (retaining the overall neutrality of the molecule of course). This is an effect of the redistribution of electron density when bonding occurs between the two Cl atoms; the point quadrupole used in the LJ potential assumes spherical geometry for each Cl atom. The charge distribution, which can be modelled using the distributed multipole analysis [41], helps to define the orientations of the liquid atoms because the charge distribution is scattered rather than spherically arranged. The potential for the long-range interactions in this model includes dipole-dipole (proportional to $1/R^3$), dipole-quadrupole ($1/R^4$) and quadrupole-quadrupole ($1/R^5$) effects.

The problem with anisotropy is, that in order to model it, we need to know how the molecules are orientated, which defeats the object. However, a good indication of the types of orientations which exist in the liquid is the orientations of the molecules in the solid; the dispersion terms C_6 (two-body) and C_8 (three-body), and the orientational dependence terms of the attractive and repulsive potentials, are generally optimised to the solid structure as a starting point.

In 1990, Wheatley and Price [42] published a potential for Cl_2 which included all the terms mentioned above, i.e.

- (i) two-body and three-body anisotropic dispersion terms
- (ii) anisotropic repulsion terms
- (iii) long-range dipole-dipole, dipole-quadrupole and quadrupole-quadrupole terms

They found that their potential could satisfactorily be used to predict certain thermodynamic behaviour, both for solids and liquids. However, their potential did not accurately reflect neutron data at 200 K. The reason for this, they felt, may be problems with the experimental data [42].

It only remains to add that Price advises "Computer simulation is too powerful a technique to be kept in storage awaiting progress in the quantification of intermolecular forces.....Simple potentials will be good enough for many purposes."

1.8 Summary

Lennard-Jones pair potentials are generally useful for molecular dynamics computer simulations of liquid properties. The simulations never reflect perfectly the pair-distribution functions given by neutron diffraction for whatever reason but are, however, very useful starting points for the derivation of liquid intermolecular structure.

Theoreticians believe the main problem with the comparative studies of neutron diffraction data and computer simulations are the general lack of good experimental work to test their potentials. A criticism sometimes levelled by experimentalists is the unreliability of the computer simulations. In this study it is hoped to reconcile both fields by acquiring good experimental data and comparing that data with reliable molecular dynamics computer simulations.

REFERENCES

- [1] TEMPERLEY, H. N. V. and TREVENA, D. H., 1978, *Liquids and their Properties - A Molecular and Macroscopic Treatise with Applications*, (Ellis Horwood Limited).
- [2] VAN-DER-WAALS, J. D., *Doctoral Dissertation*, 1873, Leiden, Germany.
- [3] AXILROD, B. M. and TELLER, E., 1943, *J. Chem. Phys.*, **11**, 299.
- [4] KIHARA, T., 1978, *Intermolecular Forces*, Translated by S. Ichimaru, (John Wiley & Sons).
- [5] ANDREANI, C., DORE, J. C. and RICCI, F. P., 1991, *Rep. Prog. Phys.*, **54**, 731, and references therein.
- [6] BERRY, R. S., RICE, S. A. and ROSS, J., 1980, *Physical Chemistry*, (John Wiley & Sons).
- [7] MAITLAND, G. C., RIGBY, M., SMITH E.B., and WAKEHAM, W. A., 1981, *Intermolecular Forces: Their Origin and Determination*, (Clarendon Press).
- [8] LENNARD-JONES, J. E., 1924, *Proc. Roy. Soc.*, **A 106**, 463.
- [9] EVANS, M. W., 1983, *J. Mol. Liq.*, **25**, 211.
- [10] EVANS, M. W. and EVANS, J. E., 1985, *Adv. Chem. Phys.*, **LXIII**, 377.
- [11] ATKINS, P. W., 1986, *Physical Chemistry*, 3rd Edn., (Oxford University Press), 593.

- [12] BOSSIS, G., QUENTREC, B. and BROT, C., 1980, *Molec. Phys.*, **39**, 123.
- [13] ALLEN, M. P. and TILDESLEY, D. J., 1987, *Computer Simulation of Liquids*, (Clarendon Press).
- [14] MAITLAND, G. C. and SMITH, E. B., 1971, *Mol. Phys.*, **22**, 861.
- [15] BARKER, J. A., FISHER, R. A. and WATTS, R. O., 1971, *Molec. Phys.*, **21**, 657.
- [16] FENDER, B. E. F. and HALSEY Jr., G. D., 1962, *J. Chem. Phys.*, **36**, 1881.
- [17] YARNELL, J. L., KATZ, M. J., WENZEL, R. G. and KOENIG, S. H., 1973, *Phys. Rev. A*, **7**, 2130.
- [18] PAGE, D. I., EGELSTAFF, P. A., ENDERBY, J.R. and WINGFIELD, B. R., 1969, *Phys. Lett. A*, **29**, 296.
- [19] BERTAGNOLLI, H., 1981, *Ber. Buns. Phys. Chem.*, **85**, 644.
- [20] BERTAGNOLLI, H., LEICHT, D. O., ZEIDLER, M. D. and CHIEUX, P., 1978, *Mol. Phys.*, **36**, 1769.
- [21] BERTAGNOLLI, H., LEICHT, D. O., ZEIDLER, M. D. and CHIEUX, P., 1978, *Mol. Phys.*, **35**, 199.
- [22] BERTAGNOLLI, H. and ZEIDLER, M. D., 1978, *Mol. Phys.*, **35**, 177.
- [23] BERTAGNOLLI, H., LEICHT, D. O. and ZEIDLER, M. D., 1978, *Mol. Phys.*, **35**, 193.

- [24] BERTAGNOLLI, H. and CHIEUX, P., 1980, *Ber. Buns. Phys. Chem.*, **84**, 1225.
- [25] STEINHAUSER, O. and BERTAGNOLLI, H., 1981, *Ber. Buns. Phys. Chem.*, **85**, 45.
- [26] KNELLER, G. R. and GEIGER, A., 1989, *Molec. Phys.*, **68**, 487.
- [27] JUNG, W. G., ZEIDLER, M. D. and CHIEUX, P., 1989, *Molec. Phys.*, **68**, 473.
- [28] BERMEJO, F. J., ENCISO, E., ALONSO, J., GARCIA, N. and HOWELLS, W. S., 1988, *Molec. Phys.*, **64**, 1169.
- [29] GUBBINS, K. E., GRAY, C. G., EGELSTAFF, P. A. and ANANTH, M. S., 1973, *Molec. Phys.*, **25**, 1353.
- [30] EGELSTAFF, P. A., PAGE, D. I. and POWLES, J. G., 1971, *Molec. Phys.*, **20**, 881.
- [31] LOWDEN, L. J. and CHANDLER, D., 1974, *J. Chem. Phys.*, **61**, 5228.
- [32] McDONALD, I. R., BOUNDS, D. G. and KLEIN, M. L., 1982, *Molec. Phys.*, **45**, 521.
- [33] BÖHM, H. J., MEISSNER, C. and AHLRICHS, R., 1984, *Molec. Phys.*, **53**, 651.
- [34] BÖHM, H. J. and AHLRICHS, R., 1985, *Molec. Phys.*, **54**, 1261.
- [35] OHBA, T. and IKAWA, S., 1991, *Molec. Phys.*, **73**, 999.
- [36] PAGE, D. I. and POWLES, J. G., 1971, *Molec. Phys.*, **21**, 901.

- [37] POWLES, J. G., 1981, *Molec. Phys.*, **42**, 757.
- [38] WALFORD, G., CLARKE, J. H. and DORE, J. C., 1977, *Molec. Phys.*, **33**, 25.
- [39] TELEMAN, O., JÖNSSON, B. and ENGSTRÖM, S., 1987, *Molec. Phys.*, **60**, 193.
- [40] PRICE, S. J., 1988, *Molecular Simulation*, **1**, 135.
- [41] STONE, A. J. and ALDERTON, M., 1985, *Molec. Phys.*, **56**, 1987.
- [42] WHEATLEY, R. J. and PRICE, S. J., 1990, *Molec. Phys.*, **71**, 1381.
- [43] Ed. LIDE, D. R., 1992, *CRC Handbook of Chemistry and Physics*, 72nd Edition, (CRC Press).
- [44] BENOIT, A-M., 1988, *Molec. Phys.*, **65**, 487.
- [45] BOTTCHEER, C. J. F. and BORDEWIJK, P., *Theory of Electric Polarization*, (Elsevier).
- [46] STEWART, J. J. P., 1990, *J. Comp. Aided Molec. Design*, **4**, 1.

**PAGE MISSING IN
ORIGINAL**

CHAPTER TWO

NEUTRON DIFFRACTION.

2.1 Introduction

In this chapter neutron diffraction is introduced, the time-of-flight (TOF) experiments performed at the Rutherford Appleton Laboratory (RAL) are described, the techniques used to derive liquid structures from diffraction data are illustrated, and the results are presented.

This neutron diffraction study was instigated by ICI in Runcorn with the aim of deriving the structure of some halogenated methanes of industrial importance. The diffraction studies were all performed at the RAL using two instruments - the Liquids and Amorphous materials Diffractometer (LAD) and the Small Angle Neutron Diffractometer for Amorphous and Liquid Structure (SANDALS).

2.2 Historical Background

In 1912, von Laue suggested that X-rays might be diffracted by a crystal. His collaborators Friedrich and Knipping [1] fired X-rays at a hydrated copper sulphate crystal and discovered that it had a regular repeating structure. This was exploited by William and Lawrence Bragg [2] who used monochromatic X-rays to derive the structure of NaCl. The technique known as X-ray diffraction is widely used, mainly for single-crystal solid structures.

In 1927, electron diffraction was discovered [3, 4]. Electron diffraction, which probes the electric potential of the scattering material, is commonly used to study surfaces and thin films.

In 1932, Chadwick discovered the neutron [5] when interacting beryllium with the alpha particles of natural polonium. The amount of neutrons (or flux) produced in this process was low (roughly 1 neutron $\text{cm}^{-2} \text{s}^{-1}$), but was sufficient to show that neutrons could also be diffracted from condensed materials [6].

The major breakthrough in the evolution of neutron diffraction came in 1942 with the development of the first nuclear-fission reactor, CP1, where CP stands for Chicago Pile. The neutron flux generated in CP1 was about 10^7 times the amount Chadwick produced in his initial experiments.

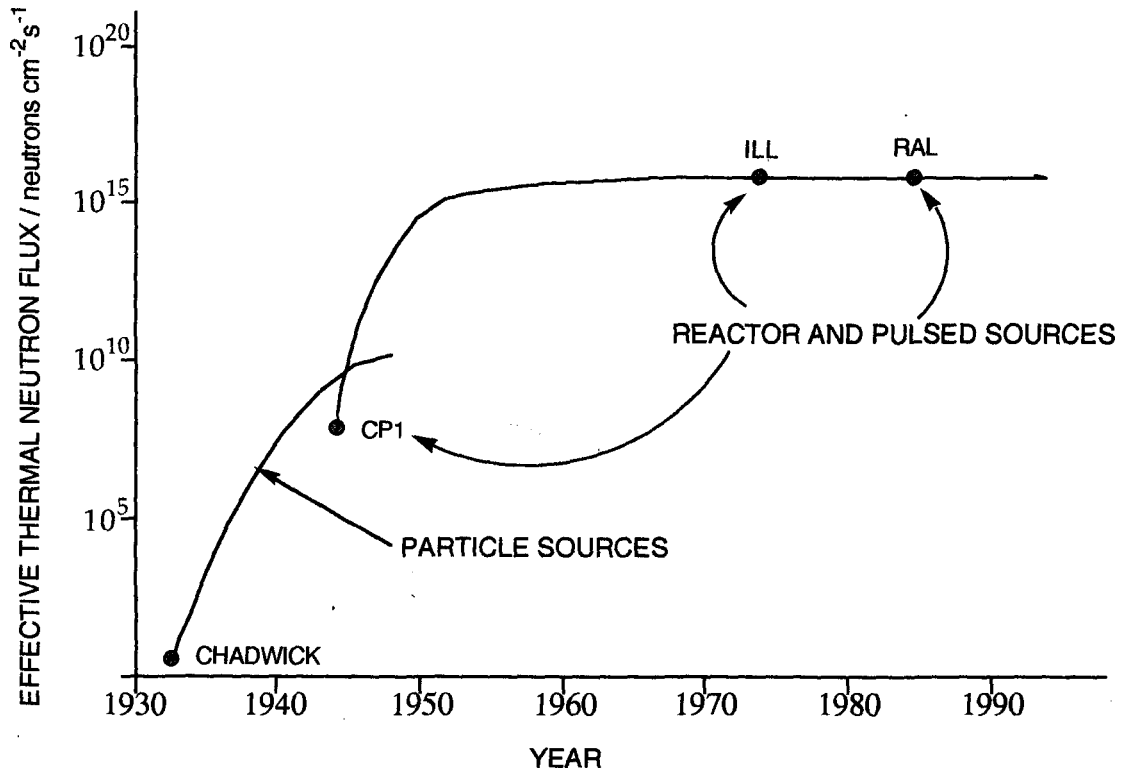


Figure 2.1 The evolution of the effective neutron flux from available neutron sources; the ILL is the reactor source in Grenoble, France and the RAL is the pulsed spallation source in Oxfordshire, UK [8].

Figure 2.1 shows how the amount of flux has risen over the past 60 years. Recently, pulsed spallation sources have been introduced in which pulsed beams of protons, that have been accelerated to high energy, collide violently with a target nucleus (uranium, tantalum, tungsten) producing neutrons and other nuclear particles (gamma particles, neutrinos, etc.). The highest neutron fluxes now available are of the order of 10^{15} neutrons $\text{cm}^{-2} \text{s}^{-1}$.

For a more in-depth account of the worldwide history of neutron diffraction a book, edited by Bacon, describes the development of the technique [7]. It includes the reminiscences of a number of respected scientists from the field of neutron scattering who were on the front line of research in the nineteen-forties and fifties.

2.3 The Neutron

The neutron is a sub-atomic particle - some of its basic properties are listed below:

Mass	$1.675 \times 10^{-27} \text{ kg}$
Charge	0
Spin	1/2
Magnetic Dipole Moment	1.913 nuclear magnetons

Traditionally the energy of the neutron has been classified into three types; epithermal, thermal and cold (figure 2.2). Reactor sources produce neutrons with energies in the thermal and cold regions. Spallation sources also produce epithermal neutrons. The neutrons of most interest in a diffraction study are the thermal neutrons.

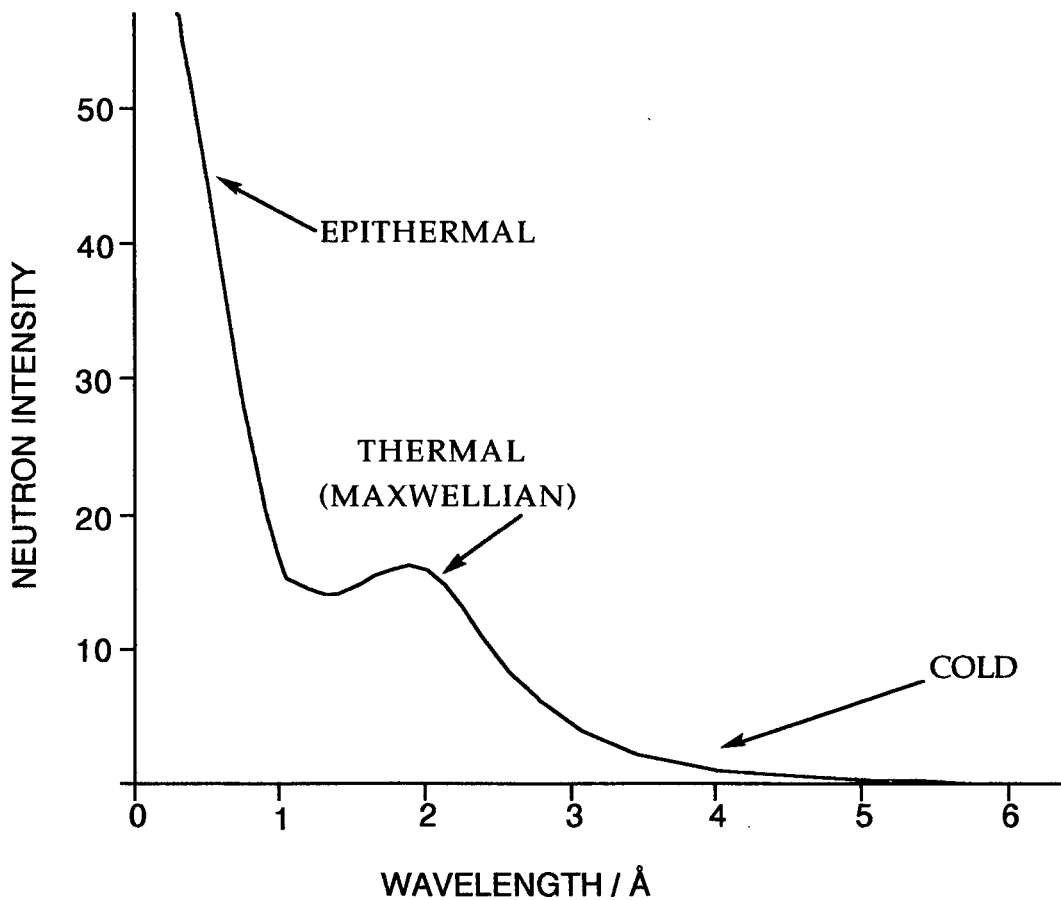


Figure 2.2 The types of neutron that can be produced from a spallation source.

Thermal neutrons are a valuable tool for investigating the structure and dynamics of condensed matter. Their usefulness derives from their characteristics;

- (i) thermal neutrons have wavelengths of the order of the interatomic spacings in condensed material,
- (ii) the energy of thermal neutrons is of the order of the vibrational excitation energies in the material,
- (iii) neutrons are uncharged and can penetrate deeply into bulk samples,

(iv) the scattering process is dependent upon the nature of the target atom and varies for both A (the atomic mass) and Z (the atomic number),

(v) interaction of the neutron's magnetic moment with unpaired electrons in magnetic material makes neutrons an excellent probe of magnetism.

2.4 Scattering and Structure

2.4.1 Elastic and Inelastic Scattering

There are two major scattering events that may occur when neutrons interact with target molecules:

- (a) **Elastic** scattering.
- (b) **Inelastic** scattering.

Elastic scattering occurs when the energy of the incident neutron is equal to that scattered, i.e., $E_{in} = E_{out}$. The elastic scattering of neutrons gives information on the **shapes** and **bond distances** in molecules, and the **intermolecular spacings** between them.

Inelastic scattering occurs when there is exchange of energy between the scatterer and the scattered neutron, i.e., $E_{in} \neq E_{out}$. Inelastic scattering can be used to look at dynamic effects such as the vibrational states, diffusion and sound modes of a system.

The two scattering events are, unfortunately, not exclusive in any scattering experiment. They must be separated to give the information required. In devising experiments it is necessary to try to minimise one of the scattering events.

2.4.2 Coherent and Incoherent Scattering

The elastic and inelastic scattering events can be further divided into two; coherent and incoherent scattering.

Coherent elastic scattering events provide structural information but incoherent elastic scattering events provide only a background scattering. Incoherent scattering occurs due to 'spin incoherence' interactions between neutrons and spinning nuclei.

Neutrons have a spin of $1/2$ and interact with target nuclei of spin, I (where $I \neq 0$ since non-spin nuclei scatter totally coherently), in one of two ways. A compound nucleus (nucleus + neutron) can take a spin of $I+1/2$ where the neutron's spin is parallel (or coherent) with that of the nucleus, or $I-1/2$ where the spins are anti-parallel (or incoherent). On average (it is not possible to predict which arrangement of spins will occur [7]), the probability of a coherent-spin compound nucleus, w_+ , is $(I+1)/(2I+1)$, and the probability for the incoherent-spin, w_- , $(I)/(2I+1)$.

b_+ and b_- , the scattering lengths for coherent and incoherent systems, are measures of the effective scattering area around a scattering nucleus. The effective scattering length for a system, $\langle b \rangle$, is equal to the average value of b among the atoms of that system. Thus

$$\langle b \rangle = \sum w_r b_r, \quad (2.1)$$

the scattering cross-section of the molecule is given by

$$\sigma = 4\pi [\sum w_r (b_r)^2], \quad (2.2)$$

the coherent scattering cross-section is given by

$$S = 4\pi [\sum w_r b_r]^2, \quad (2.3)$$

and the incoherent scattering cross-section is given by

$$s = \sigma - S. \quad (2.4)$$

In equations (2.1-2.3), b_r denotes the scattering length of the r th atom and w_r its the fractional abundance.

Even isotopes of the same element can show extremely different scattering; for example the hydrogen isotopes ^1H and ^2H :

i. Hydrogen, ^1H . $I=1/2$	ii. Deuterium, ^2H . $I=1$
$b_+ = 1.08 \times 10^{-12}$ cm	$b_+ = 0.952 \times 10^{-12}$ cm
$b_- = -4.74 \times 10^{-12}$ cm	$b_- = 0.097 \times 10^{-12}$ cm
$b = -0.375 \times 10^{-12}$ cm	$b = 0.667 \times 10^{-12}$ cm
$\sigma = 81.6$ barns	$\sigma = 7.6$ barns
$S = 1.8$ barns	$S = 5.6$ barns
$s = 79.8$ barns	$s = 2.0$ barns

The distribution of spins in an atomic array is random and the total diffraction pattern cannot be related to the position of the scattering atoms. Only the coherent elastic scattering gives interference effects and therefore information about the structure of the target material; the incoherent scattering gives a background to the data we require. Fortunately, since it is a random effect 'spin-incoherence' produces a linear background to the scattering pattern that can be removed. However, since the incoherent scattering for hydrogen is about 40 times its coherent scattering, problems inevitably occur in the data reduction. To avoid this problem, hydrogen is very often replaced by deuterium in scattering experiments.

The experiments in this study were involved solely with structural determination. Thus, the following sections only describe the mechanics of **coherent elastic scattering** and the experimental considerations involved in deriving the structure of condensed matter from diffraction

data. Descriptions of other types of neutron scattering can be found in a number of books [8-14], and reviews [15, 16].

2.4.3 Other Scattering Events

There are other events that occur which complicate the scattering pattern from a scattering system and they are described in section 2.7.

2.5 The Pulsed Time-of-Flight Experiment and the Elastic Scattering Cross-Section

In a conventional experiment, a constant beam of neutrons from a fission-reactor source is monochromated, collimated, and fired at a target (figure 2.3). The neutrons are spherically scattered over a wide range of directions defined by the angles θ and Φ . The detector could scan through the complete θ, Φ range in order to count the number of neutrons arriving at each angle, $I(\theta, \Phi)$. It has been shown however, that, for an isotropic scatterer, the intensity of the scattered neutrons is independent of Φ and so the detector need only scan along one plane of θ to attain a complete description of the scattering [12, 17]. The problem with the conventional experiment is that in order to monochromate the beam some of the neutron flux is lost. Thus, the time taken to acquire good statistics, using the conventional reactor equipment, may be long unless there is a large detector area.

In the pulsed time-of-flight (TOF) neutron diffraction experiment a 'white' collimated beam of neutrons is fired at the target in pulses lasting Δt (where Δt is typically less than 1 μ s), every $1/n$ seconds (where n is in the range 25-50). The detectors in the TOF experiment are fixed in place at a distance, L , away from the target, any number of detectors can be

used at a variety of angles, 2θ . In the TOF case, the number of neutrons, $I(\theta, t)$, and their time-of-arrival, t , from the target, at the detector, is measured.

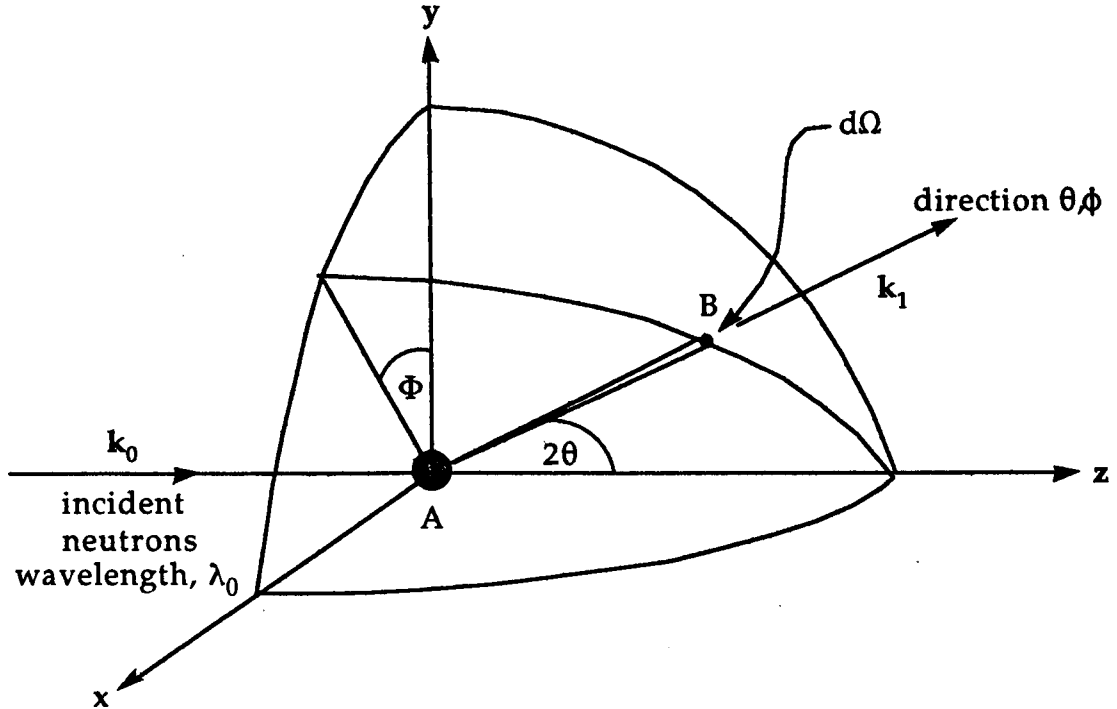


Figure 2.3 The scattering of incident neutrons by the target (A). Neutrons are counted in the detector (B) which has a small solid detection angle $d\Omega$.

The quantity that these techniques have in common is the momentum transfer wavevector, Q . Q is the amount of momentum wavevector, k , transferred out of the z -direction into the θ, Φ plane (figure 2.4);

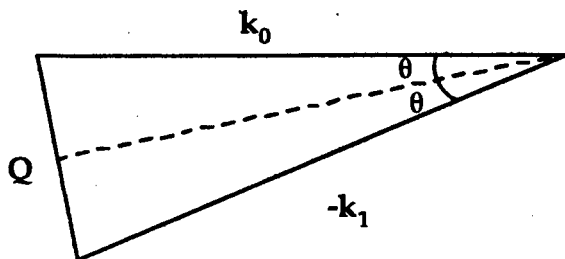


Figure 2.4 The momentum transfer wavevector, Q .

$$Q = k_0 - k_1 \quad (2.5)$$

If the scattering is elastic, the magnitude of k_0 and k_1 are the same and the magnitude of Q is given by;

$$Q (\text{\AA}^{-1}) = 2k_0 \sin\theta, \quad (2.6)$$

$$\text{where, } k_0 (\text{\AA}^{-1}) = 2\pi/\lambda_0. \quad (2.7)$$

$$\text{Hence, } Q(\text{\AA}^{-1}) = 4\pi \sin\theta/\lambda_0 \quad (2.8)$$

In the conventional experiment $I(Q) = I(\theta, \Phi)$, and Q is calculated using equation (2.8), over the angular range, since we know λ_0 . In the TOF experiment $I(Q) = I(t)$ at each angle and Q is calculated using the wavelength-time conversion (equation (2.9)) in equation (2.8);

$$\lambda (\text{\AA}) = h/p = h/mv = ht/mL, \quad (2.9)$$

where L is the distance between the target and the detector, h is Planck's constant, and m is the mass of a neutron.

In a neutron diffraction experiment, the scattered neutrons are counted without analysing their energy and the result is the differential cross-section (DCS). The DCS of the scattered neutrons, at the detector positioned at any θ, Φ angle, $d\sigma/d\Omega$, is defined by

$$d\sigma/d\Omega = I(Q) / N \Psi(Q) d\Omega, \quad (2.10)$$

where N is the number of scattering units, $\Psi(Q)$ is the incident neutron flux and $d\Omega$ is the small solid detector angle.

The DCS at a chosen angle is the probability of a scattering event and is only dependent upon Q ; if the flux doubles, the intensity, $I(Q)$ doubles.

The scattering pattern given when neutrons interact with a molecule depends upon the nature of the molecule's constituent atoms. The scattering from an atom, i , is related to its scattering length, b_i , which

		Element b (10 ⁻¹³ cm)																						
1	H -3.739																	He 3.26						
2	Li -1.90	Be 7.79																	B 5.30	C 6.6460	N 9.36	O 5.803	F 5.654	Ne 4.547
3	Na 3.63	Mg 5.375																	Al 3.449	Si 4.149	P 5.13	S 2.847	Cl 9.577	Ar 1.909
4	K 3.71	Ca 4.90	Sc 12.29	Ti -3.30	V -0.382	Cr 3.635	Mn -3.73	Fe 9.54	Co 2.50	Ni 10.3	Cu 2.50	Zn 5.680	Ga 7.288	Ge 8.193	As 6.58	Se 7.970	Br 6.795	Kr 7.80						
5	Rb 7.08	Sr 7.02	Y 7.75	Zr 7.16	Nb 7.054	Mo 6.95	Tc 6.8	Ru 7.21	Rh 5.88	Pd 5.91	Ag 5.922	Cd 5.1	In 4.065	Sn 6.226	Sb 5.641	Te 5.43	I 5.28	Xe 4.85						
6	Cs 5.42	Ba 5.25	Lanthanides	Hf 7.77	Ta 6.91	W 4.77	Re 9.2	Os 11.0	Ir 10.6	Pt 9.63	Au 7.63	Hg 12.692	Tl 8.776	Pb 9.405	Bi 8.531	Po ---	At ---	Rn ---						
7	Fr ---	Ra 10.0	Actinides																					

Table 2.1 The scattering lengths, b, of the elements in their natural abundance state [8]

is a measure of the effective scattering area around a scattering nucleus. Table 2.1 shows how the scattering length changes through the periodic table. Unlike X-ray diffraction, the scattering of neutrons does not simply depend upon the atomic number of the target atom. X-rays are scattered by electrons and so are more sensitive to heavier atoms than light ones; hydrogen is almost 'invisible' to X-rays. Neutrons are scattered by the nuclei of the target molecules. The scattering length depends on the presence of resonant energy levels in the nuclei of the atoms which can lead to absorption at certain energies. Even isotopes of the same element can scatter neutrons differently. Unlike X-rays, neutrons are very sensitive to the presence of the isotopes of hydrogen but the scattering from hydrogen and deuterium is very different.

2.6 Scattering Theory

From a diffraction experiment we want to find the intramolecular bond separations and the intermolecular structure. This is given by the pair distribution function, $g(R)$, which was introduced in Chapter One, where

$$g(R) = 1 + \frac{1}{2\pi^2\rho R} \int_0^{\infty} Q\{S(Q) - 1\} \sin(QR) dQ. \quad (2.11)$$

The quantity given in a diffraction experiment is the structure factor, $S(Q)$, where

$$S(Q) = 1 + \frac{4\pi\rho}{Q} \int_0^{\infty} \{g(R) - 1\} R \sin(QR) dR. \quad (2.12)$$

$S(Q)/\rho$ is regarded as the density of points in reciprocal space [17].

The pair distribution function, $g(R)$, and the structure factor, $S(Q)$, are related by equations (2.11) and (2.12), which are Fourier transforms. $g(R)$ can be obtained by Fourier transforming $S(Q)$ and vice versa.

It is not possible to integrate equation (2.11) between a Q -range of 0 and infinity; experimental considerations such as the incident neutron wavelength range introduce finite limits. The maximum Q -value in TOF experiments is generally between 20-50 \AA^{-1} (depending upon the instrument used and the system studied) and the minimum is roughly 0.5 \AA^{-1} .

Transforming $S(Q)$ to $g(R)$ is similar to transforming the time dependent Free-Induction-Decay spectrum given in a pulsed NMR experiment to the frequency dependent spectra [18]. In that case, the transformation is from s (time domain) $\rightarrow s^{-1}$ (frequency domain). In neutron diffraction Fourier transformation effects the change from \AA^{-1} (Q -space) $\rightarrow \text{\AA}$ (R -space).

2.6.1 Relating $S(Q)$ to the DCS(Q), $d\sigma/d\Omega$

The amplitude of the scattered neutrons, f_1 , from a nucleus, 1, is given [9] by

$$f_1 = -b_1 \exp [i(\mathbf{k}_0 - \mathbf{k}_1) \cdot \mathbf{R}_1] \quad (2.13)$$

where \mathbf{R}_1 is the vector displacement of the nucleus from a theoretical origin point.

This means that the amplitude depends upon the phase shift between the spherically scattered ($ik_1\mathbf{R}_1$) and the incident ($ik_0\mathbf{R}_1$) beams, and the scattering length of the nucleus, b_1 .

When there is an assembly of nuclei scattering the neutrons, there will be interference between the scattered waves. The overall scattering amplitude, f , is calculated by summing the individual amplitudes given by equation (2.13);

$$f = \sum -b_{\mathbf{R}} \exp [i\mathbf{Q}\cdot\mathbf{R}]. \quad (2.14)$$

In the scattering experiment it is not possible to record the amplitude of scattered neutrons but we can record their intensity, $I(\mathbf{Q})$ in a particular direction. $I(\mathbf{Q})$ is proportional to the square of the amplitude $|f|^2$, which in turn is equal to the DCS. Thus,

$$I(\mathbf{Q}) \propto \left| \sum b_{\mathbf{R}} \exp [i\mathbf{Q}\cdot\mathbf{R}] \right|^2, \quad (2.15)$$

and,

$$\left| \sum b_{\mathbf{R}} \exp [i\mathbf{Q}\cdot\mathbf{R}] \right|^2 = d\sigma/d\Omega. \quad (2.16)$$

Equation (2.16) is an important equation for neutron diffraction. It is only valid for stationary molecules but forms a useful starting point for liquids. The equation can be expanded as shown below in equations (2.17) and (2.18);

$$d\sigma/d\Omega = \sum b_{\mathbf{R}}b_{\mathbf{R}'} \exp [i\mathbf{Q}\cdot(\mathbf{R}-\mathbf{R}')], \quad (2.17)$$

$$= \sum b_{\mathbf{R}}^2 + \sum' b_{\mathbf{R}}b_{\mathbf{R}'} \exp [i\mathbf{Q}\cdot(\mathbf{R}-\mathbf{R}')], \quad (2.18)$$

where the ' means not including \mathbf{R} .

If there are N scattering nuclei;

$$d\sigma/d\Omega = N\langle b_{\mathbf{R}} \rangle^2 + N\langle b_{\mathbf{R}} \rangle^2 \sum' \exp [i\mathbf{Q}\cdot(\mathbf{R}-\mathbf{R}')], \quad (2.19)$$

where $\langle b_{\mathbf{R}} \rangle \langle b_{\mathbf{R}'} \rangle = \langle b_{\mathbf{R}} \rangle^2$ which holds because there is no correlation between $b_{\mathbf{R}}$ and $b_{\mathbf{R}'}$. $\langle b_{\mathbf{R}} \rangle$ is the average value of the scattering lengths of the atoms which constitute the molecule.

The first term is known as the self scattering term and the second the interference scattering term. The summation in the second term is the one that is of interest; it is equal to $S(\mathbf{Q}) - 1$. Hence,

$$S(\mathbf{Q}) = 1 + \sum' \exp [i\mathbf{Q} \cdot (\mathbf{R} - \mathbf{R}')] \quad (2.20)$$

Equations (2.12), (2.16) and (2.20) are the key elements in the data reduction of neutron diffraction results.

2.6.2 Intramolecular and Intermolecular Form Factors

It is sometimes convenient to split $S(\mathbf{Q})$ into two components; an intramolecular form-factor, $F_1(\mathbf{Q})$, and an intermolecular form-factor, $D_M(\mathbf{Q})$, where

$$S(\mathbf{Q}) = F_1(\mathbf{Q}) + D_M(\mathbf{Q}). \quad (2.21)$$

$D_M(\mathbf{Q})$ is the structure factor that arises due to the average arrangement of the molecules in the fluid. $F_1(\mathbf{Q})$ is the structure factor relating to the conformation of an isolated molecule

$$F_1(\mathbf{Q}) = \frac{1}{\sum b_i^2} \sum_{i,j} b_i b_j \frac{\sin(\mathbf{Q} \cdot \mathbf{r}_{ij})}{\mathbf{Q} \cdot \mathbf{r}_{ij}} \exp \left(-\frac{1}{2} \langle u_{ij}^2 \rangle Q^2 \right), \quad (2.22)$$

where b_i is the scattering length of the i th nucleus, r_{ij} is the distance between nuclei i and j ; the exponent is the Debye-Waller factor, where $\langle u_{ij}^2 \rangle$ is the mean square amplitude of vibration of atom i relative to atom

j ; this is included to account for the effect of internal thermal vibrations on the structure of the molecule.

$F_1(Q)$ usually dominates at high Q ; this property is used in the data reduction technique for LAD data (section 2.11.2.2).

2.7 Ideal Scattering Systems

2.7.1 Scattering from a Single Particle

The scattering from a single particle is equal to the scattering length, b , at all Q . Obviously no structural information may be derived from this type of scattering.

2.7.2 Scattering from a Monatomic Ideal Gas

The scattering of neutrons from a monatomic ideal gas is shown in figure 2.5. The scattering is related to $\langle b^2 \rangle$; there is no intramolecular information (monatomic gas, $F_1(Q) = 0$) and no intermolecular information ($D_M(Q) = 0$; in the gas the molecules are distributed randomly and the second summation in equation (2.18) averages to zero).

2.7.3 Scattering from a Polyatomic Ideal Gas

The scattering from a polyatomic gas gives a scattering profile as shown in figure 2.6. There are oscillations around $\langle b^2 \rangle$ that correspond to the intramolecular structure of the gas molecules. However, again there is no intermolecular structure ($D_M(Q) = 0$, $S(Q) = F_1(Q)$) because of the random orientation of the gas. The structure factor is given by removing the non-interference scattering (the first summation in equation (2.18)) from

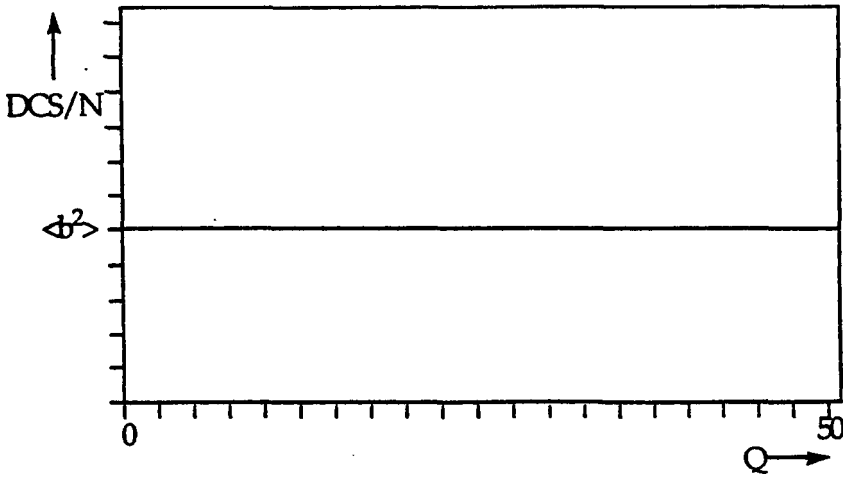


Figure 2.5 The scattering cross-section from a monoatomic ideal gas.

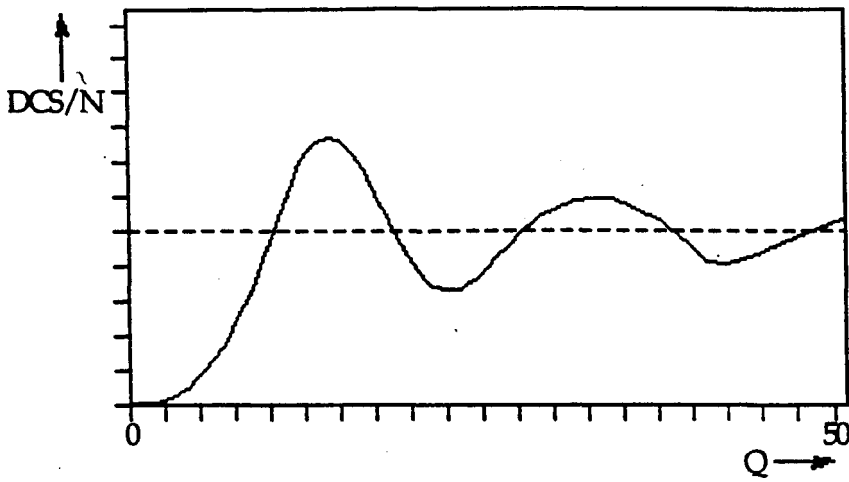


Figure 2.6 The scattering cross-section from a polyatomic ideal gas

the interference scattering (the second summation in equation (2.18)). The structure factor can be Fourier transformed to give $g(R)$ and an example is shown in figure 2.7.

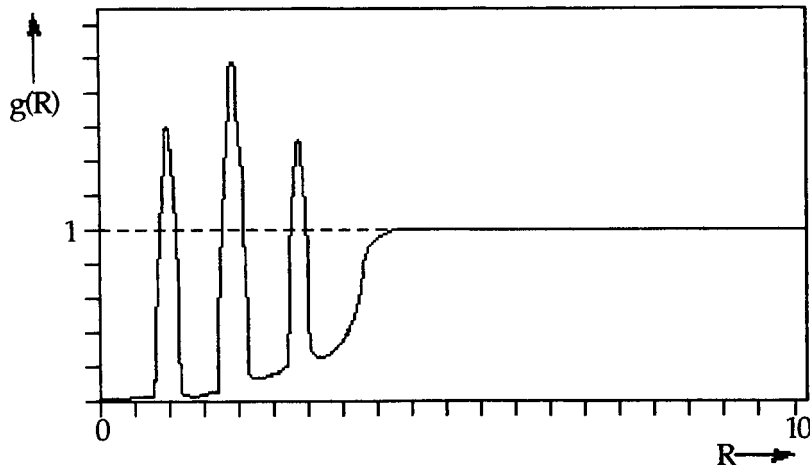


Figure 2.7 The pair distribution function for a polyatomic ideal gas

2.7.4 Scattering from Polyatomic Ideal Solids and Liquids

Scattering from solids and liquids is more complicated because there is both intermolecular and intramolecular structural information in the scattering cross-section. The difference between solids and liquids is best shown in the $g(R)$, as in figures 2.8 and 2.9.

The $g(R)$ for the solid shows a series of sharp peaks that relate to the distances between atoms throughout the solid lattice. The regular structure extends over the whole range of R . The intermolecular structure of the liquid is shown not as peaks but as oscillations about unity (cf. polyatomic gas). The intermolecular ordering in liquids generally disappears (the oscillations in the $g(R)$ die rapidly) after about only 10 Å. This shows that long-range forces are weak for most liquids.

Unlike the atoms in solids, the atoms in a liquid have no equilibrium positions and the $g(R)$ given for a liquid is a time-averaged picture of the sample's structure.

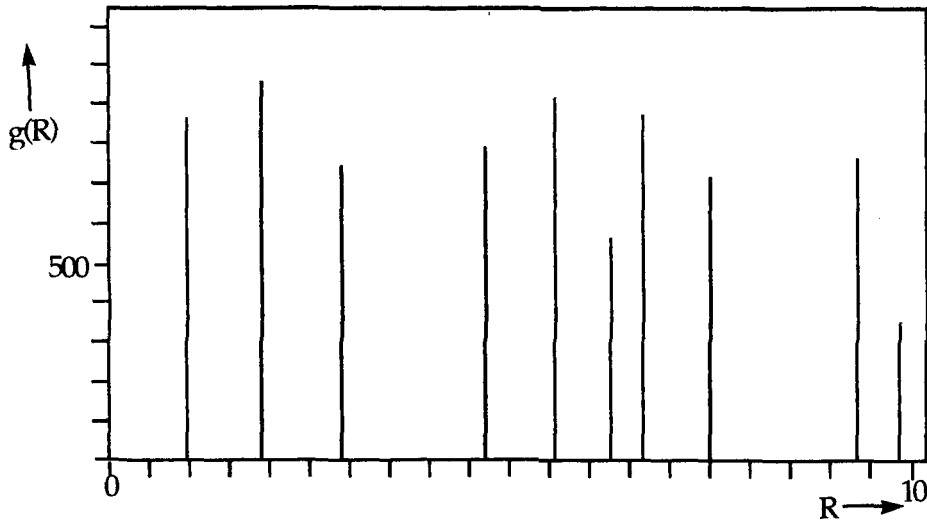


Figure 2.8 The pair distribution function for a solid

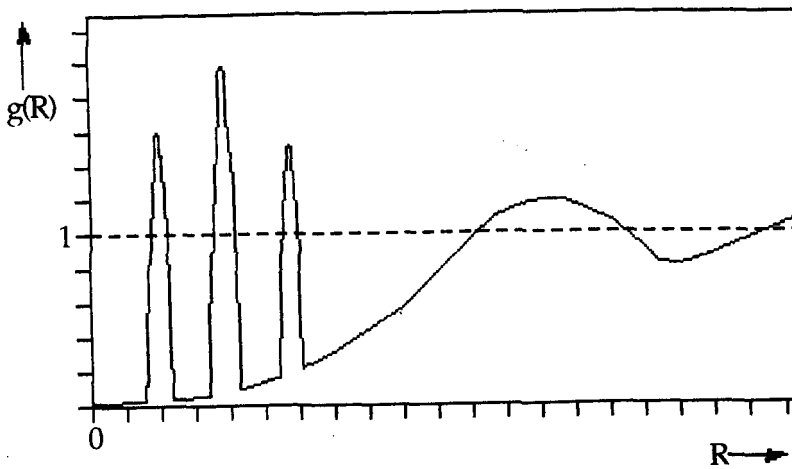


Figure 2.9 The pair distribution function for a liquid

2.8 The Time-of-Flight (TOF) Neutron Diffraction Equipment

There are many different types of neutron experiments that can be performed at the Rutherford Appleton Laboratory (RAL). Figure 2.11 shows the ground plan at the RAL.

The experiments in this study were performed on two separate occasions using two of the time-of-flight diffractometers available at the RAL. Three liquids were studied using the Liquids and Amorphous Diffractometer (LAD) and five others were studied using the Small Angle Neutron Diffractometer for Amorphous and Liquid Structures (SANDALS). The position of the LAD and SANDALS instruments are indicated in figure 2.11 by an arrow.

Although there are some differences between LAD and SANDALS there are seven principle components which apply to both (see figure 2.12):

1. neutron source
2. moderator
3. collimator
4. target sample
5. detectors
6. data storage system
7. data analysis package

2.8.1 The Neutron Source

The neutrons at the RAL are produced from a spallation source. A pulse of energetic neutrons less than 1 μ s wide is produced when a burst of high energy protons (500-800 MeV, accelerated from a synchrotron) collides with a uranium target (tantalum, lead or tungsten are alternatives). These

**PAGE MISSING IN
ORIGINAL**

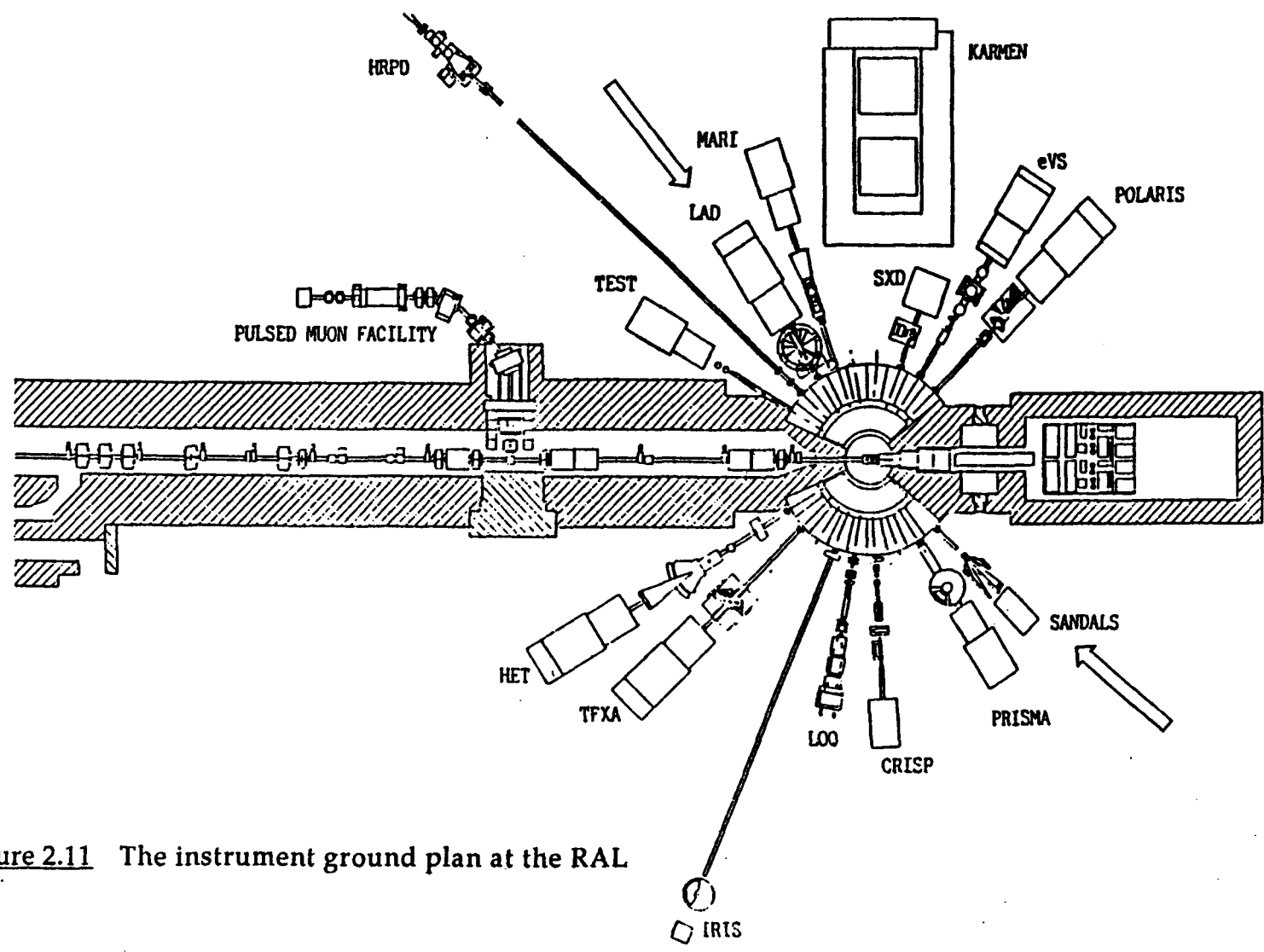


Figure 2.11 The instrument ground plan at the RAL

neutrons are too energetic for diffraction purposes and are therefore slowed down to the required energy in the moderator.

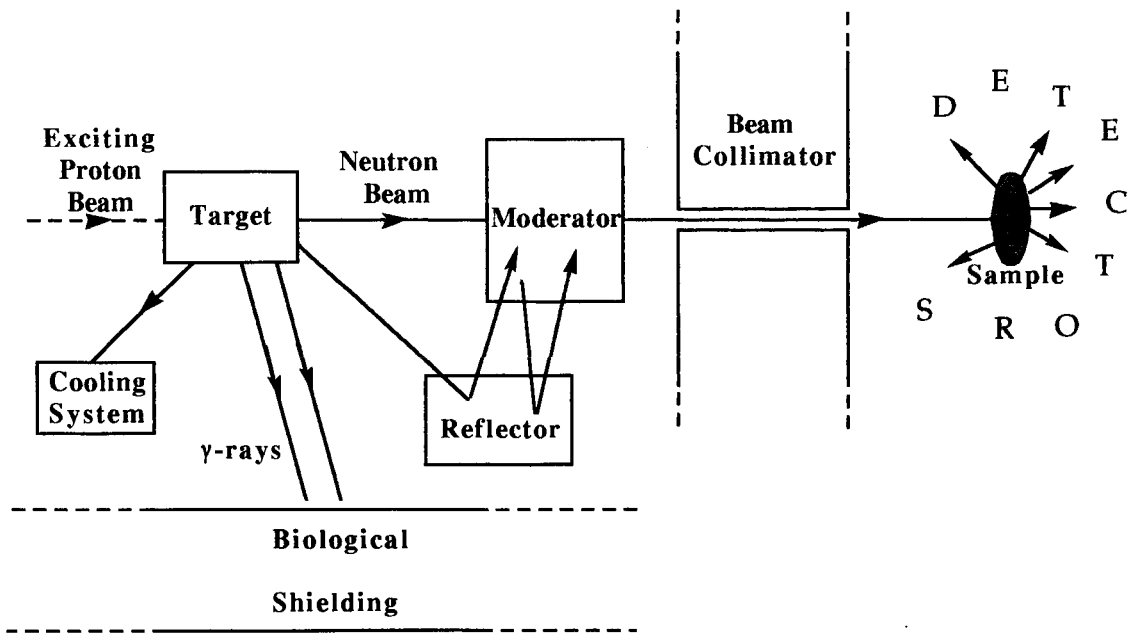


Figure 2.12 The components of a time-of-flight neutron diffraction experiment.

2.8.2 The Moderator

The neutrons produced at the spallation source pass through high inelastic scattering materials, such as water or methane, which slow the neutrons down to the required energy without broadening the pulse excessively. The moderators are kept at a constant temperature; generally 300 K for water and 100 K for methane.

2.8.3 The Collimator

The neutrons emerge from the moderator in all directions and are defined into a beam, in the direction of the sample target, using the collimator. At

the RAL the collimating materials are boron, iron and hydrogen (in the form of wax or resin). These materials provide the beam collimation without introducing extraneous particles such as γ -rays. In the LAD experiment the beam is 40 mm high and 15 mm wide (a rectangular beam) and in the SANDALS experiment the beam is a circular beam of diameter 32 mm.

2.8.4 The Target Sample

Liquified gas samples are usually held in a cylindrical high pressure container made of zirconium-titanium alloy or pure vanadium. These materials are used because the scattering from them is almost purely incoherent (they are called null-scattering material). They contribute only background scattering which is fairly easy to remove, and no Bragg peaks which are not. The pressure vessel used in this study was made from zirconium-titanium alloy and was first used by Howe *et al.* [19] for their study of NO and CO. The vessel is 55 mm high, it has an inner radius of 4.0 mm and a wall thickness of 0.5 mm. It has been regularly used for liquid diffraction experiments [19, 20] and is called the 'Wormald Cell' at the RAL. It is rated to a maximum pressure of 100 bar which is well above the pressure required in our experiments.

Dependent upon the conditions of the experiment, the pressure vessel can be heated by a furnace or cooled by a closed-cycle refrigerator. All the fluids in this experiment are liquids well below room temperature and the furnace was not used. The refrigerator cools both the top and bottom of the pressure vessel at the same time without obstructing the neutron beam.

2.8.5 The Detectors

2.8.5(a) The Incident and Transmission Monitors

The incident and transmission monitors are placed just before and just after the sample region respectively. The typical monitor counter is a scintillator detector (LAD) or a thin vanadium foil (SANDALS) that should monitor the whole neutron beam without affecting it unduly.

2.8.5(b) The Scattered Neutron Detectors

The main difference between LAD and SANDALS is the positioning of the detectors. The LAD experiment has groups of detectors placed perpendicularly at seven angles either side of the target sample (figure 2.13); thus there are fourteen detector groups in total. The angles that the detectors are placed and some relevant physical specifications are shown in table 2.2. The SANDALS experiment will eventually have four continuous banks of detectors placed circularly around the target sample extending from $3\text{-}41^\circ$ (figure 2.14). For our experiment, the angular range was limited to $11\text{-}21^\circ$. The SANDALS detector specifications are shown in table 2.3. For the purposes of the data analysis package the $11\text{-}21^\circ$ range of detectors is split into six 'groups'.

The detectors used in the LAD diffraction experiment were a mixture of ^3He gas detectors and Li-glass neutron scintillation detectors. The SANDALS experiment relies solely upon ZnS(Ag) scintillation detectors.

Any neutrons that are not scattered by the sample or have not been detected are stopped by the beam stop, which is of concrete construction. All the neutrons and other sub-atomic particles that are produced by the

spallation source must be neutralised to protect the experimenters from radiation and the whole of the equipment is shielded.

The SANDALS apparatus would have been the best choice of instrument for the first three fluids that we studied but it was not operational at that time; its advantages over LAD are related to the low angles (less inelastic scattering) used for the detectors and their higher sensitivity to neutrons.

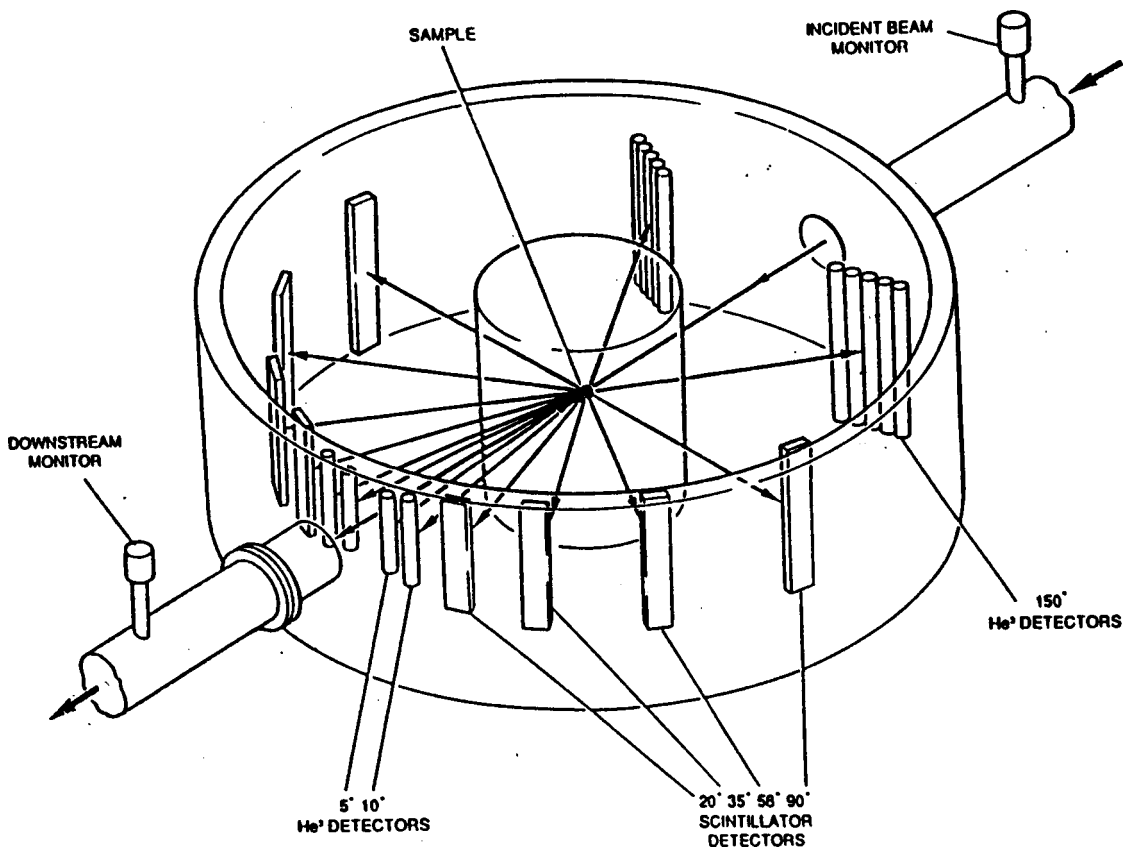


Figure 2.13 The LAD detectors

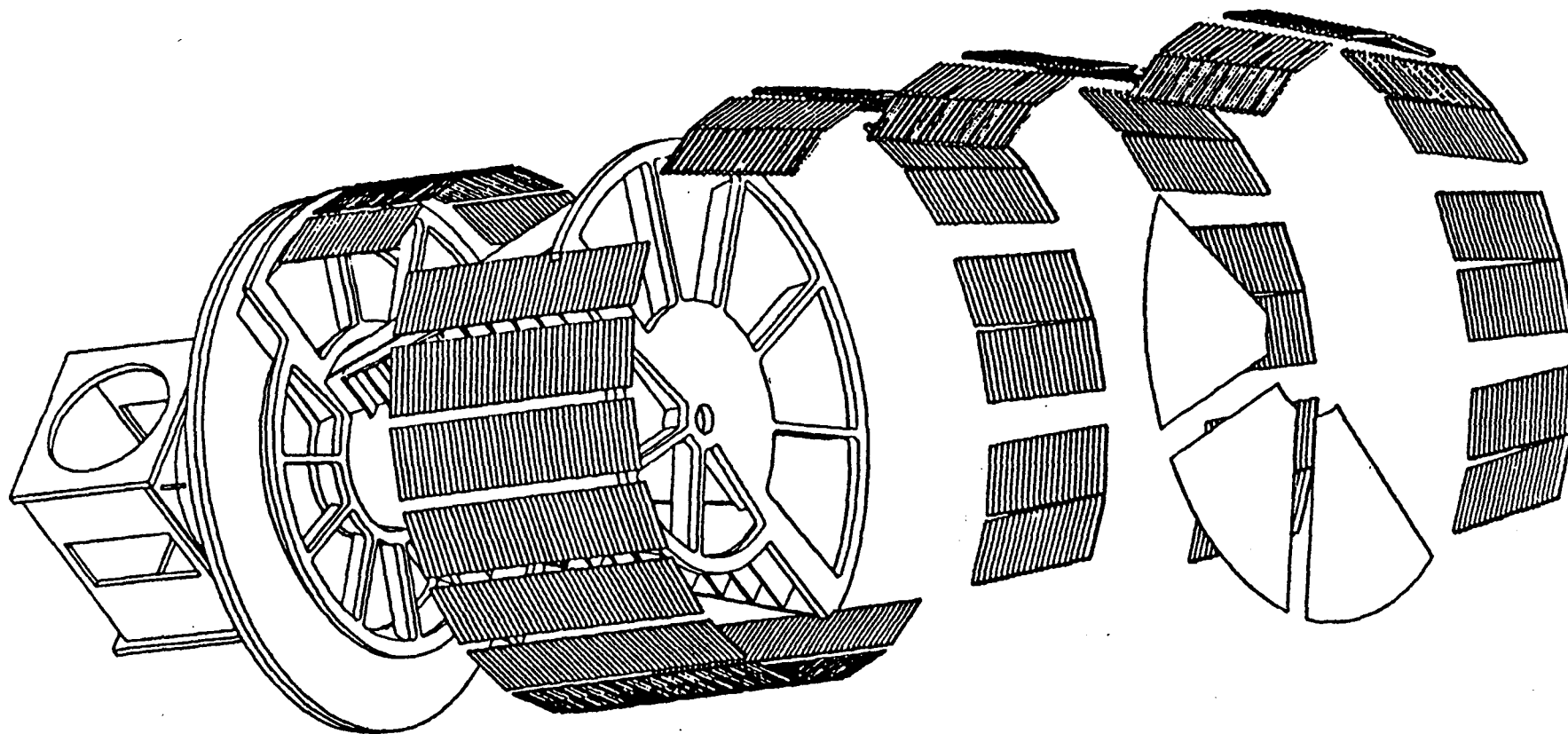


Figure 2.14 A three dimensional view of the small angle detector banks proposed for SANDALS which will span the angles 3° - 11° , 11° - 21° , 19° - 31° , and 29° - 41° . At the time of this experiment only the 11° - 21° bank was in place.

Moderator:	Methane, 100 K	
Incident flight path:	10 m	
Beam Cross Section:	Rectangular (20 mm x 50 mm)	
Detector type:	10 atm ^3He detectors at 5° , 10° and 150° , Li-glass at other angles.	
Range in 2θ (degrees)	Detector Solid Angle (steradians)	Resolution, $\Delta Q/Q$ (%)
5	0.0002	11
10	0.0002	6
20	0.016	2.8
35	0.027	1.7
58	0.027	1.2
90	0.027	0.8
150	0.048	0.5

Table 2.2 Some specifications for LAD

Moderator:	Methane, 100 K	
Incident flight path:	11 m	
Beam Cross Section:	Circular (32 mm diameter)	
Detector type:	Zinc sulphide sandwich detectors.	
Range in 2θ (degrees)	Detector Solid Angle (steradians)	Resolution, $\Delta Q/Q$ (%)
3-11	0.039	16-3
11-21	0.110	3
19-31	0.202	3
29-41	0.275	2

Table 2.3 Some specifications for SANDALS

2.8.6 The Data Storage System

Each neutron event recorded at the detectors is stored by the data acquisition electronics (DAEs). Each event is labelled according to the detector it arrived at and its time-of-arrival, which is the time it takes for a scattered neutron to travel between the target and the detector. At the RAL the time is counted on a clock which is started (every 1/50th of a second) by an electronic pulse which is generated when a burst of protons hits the target.

2.8.7 The Data Analysis Package

The final component of the experiment is the data analysis package. The user-friendly analysis package at the RAL is called ATLAS (Analysis of TOF diffraction data from Liquid and Amorphous Samples). The use of ATLAS is very well explained in a RAL report [17] and it is outlined below in sections 2.9 and 2.10.

2.9 Deriving the Structure of Liquids using Neutron Diffraction

The derivation of $g(R)$ from the experimental data is not as easy as simply relating the neutron intensity $I(\theta, t)$ to equation (2.19), removing the non-interference (or self) scattering, dividing through by $N\langle b_R \rangle^2$, adding 1 to give $S(Q)$, and then finally transforming to give $g(R)$. Unfortunately, there are a number of corrections that must be taken into account. These are illustrated in figure 2.15.

- (i) Detector corrections - no detector is perfect and the intensity of the neutrons recorded at the detector will be less than the actual intensity; the ratio of these quantities is known as the detector

- 1 Incident beam neutrons scattered once by the sample.
- 2 Incident beam neutrons multiply scattered by the sample.
- 3 Incident beam neutrons scattered by the sample container or cryostat before passing through the sample.
- 4 Transmitted beam neutrons scattered by the sample container or cryostat after passing through the sample.
- 5 Background neutrons (and other radiation) from the neutron source but not from the incident beam
- 6 Cosmic rays from outerspace
- 7 Electronic noise from the detector wires
- 8 Neutron absorbed by the sample

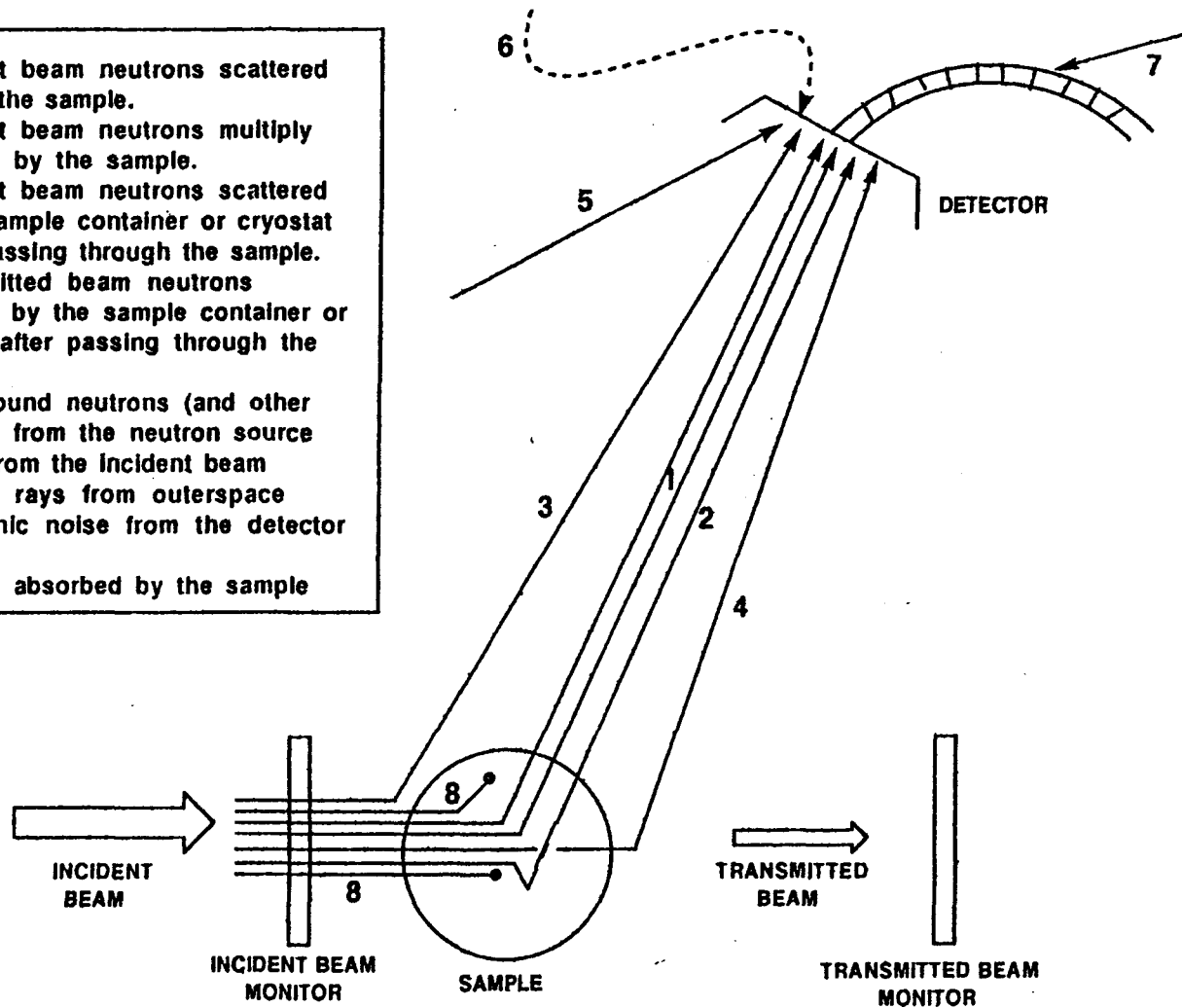


Figure 2.15 The complications which may arise during neutron scattering experiments

efficiency, $E_d(k)$, which is very difficult to quantify. Another detector correction which has to be considered is the deadtime correction. There is a short period of time after a scattering event is recorded where the detector is said to be 'dead' to other incoming neutrons. The deadtime ranges from approximately $0.1 \mu\text{s}$ for scintillator detectors to $10 \mu\text{s}$ for gas detectors. The deadtime corrections, which can be quantified, are removed from the spectra before any other corrections.

(ii) Background corrections - there are a number of ways that background scattering manifests itself; cosmic rays from outer space, noise in the detector wire or stray neutrons from other experiments. These can be minimised by good shielding but it is still necessary to measure the background scattering and remove it.

(iii) Absorption (attenuation) corrections - some neutrons are absorbed by the can or sample either by a direct nuclear reaction or by the formation of a complex nucleus. The neutrons lost in this way lead to attenuation in the beam which must be accounted for. The attenuation correction is dependent upon the energy of the incident neutrons.

(iv) Multiple scattering corrections - multiple scattering occurs when the neutron is scattered more than once before it emerges from the sample. An experiment should be designed so as to minimise the multiple scattering without adversely affecting the scattered neutron intensity.

(v) Can corrections - the can that the sample is placed in is made from highly incoherent scattering material, such as zirconium-titanium, minimising any Bragg scattering that would be difficult to remove. However the incoherent background given

from the can must be measured in a separate experiment and removed from the (can + sample) spectra.

(vi) Recoil corrections - liquid molecules are not fixed in space but move around. This means that there is no strictly elastic scattering from liquids due to recoil effects and at best the scattering is said to be 'quasi-elastic'. The recoil correction is only a problem in that it causes a shift in the Q value from its real value and this must be corrected for, if necessary.

(vii) Inelastic corrections - the 'true' inelastic scattering due to transfer of energy to vibrational energy levels in the atoms of the sample molecules rather than simply due to recoil are considered in the Placzek correction.

(viii) Incoherence corrections - these are the hardest corrections to account for because they depend upon not only our knowledge of the scattering lengths (which may only be accurate to 10%, although some are accurate to within 1% [8]) but also upon how free we consider the motion of the atoms in the liquid to be. Incoherence corrections are not explicitly removed since it is assumed that they are mainly removed as part of the self-scattering corrections. The remainder is presumed to play only a minor role in the scattering.

2.10 The Basis of the Data Analysis

The scattering experiment measures $I(\theta, t)$, where $I(\theta, t)$ is the number of neutrons arriving at a detector placed at angle θ in a given time-of-arrival, t . This is converted to $I(Q)$ using the conversions given in equations (2.6)-(2.8).

For a small ideal sample we can relate the detected count rate, $I(Q)$ to the scattering cross section $d\sigma/d\Omega$ [17], by

$$I(Q) = \Psi(k) N (d\sigma/d\Omega) E_d(k) d\Omega. \quad (2.23)$$

where N is the number of atoms in the sample, $\Psi(k)$ is the incident flux, $d\sigma/d\Omega$ is the differential cross section, $E_d(k)$ is the detector efficiency and $d\Omega$ is the detector solid angle. Ψ and E_d are independent of θ and are thus a function of k , not Q .

The experiment has four components; a run for background (B), vanadium calibration rod (V), sample can (C), and sample (S). The DCS of the sample is related to the DCS of vanadium by

$$N_S(d\sigma/d\Omega)_S = N_V(d\sigma/d\Omega)_V(S-C)/(V-B) \quad (2.24)$$

The equation can be shown to be internally consistent by looking at the make-up of the four components;

- (i) the background run stands alone and the scattering given in the run is $I_B(Q)$.
- (ii) the vanadium rod run is used to remove a few constants - the scattering is almost completely incoherent and is thought to be well understood. It is labelled V and is equal to $I_V(Q)+I_B(Q)$.
- (iii) the can run is labelled C and is equal to $I_C(Q)+I_B(Q)$.
- (iv) the sample run is labelled S and is equal to $I_S(Q)+I_C(Q)+I_B(Q)$.

Now,

$$(S-C)/(V-B) = (I_S(Q)+I_C(Q)+I_B(Q)-I_C(Q)-I_B(Q))/(I_V(Q)+I_B(Q)-I_B(Q)), \quad (2.25)$$

which gives,

$$(S-C)/(V-B) = I_S(Q)/I_V(Q). \quad (2.26)$$

Ignoring absorption or multiple scattering,

$$I_S(Q) = \Psi(k) N_S (d\sigma/d\Omega)_S E_d(k) d\Omega, \quad (2.27)$$

$$I_V(Q) = \Psi(k) N_V (d\sigma/d\Omega)_V E_d(k) d\Omega, \quad (2.28)$$

$$(S-C)/(V-B) = N_S (d\sigma/d\Omega)_S / N_V (d\sigma/d\Omega)_V, \quad (2.29)$$

which is consistent with equation (2.24).

Deriving $(d\sigma/d\Omega)_S$ from equation (2.24) should be a simple matter of multiplying what is given from $(S-C)/(V-B)$ by $N_V(d\sigma/d\Omega)_V/N_S$; quantities which are known. However, we must take into account the remainder of the corrections that were discussed in section 2.9. The most important of these are the corrections due to absorption ($A_{\chi,\chi}$) and multiple scattering (M_χ) which affect the order that the data reduction can be performed. The values of S , C , and V which include $A_{\chi,\chi}$ and $M_{\chi,\chi}$ are shown in equations (2.30)-(2.32).

$$S = \Psi(k) [N_S(d\sigma/d\Omega)_S \cdot A_{S,SC} + N_C(d\sigma/d\Omega)_C \cdot A_{C,SC} + M_{SC}(k)] E_d(k) d\Omega + I_B(Q), \quad (2.30)$$

$$C = \Psi(k) [N_C(d\sigma/d\Omega)_C \cdot A_{C,C} + M_C(k)] E_d(k) d\Omega + I_B(Q), \quad (2.31)$$

$$V = \Psi(k) [N_V (d\sigma/d\Omega)_V \cdot A_{V,V} + M_V(k)] E_d(k) d\Omega + I_B(Q), \quad (2.32)$$

where $A_{\chi,\chi}$ are the Paalman and Pings attenuation factors [21] and M_χ are the multiple scattering corrections.

This complicates matters and means the background scattering must be removed from S , C and V before these corrections can be applied. The order of the data reduction and the removal of the various corrections are outlined below.

2.10.1 Dividing out the incident spectrum

For the LAD experiment the data in each of the vanadium, the

background, the can, and the (can+sample) runs were first corrected for deadtime and then divided through by the incident spectrum (itself corrected for deadtime of course). The incident spectrum is detected in the incident monitor detector. Its intensity is given by

$$I_M(k_e) = \Psi(k) \cdot E_M(k), \quad (2.33)$$

where E_M = monitor detector efficiency

Equation (2.29) suggests that the runs do not need to be divided through by the incident spectrum but since the incident spectrum can vary slightly from run to run it is more accurate to remove it at the beginning of the analysis. This gives us the normalised spectra $NRM_S(Q)$, $NRM_C(Q)$, $NRM_V(Q)$ and $NRM_B(Q)$, which are related to the measured spectra by

$$NRM_S(Q) = C_1(k) [N_S(d\sigma/d\Omega)_S \cdot A_{S,SC} + N_C(d\sigma/d\Omega)_C \cdot A_{C,SC} + M_{SC}(k)] + NRM_B(Q), \quad (2.34)$$

$$NRM_C(Q) = C_1(k) [N_C(d\sigma/d\Omega)_C \cdot A_{C,C} + M_C(k)] + NRM_B(Q), \quad (2.35)$$

$$NRM_V(Q) = C_1(k) [N_V(d\sigma/d\Omega)_V \cdot A_{V,V} + M_V(k)] + NRM_B(Q), \quad (2.36)$$

$$NRM_B(Q) = I_B(Q) / \Psi(k) \quad (2.37)$$

where $C_1(k) = (E_d(k)/E_M(k)) \cdot d\Omega$.

With SANDALS, the incident monitor included background noise and $\Psi(k)$ was removed by calculating its ratio over the different runs.

2.10.2 Removing the Background

The $NRM_B(Q)$ spectrum is removed from each of the smoothed $NRM_V(Q)$, (can+sample) ($NRM_S(Q)$) and can ($NRM_C(Q)$) spectra. By removing $NRM_B(Q)$ from equations (2.34)-(2.36) we get the background-corrected spectra $NRM'_X(Q)$;

$$\begin{aligned} \text{NRM}'_S(Q) &= C_1(k) [N_S(d\sigma/d\Omega)_S \cdot A_{S,SC} + N_C(d\sigma/d\Omega)_C \cdot A_{C,SC} \\ &\quad + M_{SC}(k)], \end{aligned} \quad (2.38)$$

$$\text{NRM}'_C(Q) = C_1(k) [N_C(d\sigma/d\Omega)_C \cdot A_{C,C} + M_C(k)], \quad (2.39)$$

$$\text{NRM}'_V(Q) = C_1(k) [N_V(d\sigma/d\Omega)_V \cdot A_{V,V} + M_V(k)]. \quad (2.40)$$

The vanadium spectrum ($\text{NRM}'_V(Q)$) includes noise and weak Bragg reflections and it is smoothed after background-correction by fitting to Chebyshev polynomials.

2.103 Attenuation and Multiple Scattering Corrections, and Normalisation

The next step in the analysis is to remove the attenuation and multiple scattering.

Attenuation of the beam reduces the neutron count rate at the detectors. It is dependent upon the sample geometry and can be approximated by numerical methods from recorded (LAD) or estimated (SANDALS; the transmission monitor spectrum proved to be unusable due to the noise it created in the detectors) transmission cross-sections. For the cylindrical geometry of the vessel used in our experiments, the attenuation corrections are evaluated using the method of Paalman and Pings [21].

Multiple scattering is, unfortunately, only readily evaluated if we know the structure of the sample. It is approximated from the transmission cross-sections using the so-called ISOTROPIC approximation [22], which holds only if the sample scatters between 10% and 20% of the incident neutron beam [17].

The removal of the multiple scattering/attenuation corrections and normalisation of the data to the vanadium calibration follows the following steps.

- (i) removal of $A_{V,V}$ and $M_V(k)$ from equation (2.40);

$$NRM''_V(Q) = C_1(k) [N_V (d\sigma/d\Omega)_V]. \quad (2.41)$$

- (ii) dividing $NRM''_V(Q)$ by an evaluated $N_V(d\sigma/d\Omega)_V$ to give a value of $C_1(k)$.

- (iii) dividing equations (2.38) and (2.39) by $C_1(k)$ and removal of the multiple scattering;

$$NRM''_S(Q) = [N_S(d\sigma/d\Omega)_S \cdot A_{S,SC} + N_C(d\sigma/d\Omega)_C \cdot A_{C,SC}]. \quad (2.42)$$

$$NRM''_C(Q) = [N_C(d\sigma/d\Omega)_C \cdot A_{C,C}]. \quad (2.43)$$

- (iv) dividing equation (2.43) by $A_{C,C}$ and multiplying it by $A_{C,SC}$;

$$NRM'''_C(Q) = [N_C(d\sigma/d\Omega)_C \cdot A_{C,SC}]. \quad (2.44)$$

- (v) removal of $NRM'''_C(Q)$ from equation (2.42);

$$NRM'''_S(Q) = [N_S(d\sigma/d\Omega)_S \cdot A_{S,SC}]. \quad (2.45)$$

- (vi) dividing equation (2.45) by $A_{S,SC}$ gives $SINGLE_S(Q)$;

$$SINGLE_S(Q) = [N_S(d\sigma/d\Omega)_S]. \quad (2.46)$$

- (vii) dividing $SINGLE_S(Q)$ by N_S , the number of scattering units in the sample, yields $DCS_S(Q)$, which is what we require;

$$DCS_S(Q) = (d\sigma/d\Omega)_S. \quad (2.47)$$

2.10.4 Inelastic, Recoil and Self-scattering Corrections

The inelastic and recoil corrections are difficult to make and are minimised if possible. For nuclei of mass much greater than a neutron the corrections are essentially independent of the detailed dynamics of the system [23]. The corrections can be related to the temperature, the mass of the scattering atoms, the incident neutron energies and the

geometry/efficiency of the detectors. For systems such as those containing H or D, the corrections are much more complicated [24]. The inelastic corrections are assumed to apply only to the self scattering part of equation (2.15) and are calculated at the same time as the self scattering correction. This is rationalised by considering the distinct scattering to be perfectly elastic and thus no recoil or inelastic corrections need to be made. However, the scattering from liquids is only quasi-elastic because the atoms are not bound into a position like the atoms of a solid. This is especially true with hydrogen atoms and the distinct scattering for hydrogenous material may contain remnants of the inelasticity. Generally though, it is felt that the corrections will be very small for the distinct scattering and can be ignored.

The routines used in the ATLAS package to perform the inelastic, recoil and self-scattering corrections were derived by Howe, McGreevy and Howells [25].

2.10.6 Merging the Data

When all the corrections have been performed there are fourteen spectra for LAD (5-150° detection range) and six spectra for SANDALS (for the six groups in the 11-21° detection range); these corrected individual $S(Q)$ can be added together. The data for the low angles are optimal in the low- Q range, and the high- Q range is best for the higher angles.

A merged or composite $S(Q)$ is obtained by merging sections of the corrected individual $S(Q)$ from each grouping of angles. The Q -regions used are those where the data are in agreement (within the statistics of the data points) between the angles.

2.10.7 Fourier Transformation

The Fourier transformation is performed according to equation (2.12). There are problems that are encountered at this stage; the data are not integrated over an infinite range (usually the range of the data is 0.5-30 Å⁻¹) and this causes an effect called apodisation. Apodisation is the name for the spurious peaks which appear in the low-R range of the g(R) spectra when S(Q) is transformed.

2.11 The LAD Experiments

Neutron diffraction experiments were attempted on three fluid halocarbons, two of which contained hydrogen: fluoroform (CHF₃, HFC-23), chlorodifluoromethane (CHClF₂, HCFC-22), and dichlorodifluoromethane (CCl₂F₂, CFC-12) using LAD. Such fluorocarbons and chlorofluorocarbons are important industrial chemicals, notably as propellants and refrigerants [26].

2.11.1 The Experimental Components

The LAD experiment has four important components which are

- (i) the empty cell,
- (ii) the background with the cell removed,
- (iv) the vanadium calibration rod,
- (iii) the fluid halocarbon sample.

The empty cell, the background, and the vanadium calibration rod only needed to be run once for a number of samples since the cell was not repositioned during the series of experiments. The empty cell was recorded in three stages between fluid sample runs; the total time that data

was collected was 7 h which corresponded to 612 μA of current. The background was collected over 6 h (498 μA), the vanadium rod 5 h (433 μA) and the CCl_2F_2 sample for 19 h (1686 μA).

2.11.2 Dichlorodifluoromethane

2.11.2.1 Experimental

Dichlorodifluoromethane (CCl_2F_2 , A12) is an important refrigerant but it has the drawback of being ozone destructive. In the search for alternatives neutron diffraction may play its part.

CCl_2F_2 was supplied in cylinders by ICI at a purity greater than 99.98%. It was studied at a temperature of $152.5 \pm 1.5 \text{ K}$ ($\rho \approx 1.73 \text{ g cm}^{-3}$). At that temperature CCl_2F_2 is well above its freezing point but its vapour pressure is less than 0.2 kPa.

The sample was condensed into the 'Wormald cell' using the apparatus shown schematically in figure 2.16. The pressure cell (A) was chilled to 153 K. Valves (B) and (C) were opened allowing the cell and piping to be evacuated using the vacuum pump (D). Valve (C) was closed and valve (E) was opened condensing some fluid from cylinder (F) into the cell. Valves (B) and (E) were closed when the pressure gauge (G) stabilised. The sample cell was then left to reach equilibrium at 153 K. The temperature inside the cell was regulated using the closed-cycle-refrigeration unit that held the temperature constant to better than $\pm 1.5 \text{ K}$ throughout the data acquisition time. Problems with the thermocouples to the temperature controller caused this temperature fluctuation. The thermocouples were corrected after the CCl_2F_2 experiment was completed.

When the cell had reached equilibrium the shutter for the beam was opened and the data acquisition electronics were initiated. The

scattered neutrons were collected at thirteen of the detectors available on the LAD diffractometer; one of the 10° detectors failed during this run and was also unuseable for the other two experiments.

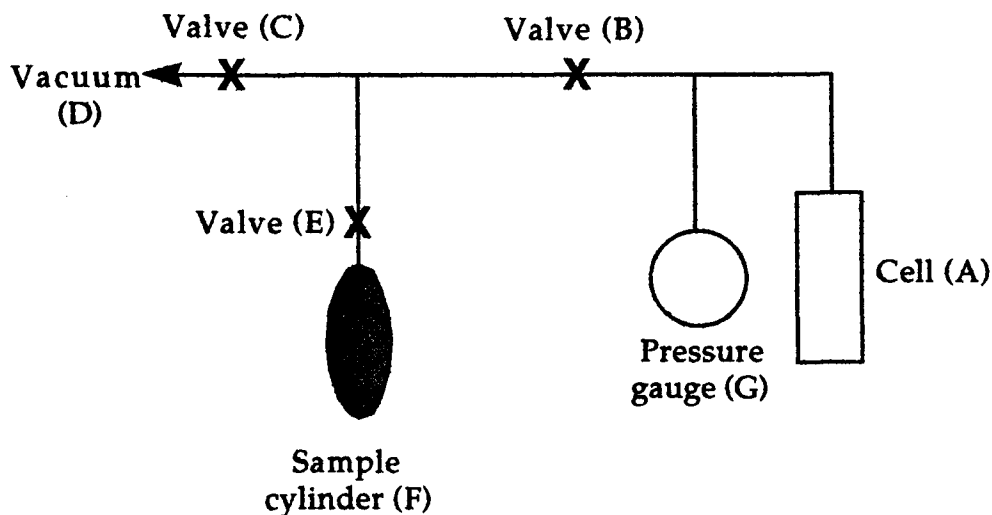


Figure 2.16 The LAD gas handling apparatus

The sample was removed at the end of the experiment by heating the cell to room temperature, opening valves (B) and (C), and evacuating using the vacuum pump.

2.11.2.2 Data Reduction

Diffraction data for CCl_2F_2 were divided by the incident monitor spectrum, normalised to vanadium, and corrected for deadtime, background, sample container, absorption, and multiple scattering using the standard methods described in references [17, 27] and outlined in section 2.10.

However modifications to the normal ATLAS procedures were necessary due to the inadequacies of the Placzek correction especially at high detector angles. This is especially important when dealing with the hydrogen-containing fluids [25] but it is described here because the method was also used for the data reduction of CCl_2F_2 . The following

modifications were adopted in the analysis, which follows a scheme similar to that outlined by Jung *et al.* [28].

- (i) the standard Placzek correction was performed for all detector angles using the average molecular mass of the atoms in the molecule,
- (ii) the $S(Q)$ from the 20° detector bank was Fourier transformed to obtain an initial estimate of the intramolecular atomic separations, R_{ij} ,
- (iii) the R_{ij} values were used in equation (2.22) (section 2.6.2) together with an estimate of the Debye-Waller factor to calculate $F_1(Q)$,
- (iv) the $F_1(Q)$ from (iii) was removed from all the $S(Q)$ s in (i) to give $D_M(Q)$ - equation (2.21),
- (v) the residual curves in (iv) were smoothed using a Chebyshev polynomial fitting routine,
- (vi) the smoothed curves in (v) were subtracted from the $S(Q)$ s in (i) to give corrected $S(Q)$ s,
- (vii) where possible the $S(Q)$ s were merged to give a composite $S(Q)$, which when transformed gave better estimates of R_{ij} ,
- (viii) the processes (iii)-(vii) were repeated iteratively,
- (ix) the MIM method (see below) was used to transform the final $S(Q)^*$ from (viii) to $g(R)$.

It is worth bearing in mind a few details pertinent to the use of this data correction method. Since $D_M(Q)$ usually decreases very much faster with increasing Q than $F_1(Q)$, the high- Q region of the structure factor is dominated by $F_1(Q)$. Thus, the difference between the calculated $F_1(Q)$ and the measured individual structure factor, can be assumed to represent any

* A copy of the $S(Q)$ from the LAD or SANDALS experiments can be obtained from Dr. K. A. Johnson, Chemistry Dept., Liverpool University.

extra inelastic correction. This method is less successful for the low- Q region where $D_M(Q)$ dominates.

Figure 2.17 shows the $S(Q)$ for CCl_2F_2 at the 20° detector angle after the Placzek corrections had been performed; a little residual curvature remained but this was removed using the modification scheme outlined above. Figure 2.18 shows the overlay of $F_1(Q)$ with the final merged $S(Q)$ for CCl_2F_2 highlighting the overlapping region at high Q , and figure 2.19 shows the intermolecular structure factor $D_M(Q)$.

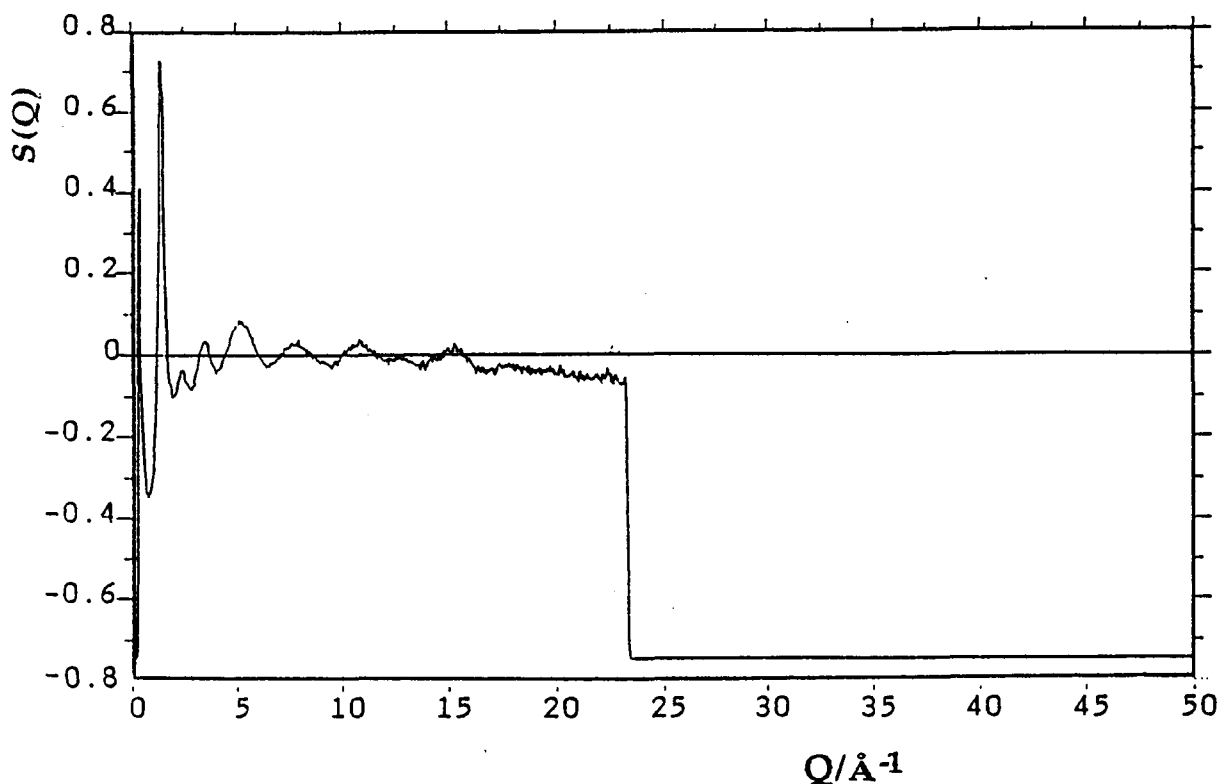


Figure 2.17 The structure factor, $S(Q)$ at the 20° detector bank.

There is a shoulder on the first peak in the $D_M(Q)$ at roughly 2.1 \AA . This could be indicative of preferential orientation (molecular correlation) in the liquid at 153 K . Similar shoulders have been found in the $D_M(Q)$ of Cl_2 [39] and CO_2 [40].

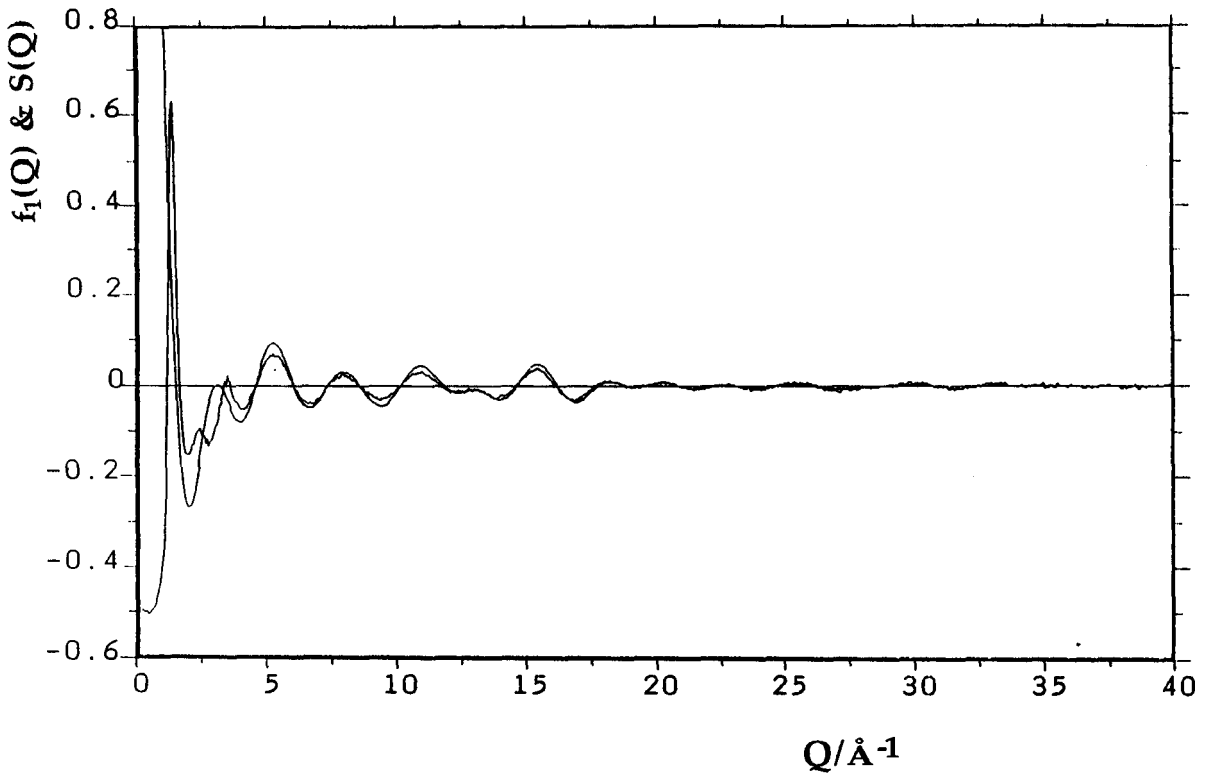


Figure 2.18 The overlay of the intramolecular form factor, $F_1(Q)$ and final merged structure factor, $S(Q)$ for CCl_2F_2 at 153 K.

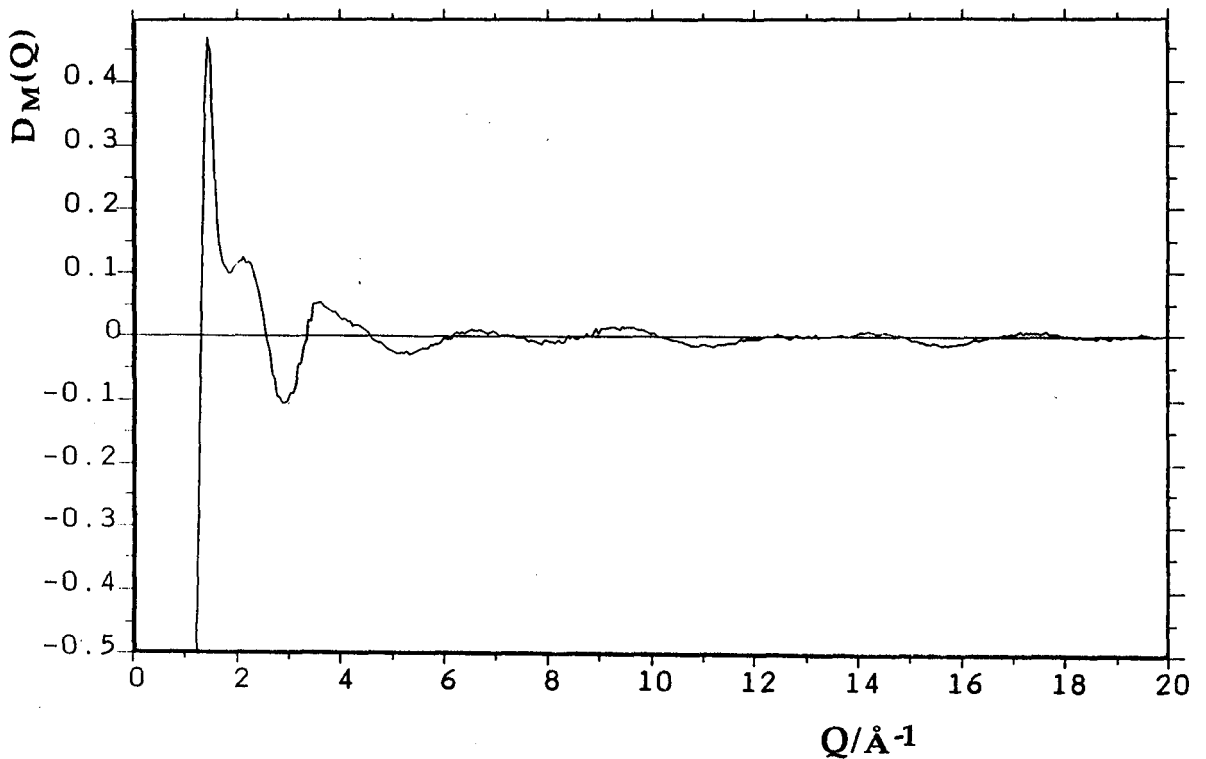


Figure 2.19 The intermolecular structure factor, $D_M(Q)$ for CCl_2F_2 at 153 K.

Composite (or merged) $S(Q)$ s were obtained by merging sections of the corrected individual $S(Q)$ at each detector angle. Figures 2.20 (a-g) show the unsmoothed data at the 5° , 10° , 20° , 35° , 58° , 90° , and 150° detector angles with the polynomially-corrected regions shown in the inset. The Q-regions merged are shown in table 2.4. These regions were chosen because the overlap between successive spectra were well within the experimental error. Figure 2.21 shows the final corrected merged $S(Q)$.

Detector Angle (degrees)	Q-region for merge/ \AA^{-1}
5	0.25 - 1.2
10	1.0 - 3.0
20	1.2 - 12
35	6 - 15
56	10 - 15
90	10 - 20
150	14 - 40

Table 2.4 The Q-regions merged for CCl_2F_2

The Minimum Information Method (MIM) approach of Soper [29] was used to transform the $g(R)$. In this technique, $g(R)$ was calculated using a one-dimensional Monte Carlo simulation, which was back-transformed to give $S(Q)$. This was then fitted to the experimental $S(Q)$. When the best fit between experimental and MIM-derived $S(Q)$ was achieved, any residual systematic differences between calculated and measured $S(Q)$ were taken to represent the inaccuracies in the inelastic corrections or normalisation, and the experimental data adjusted appropriately. It is worth noting that the MIM can also incorporate constraints. The standard one is to set to zero the $g(R)$ from the origin to a

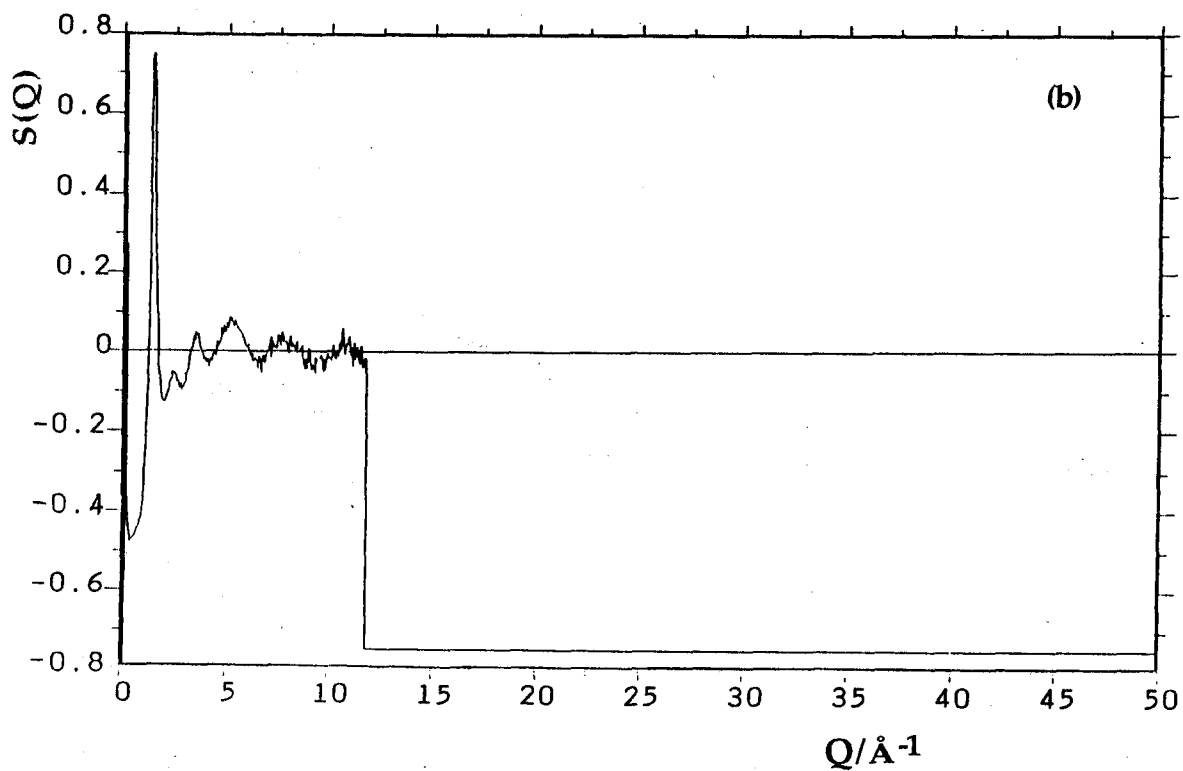
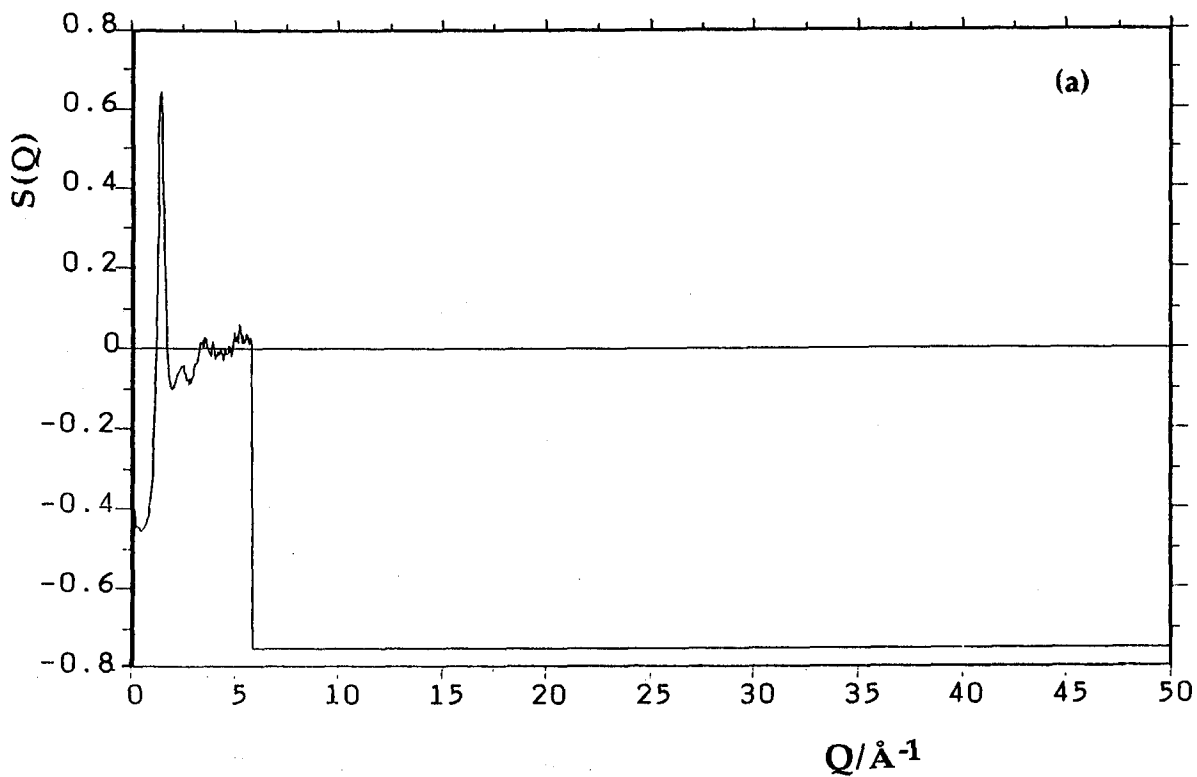


Figure 2.20 Corrected $S(Q)$ at (a) the 5° , and (b) the 10° detector banks.

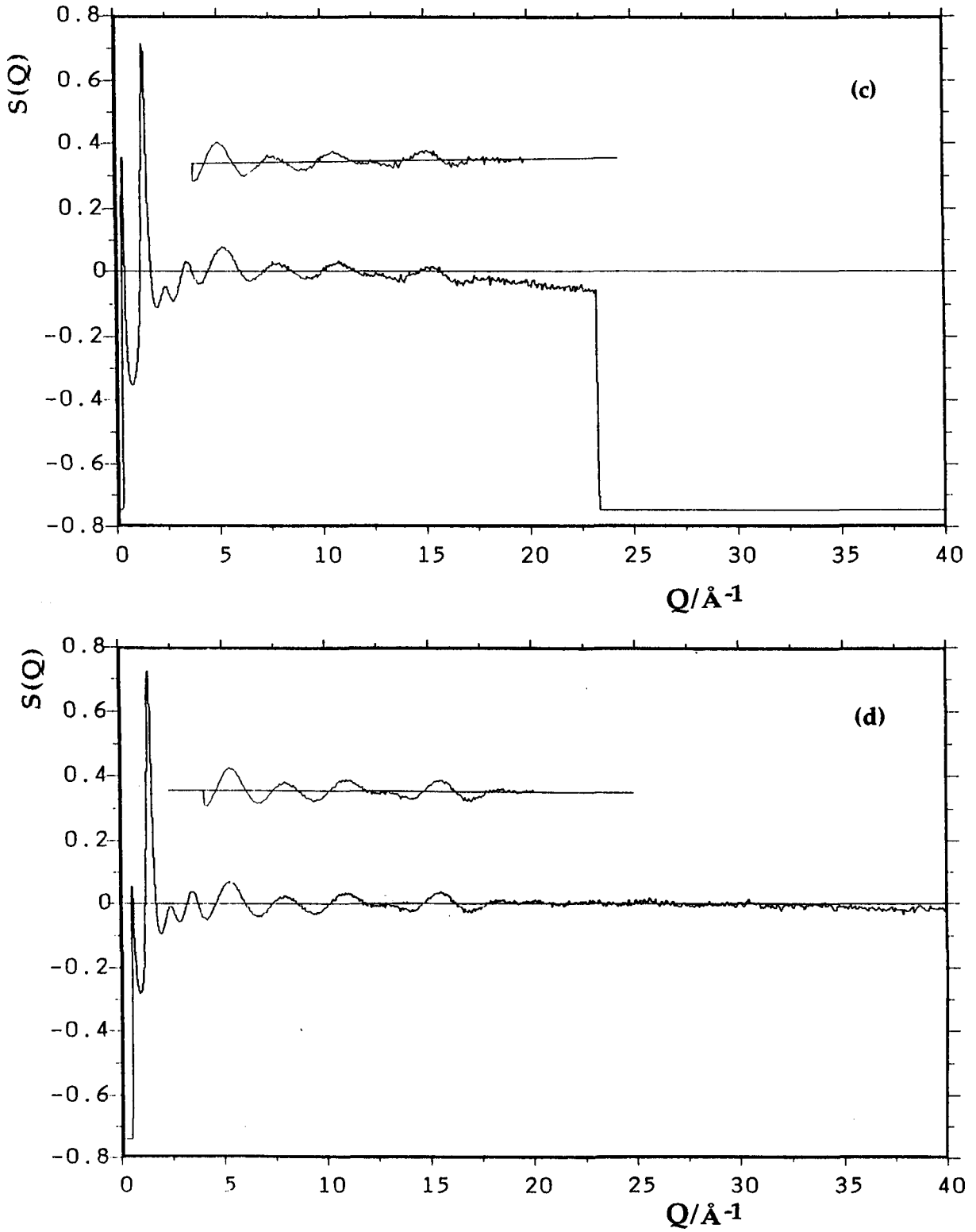


Figure 2.20 Unsmoothed $S(Q)$ at (c) the 20°, and (d) the 35° detector banks. Inset are the polynomially-corrected spectra.

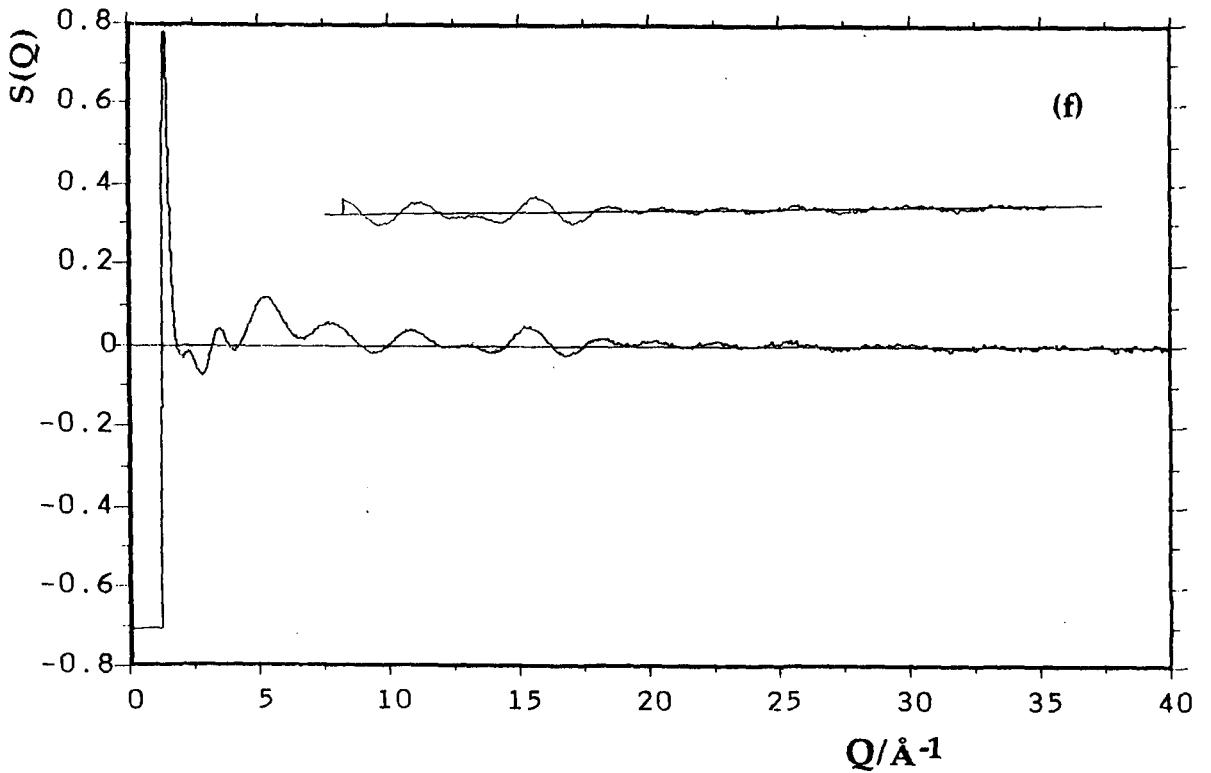
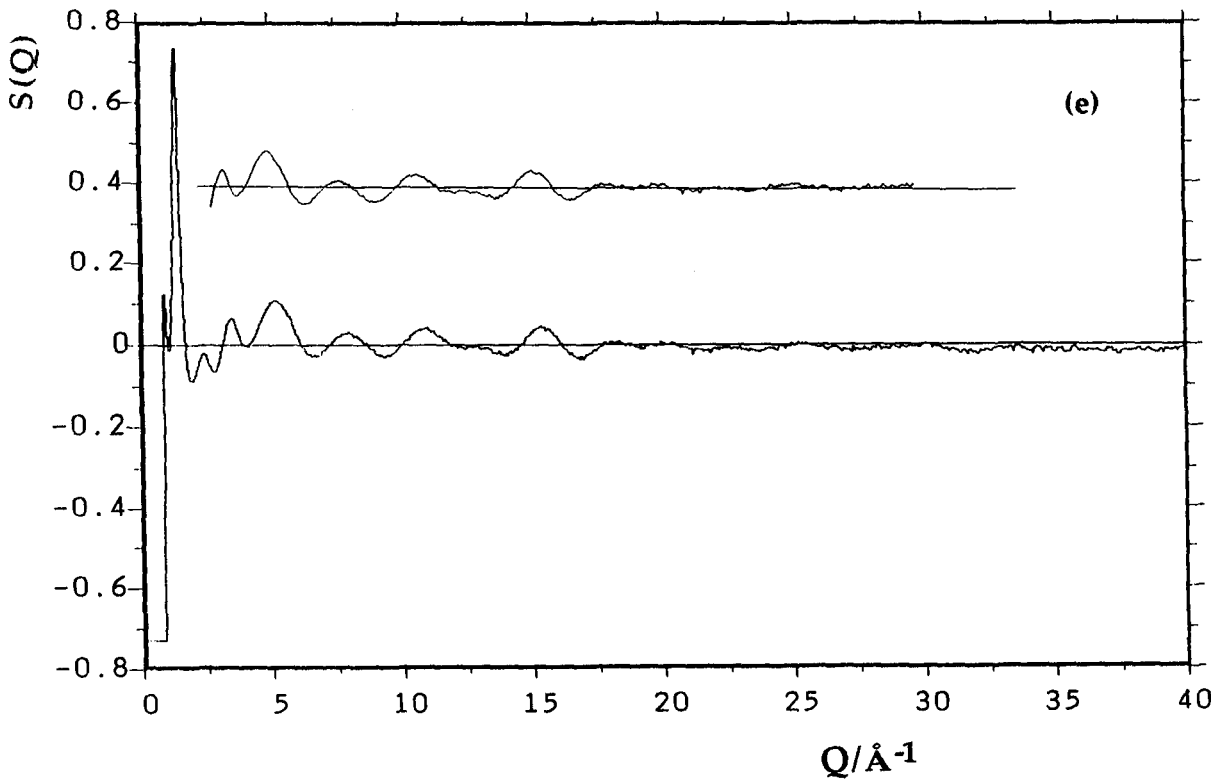


Figure 2.20 Unsmoothed $S(Q)$ at (e) the 58° , and (f) the 90° detector banks. Inset are the polynomially-corrected spectra.

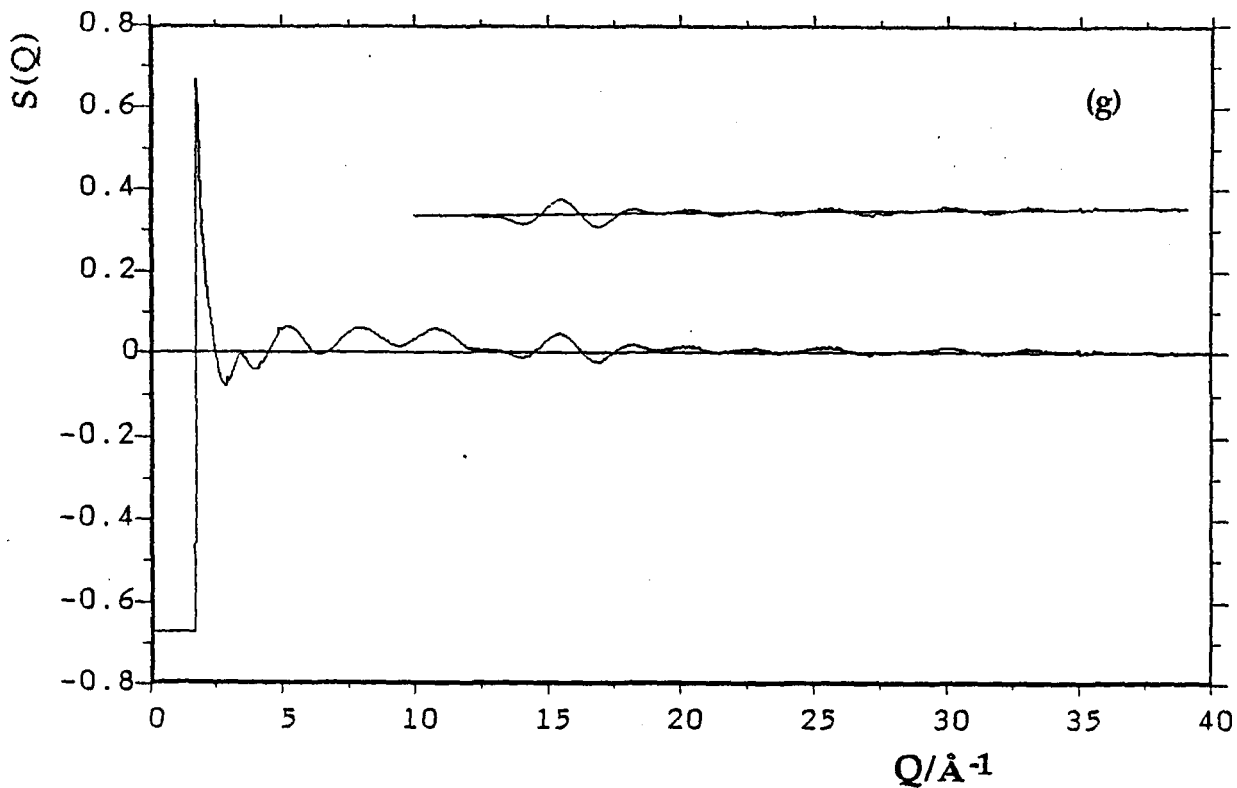


Figure 2.20 Unsmoothed $S(Q)$ at (g) the 150° detector banks. Inset is the polynomially-corrected spectrum.

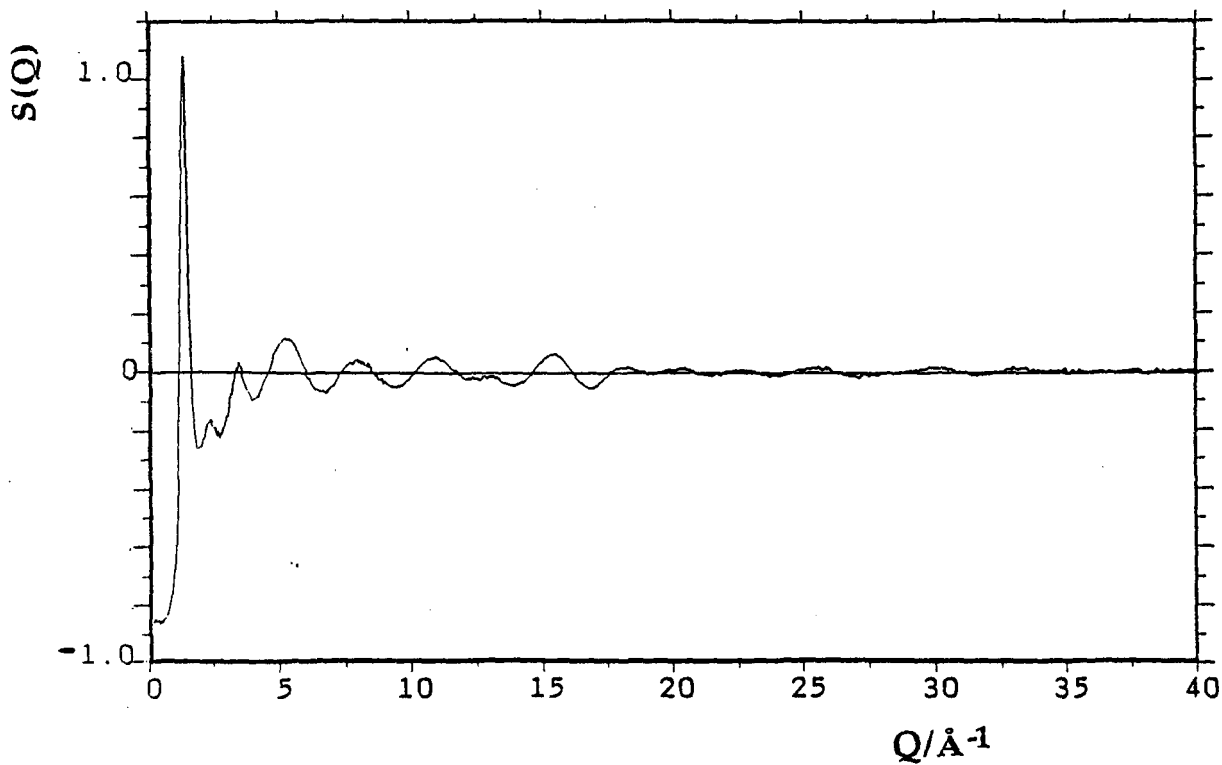


Figure 2.21 The final corrected and merged $S(Q)$ for CCl_2F_2 at 153 K.

the first peak is at 1.3 Å). Another is to constrain the $g(R)$ to be positive for all R values. The $g(R)$ obtained by MIM for CCl_2F_2 is shown in figure 2.22.

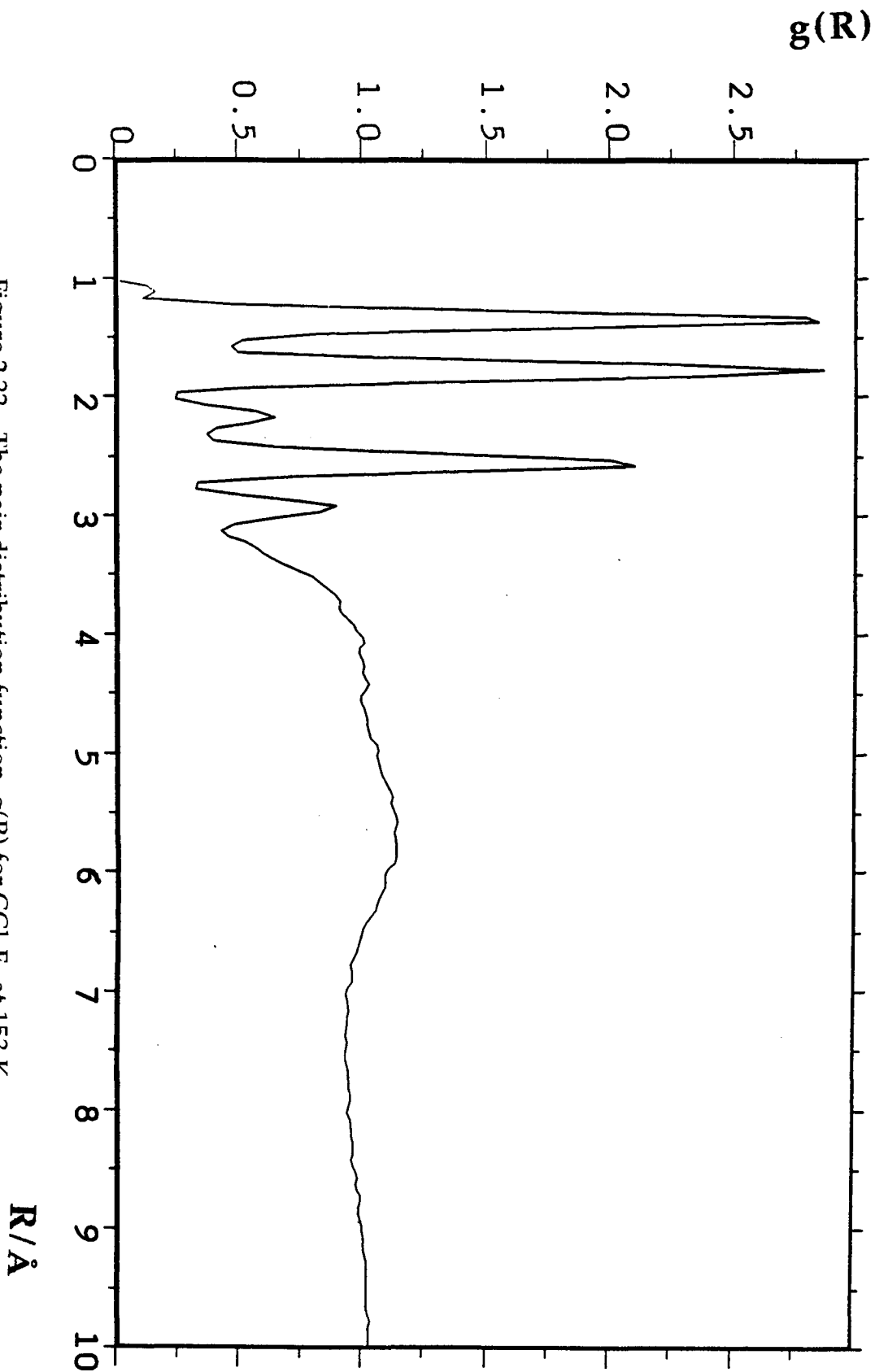


Figure 2.22 The pair distribution function, $g(R)$ for CCl_2F_2 at 153 K.

2.11.2.3 Results and discussion

The intramolecular structure for dichlorodifluoromethane is quite easy to identify in the $g(R)$; we can pick out all the intramolecular atomic separations from the $g(R)$ plot, giving a complete picture of the liquid intramolecular structure.

The positions of the intramolecular peaks in the $g(R)$ plot of CCl_2F_2 , which are all positive, were fitted to Gaussians and the following intramolecular atomic separations (in Å), together with an estimate of their uncertainties (in the last decimal place), were obtained:

C-F 1.326 (2), C-Cl 1.755 (1), F...F 2.142 (1), F...Cl 2.525 (1),
Cl...Cl 2.900 (3).

The bond angles associated with these intramolecular atomic separations were also calculated;

FCF 107.7° (1), FCCl 109.3° (1), ClCCl 111.4° (1).

The intramolecular atomic separations given by neutron diffraction compare well with those given in both a gas-phase microwave spectroscopy experiment [30] and a recent neutron diffraction study of solid CCl_2F_2 [31] as shown in table 2.5.

The intermolecular structure of CCl_2F_2 can also be observed in the $g(R)$. Three peaks are evident in the $g(R)$, centred at 4.4, 5.8 and 9.8 Å respectively, which is suggestive of preferential orientation of the molecules in liquid CCl_2F_2 . If the molecules of CCl_2F_2 were completely random in their motion only two, broad, peaks would be seen in the intermolecular region of the $g(R)$, one centred around 4.9 Å (the average distance between carbon atoms at the density of this experiment), and

consequently another around 9.8 Å. A detailed interpretation of the intermolecular structure of liquid CCl₂F₂ is only really possible, however, using molecular dynamics simulations as detailed in the next chapter.

	SOLID			LIQUID	GAS
	1.5 K	77 K	110 K	153 K	
C-F	1.334 (3)	1.329 (4)	1.323 (4)	1.326	1.345 (3)
C-Cl	1.765 (2)	1.756 (2)	1.746 (3)	1.755	1.744 (8)
F...F	2.155 (3)	2.157 (4)	2.156 (5)	2.142	2.151
F...Cl	2.543, 2.538 (4)	2.527, 2.528 (5)	2.509, 2.516 (5)	2.525	-
Cl...Cl	2.917 (2)	2.904 (2)	2.884 (3)	2.900	2.902

Table 2.5 Comparing the intramolecular atomic separations (in Å) for neutron diffraction and gas phase microwave experiments on CCl₂F₂.

2.11.3 Chlorodifluoromethane, CHClF₂, and Fluoroform, CHF₃

2.11.3.1 Experimental

The application of neutron diffraction to studies of hydrogen-containing molecules has been limited. This is due to the high inelastic and incoherent recoil of neutrons from hydrogen atoms; previous studies on small deuterium-containing molecules have encountered similar problems [32]. However, there is much interest in the possibility of non-ideal intermolecular interactions, such as hydrogen bonding, between the molecules of the hydrogen-containing halocarbons [33-36]. Chlorodifluoromethane (CHClF₂, HCFC-22) and fluoroform (CHF₃, HFC-23) are interesting examples of that type of material.

CHF₃ and CHClF₂, supplied in cylinders by ICI at a purity greater

than 99.98%, were studied at temperatures of 152.5 ± 1.0 K ($\rho \approx 0.87$ g cm⁻³) and 153.2 ± 1.0 K ($\rho \approx 1.64$ g cm⁻³) respectively. The fluids were well above their freezing points at these temperatures and their respective vapour pressures are low.

The fluids were condensed into the cell as described for CCl₂F₂. In each case the conditions in the cell (regulated by the CCR) were allowed to reach equilibrium before the data was acquired in the thirteen detectors.

The background, vanadium and empty cell measurements were the same as for CCl₂F₂. The CHF₃ sample data was acquired over 12 h (1000 μ A) and CHClF₂ over 22 h (1886 μ A).

2.12.3.2 Data Reduction

Diffraction data for CHClF₂ and CHF₃ were divided by the incident monitor spectrum, normalised to vanadium, and corrected for deadtime, background, sample container, absorption, and multiple scattering using the standard methods.

The modifications to the data reduction of CCl₂F₂ outlined in section 2.12.1.2 above were even more important in the cases of CHF₃ and CHClF₂. Substantial recoil effects are associated with scattering from hydrogen atoms at high angles and the curvature, slightly evident in the case of CCl₂F₂, was much more prominent for CHF₃ and CHClF₂. The inelastic and recoil corrections are very difficult to estimate for hydrogen-containing molecules and cannot yet be properly applied [10]; the residual curvature in the spectra after the Placzek corrections were applied was extremely high. This meant that only the data collected in the lowest four detector angles were analysed in detail for CHClF₂ and CHF₃; the higher angle detector data was discarded because the curvature was too

high to rectify accurately. Figures 2.23 and 2.24 show the overlay of $F_1(Q)$ with the final merged $S(Q)$, for CHF_3 and CHClF_2 respectively, and Figures 2.25 and 2.26 show their intermolecular structure factors, $D_M(Q)$.

Composite (or merged) $S(Q)$ s were obtained by merging sections of the corrected individual $S(Q)$ at each detector angle; Figures 2.27 and 2.28 show the final corrected merged $S(Q)$ for each liquid.

The MIM method was used to transform the $S(Q)$ s to $g(R)$ s. The $g(R)$ was constrained to be zero for all R up to 0.7 Å for both of the samples. However, the constraint of positive $g(R)$ for all R values does not hold for hydrogen-containing molecules since hydrogen has a negative scattering length. The $g(R)$ s obtained by MIM are shown in figures 2.29 and 2.30.

2.11.3.3 Results and Discussion

The intramolecular structure for the two hydrogenous halocarbons is easy to identify in the $g(R)$, although the negative contributions from X-H interactions ($X = \text{Cl}, \text{F}, \text{or C}$), with CHClF_2 , and CHF_3 , make very accurate evaluation of the intramolecular atomic separations more difficult to achieve. The negative X-H peaks could not be fitted and are the final values input into the $F_1(Q)$ equation, which were estimated by inspection of the $g(R)$. The following separations were obtained;

- (i) CHClF_2 : C-H 1.08 (3), C-F 1.35 (2), C-Cl 1.76 (1), H...F 1.97 (4), F...F 2.18 (3), H...Cl 2.34 (5), F...Cl 2.55 (2);
- (ii) CHF_3 : C-H 1.11 (2), C-F 1.32 (1), H...F 1.96 (4), F...F 2.17 (1).

The following bond angles of the fluids were also calculated;

- (i) CHClF_2 : HCF 108.3° (5), FCF 107.7° (2), HCCl 108.5° (15), FCCl 109.5° (3)
- (ii) CHF_3 : HCF 107.2° (13), FCF 110.5° (4)

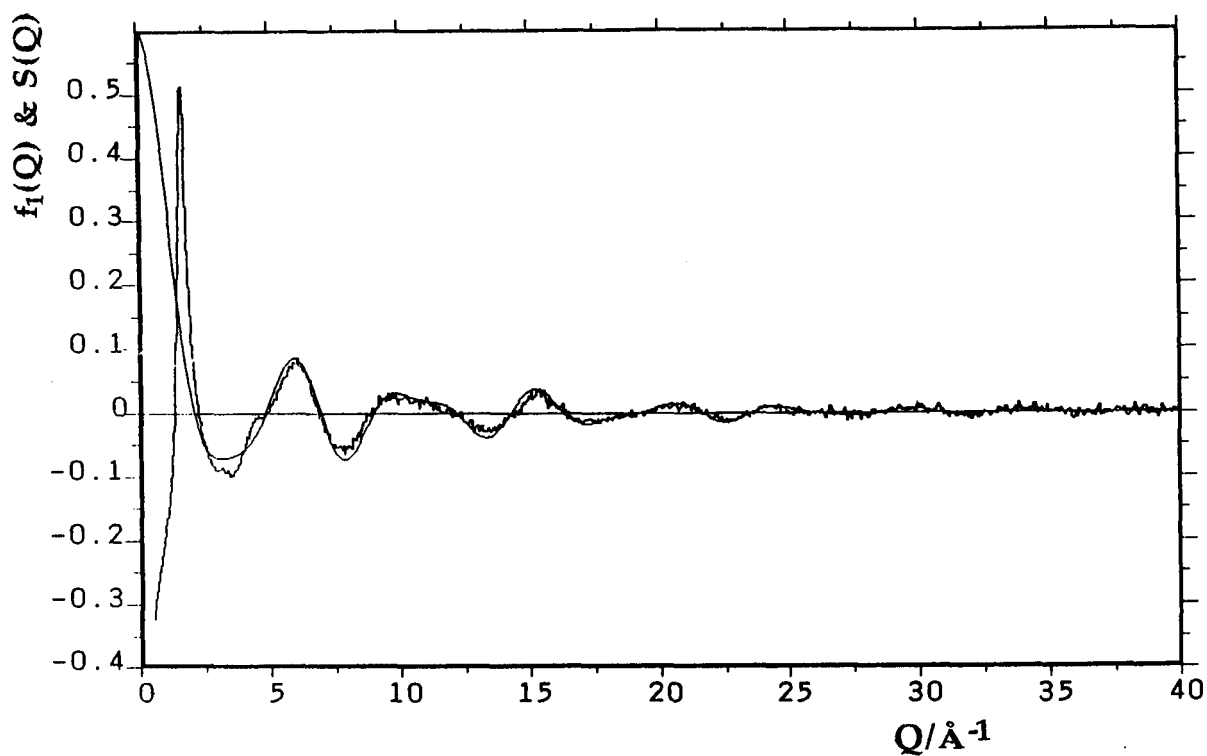


Figure 2.23 The overlay of the intramolecular form factor, $F_1(Q)$ and final merged structure factor, $S(Q)$ for CHF_3 at 153 K.

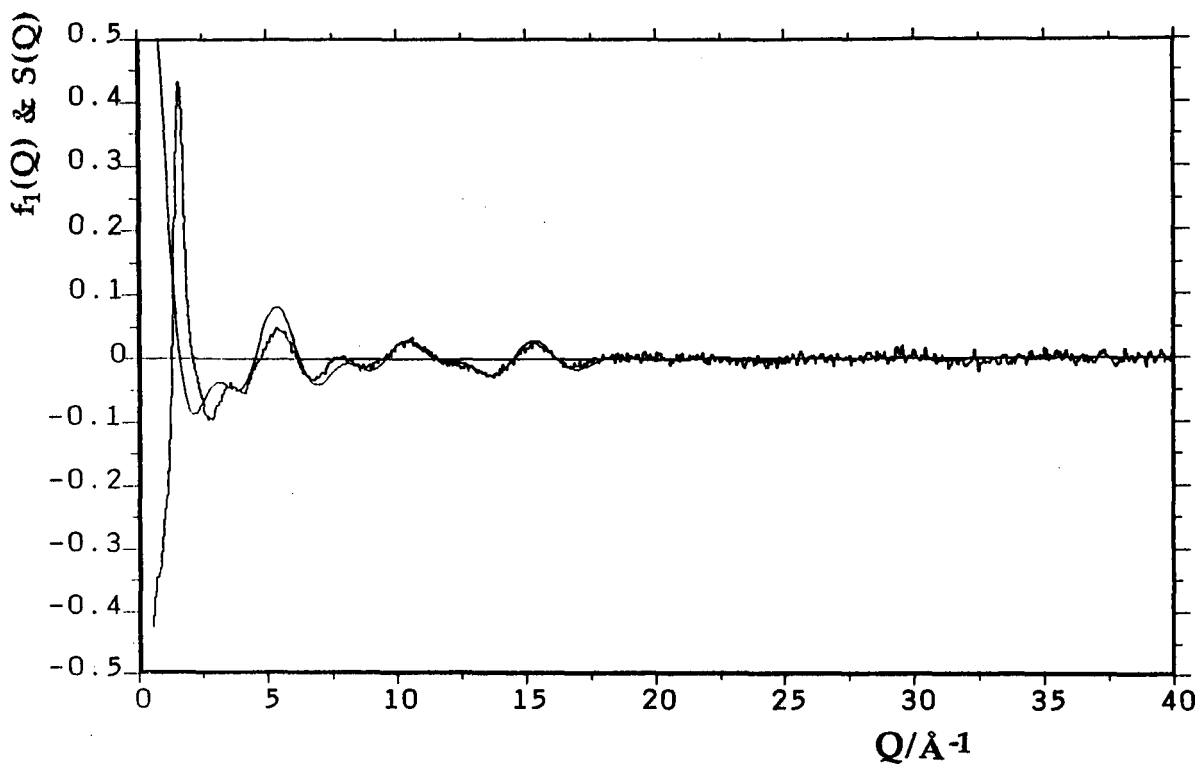


Figure 2.24 The overlay of the intramolecular form factor, $F_1(Q)$ and final merged structure factor, $S(Q)$ for CHClF_2 at 153 K.

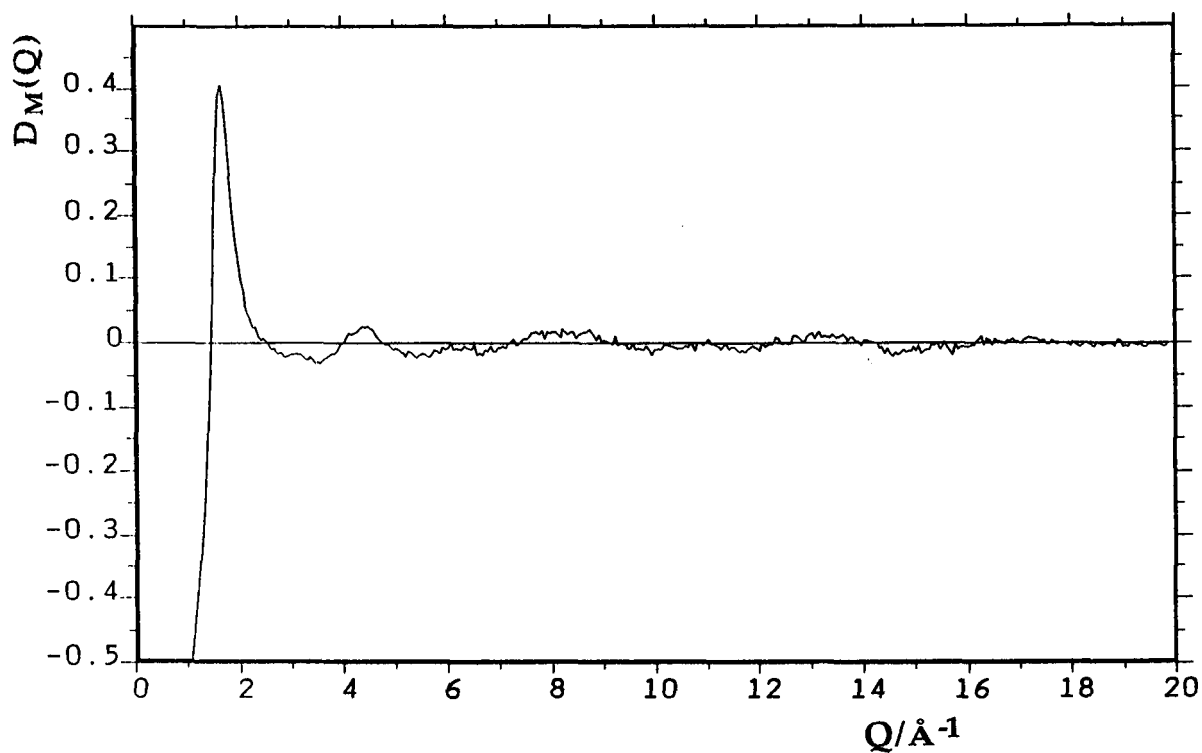


Figure 2.25 The intermolecular structure factor, $D_M(Q)$ for CHF_3 at 153 K.

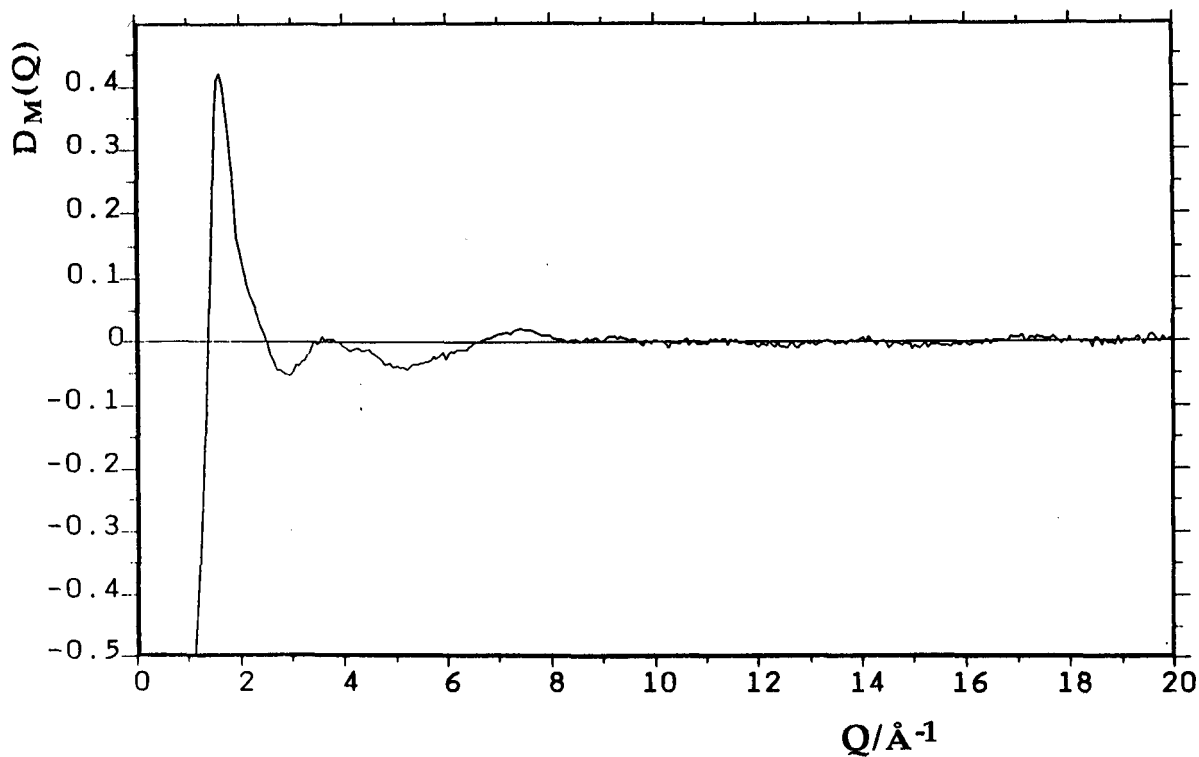


Figure 2.26 The intermolecular structure factor, $D_M(Q)$ for CHClF_2 at 153 K.

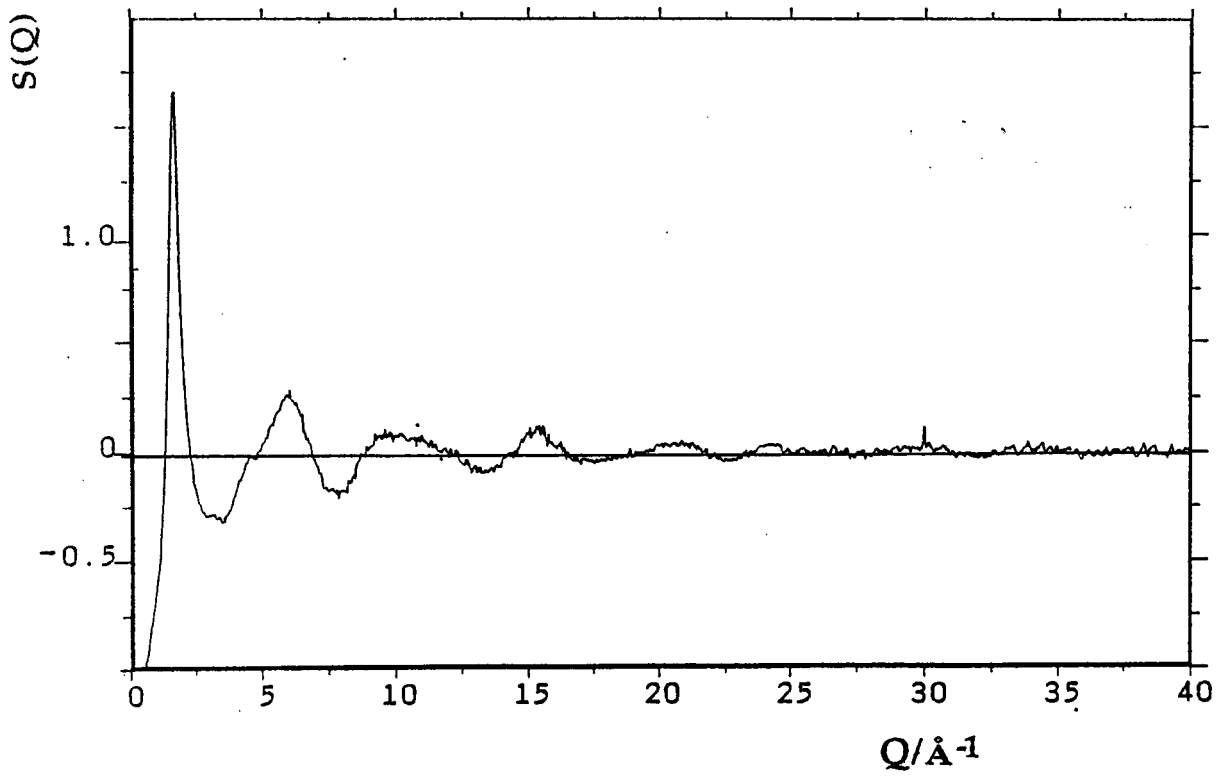


Figure 2.27 The final corrected and merged $S(Q)$ for CHF_3 at 153 K.

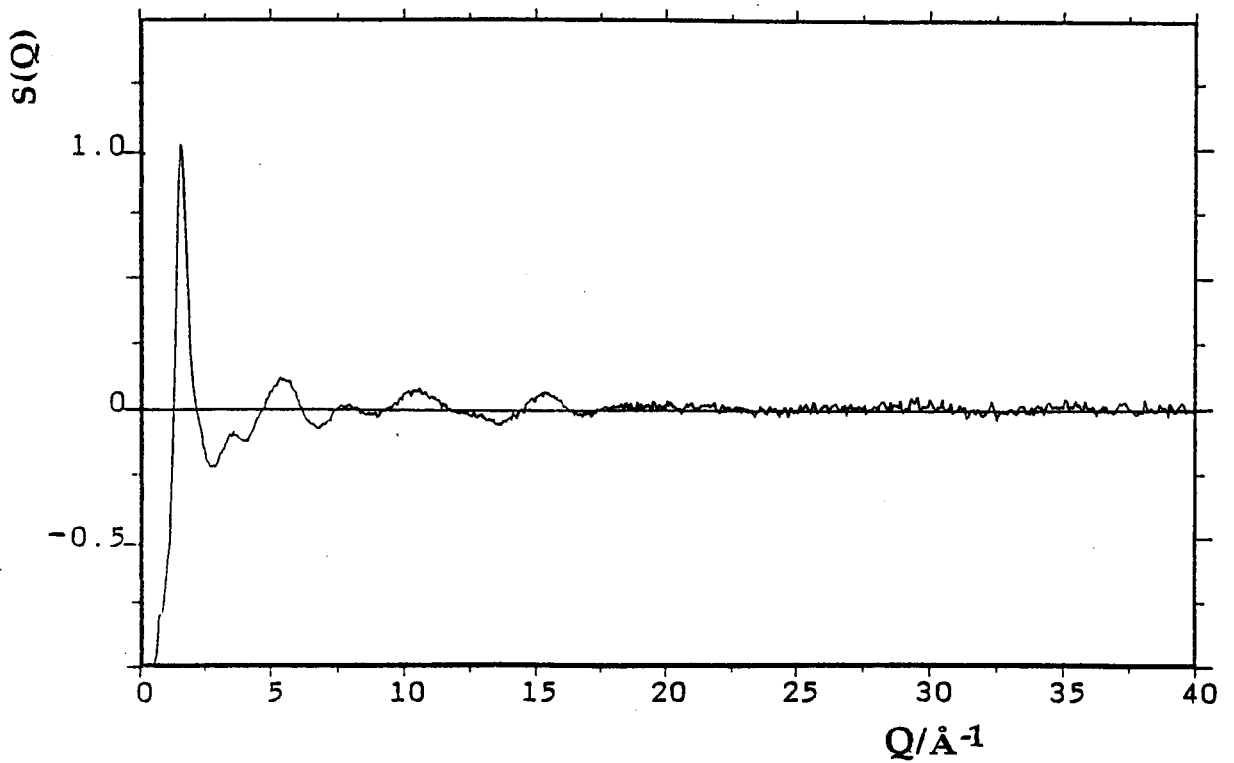


Figure 2.28 The final corrected and merged $S(Q)$ for CHClF_2 at 153 K.

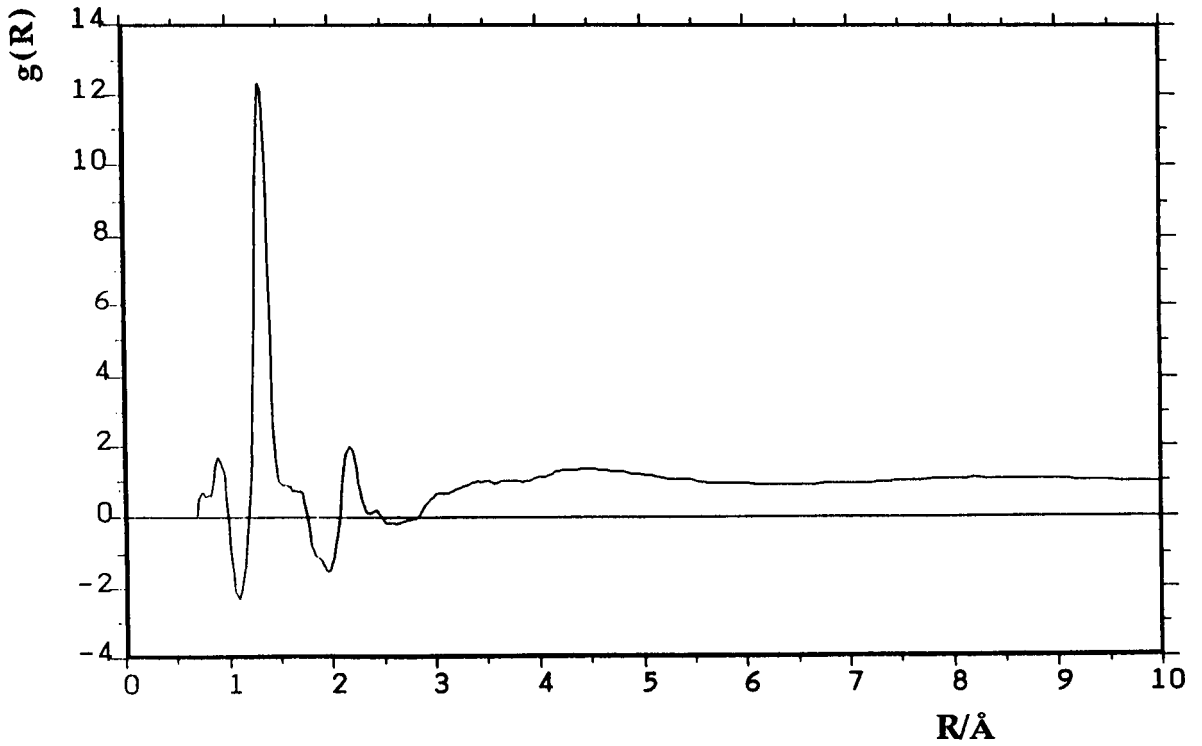


Figure 2.29 The pair distribution function, $g(R)$ for CHF_3 at 153 K.

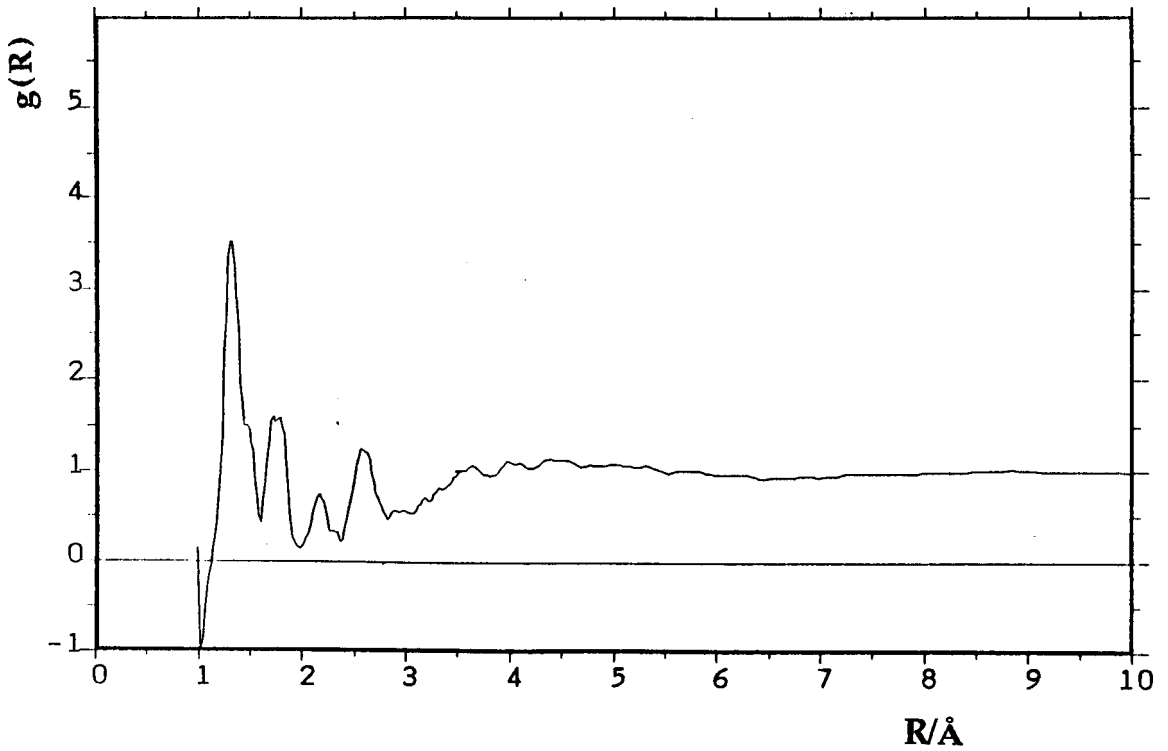


Figure 2.30 The pair distribution function, $g(R)$ for CHClF_2 at 153 K.

The values compare well with gas-phase microwave spectroscopy results CHClF_2 and CHF_3 [37, and references therein] as shown in table 2.6. This appears to show that the technique employed in the data reduction for the hydrogen-containing molecules was valid.

CHF_3			CHClF_2		
	LIQUID	GAS		LIQUID	GAS
	153 K			153 K	
C-H	1.11	1.098 (10)	C-H	1.08	1.09 assumed
C-F	1.32	1.332 (5)	C-F	1.35	1.350 (10)
H...F	1.96	-	C-Cl	1.76	1.747 (10)
F...F	2.17	2.167	H...F	1.97	-
			F...F	2.16	2.17
			H...Cl	2.33	-
			F...Cl	2.55	2.548 (10)

Table 2.6 Comparing the intramolecular bond separations (in Å) of CHF_3 and CHF_2Cl given in neutron diffraction and gas phase microwave experiments

The intermolecular regions for CHClF_2 , and CHF_3 are more difficult to interpret due to the negative contributions from $\text{X}\cdots\text{H}$ intermolecular interactions that arise due to the negative scattering length of hydrogen. There is, however, an interesting negative intermolecular peak in the CHF_3 $g(\text{R})$ at 2.5-3.0 Å, which can be assigned to $\text{H}\cdots\text{F}$ nearest neighbour contacts. Before any molecular dynamics routines were performed we assigned this peak tentatively as a rocket (or Apollo) conformation of molecules (see section 1.6.6). One point that can be noted immediately is that the interaction between H and F atoms does not indicate a strong

hydrogen bond (if it is a hydrogen bond at all), since the distance between these atoms is roughly equal to the sum of the van der Waals' radii of the two atoms (1.1 Å and 1.33 Å respectively) - if strong H-bonding existed in the liquid, the H-F distance would be much shorter [35] than 2.4 Å. The molecular dynamics simulations of CHF₃ and CHClF₂ are discussed in the next chapter.

2.12 The SANDALS experiments

SANDALS became operational in 1990 and the experiments outlined below were amongst the first attempted.

Neutron diffraction experiments were attempted on five fluid halocarbons, none of which contained hydrogen: deuterated-fluoroform (CDF₃, DFC-23), deuterated-chlorodifluoromethane (CDCIF₂, DCFC-22), trichlorofluoromethane (CCl₃F, CFC-11), chlorotrifluoromethane (CClF₃, CFC-13), and bromotrifluoromethane (CBrF₃, BrFC-13B1) using SANDALS.

2.12.1 Experimental Components

Similar to the LAD experiment, the SANDALS experiment requires the empty vessel, the background and the vanadium calibration rod to be recorded as well as the samples. The sample vessel was not moved over the duration of the experiment and so one measurement of the empty cell sufficed for the data reduction of all the samples. The diffraction data from the empty vessel were collected between fluid sample runs. The difference between the LAD and the SANDALS experiments was that the temperature in the moderator was proving to be unstable and the data collection was split into 2 h runs. After 2 h, the file containing the

raw diffraction data was closed and written to optical disk. If further data were required another 2 h run was initiated. The consecutive data acquisition could be automated for overnight running of diffraction experiments. The data acquisition time and the corresponding current recorded were as follows;

- (i) background 2 h (165 μA)
- (ii) empty cell 2 h (154 μA)
- (iii) vanadium calibration rod 2 h (179.7 μA)

2.12.2 Chlorotrifluoromethane and Bromotrifluoromethane

2.12.2.1 Experimental

Chlorotrifluoromethane and bromotrifluoromethane are refrigerants like dichlorodifluoromethane that can cause ozone destruction.

CClF_3 was studied at a temperature of $152.5 \pm 0.5 \text{ K}$ ($\rho \approx 1.73 \text{ g cm}^{-3}$), and CBrF_3 at a temperature of $152.5 \pm 1.0 \text{ K}$ ($\rho \approx 0.87 \text{ g cm}^{-3}$). Both fluids, which were supplied in cylinders from ICI at a purity greater than 99.98%, were liquid at this temperature.

Again the "Wormald cell" was used to contain the fluids, and they were condensed in a similar manner to the fluids in the LAD experiments. However, the cell filling was slightly more convoluted since a valve (H) and a dump bottle were added into the apparatus (figure 2.31). After valves (B) and (E) were closed, valve (H) was then closed. This enabled the vessel to be isolated more effectively from the outside conditions.

After temperature stabilisation the scattered neutrons were detected in the bank of detectors of angular range $11\text{-}21^\circ$ that were currently available on SANDALS.

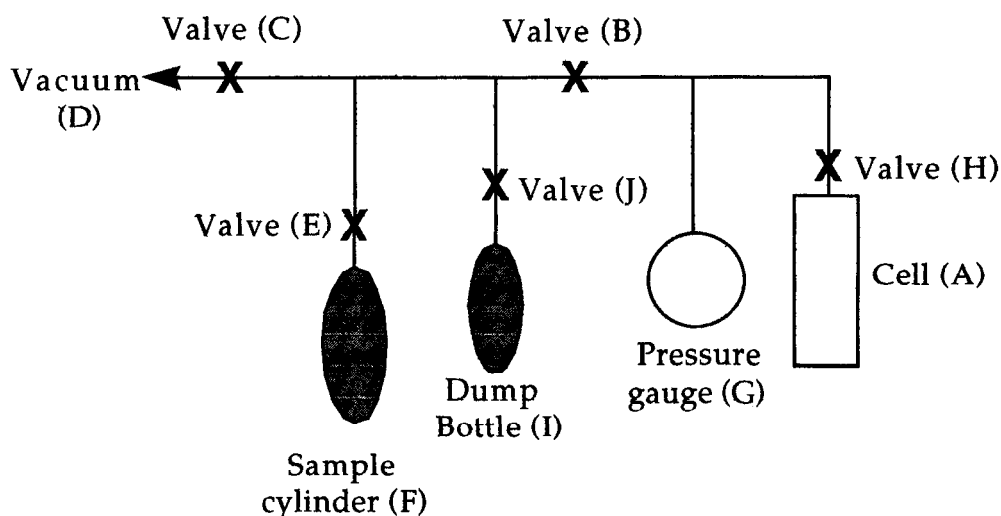


Figure 2.31 The SANDALS gas handling equipment

The samples were recorded in 2 h runs and the overall data acquisition times and currents were

- (i) CClF_3 sample 14 h (1300 μA)
- (ii) CBrF_3 sample 8 h (571 μA)

The CClF_3 sample was removed by heating the pressure vessel to room temperature, opening valves (B), (C) and (H), and evacuating using the vacuum pump. The CBrF_3 sample was removed by opening valves (J) and (C), and evacuating the dump bottle (I). Valve (C) was then closed, bottle (I) was immersed in liquid nitrogen, and valves (B) and (H) were opened. The collection of CBrF_3 in this manner rather than venting to atmosphere is done because the Br in the irradiated sample remained radioactive for about 8 days and so had to be stored securely for that period before being vented.

2.12.2.2 Data Reduction

No hydrogenous fluids were studied using SANDALS and this, coupled with the lower angles used in this experiment, led to simpler data

reduction. One problem was that if the transmission monitor was placed in the beam there was increased background scattering in the detectors. It has already been mentioned in section 2.10.1 that the lack of this monitor causes only minimal problems as long as it is possible to estimate the transmission cross-sections. The transmission cross-sections, which are energy dependent, were calculated from the scattering lengths of the atoms, which constitute the molecules of the diffracted fluids.

After the individual 2 h runs were added together, the raw diffraction data for each sample were normalised to vanadium and corrected for deadtime, background, container, attenuation and multiple scattering using the standard ATLAS methods, similarly to the LAD experiment. In the SANDALS experiment the scattered neutrons were collected at a continuous row of detectors arranged over a range of angles, from 11-20° which meant that none of the data in the SANDALS experiment had to be discarded. It was also felt that the inelastic corrections were small enough to be ignored at these angles; Placzek corrections are not exact and might have introduced errors into the data, so it is better not to perform these corrections unless absolutely necessary. However, some curvature was observed in the corrected spectra and it was removed by assuming that the baseline of the $S(Q)$ could be represented by a simple polynomial. Figures 2.32 and 2.33 show the $CClF_3$ and $CBrF_3$ overlay spectra for the six groups of detectors before the polynomial was removed. This curvature should not appear in the SANDALS spectra; it is of unknown origin and the instrument scientists are currently trying to locate its cause.

The method used to remove the curvature is outlined below;

- (i) the individual $S(Q)$ for each angle were Fourier transformed to give $g(R)$,

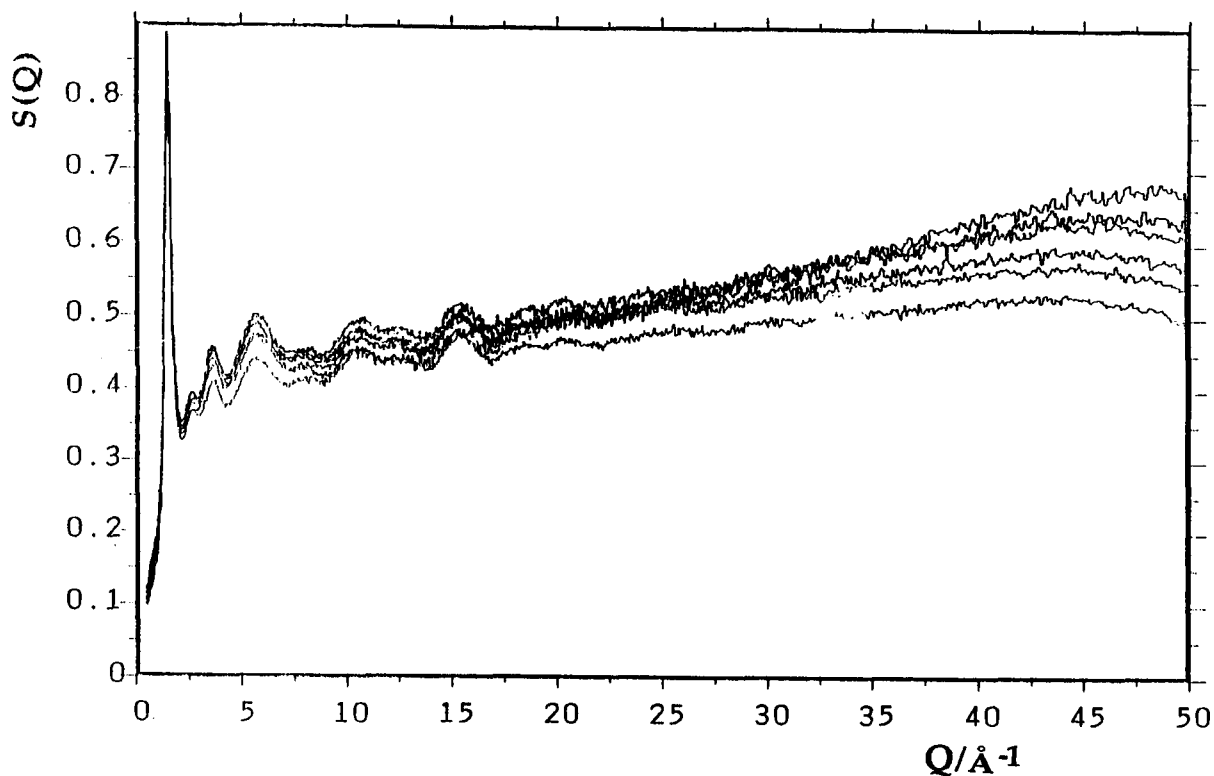


Figure 2.32 The overlay of the uncorrected $S(Q)$ for the six groups of SANDALS detectors, in the range 11° - 21° , for CClF_3 at 153 K.

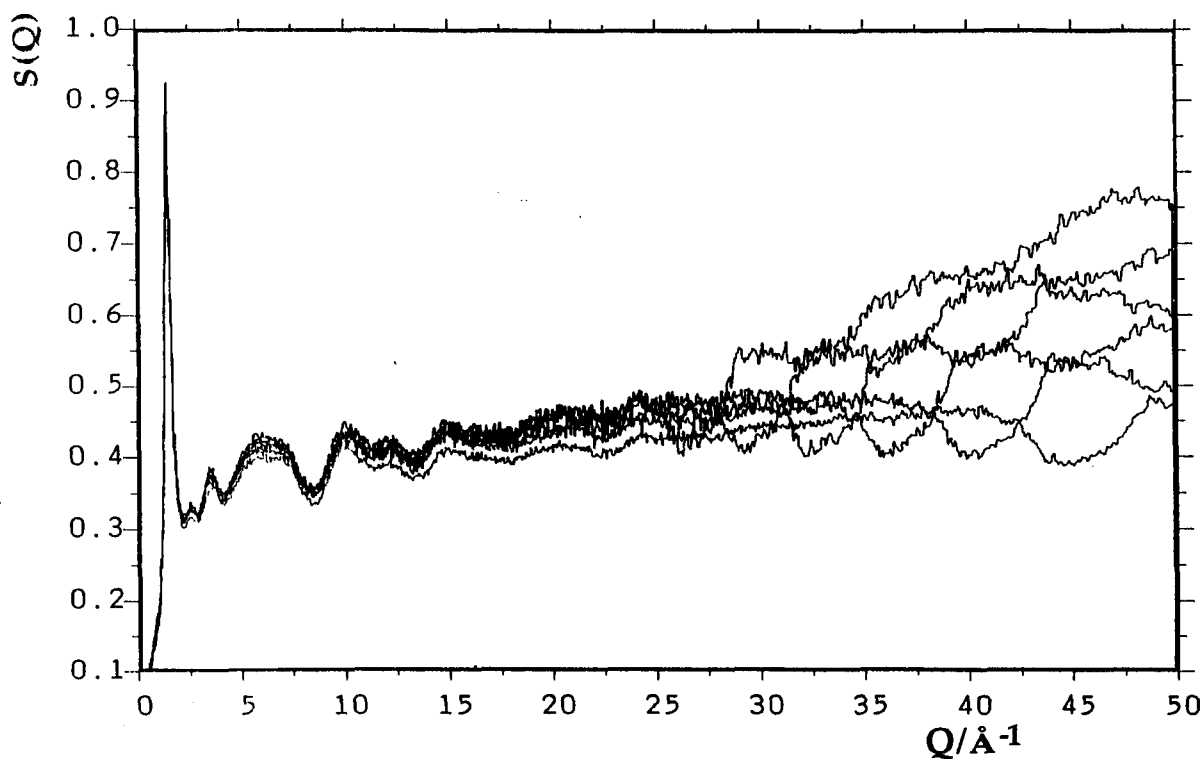


Figure 2.33 The overlay of the uncorrected $S(Q)$ for the six groups of SANDALS detectors, in the range 11° - 21° , for CBrF_3 at 153 K (the anomalous-looking curvature at high- Q in these spectra is due to Br-induced resonances).

- (ii) the spurious peaks in the $g(R)$ at low R were zeroed,
- (iii) the $g(R)$ were back-transformed to $S'(Q)$,
- (iv) the $S'(Q)$ spectrum was removed from the original $S(Q)$ spectrum,
- (v) the residual curve was smoothed by fitting a polynomial curve through it,
- (vi) the polynomial curve was removed from $S(Q)$ to give $S''(Q)$

Figures 2.34(a-f) show the finally corrected CBrF_3 $S''(Q)$ spectra for the six groups of detectors in the Q -region 0 - 30 \AA^{-1} .

The detectors in the SANDALS experiment are split up into 6 groups of increasing angular range. It is convenient to split them up in this manner in order to allow for the slight changes in the data corrections as the detector angle increases. The merging of the SANDALS data was very simple for CClF_3 since the overlap between the $S''(Q)$ for the 6 groups of detectors was nearly perfect over the whole Q -range (see figure 2.35 which shows an overlay of the six $S''(Q)$). The merging of the CBrF_3 data was slightly more complicated because the Br nuclei capture neutrons which introduces a resonance which appears at different Q -range for each group spectra (see figure 2.33). The region affected can be removed by ignoring the resonance region when the data is merged. The MIM routine was used to transform the merged $S(Q)$ to $g(R)$ constraining the $g(R)$ to be zero from the origin to 1.0 \AA .

2.12.2.3 Results and Discussion

Figures 2.36 and 2.37 show the final merged structure factors $S(Q)$ for CClF_3 and CBrF_3 respectively and the radial distribution functions $g(R)$ are

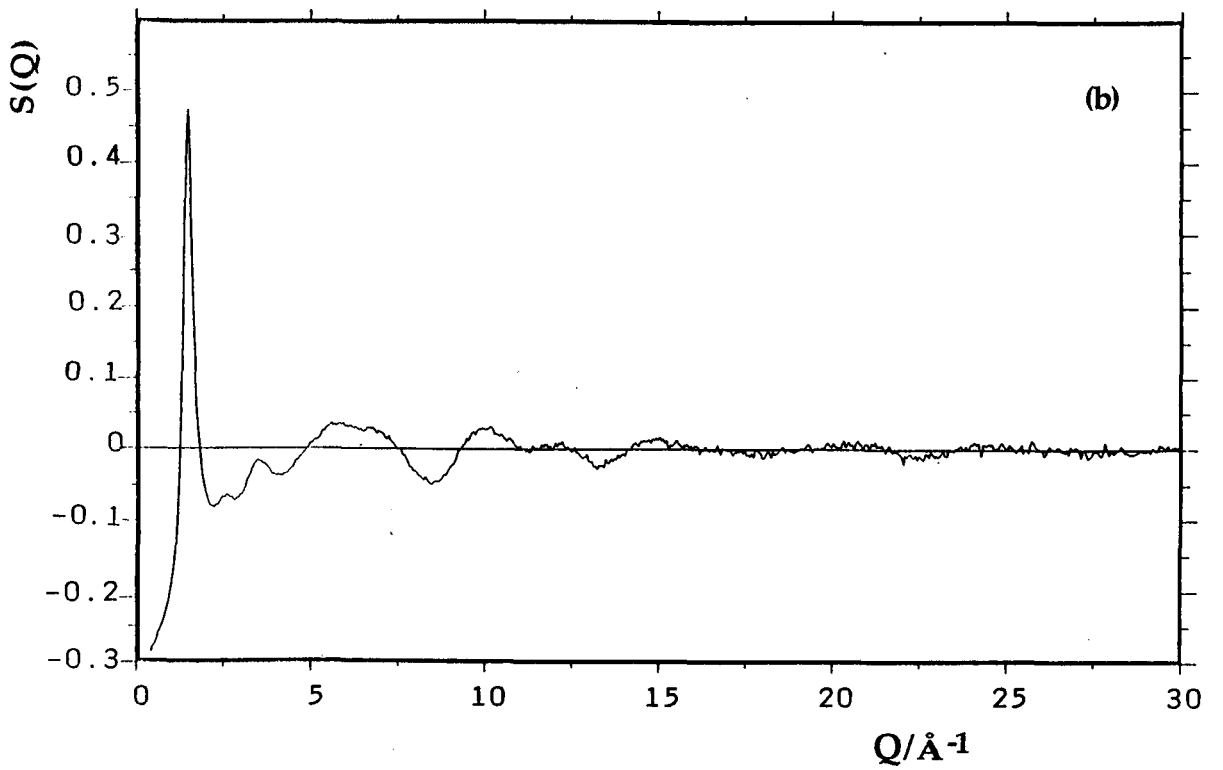
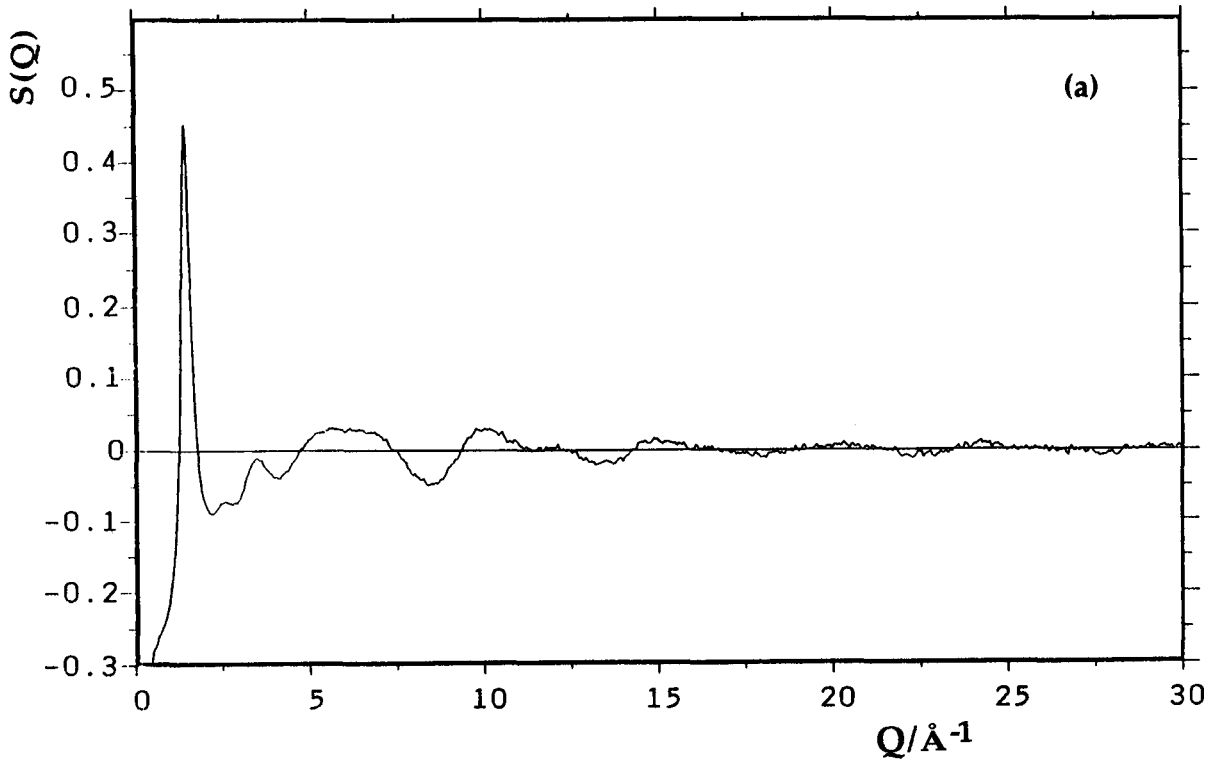


Figure 2.34 The corrected $S(Q)$, at (a) detector groups one, and (b) detector groups two, for CBrF_3 .

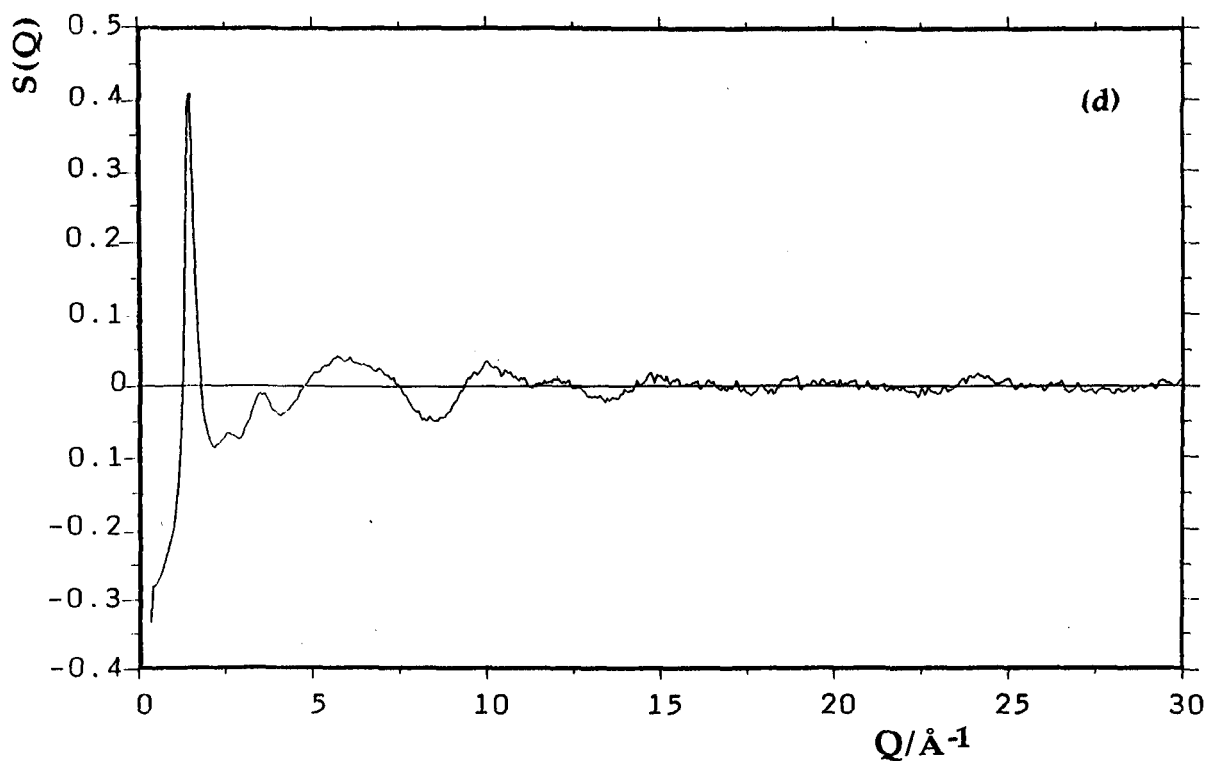
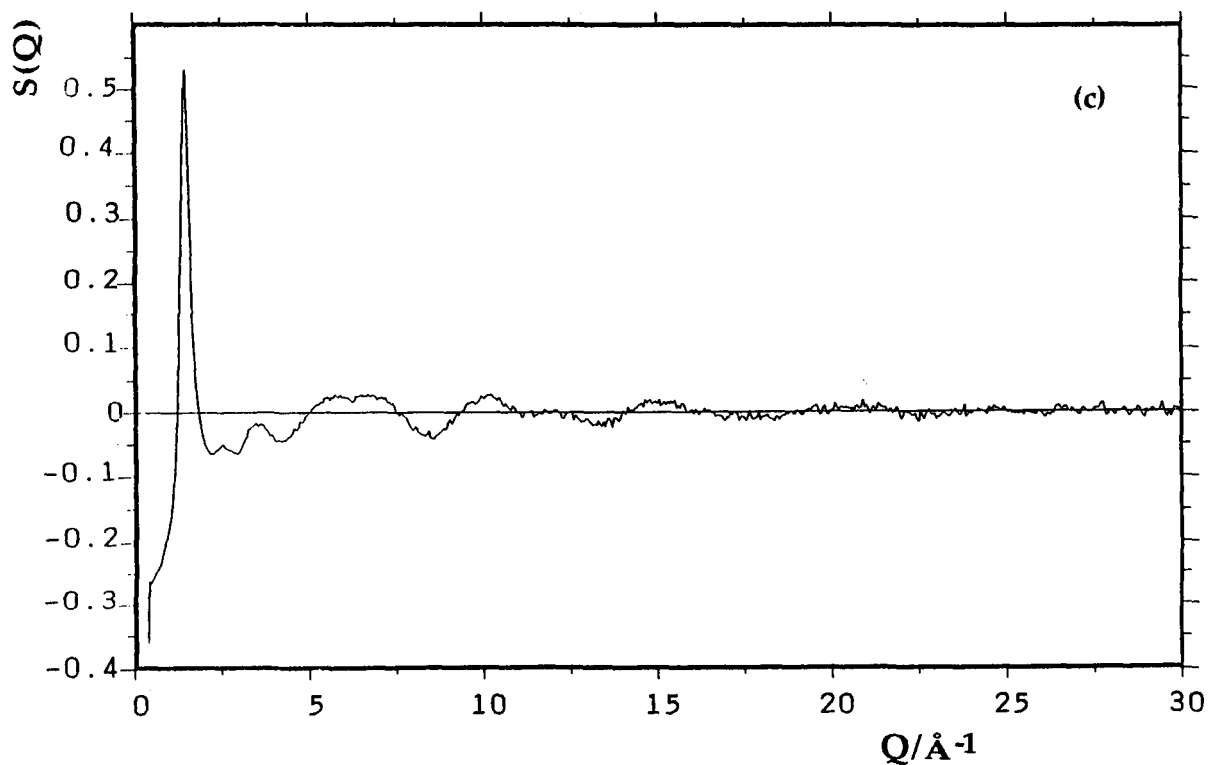


Figure 2.34 The corrected $S(Q)$, at (c) detector groups three, and (d) detector groups four, for CBrF_3 .

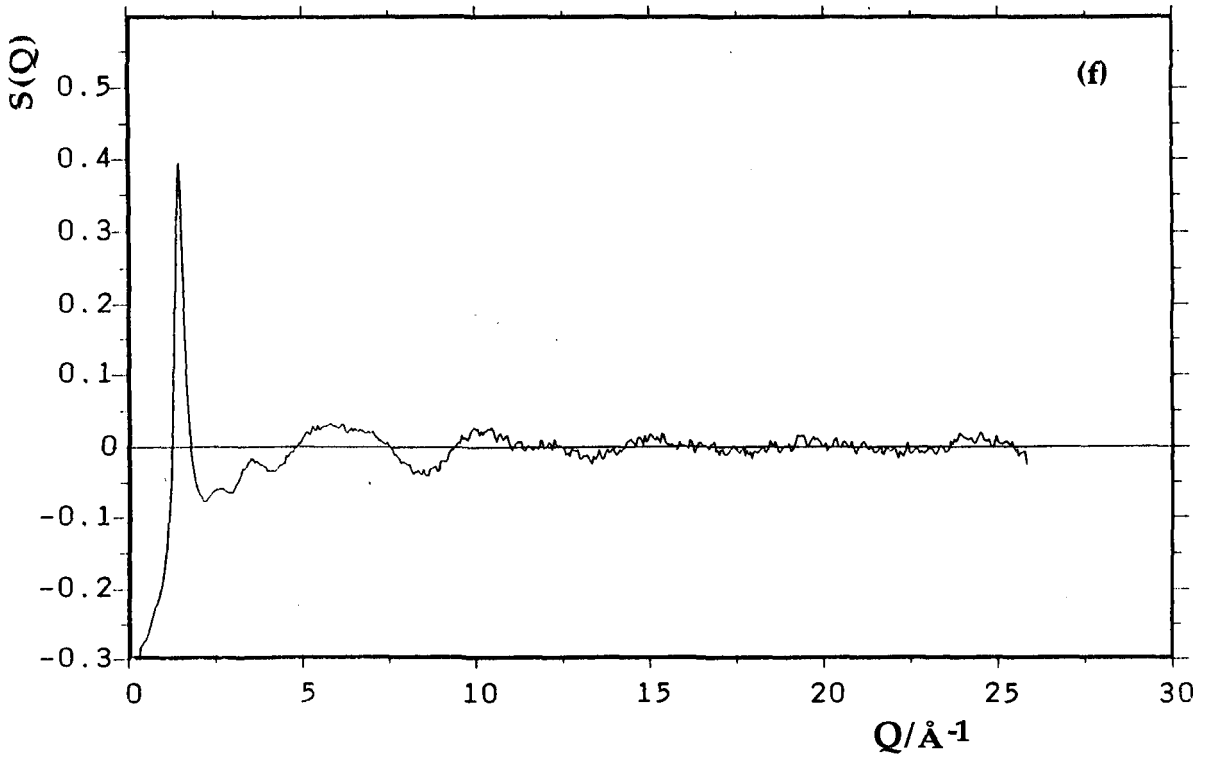
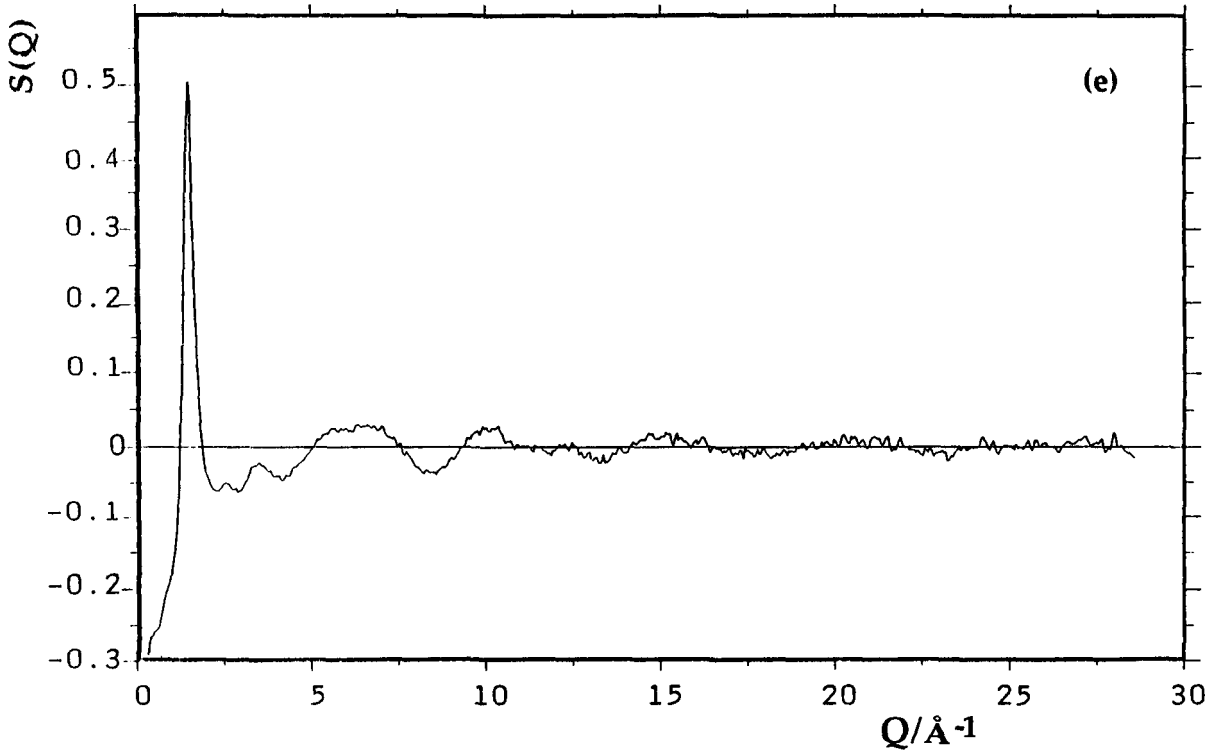


Figure 2.34 The corrected $S(Q)$, at (e) detector groups five, and (f) detector groups six, for CBrF_3 .

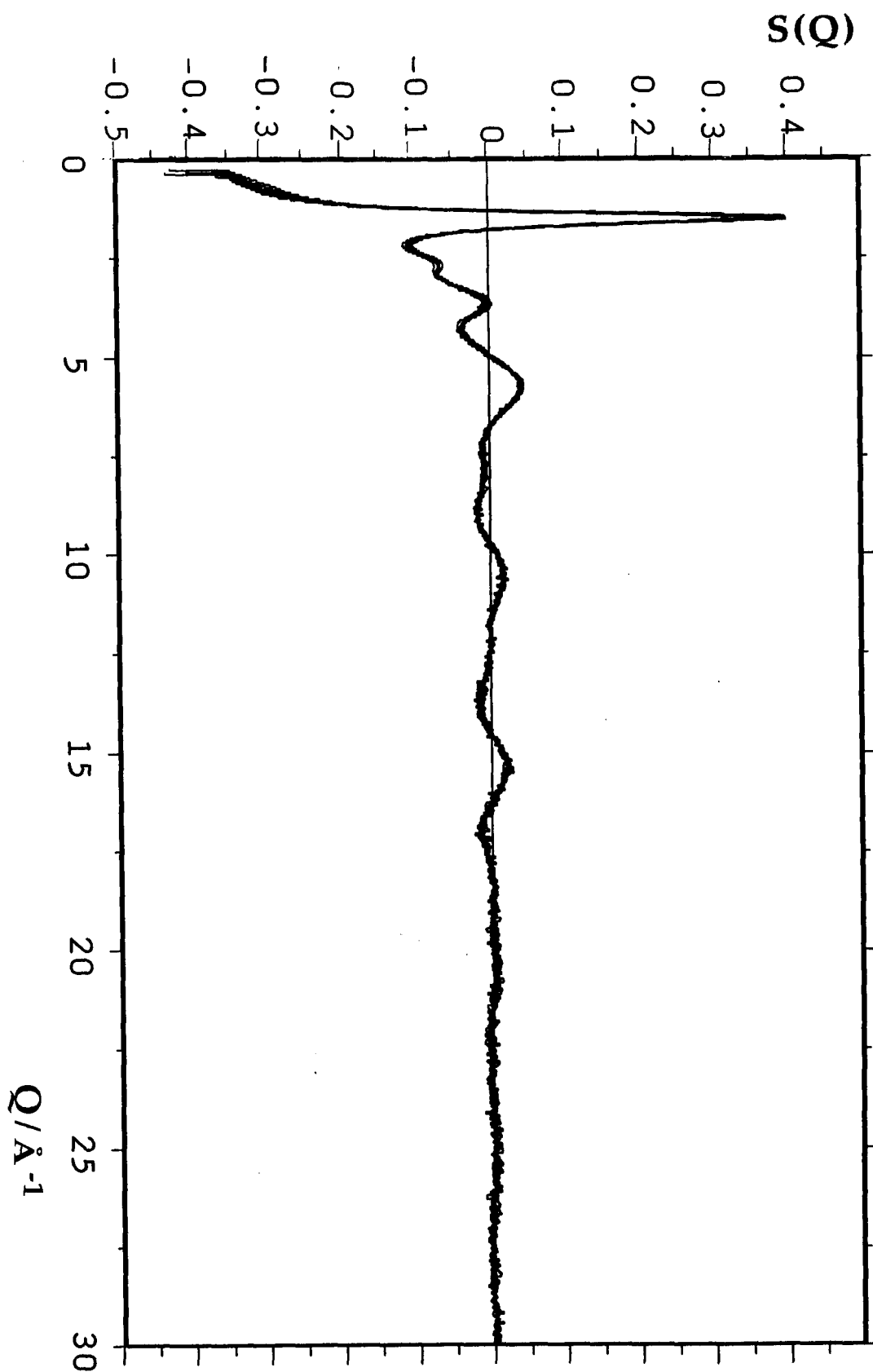


Figure 2.35 The overlay of the $S(Q)$ for the six groups of SANDALS detectors, in the range 11° - 21° , for CClF_3 at 153 K.

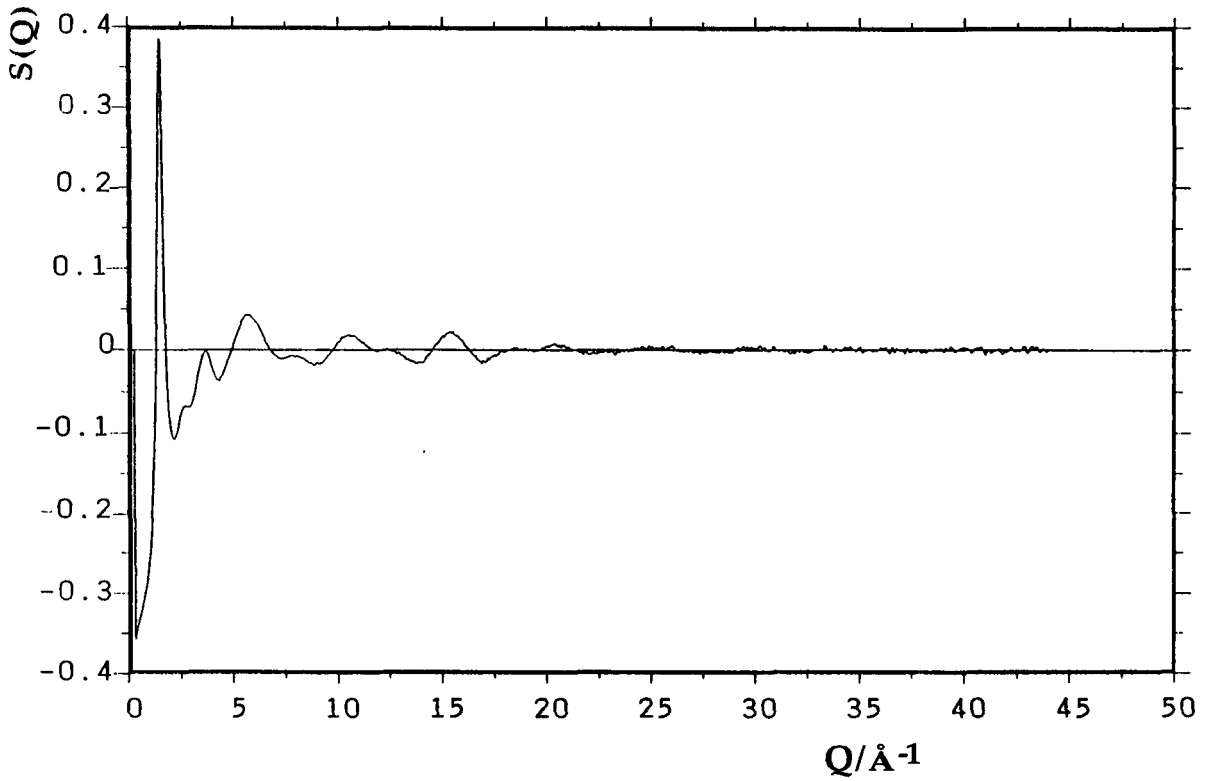


Figure 2.36 The final corrected and merged $S(Q)$ for CClF_3 at 153 K.

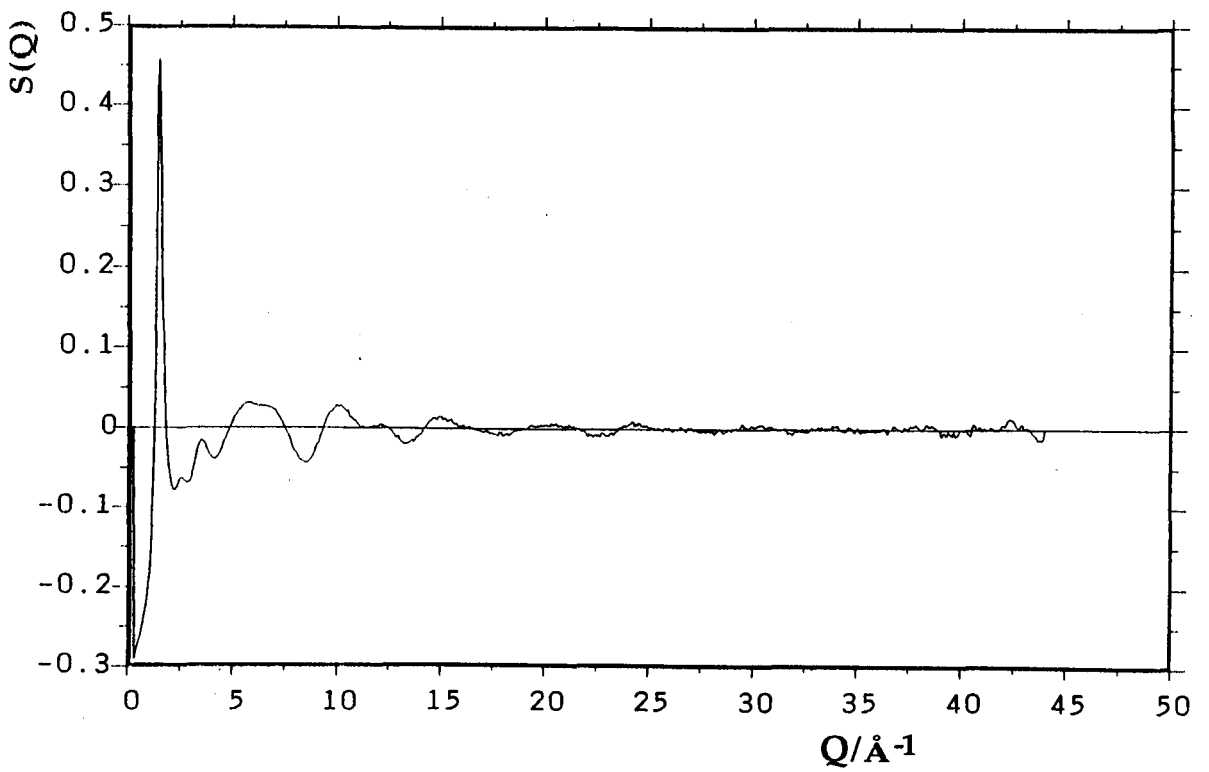


Figure 2.37 The final corrected and merged $S(Q)$ for CBrF_3 at 153 K.

shown in figure 2.38 and 2.39. In both cases the intramolecular structure is easy to identify in the $g(R)$.

The intramolecular atomic separations (in Å) and the bond angles for the two fluids are summarised below;

- (i) CBrF_3 : C-F 1.33 (1), C-Br 1.93 (2), F...F 2.17 (2), Br...F 2.69 (2)
 FCF 109.3° (3), BrCF 109.8° (3)
- (ii) CClF_3 : C-F 1.32 (1), C-Cl 1.77 (1), F...F 2.17 (2), Cl...F 2.58 (2)
 FCF 110.6° (2), FCCl 112.4° (2)

The observed intramolecular separations are very similar to those observed in the gas phase [38] as shown in table 2.7.

CF_3Cl			CF_3Br		
	LIQUID 153 K	GAS		LIQUID 153 K	GAS
C-F	1.32	1.328 (8)	C-F	1.33	1.330 (8)
C-Cl	1.77	1.740 (20)	C-Br	1.93	1.908 (20)
F...F	2.17	2.15	F...F	2.17	2.15
F...Cl	2.58	2.54	F...Br	2.69	2.68

Table 2.7 A comparison of the intramolecular bond separations from neutron diffraction and gas-phase microwave experiments for CF_3Cl and CF_3Br

Some intermolecular structure is also well defined for both compounds but there is no distinctive structure that can be defined without the assistance of molecular dynamics simulations.

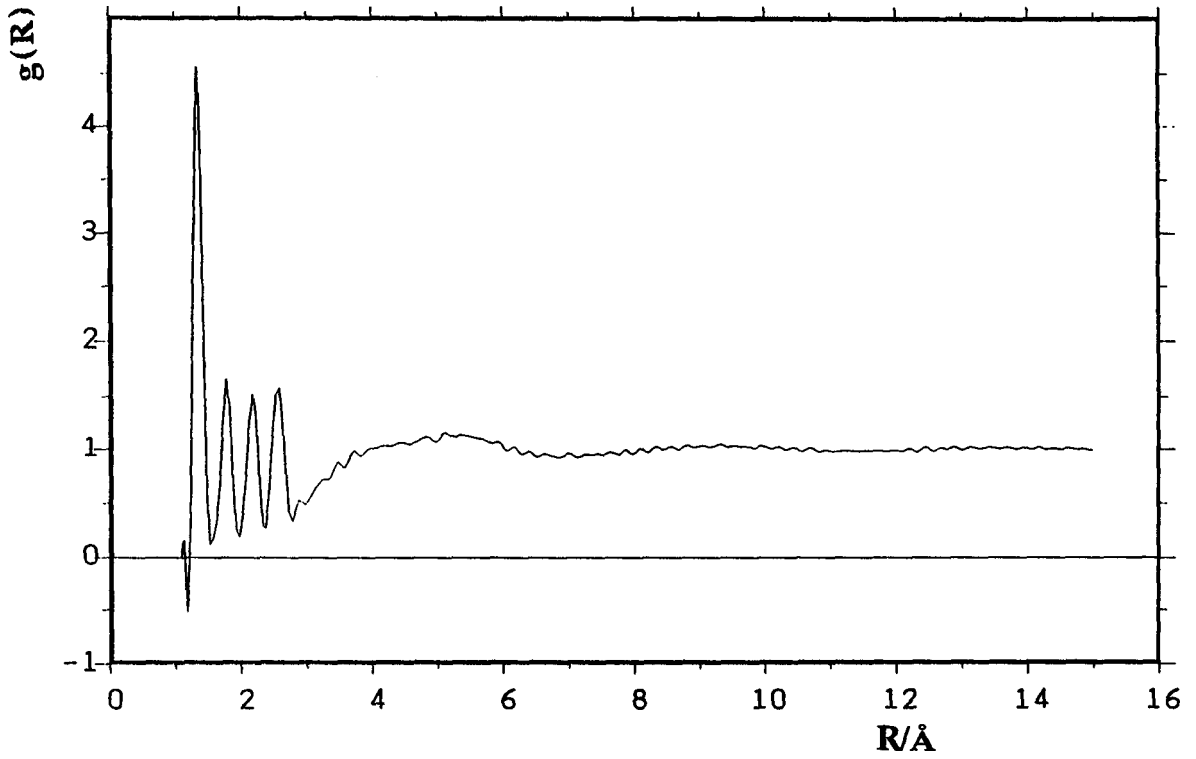


Figure 2.38 The pair distribution function, $g(R)$ for CClF_3 at 153 K.

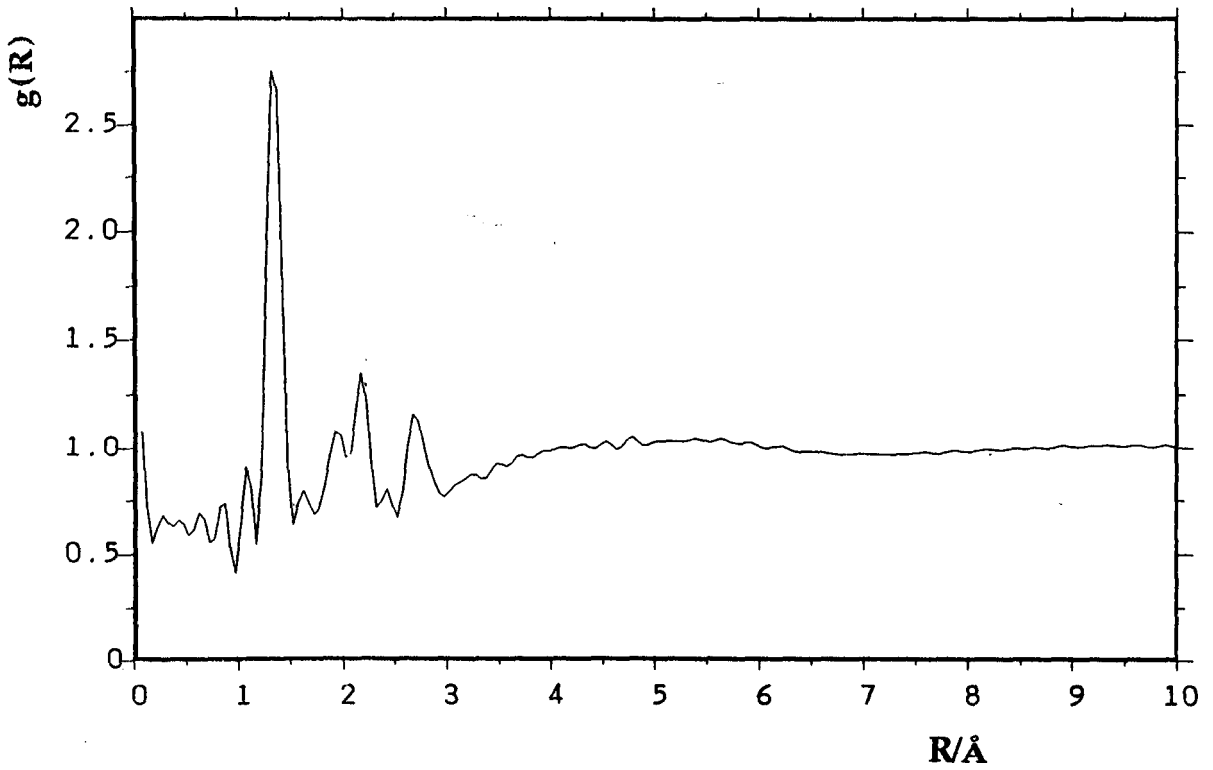


Figure 2.39 The pair distribution function, $g(R)$ for CBrF_3 at 153 K.

2.12.3 Deuterated-Chlorodifluoromethane

2.12.3.1 Experimental and Data Analysis

Deuterated-chlorodifluoromethane (CDCIF_2 , DCFC-22) is the deuterated version of the refrigerant which was studied using LAD. It was made by ICI specially for this study (it arrived on the day of the experiment). After the experiment however, its purity was found by mass spectroscopy to be greater than 90% (impurities detected were CDCl_2F , CDCl_3 , and CCl_4).

CDCIF_2 was studied at a temperature of 153.2 ± 1.0 K ($\rho \approx 1.64$ g cm^{-3}) using the "Wormald cell". The vessel was filled using the method described above, and the sample data was collected in 2 h sections for 6 h (525 μA). The data analysis was performed as described above in section 2.12.2.2.

2.12.3.2 Results and Discussion

Figures 2.40 and 2.41 show the final merged structure factor, $S(Q)$ and MIM-transformed $g(R)$ for the 90% pure CDCIF_2 sample. The intramolecular atomic separations (in Å), which were easier to identify than for CHClF_2 because the peaks are all positive, are;

C-D 1.10 (2), C-F 1.33 (1), C-Cl 1.81 (2), D-F 2.01 (2), F-F 2.17 (2),
D-Cl 2.33 (2), F-Cl 2.52 (3)

and the bond angles are;

DCF 111.3° (4), DCCl 103.7° (7), FCF 109.3° (3), FCCl 105.7° (3)

The results are compared in table 2.8 with previous gas-phase microwave spectroscopy results for CHClF_2 [37], and also the neutron diffraction results for CHClF_2 , given in section 2.11.2.3 of this thesis.

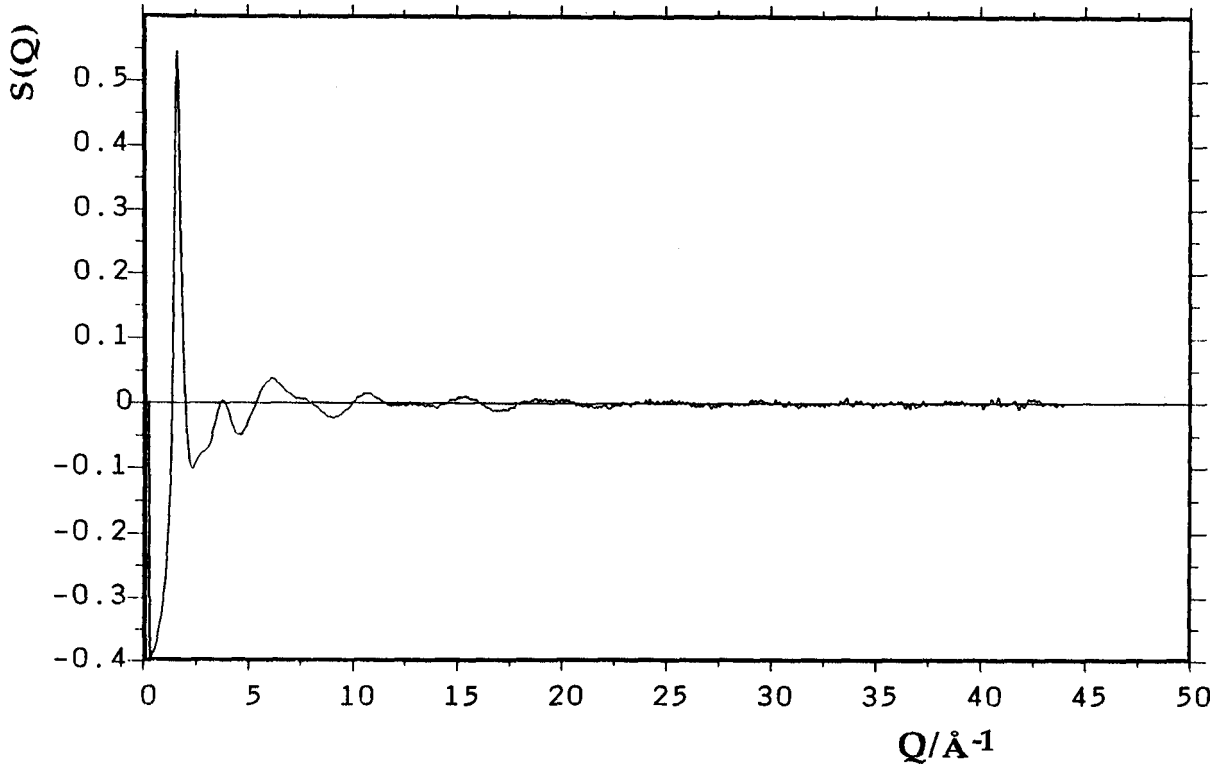


Figure 2.40 The final corrected and merged $S(Q)$ for CDClF_2 at 153 K.

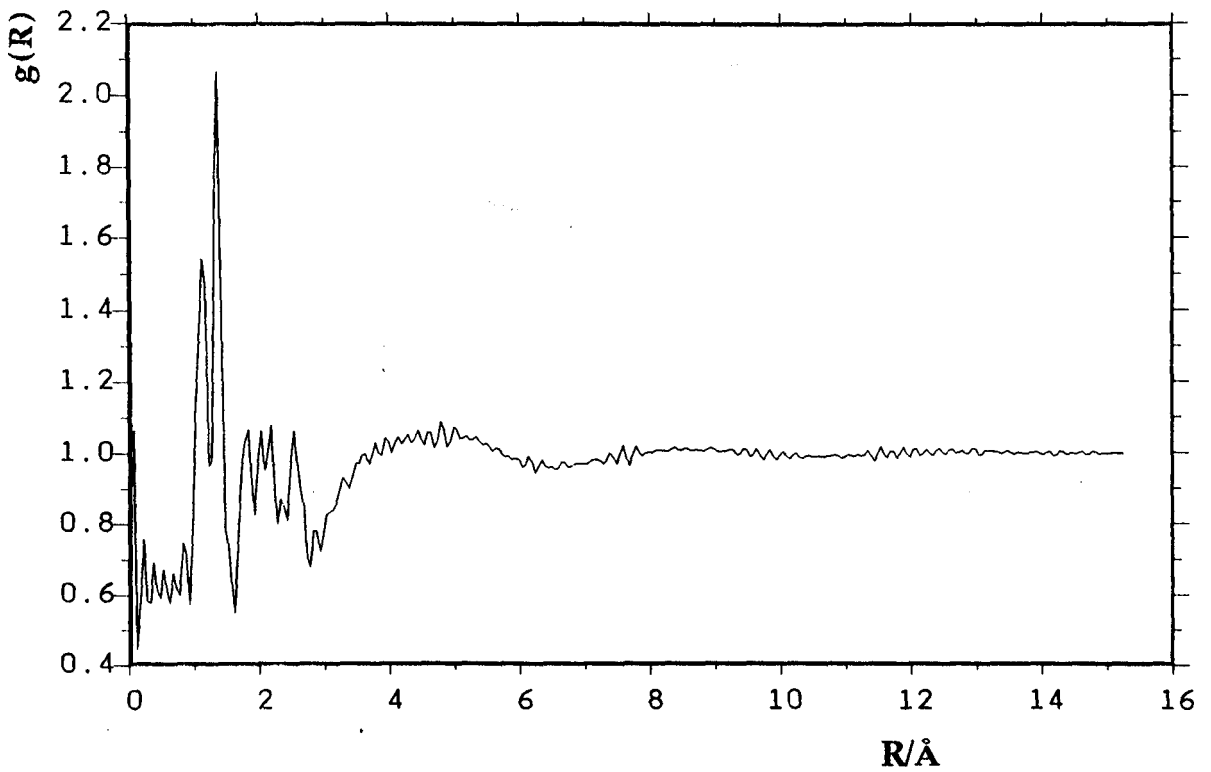


Figure 2.41 The pair distribution function, $g(R)$ for CDClF_2 at 153 K.

	CDCIF ₂	CHCIF ₂	
	LIQUID 153 K	LIQUID 153 K	GAS
C-H	1.10	1.08	1.09
C-F	1.33	1.35	1.350
C-Cl	1.81	1.76	1.747
H...F	2.01	1.97	-
F...F	2.17	2.16	2.17
H...Cl	2.33	2.33	-
F...Cl	2.52	2.55	2.548

Table 2.8 A comparison the intramolecular bond separations (in Å) given in the neutron diffraction experiment on CDF₂Cl with those given in neutron diffraction and a gas phase microwave experiments on CHF₂Cl

The intermolecular region of the $g(R)$ is well defined but there is no distinctive structure that could be identified without the assistance of molecular dynamics simulation. One comparison that can be made immediately however, is that between the intermolecular regions of CHCIF₂ and CDCIF₂. A difference spectrum should show peaks at twice the height of any X...H/D (X = C, F, Cl) peaks that are important in the orientation of the molecules; where there are significant negative peaks in the $g(R)$ of CHCIF₂, there should be corresponding positive peaks in the $g(R)$ of CDCIF₂. There does not appear to be any significant difference between the intermolecular regions of the two $g(R)$ shown in figure 2.42. The reasons could be,

(i) there is very little structure due to H/D for liquid chlorodifluoromethane which would mean the $g(R)$ of the two fluids would be similar.

(ii) there is a problem with the low Q -region of the SANDALS data, possibly a consequence of the missing transmission monitor spectra.

(iii) the purity of the CDClF_2 sample was insufficient.

It is interesting to note that the intermolecular regions in the $g(R)$ for CBrF_3 and CClF_3 also look similar to that for CDClF_2 .

Without further investigation, it was not possible to say what the cause of the similarity between the four $g(R)$ is due to. It was hoped that the problem would be solved by performing MD simulations on the four fluids.

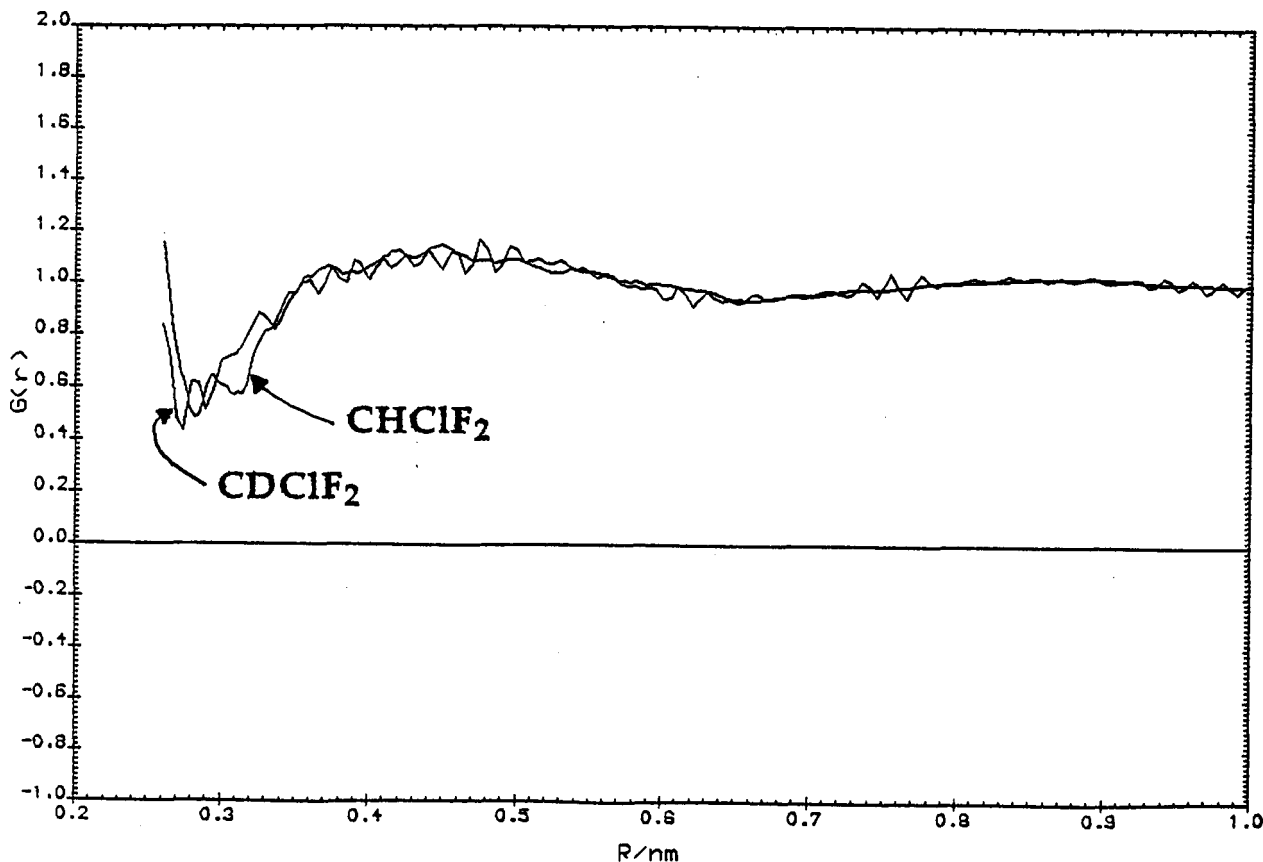


Figure 2.42 The overlay of the intermolecular regions of the $g(R)$ spectra given in the neutron diffraction studies of CHClF_2 and CDClF_2 .

2.12.4 Deuterated-fluoroform and Trichlorofluoromethane

An attempt was made to study two other liquids using SANDALS, deuterated-fluoroform (CDF_3 , DCF-23) and trichlorofluoromethane (CCl_3F , CFC-13).

The CCl_3F sample was supplied in a cylinder by ICI at a purity greater than 99.98%. The CDF_3 sample was prepared specially for this experiment, in the light of the interesting intermolecular peak which was found in the LAD g(R) of CHF_3 . It's purity was untested at the time of the SANDALS experiment.

We were unsuccessful in our attempt to condense either of the liquids into the evacuated cell. Several attempts were made to condense the samples into the cell including cooling the evacuated cell down to 50 K; all were in vain. The two samples were low pressure samples; the cylinder pressure of CCl_3F was 1.1 atm and the CDF_3 sample's pressure was 0.88 bar. Since the other samples had easily condensed into the vessel, it was surmised that the CCl_3F and CDF_3 samples had frozen in the piping leading into the vessel.

On further investigation, it was found that the refrigerated head of the CCR was not isolated from the inlet piping. Thus, the samples had probably frozen in the piping where it passed through the CCR head into the sample vessel. This problem has now been rectified. The CDF_3 sample however may not have condensed into the sample vessel due to it having escaped from the sample vessel before the experiment had begun. Using mass spectroscopy to analyse the purity of the sample, very little fluoroform was detected and the sample appeared to consist largely of air.

2.13 Concluding Remarks

The LAD and SANDALS experiments have been used in this experiment to successfully investigate the intramolecular atomic separations of six fluid halocarbons. The intermolecular regions of these fluids have also been derived in the form of a pair distribution function and those of fluoroform and dichlorodifluoromethane look very interesting from a structural point of view.

The work included in this chapter includes novel approaches to data analysis, and the studies using SANDALS represent some of the first liquid structure derivations using the instrument.

The ability to utilise molecular dynamics computer simulations in the determination of fluid structure depends very heavily on obtaining accurate pdfs from neutron diffraction studies for a comparison. With this in mind, the data analysis routine performed in this neutron diffraction experiment were performed very carefully and accurately. The MD experiments are described in the next chapter.

2.14 Future Work

The diffraction experiments described above were the first in a series in which Liverpool University and ICI, Runcorn are interested. Future work should include using SANDALS to

- (i) Repeat the CDF_3 and CCl_3F experiments which were aborted due to the refrigeration unit problems.
- (ii) Study if the shoulder on the first peak in the $D_M(Q)$ of CCl_2F_2 , changes with temperature, to see if it is due to molecular correlation.
- (iii) Repeat the CDClF_2 experiment using a purer sample.

REFERENCES

- [1] FRIEDRICH, W., KNIPPING, P. and von LAUE, M., 1912, *Sitzungsberichte der (KGL.) Bayerische Akademie der Wissenschaften*, 303.
- [2] BRAGG, W. L., 1913, *Proc. Roy. Soc. London Ser. A*, **88**, 428.
- [3] DAVISSON, C. and GERMER, L. H., 1927, *Phys. Rev.*, **30**, 705.
- [4] THOMPSON, G. P. and REID, A., 1927, *Nature Lond.*, **119**, 890.
- [5] CHADWICK, J., 1932, *Proc. Roy. Soc. London Ser. A*, **136**, 692.
- [6] MITCHELL, D. P. and POWERS, P. N., 1936, *Phys. Rev. Sci. Inst.*, **33**, 496.
- [7] Ed. BACON, G. E., 1986, *Fifty Years of Neutron Diffraction: the Advent of Neutron Scattering*, (Adam Hilger).
- [8] Eds. SKÖLD, K. and PRICE, D. L., 1986, *Methods of Experimental Physics, Volume 23; Neutron Diffraction Part A*, (Academic Press).
- [9] WINDSOR, C. G., 1981, *Pulsed Neutron Scattering*, (Taylor & Francis Ltd).
- [10] Ed. WILLIS, B. T. M., 1973, *Chemical Applications of Thermal Neutron Scattering*, (Oxford University Press).
- [11] SQUIRES, G. L., 1978, *Thermal Neutron Scattering*, (Cambridge University Press).
- [12] Eds. NEWPORT, R. J., RAINFORD, B. D. and CYWINSKI, R., 1988, *Neutron Scattering at a Pulsed Source*, (Adam Hilger).

- [13] Ed. EGELSTAFF, P. A., 1965, *Thermal Neutron Scattering*, (Academic Press).
- [14] BACON, G. E., 1977, *Neutron Scattering in Chemistry*, (Butterworths).
- [15] POWLES, J. G., 1973, *Advances in Physics*, **22**, 1.
- [16] DORE, J. C., 1989, *Inst. Phys. Conf. Ser.*, **No. 101**, 1.
- [17] SOPER, A. K., HOWELLS, W. S. and HANNON, A. C., *RAL report 89-046*, 1989.
- [18] DEROME, A. E., 1987, *Modern NMR Techniques for Chemistry Research*, Organic Chemistry Series, Vol. 6, edited by J. E. Baldwin, (Pergamon).
- [19] HOWE, M. A., WORMALD, C. J. and NEILSON, G. W., 1989, *Molec. Phys.*, **66**, 847.
- [20] ADYA, A. K. and WORMALD, C. J., 1991, *Molec. Phys.*, **74**, 735.
- [21] PAALMAN, H. H. and PINGS, C. J., 1962, *J. Appl. Phys.*, **33**, 2635.
- [22] SEARS, V. F., 1975, *Adv. Phys.*, **24**, 1.
- [23] PLACZEK, G., 1952, *Phys. Rev.*, **86**, 377.
- [24] POWLES, J. G., 1978, *Mol. Phys.*, **36**, 1181.
- [25] HOWE, M. A., MCGREAVY, R. L. and HOWELLS, W. S., 1989, *J. Phys;Condens. Matter*, **1**, 3433.

- [26] BUCKINGHAM, J., 1982, *Dictionary of organic compounds*, 5th edition, (Chapman and Hall).
- [27] HANNON, A. C., HOWELLS, W. S. and SOPER, A. K., IOP Conference Series, 1990, **107**, 193.
- [28] JUNG, W. G., ZEIDLER, M. D. and CHIEUX, P., 1989, *Molec. Phys.*, **68**, 473.
- [29] Ed. SOPER, A. K., 1989, *Proceedings of the International workshop on the static and dynamic properties of liquids*, (Springer-Verlag).
- [30] HARMONY, M. D., LAURIE, V. W., KUCZKOWSKI, R. L., SCHWENDEMAN, R. H., RAMSAY, D. A., LOVAS, F. J., LAFFERTY, W. J. and MAKI, A. G., 1979, *J. Phys. Chem. Ref. Data*, **8**, 619.
- [31] COCKCROFT, J. K. and FITCH, A. N., 1991, *Zeitschrift für Kristallographie*, **197**, 121.
- [32] BERMEJO, F. J., ENCISO, E., ALONSO, J., GARCIA, N. and HOWELLS, W. S., 1988, *Molec. Phys.*, **64**, 1169.
- [33] CRESWELL, C. J. and ALLRED, A. L., 1963, *J. Amer. Chem. Soc.*, **85**, 1723.
- [34] POGORELYI, V. K. and VISHNYAKOVA, T. B., 1984, *Russian Chemical Reviews*, **53**, 12.
- [35] REICHARDT, C., 1988, *Solvents and Solvent Effects in Organic Chemistry*, 2nd edition, (VCH).

- [36] RUBIO, R. G., ZOLLWEG, J. A. and STREETT, W. B., 1989, *Ber. Bunsenges. Phys. Chem.*, **93**, 791.
- [37] Eds. CALLOMON, J. H., HIROTA, E., KUCHITSU, K., LAFFERTY, W. J., MAKI, A. G. and POTE, C. S., 1976, *Landolt-Börnstein numerical data and functional relationships in science and technology*, Group II, Vol. 7, (Springer-Verlag), p. 124 and references therein.
- [38] SHERIDAN, J. and GORDY, W., 1952, *J. Chem. Phys.*, **20**, 91.
- [39] ANDREANI, C., DORE, J. C. and RICCI, F. P., 1991, *Rep. Prog. Phys.*, **54**, 731.
- [40] ADYA, A. K. AND WORMALD, C. J., 1991, *Molec. Phys.*, **74**, 735.

CHAPTER THREE

MOLECULAR DYNAMICS

3.1 Introduction

Computer simulations have been used to model numerous physical systems under a wide variety of conditions, with varying degrees of success. Comparison of simulated and experimental results can lead to an increased understanding of the system being studied.

The modelling technique used in this study for determining the liquid structure of halocarbons is called Molecular Dynamics (MD). MD simulations have been applied by a number of groups studying a wide range of liquids. The simplest liquid systems such as argon have been successfully modelled using MD [1]. More complicated, molecular fluid systems, such as hydrogen fluoride [2] and carbon tetrachloride [3-7] however, are more difficult to simulate effectively.

MD simulations involve modelling the behaviour of fluid molecules in a box using classical mechanics for their motion and potential equations for the forces between them. There are a number of programmes that can be used to run MD simulations; a series of programmes is available on the CCP5 library, which is co-ordinated by the SERC. The programme used in this study was called MDMPOL; it was coded by D. Fincham and W. Smith [8].

There are few books that describe the use of MD for the modelling of fluid structure and behaviour; Allan and Tildesley's "Computer Simulations of Liquids" [9] and Heermann's "Computer Simulation Methods in Theoretical Physics" [10] are the most comprehensive. A good introduction to MDMPOL is the CCP5 booklet, "A Molecular Dynamics

Programme for the Simulation of Polyatomic Molecular Liquid Mixtures Incorporating Long Range Electrostatic (Fractional Charge) Effects via the Ewald Sum" [8].

3.2 The Motivation for Simulation

The motivation behind the use of computer simulation is two-fold:

- (i) theoretical models can be tested,
- (ii) experimental results can be analysed.

Experimental results can sometimes be difficult to interpret on their own due to their macroscopic nature. Computer simulations can arrive at the same results from a first-principle, microscopic direction. Results from a simulation that match experimentally-derived results may be analysed in greater detail than is possible for the experimental data alone. Appropriate simulations should model more than one set of experimental results if any subsequent analysis is to be viable. In this study, MD simulations were used to generate pair distribution functions (pdfs) of various liquids. The simulated pdfs were compared with the neutron-diffraction experimentally-derived pdfs that were described in the previous chapter. The thermodynamic results calculated in the simulation were also compared with previously-reported experimental data as a further check on the validity of the simulation.

If a computer model reflects experimental data accurately, the simulation can be used to provide a detailed description of the individual atom-atom pair distribution functions and hence the liquid structure. It is worth noting however, that although the MD simulation may reproduce the experimental data accurately, it can only be assumed, not proven, that the model is a realistic description of the true situation.

3.3 MDMPOL; Liquid Molecules in a Box

MDMPOL simulates a microcanonical ensemble of molecules that imposes the restrictions of constant total energy (E), volume (V) and number of molecules (N). As the name suggests, a Molecular Dynamics programme follows the dynamic progress of molecules in a box over a period of time. From their initial positions, motional directions, accelerations and velocities, the movement of the molecules in the box develops according to the forces acting upon them.

The total energy E , of the system is given by,

$$E = \text{Potential Energy (U)} + \text{Kinetic Energy (KE)}. \quad (3.1)$$

The potential energy affects the interaction of the molecules with one another and the kinetic energy dictates how the molecules move because of those interactions. MDMPOL uses calculations of these quantities to manipulate a simulated system in a manner equivalent to that occurring in a real system.

3.3.1 Potential Energy

Two models, based on site-site effective-pair potentials, have been widely used in previous studies to simulate a variety of halogenated methanes; the test particle model potential (T-model) for CH_3F [11], CHF_3 [11], CH_3Cl [11], CH_2Cl_2 [12], CHCl_3 [12], and CHClF_2 [13], and the Lennard-Jones (LJ) potential for CCl_4 [7], CF_4 [14], CH_2Cl_2 [15], CHCl_3 [16], CHClF_2 [17] and CCl_2F_2 [17]. The simulations in this study, carried out using MDMPOL [8], use an effective-pair potential derived from the LJ site-site potential-energy function that incorporates long-range electrostatic (fractional

charge) effects. The potential energy between two atoms (a and b) on different molecules (i and j) is given by,

$$U_{ab}(\mathbf{R}_{ij}) = 4\epsilon_{ab}[(\sigma_{ab}/\mathbf{R}_{ij})^{12} - (\sigma_{ab}/\mathbf{R}_{ij})^6] + q_a q_b / 4\pi\epsilon_0 \mathbf{R}_{ij} \quad (3.2)$$

[LJ POTENTIAL PART] [LONG-RANGE PART]

where \mathbf{R}_{ij} is the distance between atom a on molecule i and atom b on molecule j, ϵ_{ab} and σ_{ab} are the LJ interaction parameters, q_a is the fractional charge on atom a, q_b is the fractional charge on atom b, and ϵ_0 is the permittivity of free space.

3.3.1.1 The LJ Potential Equation

The LJ potential (figure 1.4) is chosen because it is easily differentiated whilst giving a fairly accurate representation of the liquid, both qualitative and quantitative.

Generally, the choice of the LJ parameters is a matter of trial and error. The values of ϵ and σ depend not only upon the type of atom in question but also the make-up of the molecule; the values of ϵ_{ClCl} and σ_{ClCl} between two molecules of CCl_4 are not the same as those between the Cl atoms of two CClF_3 molecules (although they may be similar). However, a good starting point for σ , if previous estimates are not available, is the van der Waals' radius. For ϵ , the higher the polarisability, the higher is the value of ϵ . Some values of ϵ and σ have been calculated in previous experiments and they are listed in reference [9]. The starting-point values of interest in this study are shown in table 3.1. The ϵ and σ estimates shown are for like-atoms only and the values of ϵ_{CCl} and σ_{CCl} between the C and Cl atoms of CCl_4 , for example, must be approximated using the Lorentz-Berthelolt mixing rules;

$$\epsilon_{\text{CCl}} = [\epsilon_{\text{CC}}\epsilon_{\text{ClCl}}]^{1/2}, \quad (3.3)$$

$$\sigma_{\text{CCl}} = 1/2[\sigma_{\text{CC}} + \sigma_{\text{ClCl}}]. \quad (3.4)$$

The ϵ and σ values used in MDMPOL are not the same as would be given between two isolated atoms because the LJ effective-pair potential introduces an estimate of the three-body effects.

Atom	Reference	$\epsilon/k_B K$	σ/nm
H	[18]	8.6	0.281
C	[19]	51.2	0.335
F	[20]	52.8	0.283
Cl	[20]	173.5	0.335
Br	[20]	257.2	0.354

Table 3.1 Starting point values for the LJ parameters, ϵ and σ

The total potential energy acting on a molecule is obtained by summing all the unique pair-wise interactions acting upon each atom of that molecule due to its vicinity to all the other atoms in the system; this is the net potential acting upon that molecule, w_i ;

$$w_i = \sum_{i \neq j} U(R_{ij}) \quad (3.5)$$

The sum of all the net potentials acting on all the molecules in the system is equal to the total potential of the system, $U(R_i)$;

$$U(R_i) = \sum w_i \quad (3.6)$$

3.3.1.2 The Long-Range Electrostatic-Charge Contribution to the Potential Equation

In a MDMPOL simulation there is the option of adding a small fractional charge to any of the atomic sites on the molecule being studied. The fractional charges can be calculated using the Mulliken population analysis [21] or similar; they should be physically reasonable and should add up to zero. The long-range potential may add up to 10% to the value of the potential energy but it may alternatively have no effect at all [3, 5-7]; some or all of the fractional charges may be set to zero.

3.3.2 Kinetic Energy

The kinetic energy term in equation (3.1) can be further split into three parts;

$$\begin{aligned} \text{KE} &= \text{Translational Kinetic Energy (TKE)} + \\ &\quad \text{Rotational Kinetic Energy (RKE)} + \\ &\quad \text{Vibrational Kinetic Energy (VKE)}. \end{aligned} \tag{3.7}$$

For simplicity, when simulating molecular systems using MDMPOL, the fluid molecules are not allowed to vibrate but are kept rigid. This obviates the need for calculating vibrational energies, VKE, and decreases computing time.

The rotational and translational motion of the molecules in the MD simulation can be calculated using the classical equations of motion.

The translational kinetic energy (TKE) and the rotational kinetic energy (RKE) of a system are dependent upon the system temperature. The higher the temperature, the faster the particles will attempt to move. For a non-linear quasi-tetrahedral molecule;

$$\text{RKE} = \text{TKE} = 3/2 nRT = 3/2 Nk_B T, \quad (3.8)$$

where, $n=N/L$ (L =Avogadro's number), and k_B is Boltzmann's constant.

The linear and rotational motions of the molecules in the box are governed by the forces acting on each atom of each molecule. Consider the forces, F_{ij} , acting on the atoms of molecule i caused by molecule j , in figure 3.1.

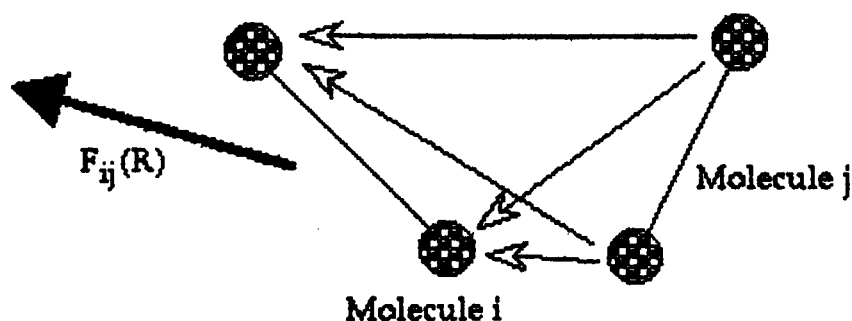


Figure 3.1 The forces acting on the atoms of molecule i

They are calculated by differentiating the pair-wise potential energy,

$$F_{ij}(\mathbf{R}) = - \mathbf{X} \, dU(\mathbf{R}_{ij})/d\mathbf{R}_{ij}, \quad (3.9)$$

where \mathbf{X} is a unit vector indicating the direction of the force.

Equation (3.9) shows the necessity of having an easily differentiable potential energy equation, like the LJ potential, if the simulation is going to be computationally efficient.

In a system of N molecules, more than one pair-wise force acts upon each atom in the system. The total force acting upon an individual molecule, i , is the sum of the effective pair-wise forces acting upon the atoms of that molecule;

$$F_i(\mathbf{R}) = \sum_{j \neq i} F_{ij}(\mathbf{R}) \quad (3.10)$$

Equation (3.10) is only an approximation of the system because, as was explained in Section 1.4.2, three-body effects may be significant.

All the atoms in the system will exert a pair-wise force on the molecule, either repulsive or attractive. The atoms that are generally most influential in determining how a molecule moves are those that are the closest to the molecule.

3.3.2.1 Linear Motion

Molecular dynamics simulations rely on the continual and accurate updating of the positions (\mathbf{R}), velocities (\mathbf{v} or $d\mathbf{R}/dt$) and accelerations (\mathbf{a} or $d^2\mathbf{R}/dt^2$) of all the molecules in the system as the simulation progresses in time (t).

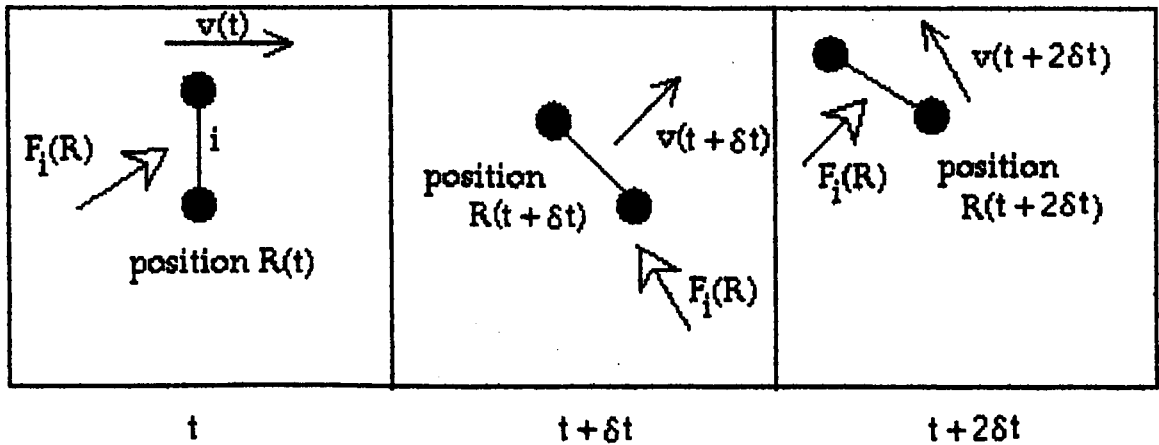


Figure 3.2 The linear motion of molecule i

Consider the molecules in figure 3.2. At some time t molecule i is in position $\mathbf{R}(t)$, travelling with a velocity, $\mathbf{v}(t)$. There is a force acting upon it causing it to change position with an acceleration $\mathbf{a}(t)$. The acceleration of molecule i is related to the force acting upon it,

$$\mathbf{F}_i(\mathbf{R}) = m_i \cdot d^2\mathbf{R}/dt^2, \quad (3.11)$$

where m_i is the mass of molecule i and $d^2\mathbf{R}/dt^2$ is its linear acceleration.

The velocity and position of molecule i at some time (δt) later will depend upon the acceleration acting upon it.

The general method of updating the dynamics of the system is to use one of the Verlet-type schemes or algorithms. These schemes, first described by Verlet in 1967 [9, 22], are direct solutions to equation (3.11). The algorithm used in MDMPOL is called the half-step leap-frog scheme,

$$\mathbf{v}(t+1/2\delta t) = \mathbf{v}(t-1/2\delta t) + \delta t \mathbf{a}(t), \quad (3.12)$$

$$\mathbf{R}(t+\delta t) = \mathbf{R}(t) + \delta t \mathbf{v}(t+1/2\delta t), \quad (3.13)$$

$$\mathbf{v}(t) = 1/2(\mathbf{v}(t+1/2\delta t) - \mathbf{v}(t-1/2\delta t)). \quad (3.14)$$

The computer stores current positions $\mathbf{R}(t+\delta t)$, accelerations $\mathbf{a}(t)$, and mid-step velocities $\mathbf{v}(t+1/2\delta t)$. The force calculated in equation (3.10) is used to update the acceleration (equation 3.11), and thus the half-step velocity and positions of the molecules. These positions can be used to calculate the new potential acting on the molecules (equation 3.2), which is used to update the force, and so on. The value of δt in the MDMPOL simulation is arbitrary with the proviso that it must be significantly less than the time the molecule takes to travel its own length. $\mathbf{v}(t)$ is calculated in equation (3.14) so that the average translational kinetic energy (TKE) may be calculated,

$$\text{TKE} = 1/2 \sum m_i v_i^2. \quad (3.15)$$

The kinetic energy is calculated to see that it does not change dramatically from the norm at that temperature (equation (3.8)).

3.3.2.2 Rotational Motion

Other Verlet algorithms are used to calculate the rotational motion. These algorithms update the rotational velocity, rotational acceleration and the positions of the atoms of the molecules in the simulation from the torque acting upon the molecules. The torque acting about the centre-of-mass of the molecule is dependent upon the positions, masses, moments of inertia and rotational velocities of all the atoms of all the molecules, and the angles they make with one another. A suitable leap-frog algorithm is very complicated and is described in references [8, 9].

3.3.3 Conventions

MD simulations involve studying the behaviour of molecules moving in a cubic box (with sides of length L). The accuracy of this system is limited by the number of molecules (N) in this box. The value of N is generally restricted to between 100 and 1000 molecules by the computation time needed to perform the simulation; the time taken to evaluate forces and potential energies is proportional to N^2 . To model a real (infinite) system using this limited number of molecules, the Periodic Boundary Condition (PBC) is used. The PBC views the liquid as a pseudo-infinite periodic assembly of boxes where the contents and dynamics of the particles in each box are identical at all time. Without the PBC, the particles would be affected by the surfaces of the box. The PBC is illustrated in figure 3.3; as particle a reaches the left-hand side of box 1 it reappears on the right-hand side of box 1 (conserving the number density in box 1). Allied to the PBC is the Minimum Image Convention (MIC). The MIC is used so that a particle can never "see" its own image. The MIC is illustrated in figure 3.4; the Lennard-Jones potential is limited to a spherical range, R , which is equal

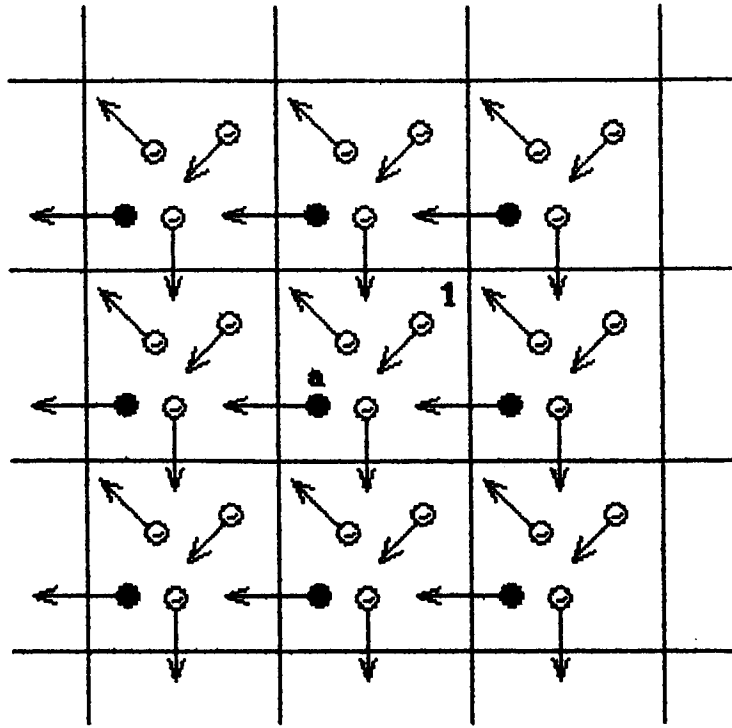


Figure 3.3 The Periodic Boundary Condition (PBC)

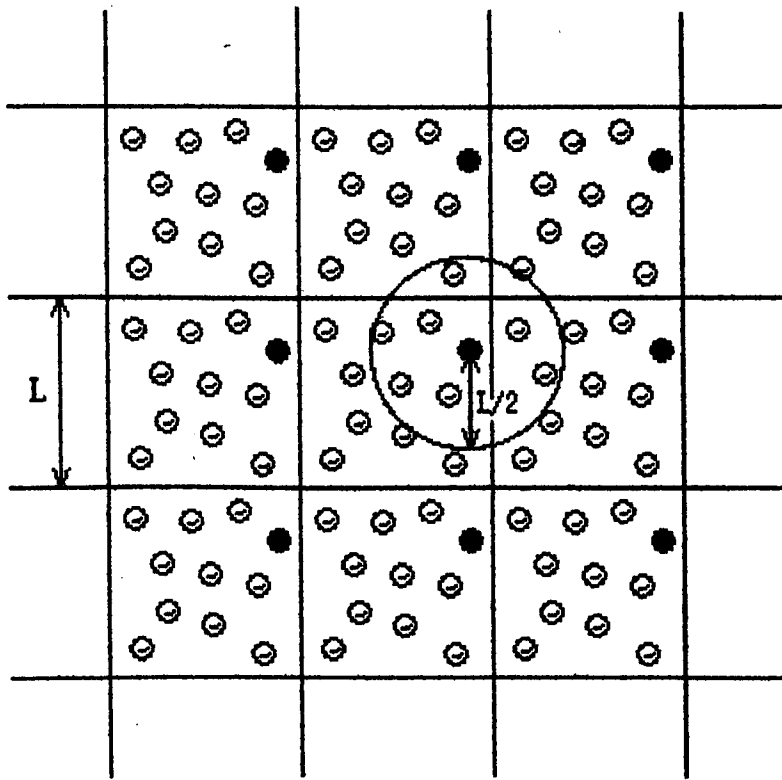


Figure 3.4 The Minimum Image Convention (MIC)

to half the box width ($L/2$). Using the MIC the potential force acting on each particle is affected only by the pair-potential of those particles within its cut-off sphere, of radius $L/2$. These may be those particles in its own box or those in the nearest image box (the MIC means that this does not include the image of itself). This means that particle a 's potential force will not affect the motion of all the particles in its own box but only $(V_{\text{sphere}}/V_{\text{box}})*N$, or roughly half of them. The larger the value of N , the larger is the value of $L/2$, which is the effective cut-off distance for the pdf given in the simulation. The minimum recommended size for the sides of the cubic box used in a LJ-type simulation is $L=6\sigma$ [9]. Any less than this value and the particles in the box may 'sense' the periodicity of the lattice. The MIC is only a limitation when looking at systems where long-range forces are especially important. In MDMPOL, the long-range behaviour of the fluid is taken into consideration using the long-range electrostatic addition to the LJ potential energy equation (equation (3.2)). The long-range potential is summed over the whole infinite lattice, set-up by the Periodic Boundary Conditions, using the Ewald summation method which rapidly converges as described in reference [8].

3.3.4 Data Input

MDMPOL runs over a series of subroutines. The initial parameters are:

- i. the job allocation time. The programme can be instructed to use a certain amount of computing time before closing down which is important when running a time-intensive programme. The alternative is to set the job allocation time to a very large value so that the programme will run to completion regardless of the amount of computing time it uses.

- ii. the system parameters the programme requires; the number of molecules ($N=4n^3$, n =integer, for a fcc lattice), the number of atoms per molecule (in our case five), the x, y, z positions of the atoms (considering the position of the central atom (carbon) to be (0.0,0.0,0.0)), the like-LJ parameters (ϵ_a and σ_a) and masses (m_a) of each atom (a) on the molecule, and the fractional charge on each of those atoms (q_a). The ϵ_a values may be input either in units of K or J, the σ_a values in nm, the masses in atomic mass units and the fractional charges in units of electronic charge (e).
- iii. the system conditions; the molar volume (in $\text{m}^3 \text{mol}^{-1}$) and temperature (in K).
- iv. the computational conditions; the number of time steps, the number of equilibration steps, the amount of time (in ps) between one time step and the next, and the Ewald convergence parameters.

3.3.5 Setting up the Molecules in the Box

MD simulations are usually run in a cubic box where the molecules are initially arranged on a face-centred cubic lattice. The molecules are arranged so that the centre of mass of the molecule lies on the lattice point. Initially, each molecule is assigned a random velocity so that there is no overall linear momentum, P ($P = \sum m_i v_i = 0, i=1,2,\dots,N$) and the average kinetic energy is equal to $3/2Nk_B T$ (k_B =Boltzmann's constant). The initial angular velocities are, for simplicity, set to zero but the orientations of the molecules are randomised about their lattice points.

3.3.6 Equilibration

It is necessary to run the MDMPOL computer simulation for a period of time before collecting data so that the initial (solid-like) lattice structure is 'melted' out. This is the equilibration step of the simulation. During this period, the kinetic energy of the system (both rotational and linear) is manipulated to suit the system temperature. The equilibration period is usually between 500 and 5000 time steps long. After a successful equilibration the total energy of the system has stabilised.

3.3.7 The Simulation of Liquids

After the equilibration period, the computer calculates and permanently stores the positions, translational kinetic, rotational kinetic, and potential energies (including the long-range potential energy) of all the molecules in the system, at each time step. From these values it calculates the average translational, rotational, potential, and total energies, and translational, rotational and total temperatures of the system, together with their rms deviations. These parameters are updated at each time step until either the computer allocation time or the number of time steps has been exceeded. The computer then calculates rolling averages to give average system energies and temperatures.

3.3.8 Checking the Results

When a simulation is complete the stored data can be checked. The important check is that the total energy is stable and that the temperature is reasonably close to the input temperature.

It is also useful to compare the energies from the simulation with experimental values of the enthalpy of vaporisation, ΔH_v [23]. The

average potential energy from the simulation can be approximated [15] to ΔH_v using,

$$\langle U \rangle \sim RT - \Delta H_v, \quad (3.16)$$

and the total energy [17] using,

$$\langle E \rangle \sim \langle U \rangle + 3RT. \quad (3.17)$$

The equations are only approximations because they consider a gas to be ideal, and thus $U_{\text{gas}} = 0$ and $pV = nRT$.

The values of $\langle U \rangle$ and $\langle E \rangle$ are important parameters for checking the validity of the simulation. If $\langle U \rangle$ or $\langle E \rangle$ vary dramatically from the experimentally determined values, then the simulation is not a good one, even if the pair distribution function obtained in the simulation compares well with experiment.

3.3.9 The Pair Distribution Function

The pair distribution function (pdf) is not explicitly derived in MDMPOL. The values that were required to calculate the pdfs required in this study were all output by the MDMPOL programme, but the code was not included. The FORTRAN required to build the pdf is explained in reference [9] and was written into MDMPOL by an American student, David Norris, who worked at ICI in the summer of 1990. His programme had two functions;

- i. It could build up the total pdf of the liquid under simulation,
- ii. It could build up the pdf of the individual atoms of the system, i.e. for AXY_3 , the pdfs for AX, AY, XY, AA, XX, and YY.

The pair distribution function was calculated by sorting the separations between atoms into histogram bins. Each bin contained those separations from a central atom that fell within a spherical ring of width δR (see section 1.3). For convenience we chose to have 501 bins within the MIC cut-off distance of one half-width of the box. Each atom on each molecule was considered in turn at each time step and the atomic separations were added to the appropriate histogram bin to build up the pdf.

3.3.10 Manipulating and Plotting the Pdf

A programme was written by myself, David Norris and Andrew Burgess, called RDFPLOT*. It was used to manipulate the results from MDMPOL and had several functions:

- (i) the total and individual pdfs could be normalised
- (ii) a neutron-weighted pdf could be calculated
- (iii) the simulated pdfs could be plotted
- (iv) experimental results could be plotted
- (v) experimental and neutron weighted pdfs could be overlaid
- (vi) areas under the simulated pdfs could be integrated

3.3.10.1 Normalisation of the Pdfs

The RDFPLOT routine reads in the binned data created in MDMPOL. These data, IHIST, are the pdf given by binning the data over all the atoms in the box (NMINBOX) and all the time-steps (ICOUNT). NMINBOX is equal to the number of molecules in the box (NSPEC) multiplied by the number of atoms on each molecule (NSITE). The RDF subroutine in

* RDFPLOT can be obtained from Dr. K. A. Johnson, Chemistry Department, Liverpool University.

RDFPLOT averages this pdf over the number of time-steps and number of atoms,

$$\text{FNUM}(\text{IBIN}) = \frac{\text{IHIST}(\text{IBIN})}{(\text{ICOUNT} \times \text{NMINBOX})} \quad (3.18)$$

The pdf (FNUM) is then normalised to ideal gas behaviour (see section 1.3). The normalisation involves dividing the total number of atoms in the box by the volume of the box (VOLUME) to get the average number density, ρ , of the atoms in the box. The total number of molecules that is in each bin (or spherical ring) if the fluid acts like an ideal gas is therefore,

$$\text{FIDEAL}(\text{IBIN}) = \frac{4}{3} \pi \rho [(R+\delta R)^3 - R^3], \quad (3.19)$$

$$= \frac{4}{3} \times \frac{\text{NMINBOX}}{\text{VOLUME}} \times [\text{RUPPER}^3 - \text{RLOWER}^3], \quad (3.20)$$

where RUPPER is the radius of the outer sphere ($R+\delta R$) and RLOWER is the radius of the inner sphere (R).

The normalised number in each bin, GR(IBIN) is thus;

$$\text{GR}(\text{IBIN}) = \frac{\text{FNUM}(\text{IBIN})}{\text{FIDEAL}(\text{IBIN})} \quad (3.21)$$

3.3.10.2 Calculating Neutron Weighted Pdfs

The comparison of computer simulated and experimental results was not direct. In neutron-diffraction experiments some atoms dominate the diffraction pattern more than others. RDFPLOT was used effectively to turn the simulated data into neutron-diffraction data by weighting the atom-atom individual pair distribution functions according to their 'visibility' to coherent neutrons (their cross-section and concentration both affect the weighting). For example, in a diffraction experiment of VCl_4 , the only significant pattern that would be given would be that from the Cl-Cl

interatomic separations since vanadium is almost invisible to coherent neutrons:

The intermolecular structure factor, $D_m(Q)$ for VCl_4 can be expressed as

$$D_m(Q) = [C_{VV}b_V^2a_{VV}(Q) + C_{VCl}b_Vb_{Cl}a_{VCl}(Q) + C_{ClCl}b_{Cl}^2a_{ClCl}(Q)] / (b_V + 4b_{Cl}) \quad (3.22)$$

where C_{XY} is the total number of pair-wise interactions there are between atom(s) X on one VCl_4 molecule and atom(s) Y on another, b_X is a scattering length and $a_{XY}(Q)$ is a partial pair-wise intermolecular structure factor.

C_{XY} is given from a table such as shown in table 3.2.


























Atom	V	Cl	Cl	Cl	Cl
V					
Cl					
Cl					
Cl					
Cl					

Table 3.2 The C_{XY} values for VCl_4

Thus, $C_{VV} = 1$, $C_{VCl} = 8$ and $C_{ClCl} = 16$.

The scattering lengths are tabulated in Chapter Two, and from that table, $b_V \sim 0$ and $b_{Cl} \sim 10$. The pdf that corresponds to these values is

$$g(R) = [1 \times 0 \times 0 \times g_{VV}(R) + 8 \times 0 \times 10 \times g_{VCl}(R) + 16 \times 10 \times 10 \times g_{ClCl}(R)] / (0+10+10+10+10)^2 \quad (3.23)$$

$$= g_{ClCl}(R) \quad (3.24)$$

3.3.10.3 Plotting the Simulated Pdfs

The simulated results, which included total pdfs, individual pdfs and neutron weighted pdfs were plotted using the plotting package GINO. The pdfs were plotted against R in increments of δR , with $GR(\text{IBIN})$ plotted at the centre of the bin interval, $((\text{IBIN}-1) \cdot R + \delta R / 2)$. The data could be plotted between any chosen x, y limits, with a broken or solid line.

3.3.10.4 Plotting the Experimental Results

RDFPLOT could also plot the neutron-diffraction results. The results from those experiments were downloaded from the RAL computer and read in to RDFPLOT. They could be plotted, using GINO, in a similar fashion to the simulated data.

3.3.10.5 Overlaying Pdfs

One of the most important aspects to this programme was the ability to overlay spectra. The simulated and experimental results could be plotted together for comparison.

3.3.10.6 Integrating Regions of the Pdf

One of the advantages of the simulated MDMPOL results over those given by neutron-diffraction experiments is the ability to look at them in greater detail. Once the MDMPOL results compared well with experiment, it was possible to investigate the structure of the fluids being studied by looking at the individual pdfs. A good example again is VCl_4 , whose neutron-diffraction results show only the interactions between the Cl atoms. MD results could help to show the structure of the fluid because all

the interactions are 'visible' in MD calculations (neutron weighting would remove the VCl and VV contributions to the structure, showing only the ClCl contribution when comparing simulation with experiment). The vanadium atoms affect the structure of liquid VCl₄ even though they are 'invisible' to neutrons.

One of the ways of investigating the structure of fluids using the individual pairs is to integrate these spectra in certain regions,

- (i) in the intramolecular region.
- (ii) in the intermolecular region.

The integration of the intramolecular region helps to show that the simulation has worked properly. The ratio of the areas under the intramolecular peaks should correspond to that expected. For example, for VCl₄ the ratio of the peak areas for V-Cl and Cl-Cl should be 4:6 in the total pdf spectrum.

Individual pdfs have peaks and troughs in the intermolecular region, which correspond to regions in the fluid of greater and lesser number density compared with ideal gas respectively. The method used in this study to facilitate the investigation of the structure was to integrate the intermolecular part of the respective individual pdf to the centre of the first trough in order to identify the number of atoms in the nearest neighbour shell.

The first step in the integration routine is to reverse the normalisation routine, shown in Section 3.3.10.1, to get FNUM(IBIN). FNUM(IBIN) was then multiplied by NSITE, to obtain the number of X-Y pairs at a distance R from each other averaged both over time and number of molecules

$$\text{NUMXY}(\text{IBIN}) = \text{FNUM}(\text{IBIN}) \times \text{NSITE} \quad (3.25)$$

NUMXY(IBIN) is then divided by the number of XY vectors (C_{XY}) involved in order to obtain the average number of individual XY distances

$$\text{NUMVEC}(\text{IBIN}) = \frac{\text{NUMXY}(\text{IBIN})}{C_{XY}} \quad (3.26)$$

The next manipulation of the data is to multiply NUMVEC(IBIN) by the number of Y atoms on the molecule next to the X molecule (NY).

$$\text{INT}(\text{IBIN}) = \text{NUMVEC}(\text{IBIN}) \times \text{NY} \quad (3.27)$$

Finally INT(IBIN) can be added up over the range of IBIN desired.

As an example, consider integrating the intermolecular region of an (imaginary) individual pair distribution function for the V-Cl pairs of the VCl_4 molecule; NSITE = 5, $C_{\text{VCl}} = 8$, and NY = 4. For the Cl-V pairs NSITE = 5, $C_{\text{VCl}} = 8$, and NY = 1.

3.4 Experimental

MDMPOL was run for all of the liquids that were studied using neutron-diffraction: dichlorodifluoromethane (CFC-12, CCl_2F_2), fluoroform (HFC-23, CHF_3), chlorotrifluoromethane (CFC-13, CClF_3), bromotrifluoromethane (BCFC-13B1, CBrF_3), chlorodifluoromethane (HCFC-22, CHClF_2), and deuterated chlorodifluoromethane (d-HCFC-22, CDClF_2). However, before these fluids were simulated the MDMPOL programme was checked by studying dichloromethane, CH_2Cl_2 .

3.4.1 Dichloromethane

The MDMPOL programme was coded to work on a CRAY. The computer used in this study was a SUN 4/110 workstation at ICI Runcorn. Slight

modifications to MDMPOL were necessary so that it would work on the SUN. A check that the programme had been installed properly involved running a simulation of 108 dichloromethane molecules and checking the results against those listed in the MDMPOL manual. The simulation was successful and the results compared well with those listed.

3.4.2 Dichlorodifluoromethane

The second molecule that was chosen to be simulated using MDMPOL was dichlorodifluoromethane (CCl_2F_2 , CFC-12). This molecule was the first of the LAD neutron-diffracted molecules to bear results [24], and previous MD experiments had been performed on it [17].

3.4.2.1 Input Parameters

In 1989, Mountain and Morrison [17] studied CFC-12 using a LJ-based computer-simulation programme that incorporated fractional charges. By comparing their simulated thermodynamic results with those from experiment, they were able to optimise values of the LJ parameters ϵ and σ . This was useful for this study because it saved us having to optimise these values from initial estimates such as those given in table 3.1. Table 3.3 shows the parameters used by Mountain and Morrison in their work in comparison to those used in this study.

The LJ parameters used by Mountain & Morrison in their study were also adopted for ours. Other parameters, however, were adjusted in the light of the neutron-diffraction results. The individual molecules of CCl_2F_2 in our simulation had the geometry derived in our neutron-diffraction experiment [24]; those in the Mountain and Morrison simulation were gas-phase microwave-derived bond distances [25]. These slight changes in the interatomic bond separations (which are also

compared in table 3.3) slightly affected our choice of fractional charges. The fractional charges used in this study were taken from the extensive database of Cooper et al. [21]. The bond distances from the neutron-diffraction experiment were compared with those from Mulliken population analysis calculations; the best comparison was with the TZV+P basis set and the values of q chosen in this study were the ones associated with that basis set.

Parameter	Mountain & Morrison	This study
Temperature/ K	200	153
ϵ_C / K	45.5	45.5
ϵ_F / K	40.6	40.6
ϵ_{Cl} / K	134.4	134.4
σ_C / nm	0.315	0.315
σ_F / nm	0.320	0.320
σ_{Cl} / nm	0.329	0.329
q_C	0.2280	0.46/0.00
q_F	-0.0948	-0.18/0.00
q_{Cl}	-0.0192	-0.05/0.00
N	108	32/108
δt /fs	2	5
C-F/Å	1.345	1.326
C-Cl/Å	1.744	1.755
F...F/Å	2.151	2.142
F...Cl/Å	-	2.525
Cl-Cl/Å	2.902	2.900

Table 3.3 Input parameters for the MD simulation of CCl_2F_2

MDMPOL requires the bond distances to be input in x,y,z format as shown in Table 3.4. The C atom was chosen as the 0.0,0.0,0.0 point and the other positions were calculated.

Atom	x	y	z
C	0.0000	0.0000	0.0000
F	0.1071	0.0000	-0.0782
F	-0.1071	0.0000	-0.0782
Cl	0.0000	-0.1450	0.0989
Cl	0.0000	0.1450	0.0989

Table 3.4 The bond distances of CCl₂F₂ in x, y, z format

3.4.2.2 The Simulations

Four simulations were performed on CCl₂F₂ using the parameters shown in tables 3.3 and 3.4:

- i. 32 ($N=4n^3$, $n=2$) molecules including the Cooper [21] fractional charges,
- ii. 32 molecules excluding fractional charges,
- iii. 108 ($n=3$) molecules including the Cooper fractional charges,
- iv. 108 molecules excluding fractional charges,

and a fifth simulation was performed to find out how well-optimised the Mountain and Morrison parameters [17] parameters were.

- v. 108 molecules using the estimated LJ parameters from Allan and Tildesley's book [9] (see table 3.1) and the fractional charges from Cooper *et al.* [21].

(i, ii) The first simulations proceeded with 32 molecules primarily because simulation time depends upon N^2 . A significant saving in

simulation time was achieved by studying only 32 molecules when checking to see if the simulation was working properly. Simulations were run either including fractional charges or excluding them to see if they were necessary to describe the structure of the fluid. The parameters specifically relating to the 32 molecule simulations were

Half Box Length = 0.7880 nm

Total Number of Time-steps = 10000

Number of Equilibration Steps = 2500

Real Time for Simulation = 37.5 ps

(iii, iv) The 108 molecule simulations were run because their R-range extended to 11 Å (rather than only 7 Å for 32 molecules). The parameters specifically relating to the 108 molecule simulations were

Half Box Length = 1.182 nm

Total Number of Time-steps = 10000

Number of Equilibration Steps = 2500

Real Time for Simulation = 37.5 ps

(v) All the parameters in this simulation (excluding the LJ parameters) are the same as for the other 108 molecule cases above.

In all cases the job-allocation time was set so that the simulations would run for the whole 10000 time-steps.

3.4.2.3 Thermodynamic Comparisons

The results given in the simulation of CFC-12 are shown in table 3.5. The approximate values of $\langle U \rangle$ and $\langle E \rangle$ shown in table 3.5 were calculated using equations (3.16) and (3.17) from the ΔH_v values given in reference [23]. There is no difference between the values of $\langle U \rangle$ and $\langle E \rangle$ for the Mountain and Morrison 32 molecule and 108 molecule cases with or

without the fractional charges and they all correspond closely to the experimentally-derived values [23].

Quantity	Simulation (i)	Simulation (ii)	
$\langle U \rangle / \text{kJ mol}^{-1}$	-22.35 ± 0.22	-22.24 ± 0.23	
$\langle E \rangle / \text{kJ mol}^{-1}$	-18.5427 ± 0.0170	-18.4862 ± 0.0174	
TKE/ kJ mol^{-1}	1.85 ± 0.21	1.83 ± 0.23	
RKE/ kJ mol^{-1}	1.96 ± 0.20	1.92 ± 0.22	
Temperature/K	154.9 ± 8.9	150.5 ± 9.4	
$\Delta H_v^\ddagger / \text{kJ mol}^{-1}$	24.30 ± 0.43	24.516 ± 0.46	
$\langle U \rangle^\dagger / \text{kJ mol}^{-1}$	-23.01 ± 0.50	23.26 ± 0.53	
$\langle E \rangle^\square / \text{kJ mol}^{-1}$	-19.15 ± 0.72	19.50 ± 0.75	
Quantity	Simulation (iii)	Simulation (iv)	Simulation (v)
$\langle U \rangle / \text{kJ mol}^{-1}$	-22.59 ± 0.13	-22.40 ± 0.13	-31.35 ± 0.21
$\langle E \rangle / \text{kJ mol}^{-1}$	-18.6548 ± 0.0011	-18.5377 ± 0.0010	-27.5775 ± 0.0022
TKE/ kJ mol^{-1}	1.95 ± 0.13	1.92 ± 0.12	1.89 ± 0.15
RKE/ kJ mol^{-1}	1.98 ± 0.12	1.94 ± 0.12	1.88 ± 0.15
Temperature/K	157.9 ± 5.3	154.8 ± 5.3	151.1 ± 8.5
$\Delta H_v^\ddagger / \text{kJ mol}^{-1}$	24.17 ± 0.24	24.33 ± 0.24	24.49 ± 0.48
$\langle U \rangle^\dagger / \text{kJ mol}^{-1}$	-22.86 ± 0.25	-23.04 ± 0.25	-23.23 ± 0.48
$\langle E \rangle^\square / \text{kJ mol}^{-1}$	-18.94 ± 0.26	-19.18 ± 0.26	-19.46 ± 0.69

Table 3.5 The results from the five simulations of CCl_2F_2

‡ Enthalpy of vaporisation data are available to 173 K [23]. Extrapolation to 153 K does not introduce any significant error. The main uncertainty in ΔH_v is due to the uncertainty in the temperature.

† Calculated using equation (3.16)

□ Calculated using equation (3.17)

This suggests that fractional charges make little or no difference to the total or potential energy of CFC-12. The parameters in simulation (v) taken from reference [9] however give totally the wrong energy indicating that the Mountain and Morrison LJ parameters [17] are well optimised.

3.4.2.4 The Total and Neutron-Weighted Pair Distribution Functions

The total unweighted pair distribution functions for the different cases were plotted using RDFPLOT. A check that the x,y,z co-ordinates for the atoms of each molecule were input properly was to check the intramolecular region of the pdf. The peaks should be centred about the appropriate bond length within the experimental error introduced by binning the data - in this case there were 501 bins so the error is equal to the Minimum Image cut-off distance divided by 501 (0.0016 nm for 32 molecules and 0.0024 nm for 108). The intramolecular peaks were also integrated to see if they correspond to those expected. In the case of CFC-12, the integral ratios for C-F, C-Cl, F-F, F-Cl, Cl-Cl should be 2,2,1,4,1 respectively which corresponded exactly to the measured values for each total pdf.

The next step was to calculate the neutron weighted pair distribution function. There are six different atom-atom intermolecular interactions that make up the total pdf for CFC-12; C-C, C-F, C-Cl, F-F, F-Cl, and Cl-Cl. The intermolecular structure factor $D_m(Q)$ for CFC-12 can be expressed as

$$D_m(Q) = \frac{(C_{CC}b_C^2a_{CC}(Q) + C_{CCl}b_Cb_{Cl}a_{CCl}(Q) + C_{CF}b_Cb_Fa_{CF}(Q) + C_{FF}b_F^2a_{FF}(Q) + C_{ClF}b_{Cl}b_Fa_{ClF}(Q) + C_{ClCl}b_{Cl}^2a_{ClCl}(Q))}{(\sum b_i)^2}, \quad (3.28)$$

where C_{XY} is the total number of pair-wise interactions there are between atoms X and Y on two molecules of CCl_2F_2 , b_X is a scattering length, a_{XY} is a partial pair-wise intermolecular structure factor and $\Sigma b_i = (b_C + 2b_F + 2b_{Cl})$.

The values of C_{XY} can be derived from table 3.6.


























Atom	C	F	F	Cl	Cl
C					
F					
F					
Cl					
Cl					

Table 3.6 The C_{XY} values for CCl_2F_2

Thus, for CFC-12 the C_{XX} contributions of C-C, C-F, C-Cl, F-F, F-Cl, and Cl-Cl distances $D_M(Q)$ are 1, 4, 4, 4, 8, and 4.

If we use the b_X values from Skold [26] (which for C, F, and Cl are 6.646, 5.654, 9.577 femtometres respectively), this leads to a corresponding neutron weighted pdf

$$g(R) = 0.0321g_{CC}(R) + 0.1849g_{CCl}(R) + 0.1092g_{CF}(R) + 0.2664g_{ClCl}(R) + 0.0929g_{FF}(R) + 0.3146g_{ClF}(R), \quad (3.29)$$

where g_{XY} is an individual pair-wise pdf.

A comparison between 32 (charged) and 108 (charged) molecule neutron-weighted spectra is shown in figure 3.5 and between 108 (charged) and 108 (uncharged) in figure 3.6. The neutron-weighted 108 molecule spectra oscillate about unity at high R which is a check that equation (3.29) is correct. There is a tail off at approximately 7.0 Å in the 32 molecule case

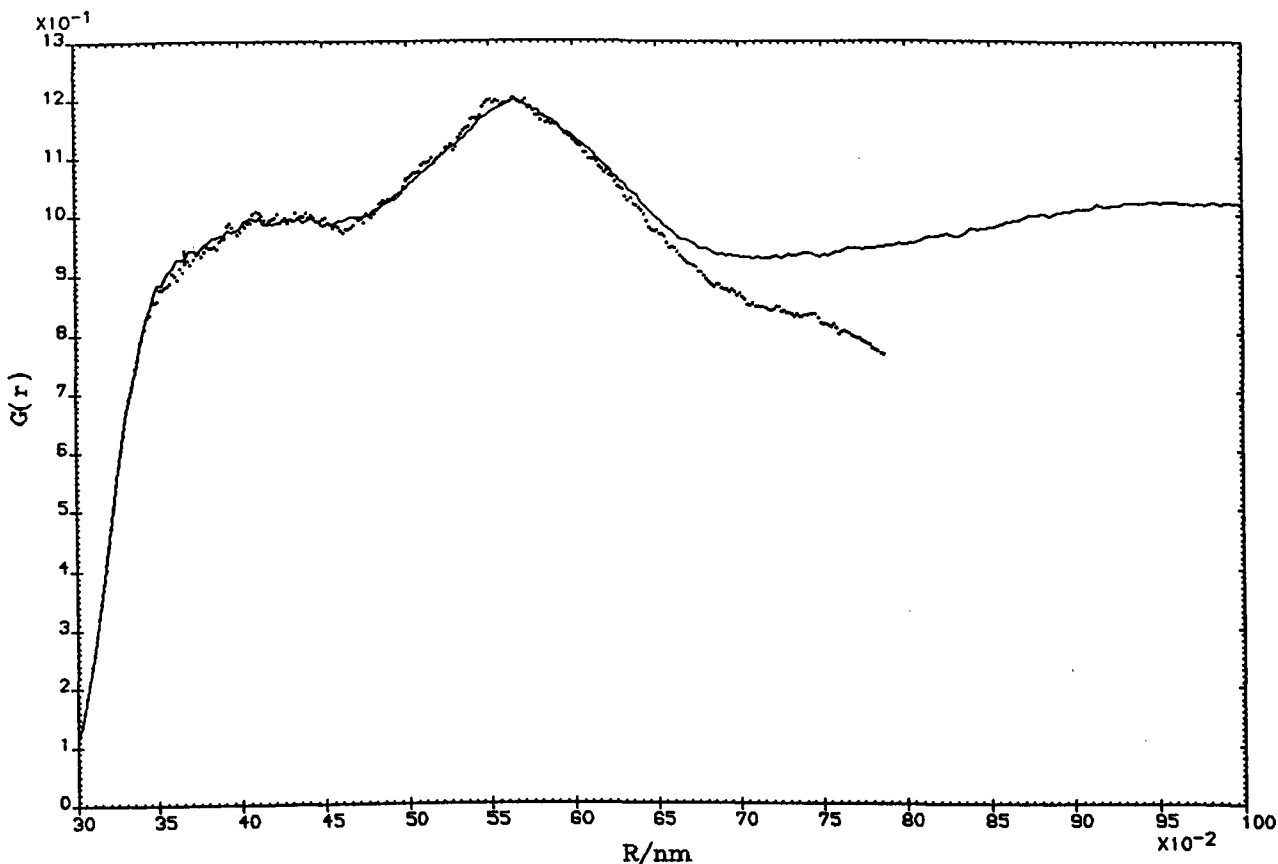


Figure 3.5 A comparison of 32 (---) and 108 (—) molecule MD simulations of CCl_2F_2

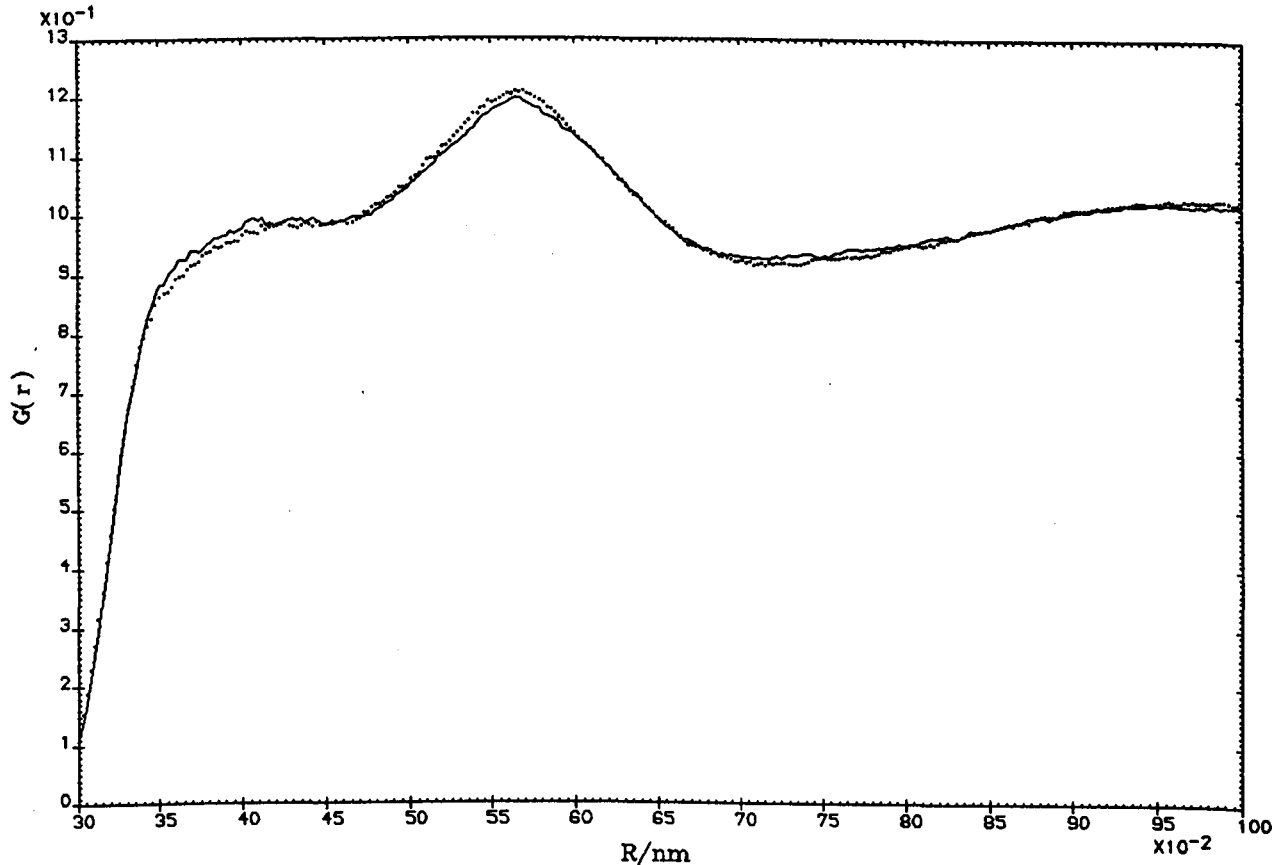


Figure 3.6 A comparison of CCl_2F_2 pdfs for non-charged (—) and charged (---) 108 molecule MD simulations

showing the failure of the PBC close to its maximum distance when simulating with so few molecules. For CCl_2F_2 , the largest value of σ is 3.29 Å and following the advice quoted in section 3.3.3 the minimum half-width of the box [9] should be roughly 10 Å; the half-width of the 32 molecule box was only 7.88 Å.

The neutron-weighted MD simulation for the 108 charged-molecule simulation is compared with the neutron-diffraction results in figure 37. There is quite a good match with the general features of the experimental pdf being reflected in the MD simulation. Since the experimental and simulated energies are also well matched, further refinement of the LJ parameters was considered unnecessary.

3.4.2.5 The Individual Pair Distribution Functions and their Integration

Since the neutron-weighted and experimental pdfs agree, it seemed reasonable to assume that the LJ model gives a reasonable representation of the structure of liquid CCl_2F_2 . The MD data were consequently broken down into individual pdfs so that the structure of CCl_2F_2 could be studied in some detail. The individual pdfs given for the charged 108 molecule case are shown in figures 3.8 (a-f). They are essentially the same as those given by the uncharged system which shows that the fractional charges make little or no difference to the structure of liquid CCl_2F_2 .

The first peaks in the individual pdfs were integrated using the method outlined in Section 3.3.10.6 and the results are shown in table 3.7.

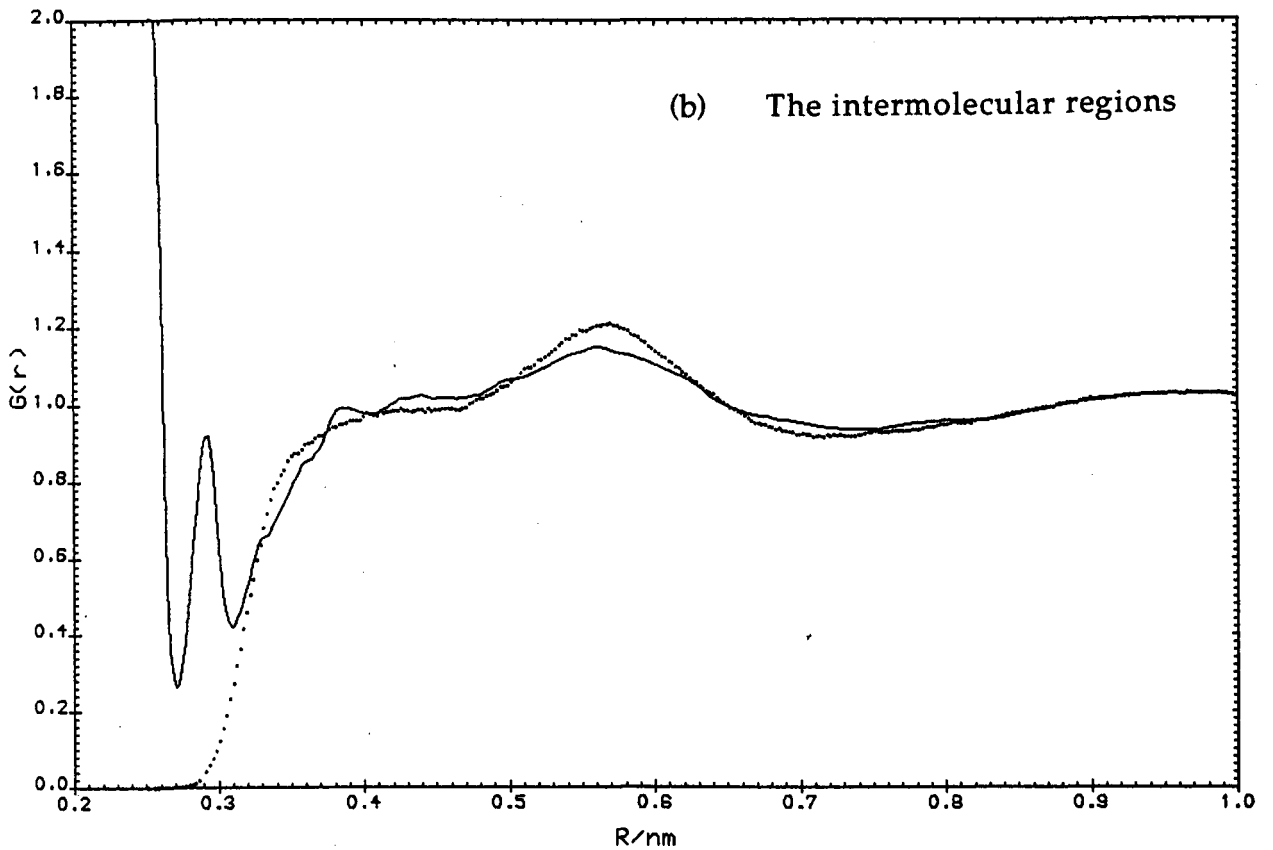
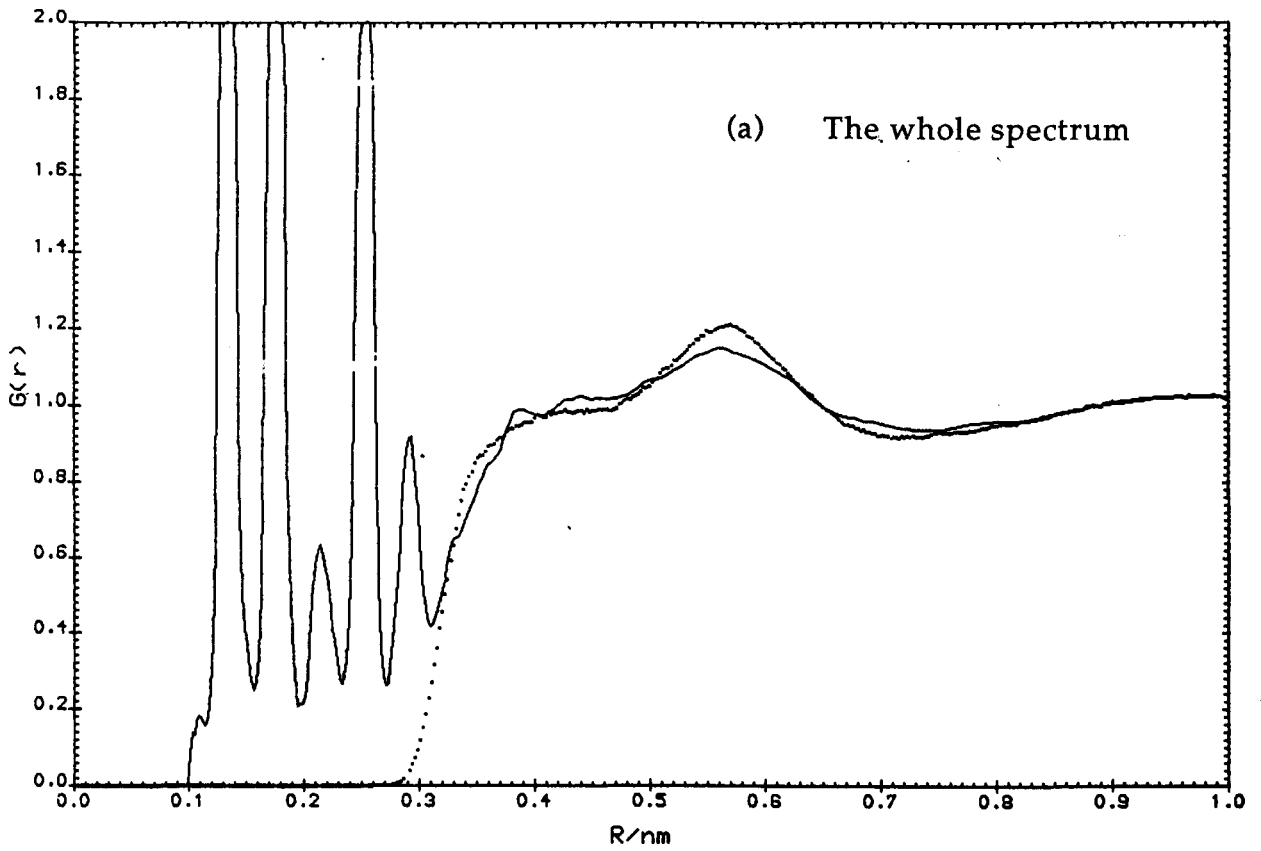


Figure 3.7 A comparison of the CCl_2F_2 pdfs given by MD simulation (-) and neutron diffraction (-)

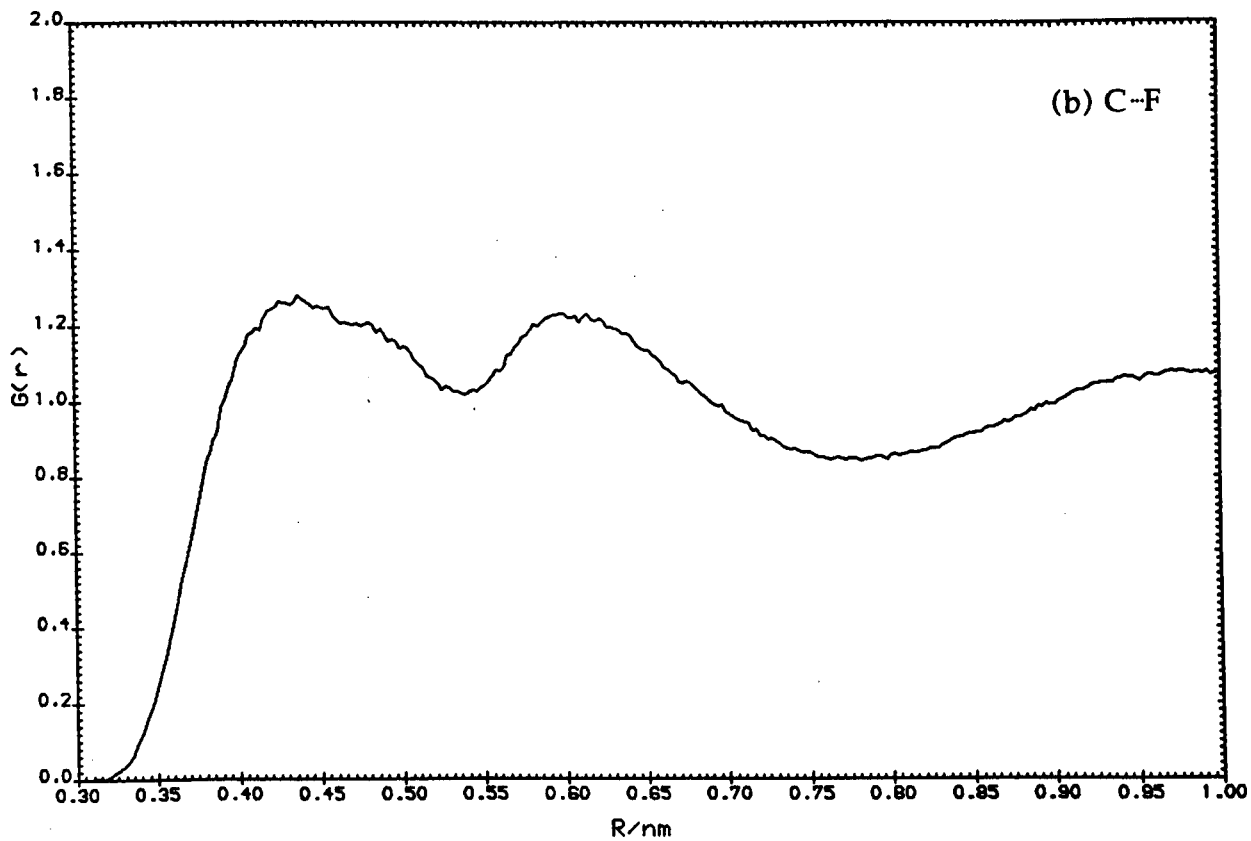
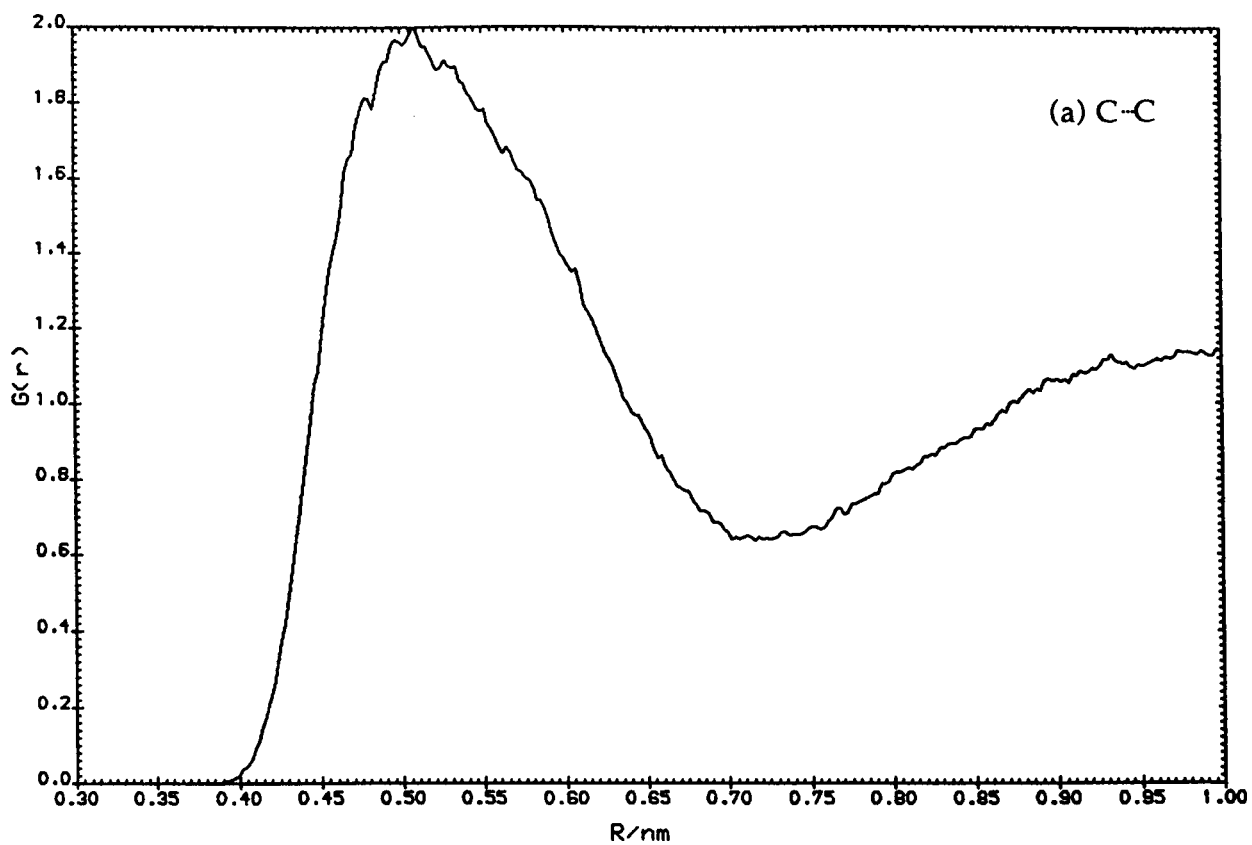


Figure 3.8 The individual pdfs from the MD simulation of CCl_2F_2

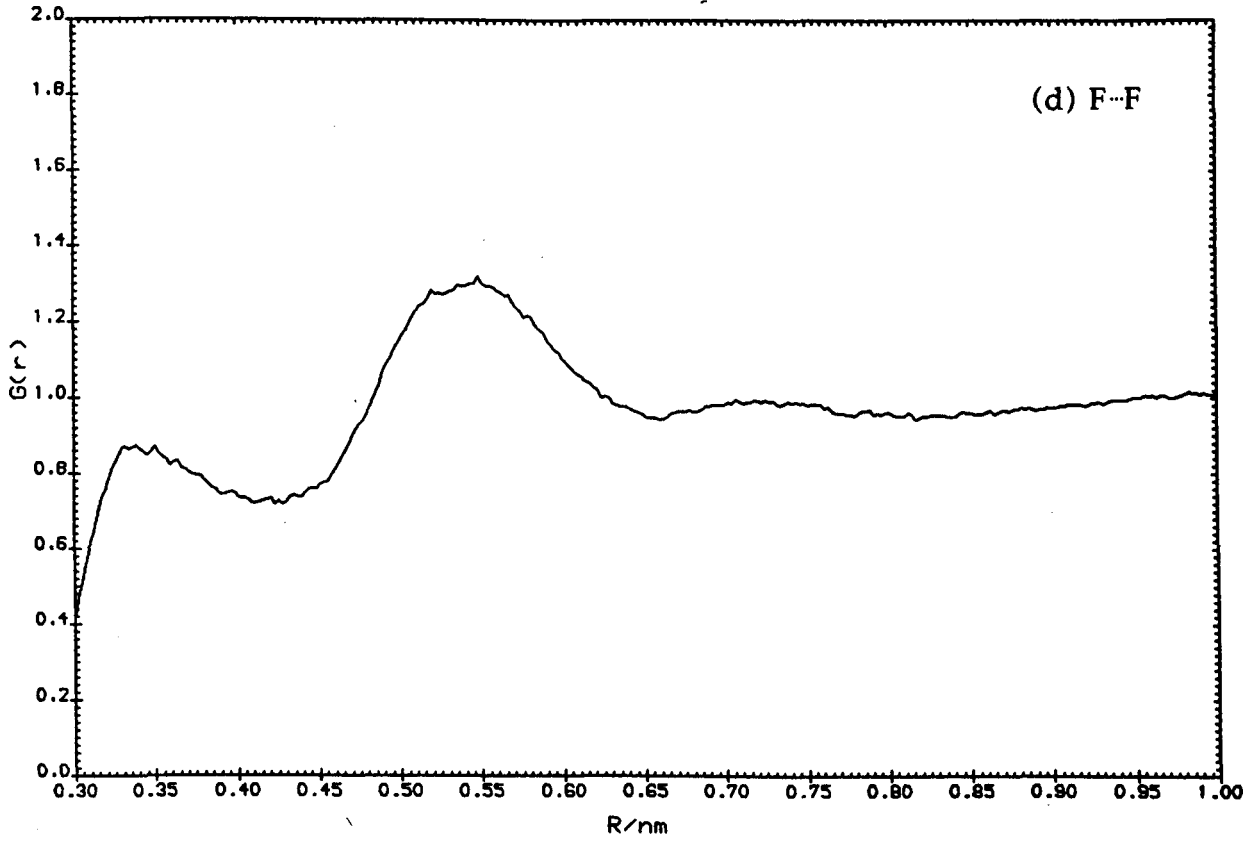
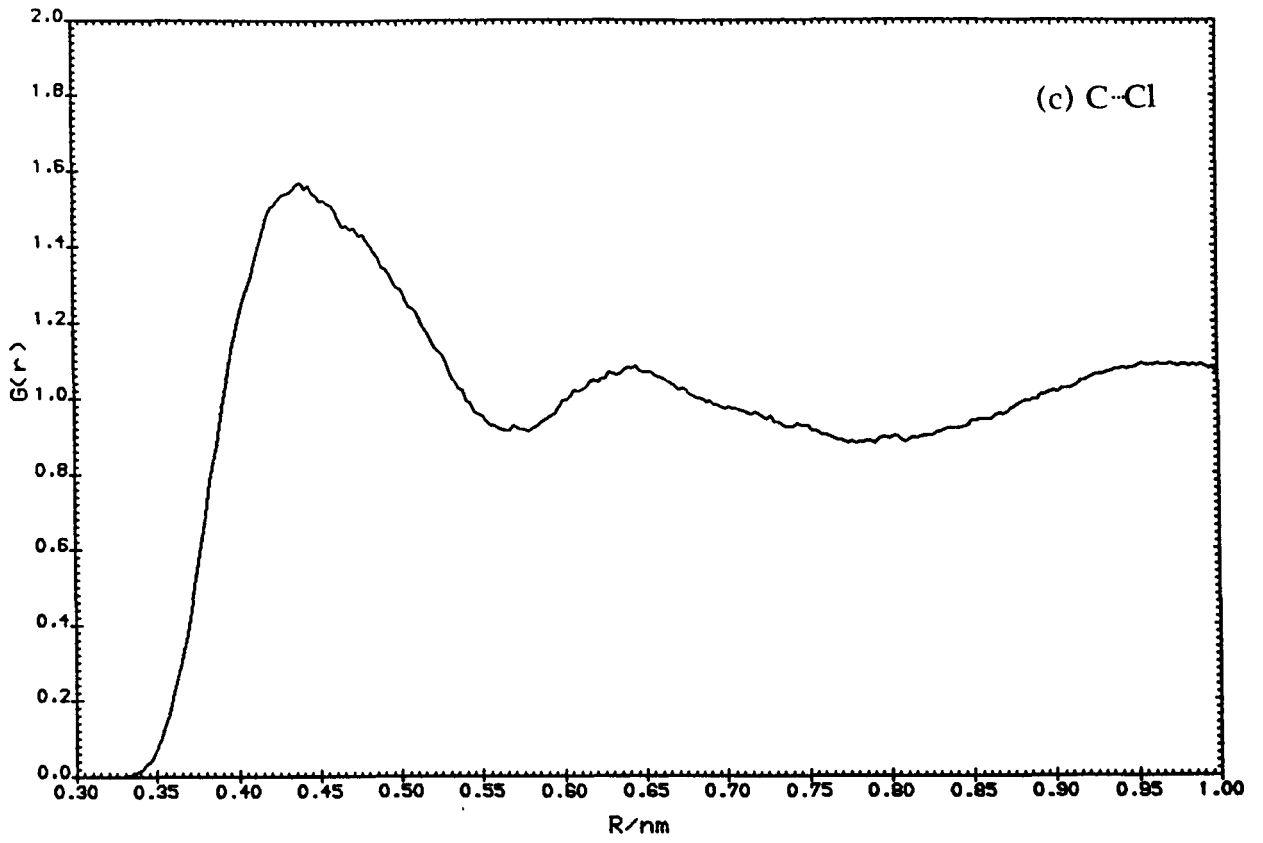


Figure 3.8 The individual pdfs from the MD simulation of CCl_2F_2

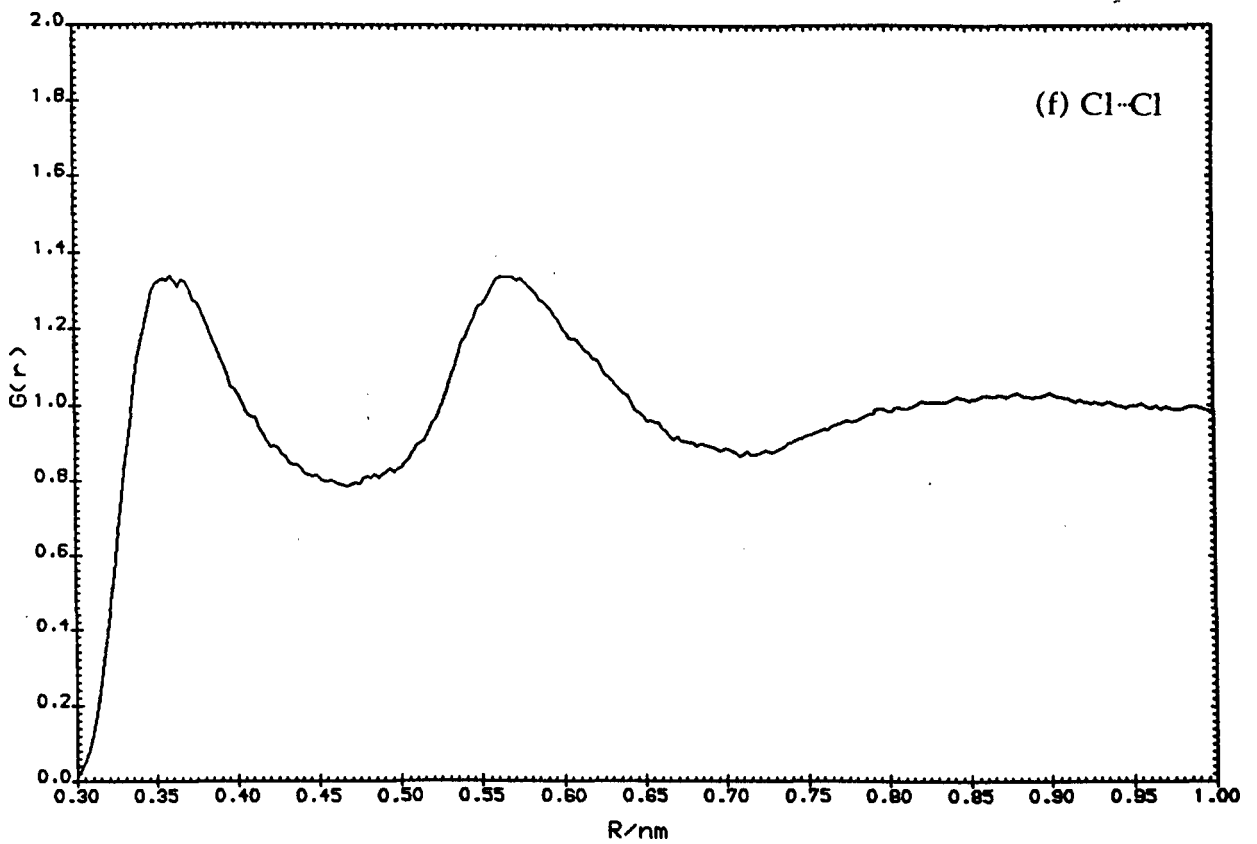
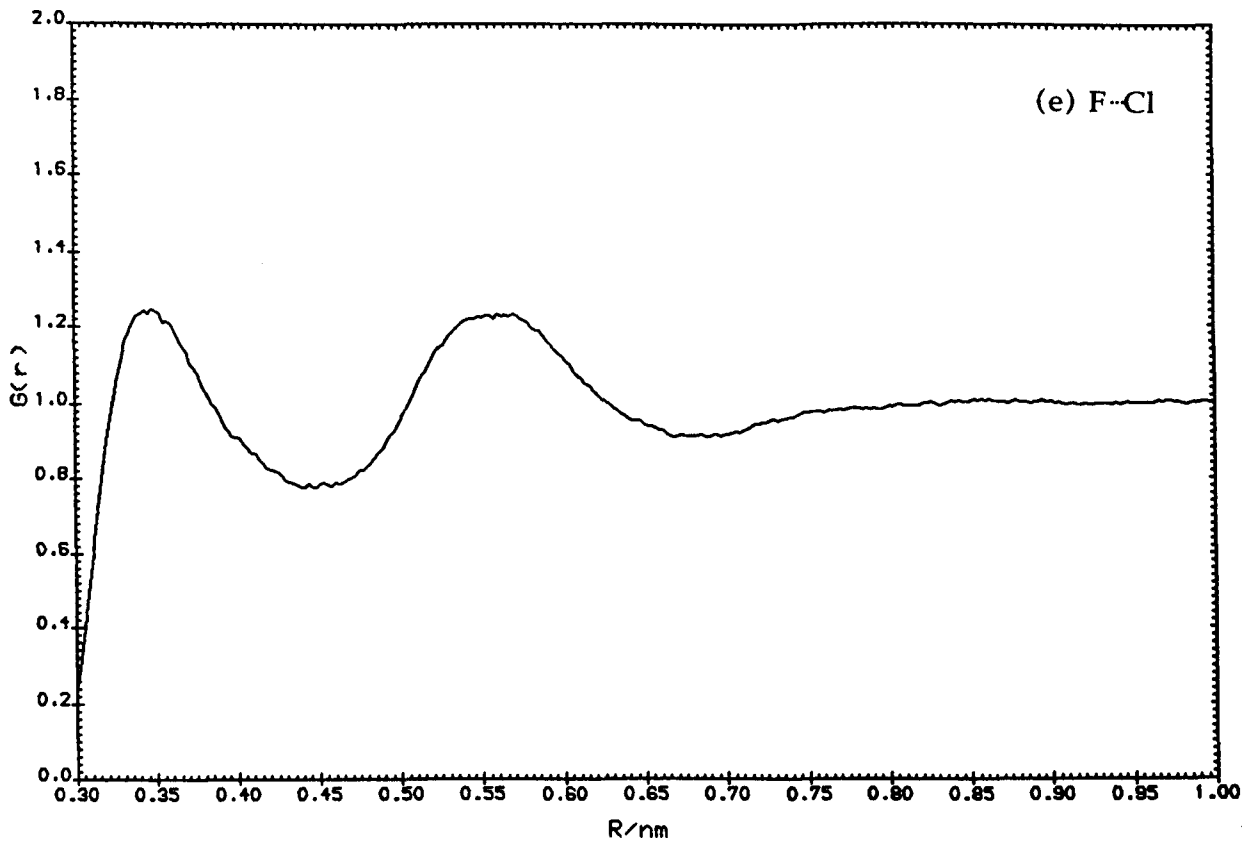


Figure 3.8 The individual pdfs from the MD simulation of CCl_2F_2

Pair (XY)	C_{XY}	N_Y	Peak Maximum/nm	Integral Range/nm	Number of Neighbours
C--C	1	1	0.51	03 - 073	13.0 ± 1.0
C--F	4	2	0.44	03 - 054	8.7 ± 0.8
F--C		1			4.3 ± 0.8
C--Cl	4	2	0.44	03 - 057	11.4 ± 0.8
Cl--C		1			5.7 ± 0.8
F--F	4	2	0.34	03 - 043	2.9 ± 0.3
F--Cl	8	2	0.35	03 - 045	4.2 ± 0.7
Cl--F					
Cl--Cl	4	2	0.36	03 - 047	5.0 ± 0.6

Table 3.7 The number of nearest neighbours for CCl_2F_2

3.4.2.6 Discussion of the Structure

The results of the integration indicate that there are between 12 and 14 'nearest-neighbour' carbon atoms within 7 Å of a central carbon atom. This is very similar to the packing density in solid CCl_2F_2 [27]. The solid structure is orthorhombic $Fdd2$, where the molecules form columns with ferroelectrically aligned dipoles. In this structure the fluorine atoms are as far away from each other within the confines of the structure and the chlorine atoms are closed packed in as many places as possible. This propensity against close F--F contacts is inherent in the liquid structure where the number of F--F nearest neighbours is low compared with that for F--Cl and Cl--Cl.

The liquid structure of CCl_2F_2 is not going to be an easily defined structure like that of the solid since a number of different configurations

of the molecules will be important. Previous work by McDonald *et al.* [7] suggested that for CCl_4 only two dimeric configurations were important. These configurations are identified as the 'rocket' model (following McDonald *et al.*) and the 'straddle' model (our term). Using the reasoning explained in the McDonald paper [7], the important contributions to the structure of CFC-12 can be chosen from a total of ten possible configurations. Each of these configurations is illustrated in figures 3.9 (A-J).

To assess the probability of each structure we can start by looking at the intermolecular separations as indicated in the C-F and C-Cl pdfs. If we take the average C-C separation to be 5.1 Å, the C-F intramolecular bond length to be 1.326 Å and the C-Cl intramolecular bond length to be 1.755 Å, we can calculate where the nearest C-F and C-Cl peaks should occur. For rocket-type structures these occur at about 3.8 Å and 3.3 Å respectively. Inspection of the relevant pdfs shows no indication of any significant probability in these regions. For this reason we conclude that there is a low probability of any two CFC-12 molecules being arranged in a rocket conformation.

The discussion of the different straddle configurations can be simplified by considering their occurrence to be due to the relative energetics of F-F, Cl-Cl and F-Cl interactions. The relative proportions of these interactions can be gauged from integrals given in table 3.7. The integrals indicate that there is a greater likelihood of Cl-Cl contacts than F-Cl contacts, which in turn is more likely than F-F contacts. As we found no difference in the pdfs with and without fractional charges, we can assume that this non-statistical distribution is due to the large difference in the polarisability of the chlorine and fluorine atoms. The integrals suggest that the different straddle configurations will most likely

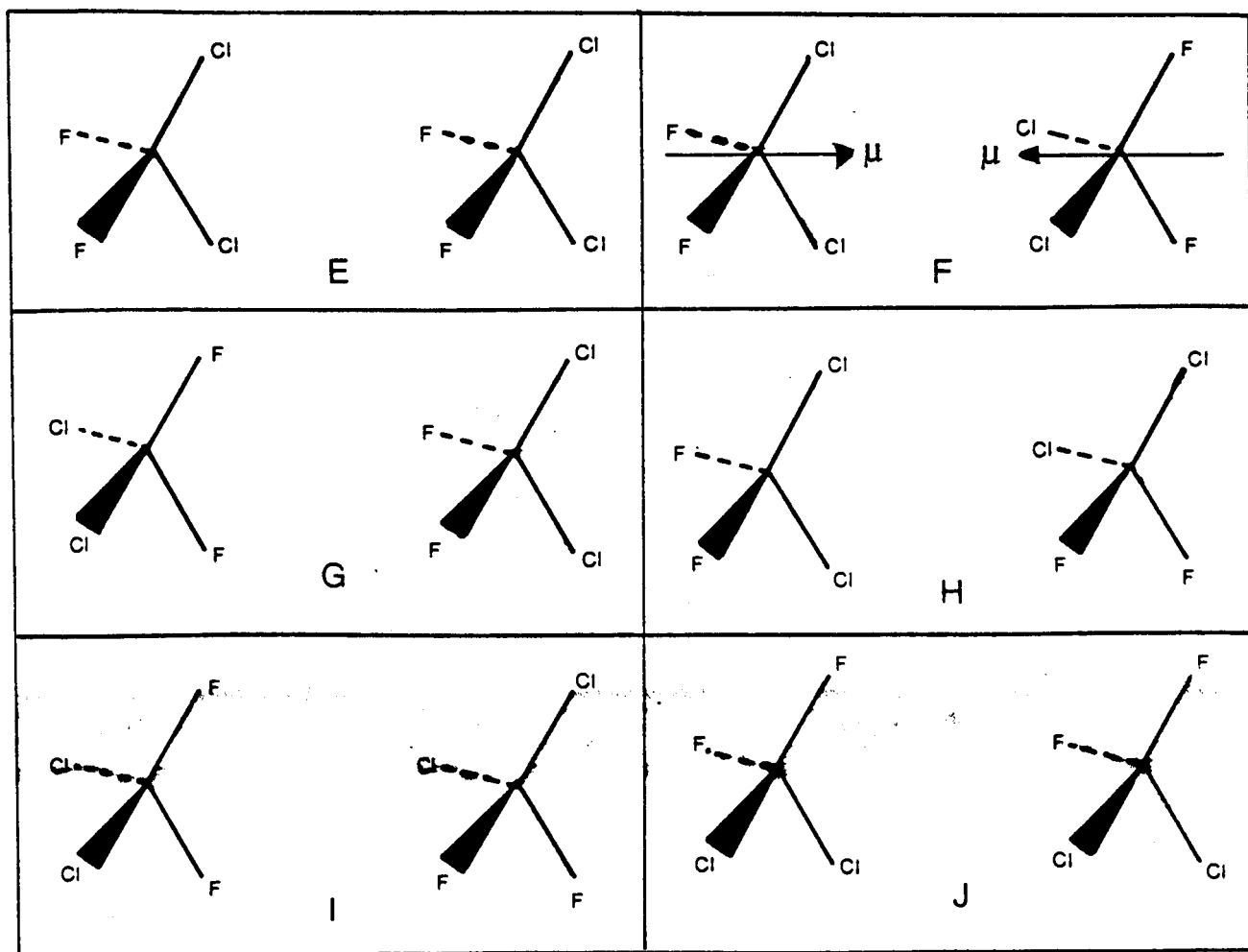
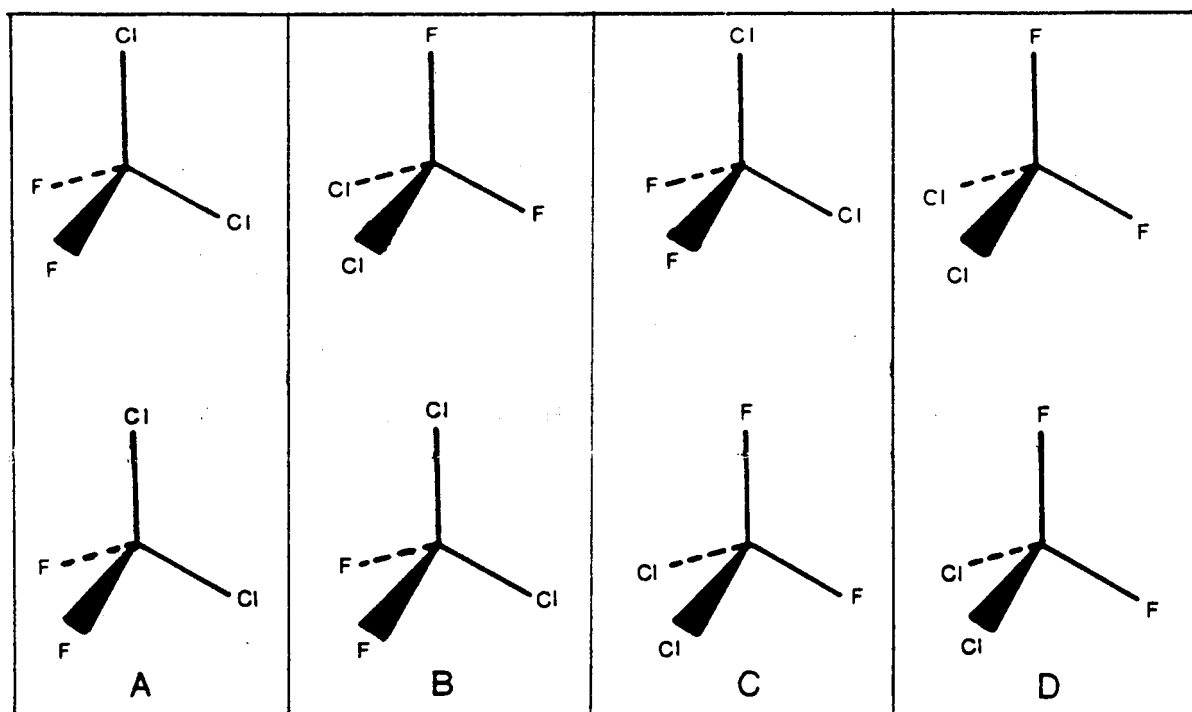


Figure 3.9 The possible rocket (A-D) and straddle (E-J) configurations of CCl_2F_2 molecules in the liquid phase. The direction of the dipole moment, μ , for CCl_2F_2 is shown in configuration F

occur in the order $F > H > E > J > I > G$. The first three configurations (F, H and E) will probably dominate the structure of liquid CFC-12.

3.4.3 Fluoroform

Although Bohm et al. [12] had previously simulated the structure of fluoroform using the test-particle method, this experiment was the first LJ Molecular Dynamics simulation on fluoroform (CHF_3 , HFC-23). It was thus necessary to adjust the starting LJ parameters to give the right energy and pdf.

3.4.3.1 Input Parameters

The Molecular Dynamics simulation of fluoroform had as its starting point the LJ parameters listed in reference [9] and the charges from the Cooper paper [21] as shown in table 3.8.

The individual molecules of CHF_3 had the geometry derived in our neutron diffraction experiment. The bond distances are shown in their x, y, z format in table 3.9.

The first test run (1000 time-steps and 500 equilibration steps) using the parameters in tables 3.8 and 3.9 did not match the average total energy, $\langle E \rangle$ which should be approximately $13.60 \text{ kJ mol}^{-1}$ at 153 K. The associated neutron-weighted pdf (figure 3.10) however, looked similar to the experimental neutron-diffraction results (figure 2.29). A second run that excluding fractional charges had an $\langle E \rangle$ that was too low and a pdf (figure 3.11) that poorly compared to the neutron-diffraction results. Our conclusions were that fractional charges were important in this simulation and the LJ parameters needed adjusting.

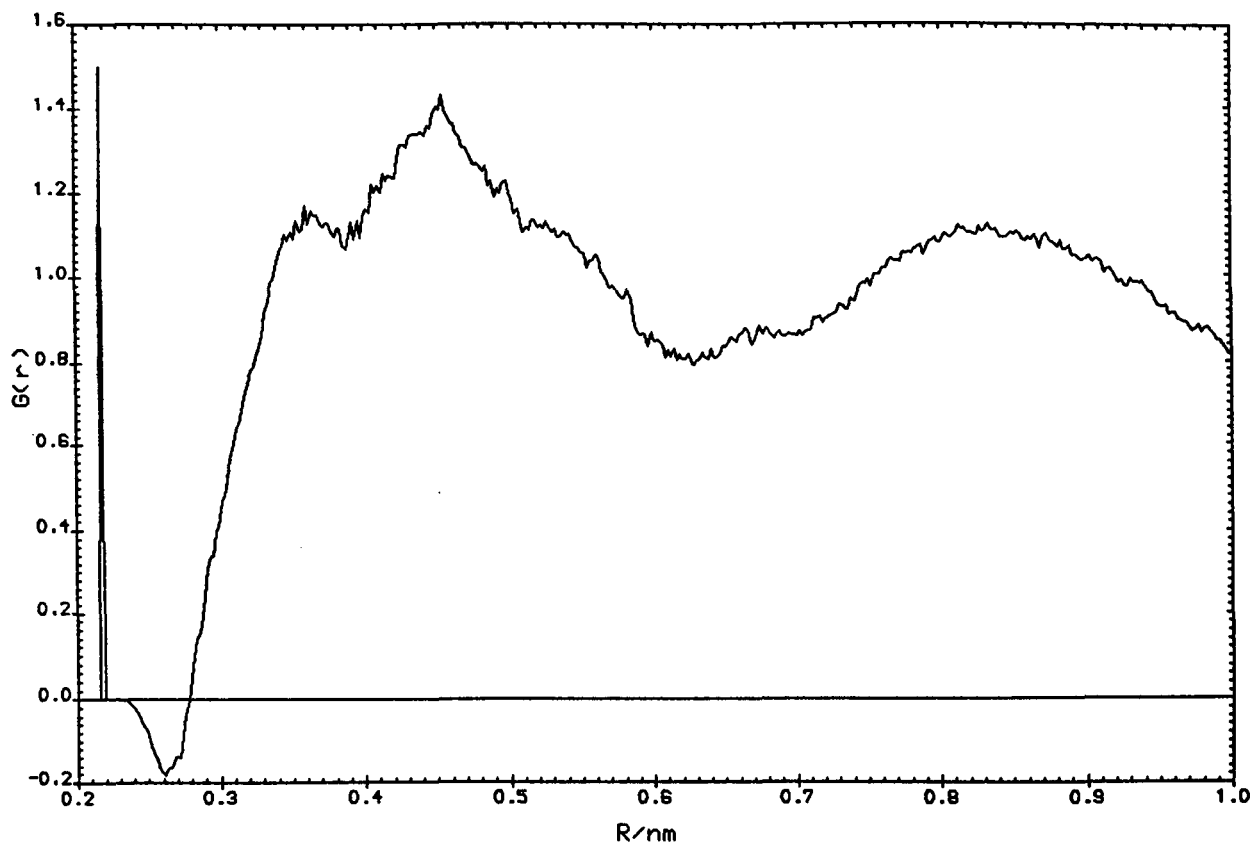


Figure 3.10 The neutron-weighted test-pdf from the 108 molecule MD simulation of CHF_3 including fractional charges

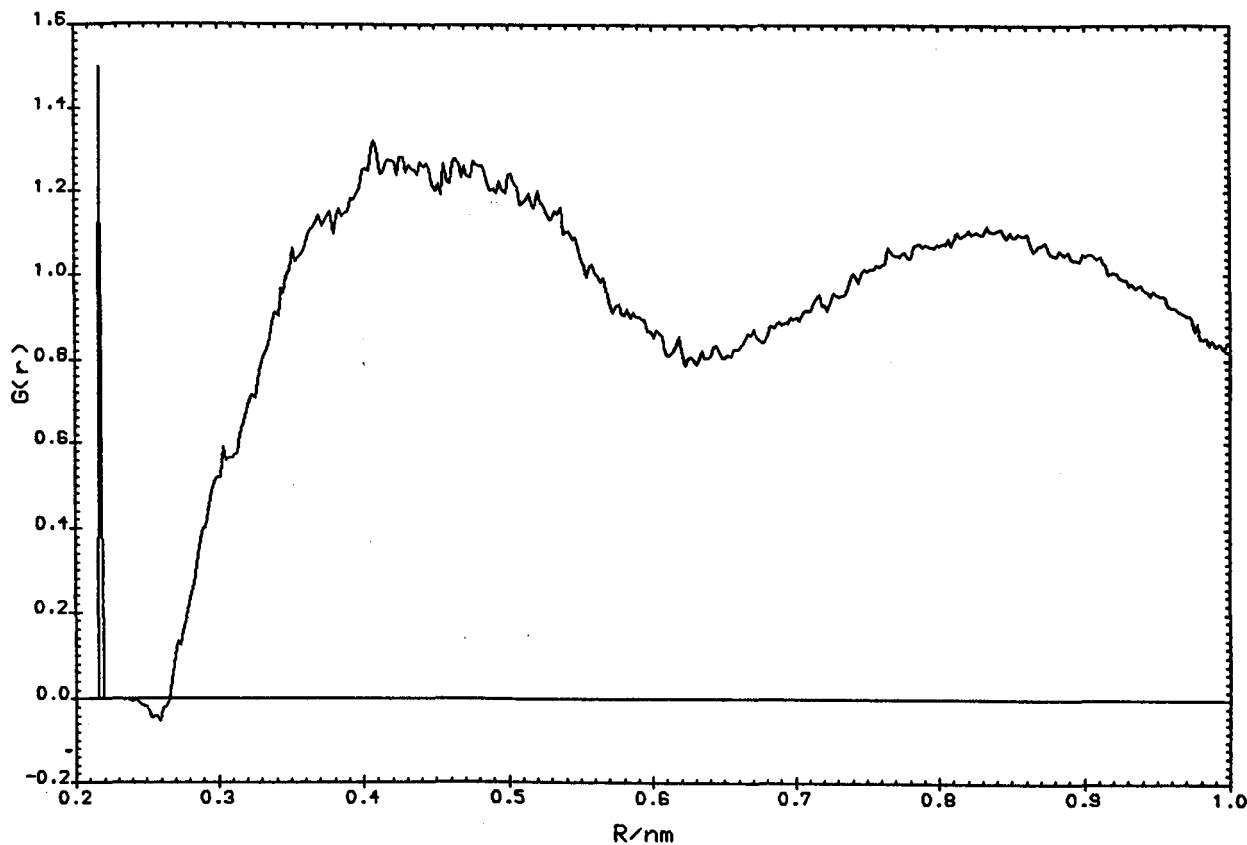


Figure 3.11 The neutron-weighted test-pdf from the 108 molecule MD simulation of CHF_3 without fractional charges

Parameter	This study
Temperature/ K	153
ϵ_C / K	51.2
ϵ_F / K	52.8
ϵ_H / K	8.6
σ_C / nm	0.335
σ_F / nm	0.283
σ_H / nm	0.281
q_C	0.60
q_F	-0.23
q_H	0.1
N	108
δt /fs	2

Table 3.8 Input parameters for the MD simulation of CHF_3

Atom	x	y	z
C	0.0000	0.0000	0.0000
H	0.0000	0.0000	0.1110
F	-0.0630	0.1092	-0.0390
F	-0.0630	-0.1092	-0.0390
F	0.1261	0.0000	-0.0390

Table 3.9 The bond distances of CHF_3 in x, y, z format

Several other test runs were performed with slight changes being made to the LJ parameters until the energy and the neutron-weighted pdf matched the respective experiment. A few examples of the changes that were made

to the LJ parameters, and a comparison of the $\langle E \rangle$ associated with them, are shown in table 3.10.

Run	T/K	ϵ_C	ϵ_H	ϵ_F	σ_C	σ_H	σ_F	$\langle E \rangle$
i	152.8	45	15	44	0.355	0.281	0.295	-17.84
ii	144.6	45	15	38	0.355	0.281	0.295	-16.46
iii	149.3	45	10	35	0.355	0.281	0.295	-14.64
iv	152.9	45	10	34	0.355	0.281	0.295	-14.16
v	154.2	45	10	30	0.355	0.281	0.295	-13.08

Table 3.10 A comparison of $\langle E \rangle$ for some of the test simulations of CHF_3

3.4.3.2 The Final Simulation

The simulation finally chosen for a 5000 time-step run had the parameters shown for run (v) in table 3.10. The results from that simulation, and a complete comparison with the experimental values taken from reference [23] are shown in table 3.11.

3.4.3.3 The Total and Neutron-Weighted Pair Distribution Functions

The total unweighted pdf was plotted using RDFPLOT. The intramolecular region was checked to see that the x, y, z co-ordinates were input correctly and the intramolecular peaks were integrated. The integral ratios for C-F, C-H, H-F, and F-F were 3, 1, 3, 3 as expected.

Quantity	Simulation (v)
$\langle U \rangle / \text{kJ mol}^{-1}$	-17.26 ± 0.15
$\langle E \rangle / \text{kJ mol}^{-1}$	-13.5196 ± 0.0010
TKE/ kJ mol^{-1}	147.63 ± 10.64
RKE/ kJ mol^{-1}	152.37 ± 9.93
Temperature/K	150.0 ± 6.0
$\Delta H_v^\ddagger / \text{kJ mol}^{-1}$	18.84 ± 0.33
$\langle U \rangle^\dagger / \text{kJ mol}^{-1}$	-17.59 ± 0.38
$\langle E \rangle^\square / \text{kJ mol}^{-1}$	-13.85 ± 0.57

Table 3.11 The results in full, from simulation (v) of CHF_3

‡ Enthalpy of vaporisation data are available to 153 K [23]. Extrapolation to 150 K does not introduce any significant error. The main uncertainty in ΔH_v is due to the uncertainty in the temperature.

† Calculated using equation (3.16)

□ Calculated using equation (3.17)

Six different atom-atom intermolecular interactions make up the total pdf for HFC-23; $\text{C}\cdots\text{C}$, $\text{C}\cdots\text{H}$, $\text{C}\cdots\text{F}$, $\text{H}\cdots\text{H}$, $\text{H}\cdots\text{F}$, and $\text{F}\cdots\text{F}$. The neutron-weighted intermolecular structure factor for fluoroform can be expressed as

$$D_m(Q) = (C_{CC}b_C^2a_{CC}(Q) + C_{CH}b_Cb_Ha_{CH}(Q) + C_{CF}b_Cb_Fa_{CF}(Q) + C_{HH}b_H^2a_{HH}(Q) + C_{HF}b_Hb_Fa_{HF}(Q) + C_{FF}b_F^2a_{FF}(Q)) / (\sum b_i)^2, \quad (3.30)$$

where $\sum b_i = (b_C + b_H + 3b_F)$

The values of C_{XY} are shown in table 3.12.


























Atom	C	H	F	F	F
C					
H					
F					
F					
F					

Table 3.12 The C_{XY} values for CHF_3

For CFC-23, the C_{XX} values for C-C, C-H, C-F, H-H, H-F, and F-F are 1, 2, 6, 1, 6, and 9 respectively.

If we use the b_X values from Skold [26] (which for C, H, and F are 6.646, -3.739, and 5.654 femtometres respectively), the neutron weighted pdf

$$g(R) = 0.1119g_{CC}(R) - 0.1259g_{CH}(R) + 0.5711g_{CF}(R) + 0.0354g_{HH}(R) - 0.3213g_{HF}(R) + 0.7288g_{FF}(R), \quad (3.31)$$

The neutron-weighted 108 molecule spectrum shown in figure 3.12 oscillates about unity at high R indicating that equation (3.31) is correct.

The neutron-weighted MD simulation for the 108 charged-molecule simulation is compared with the neutron-diffraction results in figure 3.13. There is quite a good match, with the general features of the experimental pdf being reflected in the MD simulation. Since the experimental and simulated energies are also well matched, further refinement of the LJ parameters was considered unnecessary.

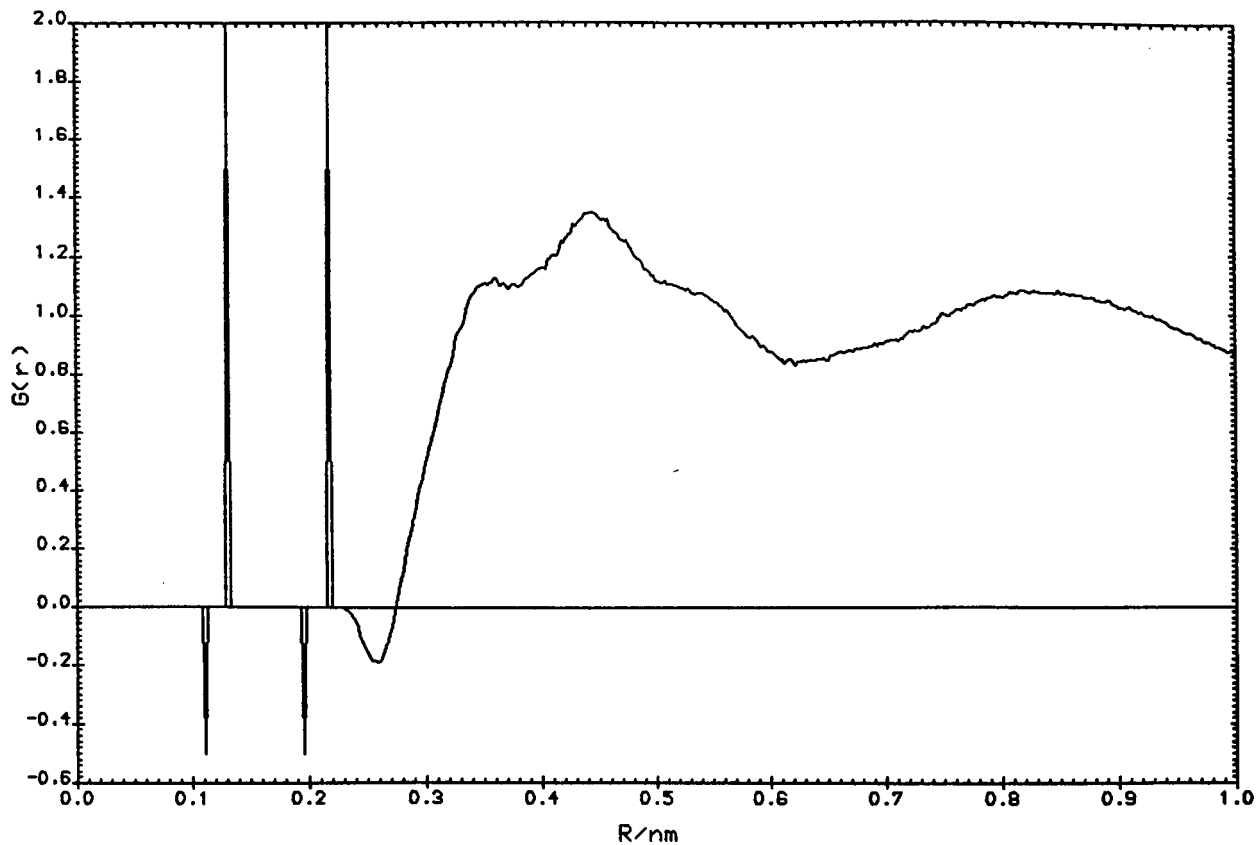


Figure 3.12 The neutron-weighted pdf given by the 108 molecule MD simulation of CHF_3 including fractional charges

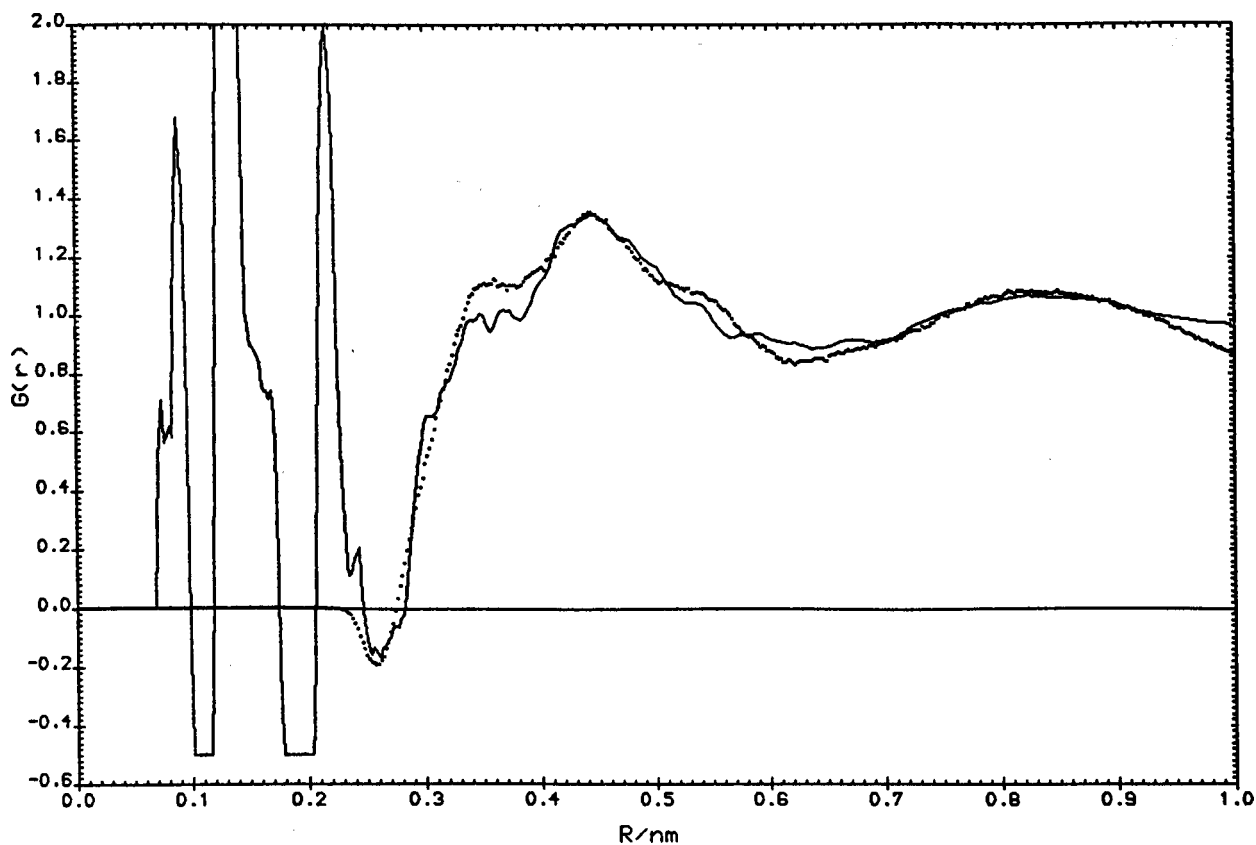


Figure 3.13 A comparison of the CHF_3 pdfs given by MD simulation (---) and neutron diffraction (—)

3.4.3.4 The Individual Pair Distribution Functions and their Integration

The LJ model appeared to give a reasonable representation of the pdf of liquid CHF₃ and the MD data was consequently broken down into individual pdfs so that the structure of CHF₃ could be studied in some detail. The individual pdfs given for the simulation are shown in figures 3.14 (a-f).

The first peaks in the individual pdfs were integrated using the method outlined in Section 3.3.10.6 and the results are shown in table 3.13.

Pair (XY)	C _{XY}	NY	Peak Maximum/nm	Integral Range/nm	Number of Neighbours
C...C	1	1	0.45	0.2 - 0.59	12.0 ± 1.0
C...H H...C	2	1	0.39	0.2 - 0.45	4.1 ± 0.8
C...F F...C	6	3 1	0.36	0.2 - 0.47	12.8 ± 0.8 4.3 ± 0.8
H...H	1	1	0.45	0.2 - 0.59	11.4 ± 0.3
H...F F...H	6	3 1	0.28	0.22 - 0.37	4.8 ± 0.7 1.6 ± 0.5
F...F	9	3	0.31	0.22 - 0.39	6.5 ± 0.6

Table 3.13 The number of nearest neighbours for CHF₃

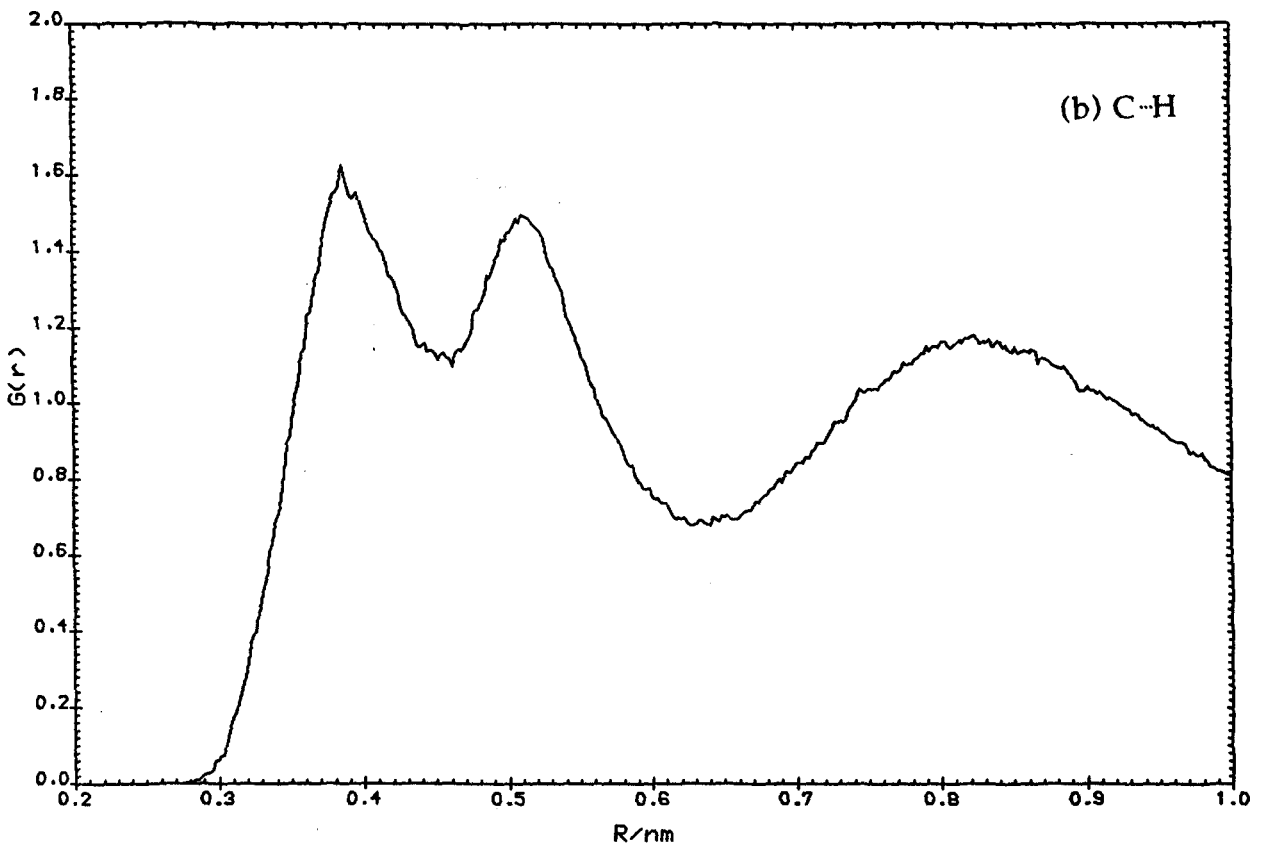
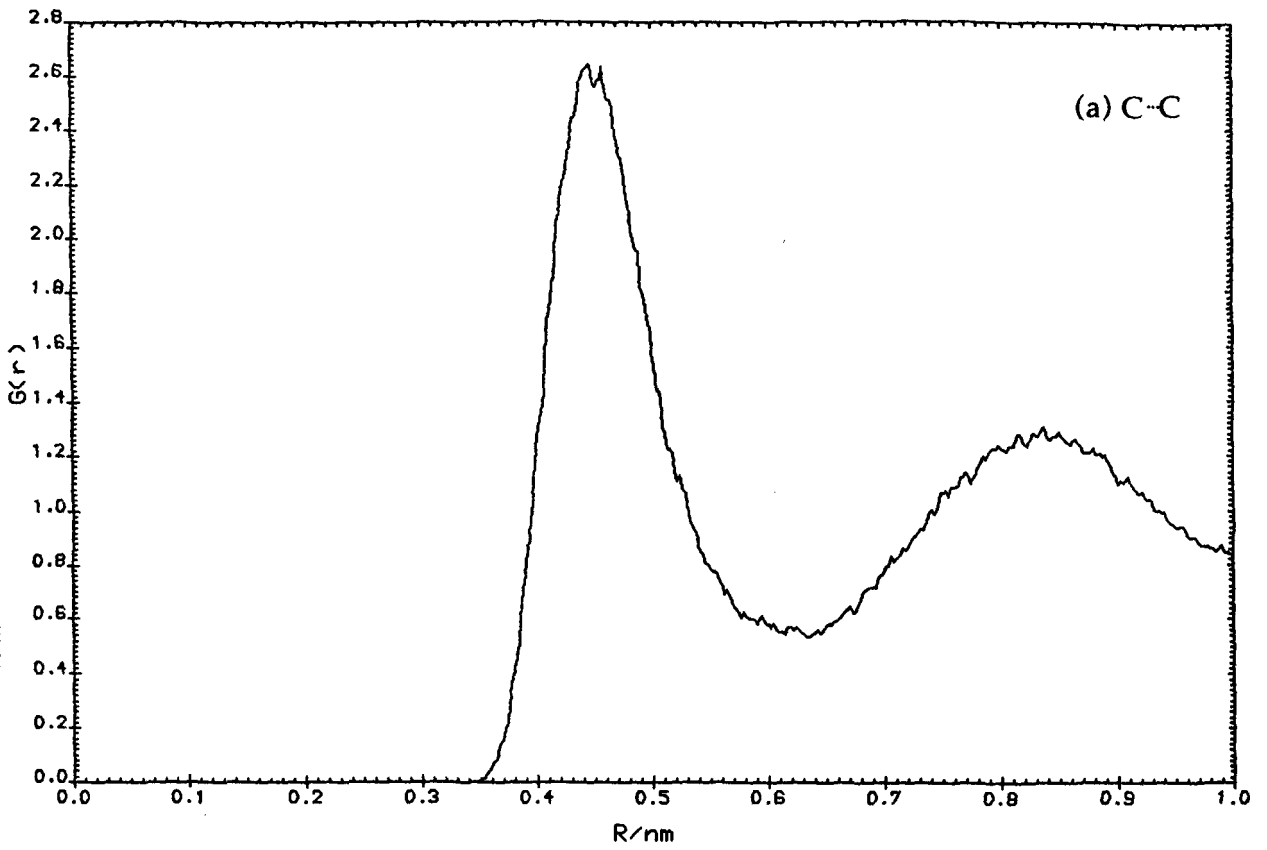


Figure 3.14 The individual pdfs from the MD simulation of CHF_3

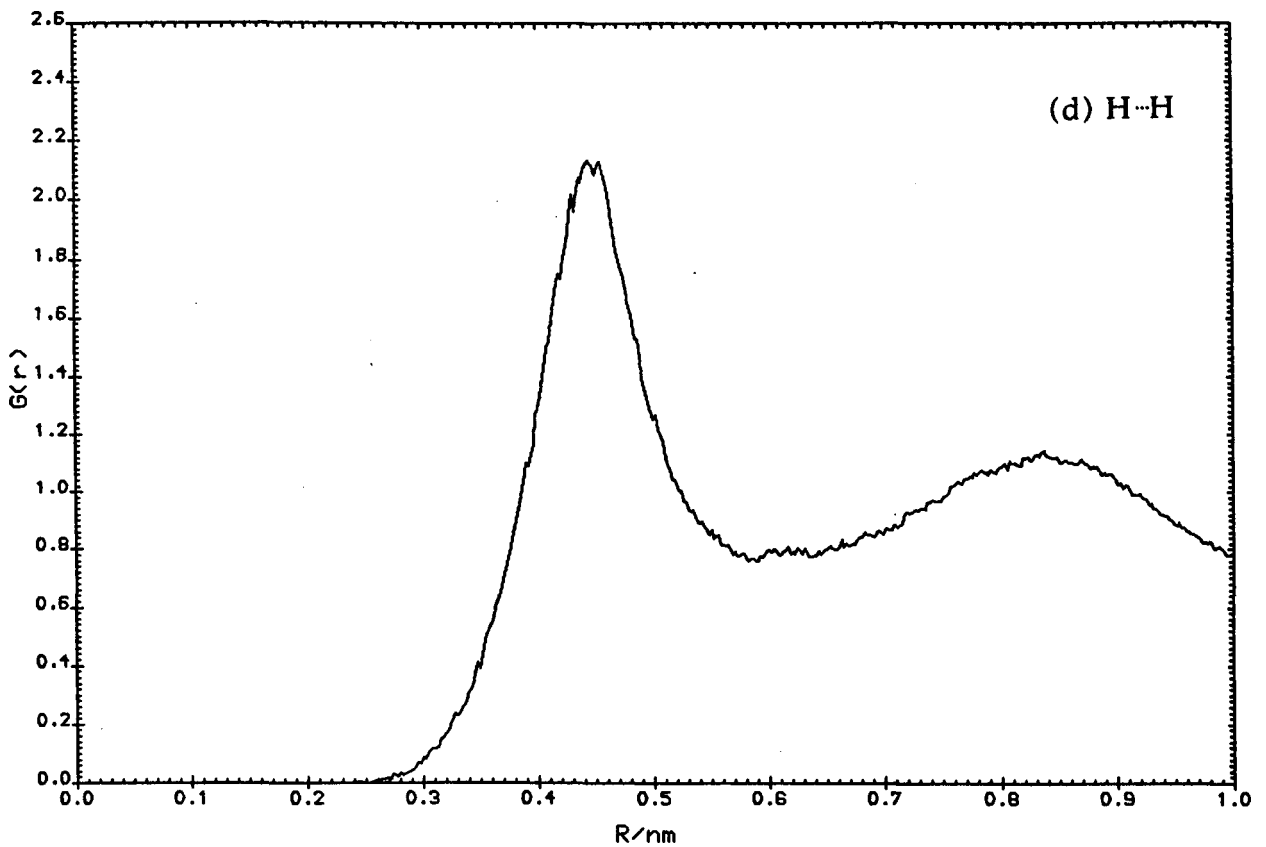
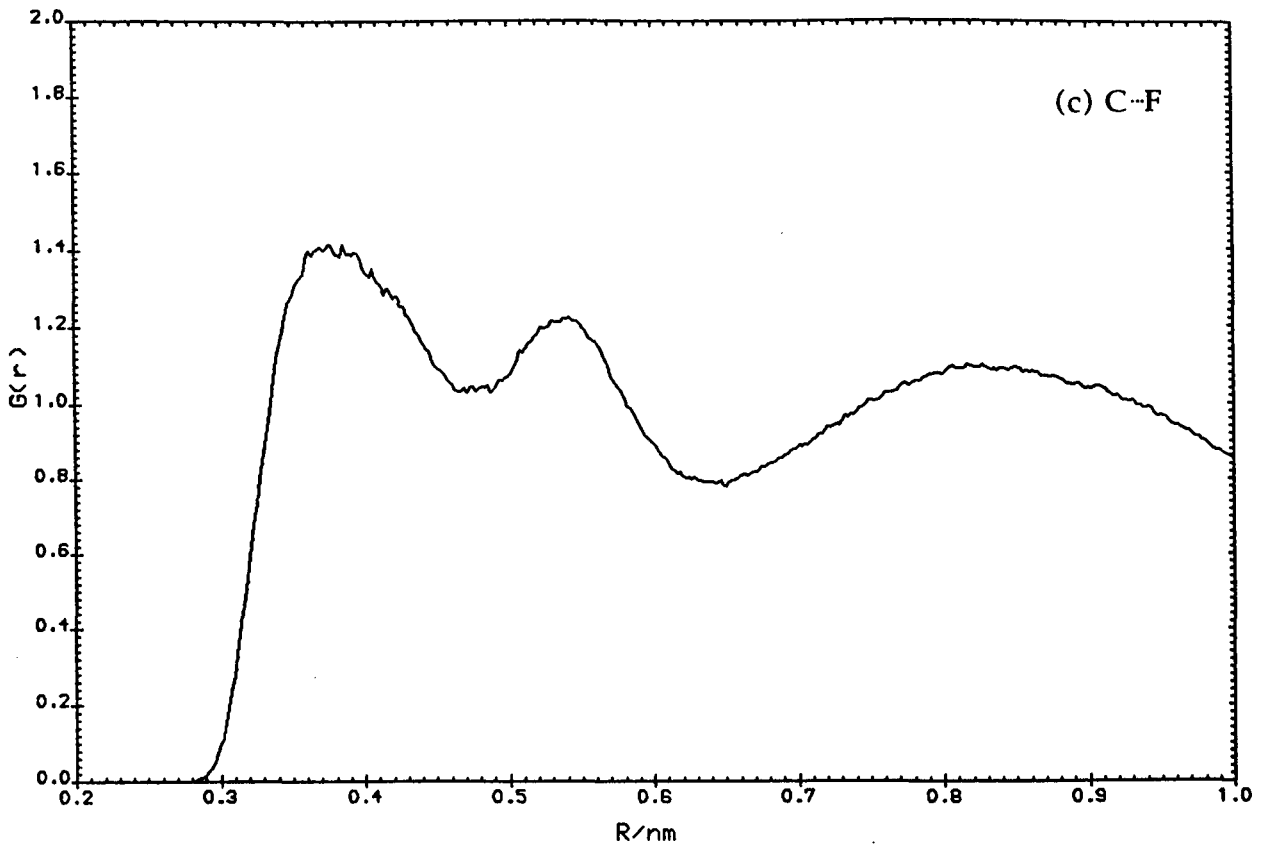


Figure 3.14 The individual pdfs from the MD simulation of CHF_3

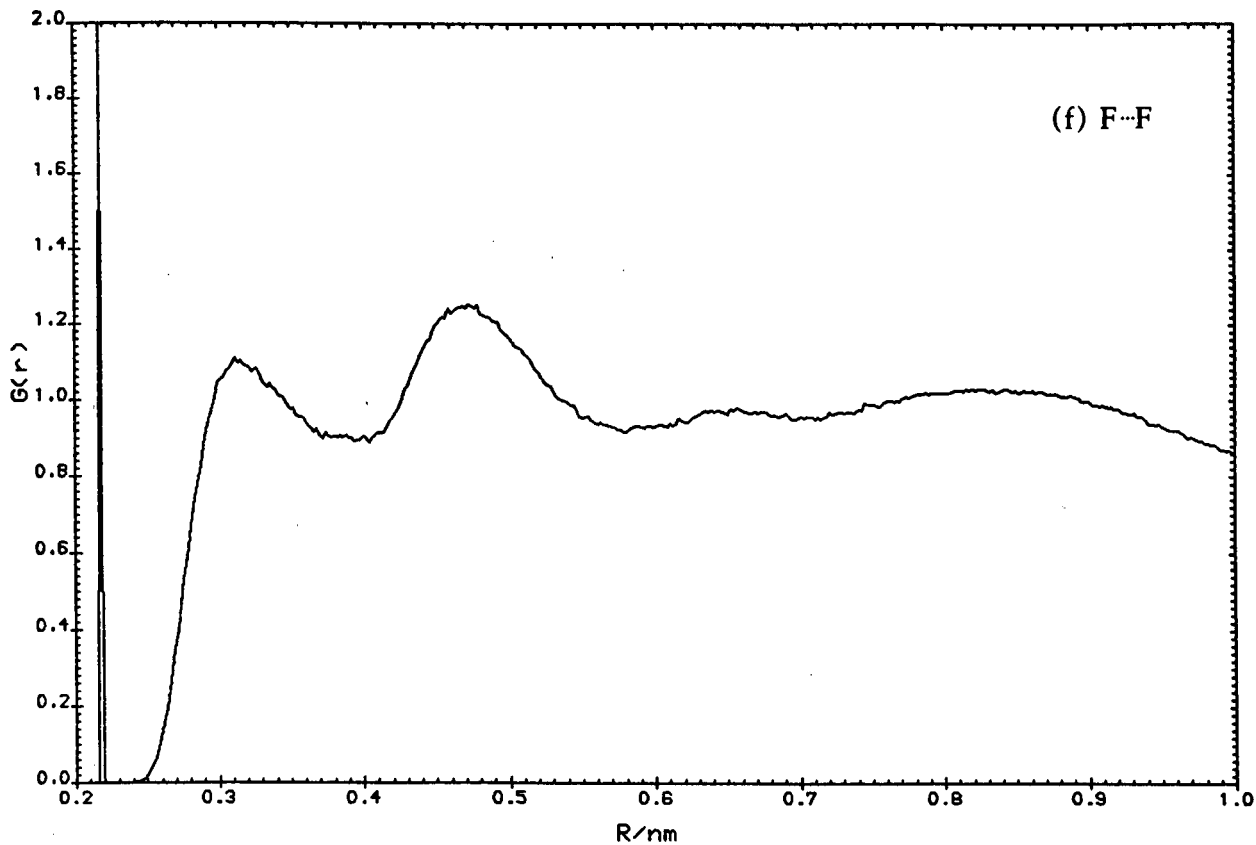
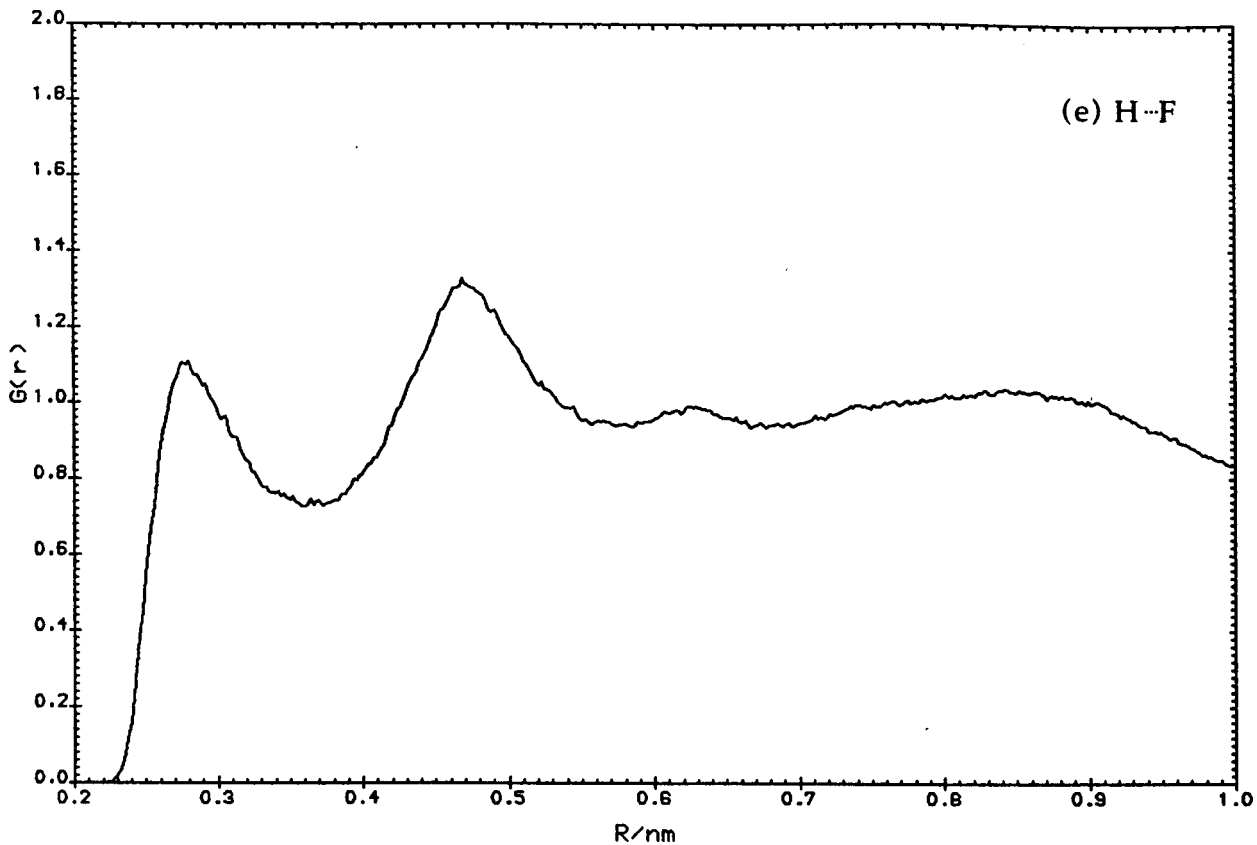


Figure 3.14 The individual pdfs from the MD simulation of CHF_3

3.4.3.5 The Discussion of the Structure

In discussing the structure of fluoroform there are some important points to note that arise from the individual pdfs and their integrals.

(i) The short range negative peak appearing at roughly 2.5 Å in the experimental neutron diffraction pdf is also found in the MD pdf and has as its origin a short range H-F interaction.

(ii) The appearance of our pdfs follow those given in a previous study by H. J. Bohm *et al.* [12]. They used the test-particle model to generate pdfs for CHF₃, but made no inferences on the orientation of the molecules from their results.

(iii) The H-H pdf and C-C pdf are very similar; their first peaks coincide at a distance of 0.45 nm and their integrals are similar. This would suggest that a rocket conformation is important (see figure 3.15). The second peak in the individual F-F spectrum has a maximum of 0.47 nm which would appear to bear out the conclusion that the rocket is important. The integrals of C-H and C-F which are in a ratio of roughly 1:3 also indicates the presence in the structure of a significant rocket population. A rocket conformation, however, should give a significant peak at 0.34 nm in the C-H spectrum. The probability of the C-H atoms being at this distance is less than that for an ideal gas. The peak maximum is at 0.38 nm suggests that the rocket conformation is skewed (by up to 45° - a skewed straddle structure) as shown in figure 3.16.

(iv) The first peak in the F-F pdf at 0.31 nm and in the C-F pdf at 0.38 nm indicate the presence of this skewed straddle structure. Other evidence lies in the second peak maxima of the H-F and F-F pdfs which coincide at roughly 0.47 nm.

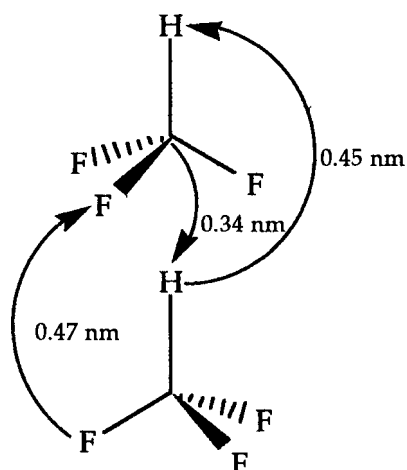


Figure 3.15 The Rocket conformation of CHF₃ molecules

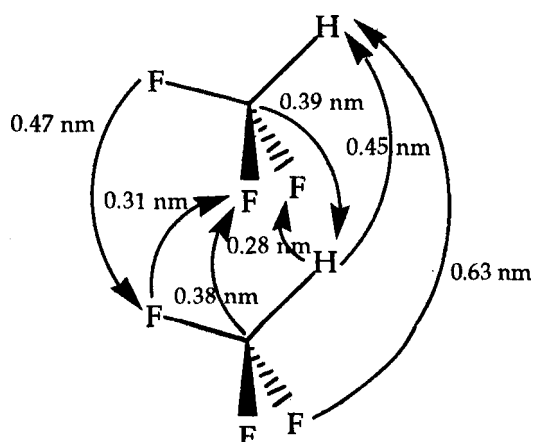


Figure 3.16 The skewed straddle/rocket conformation of CHF₃ molecules

(v) There is minimal probability of two H atoms coming close to one another. The high integral for H...H is due to the wide integral range of the first peak. The charge distribution on the molecule is probably the important factor considering that the fractional charges were important in this simulation.

In the structure of liquid CHF₃, we conclude that the important orientation of the molecules is the skewed straddle/rocket shown in figure 3.16.

3.4.4 Chlorodifluoromethane and Deuterated-Chlorodifluoromethane

Mountain and Morrison [17] performed the MD simulation of chlorodifluoromethane (CHClF_2 , HCFC-22) at the same time as their simulation of CFC-12. We used their LJ parameters as the starting point in this simulation and assumed that CHClF_2 and CDClF_2 would have the same LJ parameters. CHClF_2 had also been previously simulated, using the test-particle method, by Sagarik and Ahlrichs [13].

3.4.4.1 Input Parameters

The Mountain and Morrison parameters (using the charges of Cooper et al. [21]) and those finally used by us are listed in table 3.14.

The individual molecules of CHClF_2 had the geometry derived in our neutron diffraction experiment. The bond distances are shown in their x, y, z format in table 3.15.

The $\langle E \rangle$ that we obtained using the Mountain and Morrison parameters was about 65% too high and on removing the charges about 10% too low. We were unable to repeat the results of Mountain and Morrison using the Cooper charges ($q_{\text{C}} 0.52$, $q_{\text{H}} 0.18$, $q_{\text{F}} -0.30$, $q_{\text{Cl}} -0.10$). The charges that Mountain and Morrison published seemed artificial with a negative charge on the hydrogen atom and we did not attempt to use them.

Parameter	Mountain & Morrison	This study
Temperature/ K	206	153
ϵ_C / K	54.6	54.6
ϵ_F / K	46.2	46.2
$\epsilon_{H/D}$ / K	42.0	42.0
ϵ_{Cl} / K	147.0	147.0
σ_C / nm	0.315	0.315
σ_F / nm	0.298	0.298
$\sigma_{H/D}$ / nm	0.217	0.240
σ_{Cl} / nm	0.336	0.329
q_C	0.4642	0.00
q_F	-0.205	0.00
$q_{H/D}$	-0.013	0.00
q_{Cl}	-0.0412	0.00
N	108	108
δt /fs	2	5

Table 3.14 Input parameters for the MD simulations of CH/DCIF₂

Atom	x	y	z
C	0.0000	0.0000	0.0000
H/D	-0.0330	0.1028	0.0000
F	-0.0451	-0.0625	-0.1085
F	-0.0451	-0.0625	0.1085
Cl	0.1760	0.0000	0.0000

Table 3.15 The bond distances of CH/DCIF₂ in x, y, z format

After some slight modification of the LJ parameters, and using no charges on the atoms, the $\langle E \rangle$ were correctly matched for both CHClF_2 and CDClF_2 . The results from the simulations (5000 time-steps, 2000 equilibration steps) using no charges are shown in table 3.16.

Quantity	CHClF_2	CDClF_2
$\langle U \rangle / \text{kJ mol}^{-1}$	-22.93 ± 0.13	-22.94 ± 0.13
$\langle E \rangle / \text{kJ mol}^{-1}$	-19.0018 ± 0.0014	-19.1149 ± 0.0013
TKE/ kJ mol^{-1}	1.97 ± 0.12	1.89 ± 0.12
RKE/ kJ mol^{-1}	1.96 ± 0.13	1.93 ± 0.12
Temperature/K	157.4 ± 5.1	153.2 ± 5.36
$\Delta H_v^\ddagger / \text{kJ mol}^{-1}$	22.52 ± 0.30	25.06 ± 0.42
$\langle U \rangle^\dagger / \text{kJ mol}^{-1}$	-23.21 ± 0.35	-23.79 ± 0.37
$\langle E \rangle^\square / \text{kJ mol}^{-1}$	-19.29 ± 0.37	-18.70 ± 0.44

Table 3.16 The results from the MD simulations of CHClF_2 and CDClF_2

‡ Enthalpy of vaporisation data are available to 183 K [23]. Extrapolation to 153 K does not introduce any significant error. The main uncertainty in ΔH_v is due to the uncertainty in the temperature.

† Calculated using equation (3.16)

□ Calculated using equation (3.17)

3.4.4.2 The Total and Neutron-Weighted Pair Distribution Functions

The total unweighted pdfs were plotted using RDFPLOT. The intramolecular region was checked to see that the x, y, z co-ordinates were input correctly and the intramolecular peaks were integrated. The integral ratios for C-H/D, C-F, C-Cl, H/D-F, H/D-Cl, F-F, and F-Cl were 1, 2, 1, 2, 1, 1, 2 as expected.

Ten different atom-atom intermolecular interactions make up the total pdf for CHClF_2 and CDClF_2 ; C-C, C-H/D, C-F, C-Cl, H/D-H/D, H/D-F, H/D-Cl, F-F, F-Cl, and Cl-Cl. The neutron-weighted intermolecular structure factor for the two fluids can be expressed as

$$D_m(Q) = (C_{CC}b_C^2a_{CC}(Q) + C_{CX}b_Cb_Xa_{CX}(Q) + C_{CF}b_Cb_Fa_{CF}(Q) + C_{CCl}b_Cb_{Cl}a_{CCl}(Q) + C_{XX}b_X^2a_{XX}(Q) + C_{XF}b_Xb_Fa_{XF}(Q) + C_{XCl}b_Xb_{Cl}a_{XCl}(Q) + C_{FF}b_F^2a_{FF}(Q) + C_{FCl}b_Fb_{Cl}a_{FCl}(Q) + C_{ClCl}b_{Cl}^2a_{ClCl}(Q))/(\sum b_i)^2, \quad (3.32)$$

where $\sum b_i = (b_C + b_X + 2b_F + b_{Cl})$, and X = H or D.

The values of C_{XY} are shown below in table 3.17.

Atom	C	H/D	F	F	Cl
C					
H/D					
F					
F					
Cl					

Table 3.17 The C_{XY} values for CHClF_2 and CDClF_2

For CHClF_2 and CDClF_2 , the C_{XX} values of C-C, C-H/D, C-F, C-Cl, H/D-H/D, H/D-F, H/D-Cl, F-F, F-Cl, and Cl-Cl are 1, 2, 4, 2, 1, 4, 2, 4, 4, and 1.

If we use the b_X values from Skold [26] (C 6.646, F 5.654, Cl 9.577, D 6.671, H -3.793), the neutron weighted pdf for CHClF_2 is given by

$$g(R) = 0.0780g_{CC}(R) - 0.0878g_{CH}(R) + 0.2655g_{CF}(R) + 0.2249g_{CCl}(R) + 0.0247g_{HH}(R) - 0.1494g_{HF}(R) - 0.1265g_{HCl}(R) + 0.2259g_{FF}(R) + 0.3826g_{FCl}(R) + 0.1620g_{ClCl}(R) \quad (3.33)$$

and for CDClF_2 is given by

$$\begin{aligned} g(R) = & 0.0378g_{\text{CC}}(R) + 0.0758g_{\text{CD}}(R) + 0.1285g_{\text{CF}}(R) + 0.1088g_{\text{CCl}}(R) + \\ & 0.0380g_{\text{DD}}(R) + 0.1290g_{\text{DF}}(R) + 0.1092g_{\text{DCl}}(R) + 0.1093g_{\text{FF}}(R) + \\ & 0.1852g_{\text{FCl}}(R) + 0.0784g_{\text{ClCl}}(R) \end{aligned} \quad (3.34)$$

The neutron-weighted 108 molecule spectra shown in figure 3.17 oscillate about unity at high R which confirms that equations (3.33) and (3.34) are correct.

The neutron-weighted pdfs for both compounds do not match the experimental pdfs (figure 3.18) and this is especially so for CHClF_2 . In the case of CDClF_2 , the MD simulation pdf shows a double peak in the 0.3-0.7 Å region where only a single peak appears in the neutron diffraction pdf, although the general peak heights match. This would indicate that the MD simulation is forcing the CDClF_2 molecules to be 'too structured'. In the case of CHClF_2 , there is no match at all. The reasons for this are not clear as yet because the individual pdfs are similar to those found by Sagarik and Ahlrichs [13] in their test-particle experiment.

3.4.4.3 Discussion of the Structure

Although the energy of the simulations were close to those expected, the neutron-weighted and neutron-diffraction pdfs did not match. It is not worth attempting to derive the structure of CHClF_2 or CDClF_2 until a better match between spectra can be achieved. This may involve introducing potentials that can incorporate multipoles on the atoms. More sophisticated MD packages are now being studied at Liverpool.

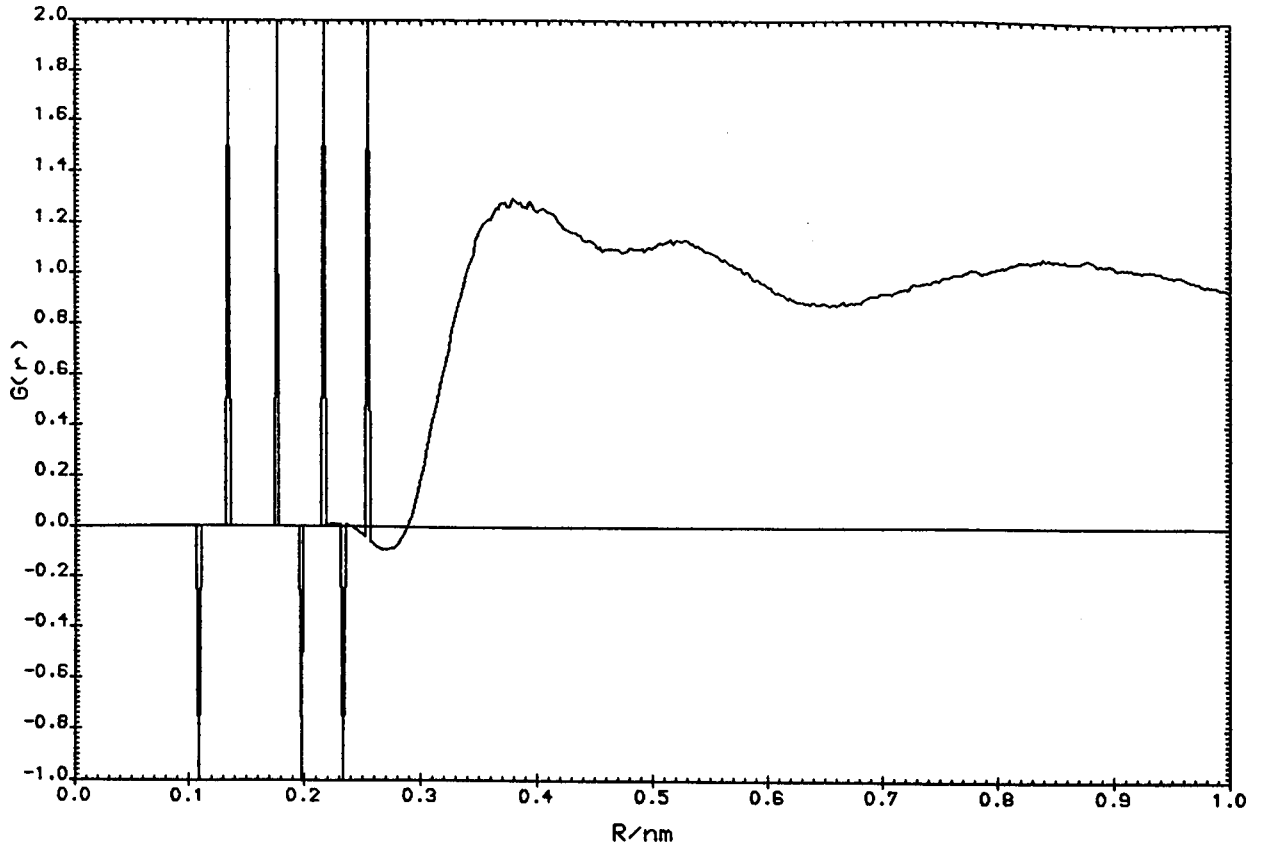


Figure 3.17 (a) The neutron-weighted pdf given by the 108 molecule MD simulation of CHClF_2

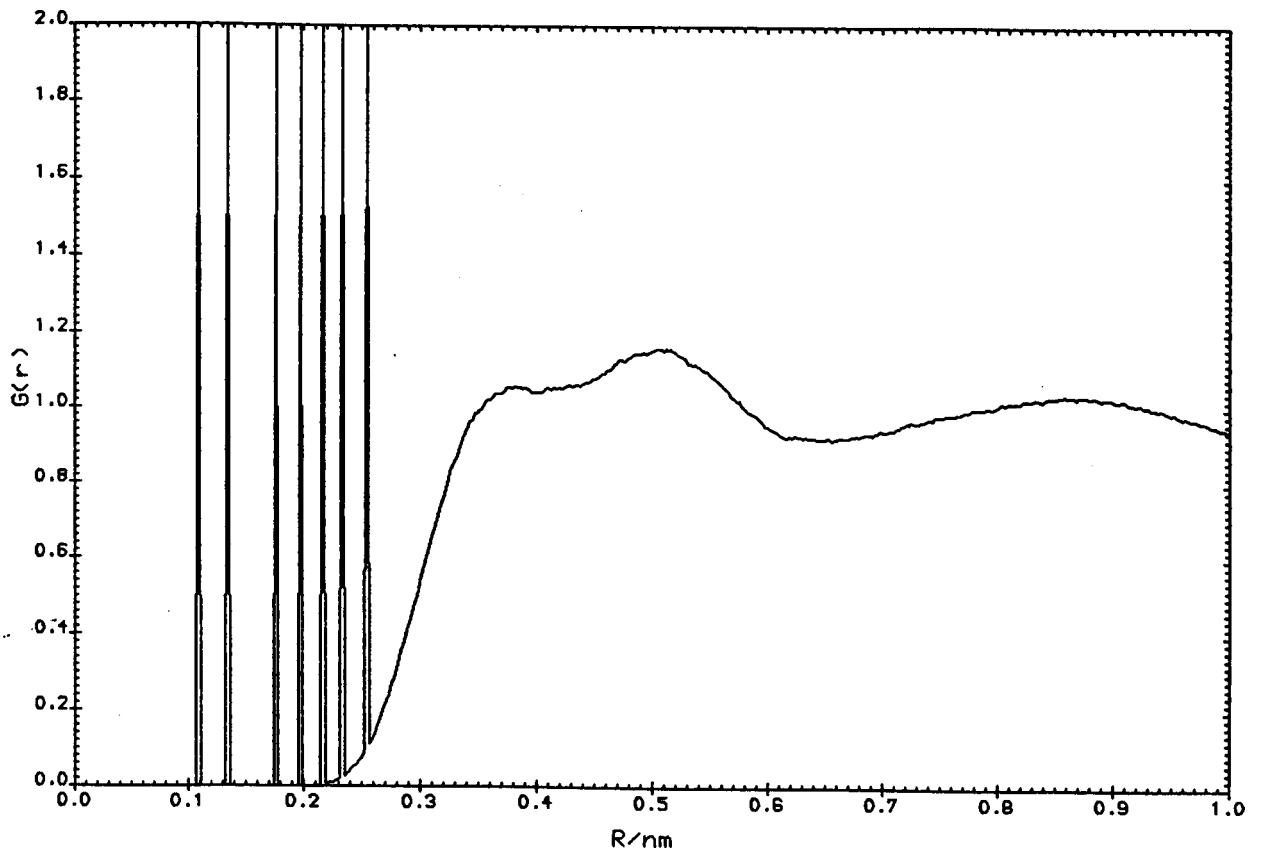


Figure 3.17 (b) The neutron-weighted pdf given by the 108 molecule MD simulation of CDCIF_2

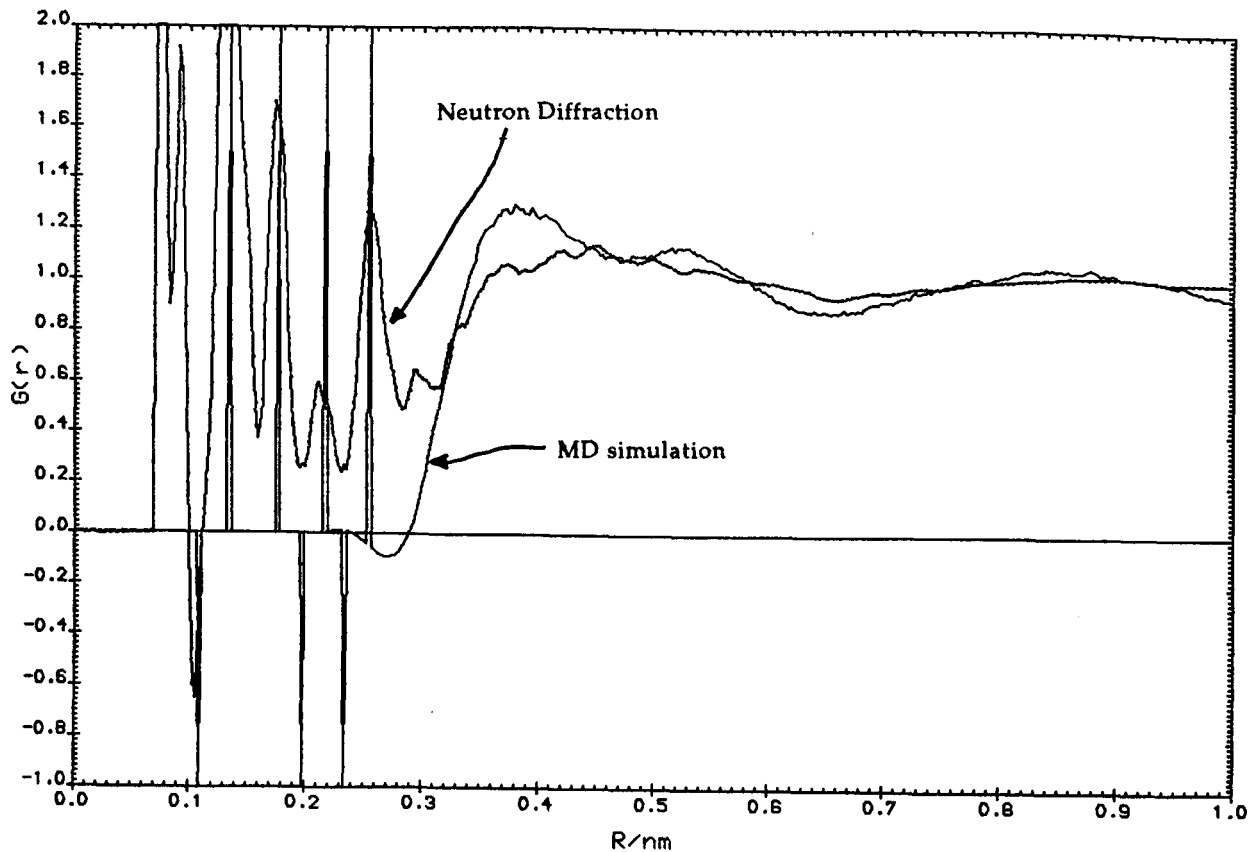


Figure 3.18 (a) A comparison of the CHClF_2 pdfs given by MD simulation and neutron diffraction

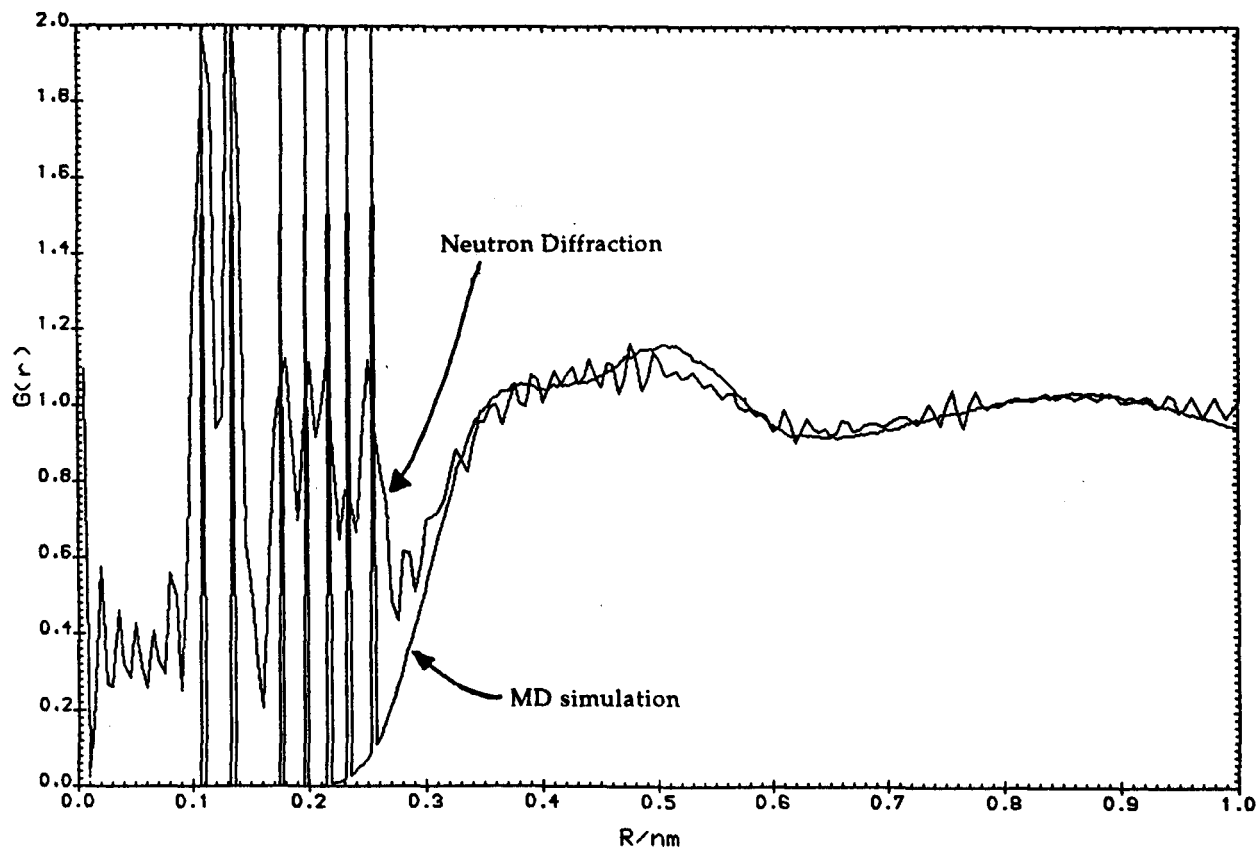


Figure 3.18 (b) A comparison of the CDClF_2 pdfs given by MD simulation and neutron diffraction

3.4.5 The Other Simulations

The other molecules that were simulated using MD were chlorotrifluoromethane (CFC-13, CClF_3) and bromotrifluoromethane (BCFC-13B1, CBrF_3). No previous MD simulations had been performed on these fluids and the LJ parameters were adjusted from their starting values.

3.4.5.1 Input Parameters

After a number of simulations the input parameters listed in table 3.18 gave the best comparison with previous thermodynamics experiments [23].

Parameter	CClF_3	CBrF_3
Temperature/ K	153	153
ϵ_C / K	45	45
ϵ_F / K	114	155
$\epsilon_{\text{Cl/Br}}$ / K	35	35
σ_C / nm	0.320	0.315
σ_F / nm	0.290	0.320
$\sigma_{\text{Cl/Br}}$ / nm	0.350	0.354
q_C	0.00	0.00
q_F	0.00	0.00
$q_{\text{Cl/Br}}$	0.00	0.00
N	108	108
δt / fs	5	5

Table 3.18 Input parameters for the MD simulations of CClF_3 and CBrF_3

The x, y, z parameters are shown in tables 3.19 and 3.20.

Atom	x	y	z
C	0.0000	0.0000	0.0000
F	0.1264	0.0000	-0.0448
F	-0.0632	0.1092	-0.0448
F	-0.0632	-0.1092	-0.0448
Cl	0.0000	0.0000	0.1773

Table 3.19 The bond distances of CClF_3 in x, y, z format

Atom	x	y	z
C	0.0000	0.0000	0.0000
F	0.1238	0.0000	-0.0458
F	-0.0619	0.1072	-0.0458
F	-0.0619	-0.1072	-0.0458
Br	0.0000	0.0000	0.1930

Table 3.20 The bond distances of CBrF_3 in x, y, z format

The simulations were performed over 5000 time-steps with 2000 equilibration steps.

3.4.5.2 Thermodynamic Comparisons

The results of the two simulations are shown in table 3.21.

Quantity	CClF ₃	CBrF ₃
$\langle U \rangle / \text{kJ mol}^{-1}$	-16.34 ± 0.13	-19.88 ± 0.13
$\langle E \rangle / \text{kJ mol}^{-1}$	-12.4333 ± 0.0012	-16.1537 ± 0.0016
TKE/kJ mol ⁻¹	1.98 ± 0.13	1.85 ± 0.12
RKE/kJ mol ⁻¹	1.93 ± 0.12	1.88 ± 0.13
Temperature/K	156.5 ± 5.2	149.6 ± 5.1
$\Delta H_v^\ddagger / \text{kJ mol}^{-1}$	17.19 ± 0.20	20.47 ± 0.21
$\langle U \rangle^\dagger / \text{kJ mol}^{-1}$	-15.88 ± 0.24	-19.22 ± 0.23
$\langle E \rangle^\circ / \text{kJ mol}^{-1}$	-11.98 ± 0.37	-15.49 ± 0.38

Table 3.21 The results from the MD simulations of CClF₃ and CBrF₃

‡ Enthalpy of vaporisation data are available to 153 K for CClF₃ and 173 K for CBrF₃ [23]. Extrapolation to 150 K does not introduce any significant error. The main uncertainty in ΔH_v is due to the uncertainty in the temperature.

† Calculated using equation (3.16)

◻ Calculated using equation (3.17)

3.4.5.3 The Total and Neutron-Weighted Pair Distribution Functions

The total unweighted pdfs were checked as described above.

The neutron-weighted structure factors for CFC-13 and BCFC-13B1 are similar to that for CHF₃. Using the b_x values from Skold [26] (C 6.646, F 5.654, Cl 9.577, Br 6.795), the corresponding neutron-weighted pdf for CClF₃

$$g(R) = 0.0401g_{CC}(R) + 0.2046g_{CF}(R) + 0.1156g_{CCl}(R) + 0.2950g_{FF}(R) + 0.2613g_{ClF}(R) + 0.0832g_{ClCl}(R), \quad (3.35)$$

and for CBrF_3

$$g(R) = 0.0478g_{\text{CC}}(R) + 0.2439g_{\text{CF}}(R) + 0.0977g_{\text{CBr}}(R) + 0.2494g_{\text{FF}}(R) + 0.3113g_{\text{BrF}}(R) + 0.0500g_{\text{BrBr}}(R), \quad (3.36)$$

The simulated spectra are shown in figures 3.19 and 3.20 respectively and a comparison with the neutron-diffraction pdfs in figures 3.21 and 3.22.

The comparison is not very good in either case, although the energies are well matched. Indeed, a similar result to that obtained for CDClF_2 is obtained. That is, the MD simulation suggests that there should be two peaks in all three intermolecular regions up to 0.6 nm but only one peak was observed in the respective diffraction experiment. The MD simulations for CClF_3 , CBrF_3 and CDClF_2 give very similar results even though their LJ parameters are different which indicates that the fluorine atoms may be greatly influencing the simulation results. The similarities in the results from the diffraction experiments is suggestive either of a monatomic gas-type uncorrelated structure for each of the fluids or a problem in the data analysis of the diffraction results.

The results from these three MD experiments shows why it is necessary to have more than one experiment with which to compare the results of simulations.

3.4.5.3 Discussion of the Structure

The structure of CFC-13 and BCFC-13B1 can not be discussed further because the simulated pdf did not match the experimental pdf. Again the problem may be solved by using a different potential equation or one that can incorporate a more rigorous description of the charge distribution in the molecules.

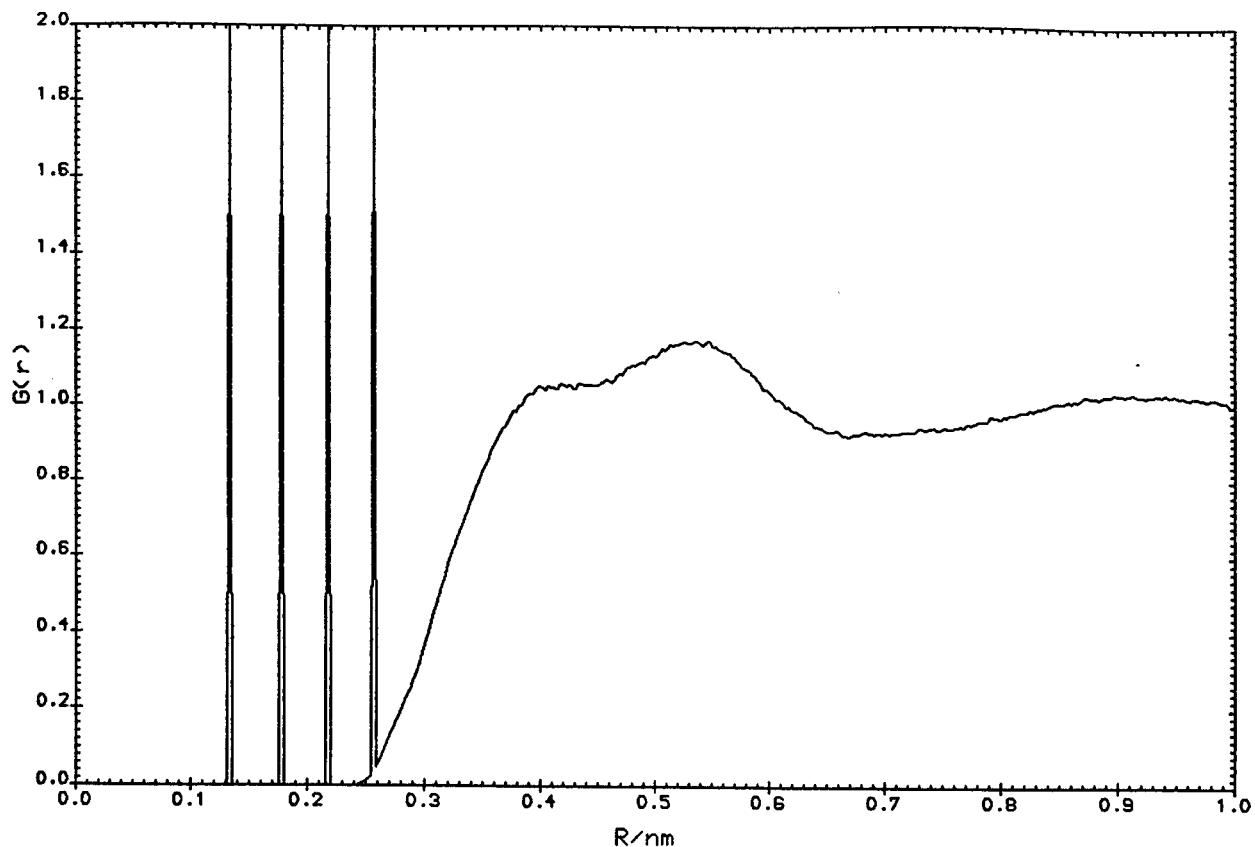


Figure 3.19 The neutron-weighted pdf given by the 108 molecule MD simulation of CClF_3

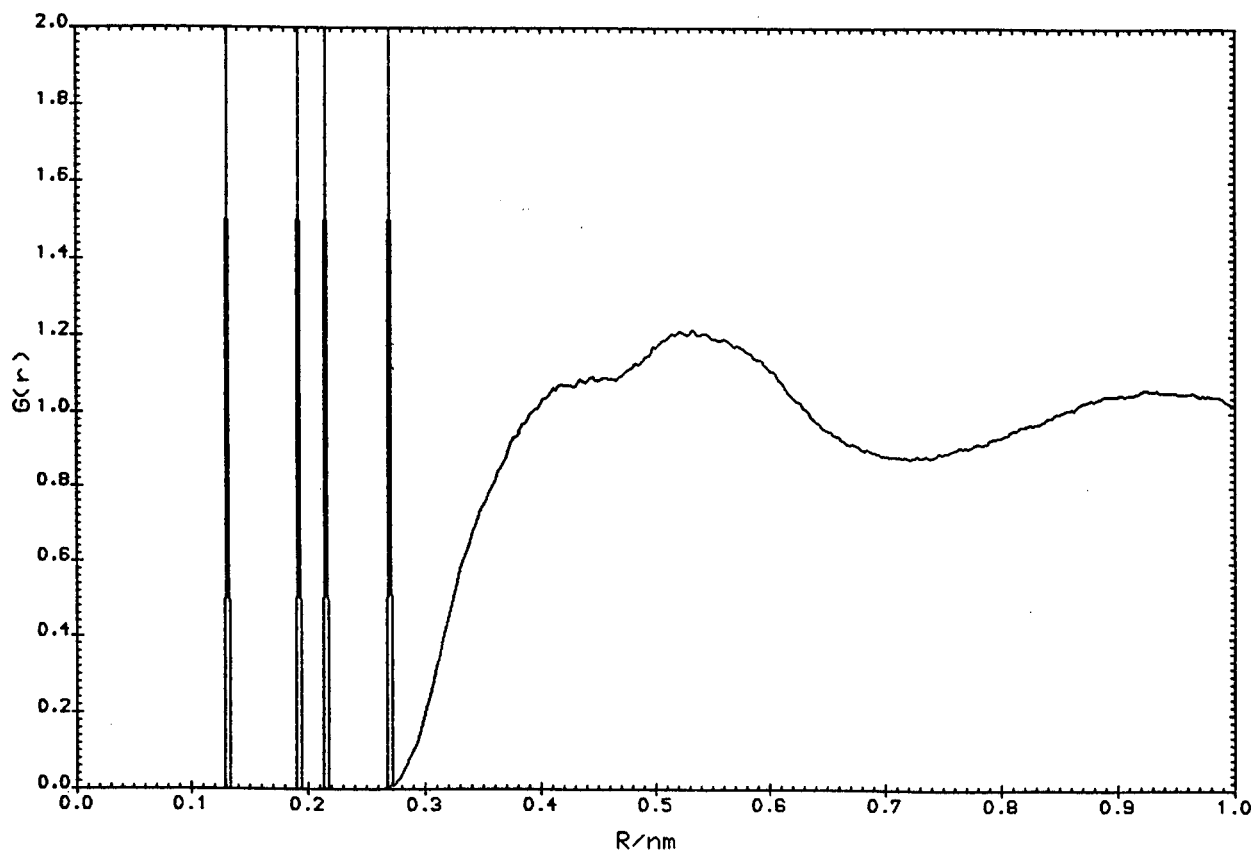


Figure 3.20 The neutron-weighted pdf given by the 108 molecule MD simulation of CBrF_3

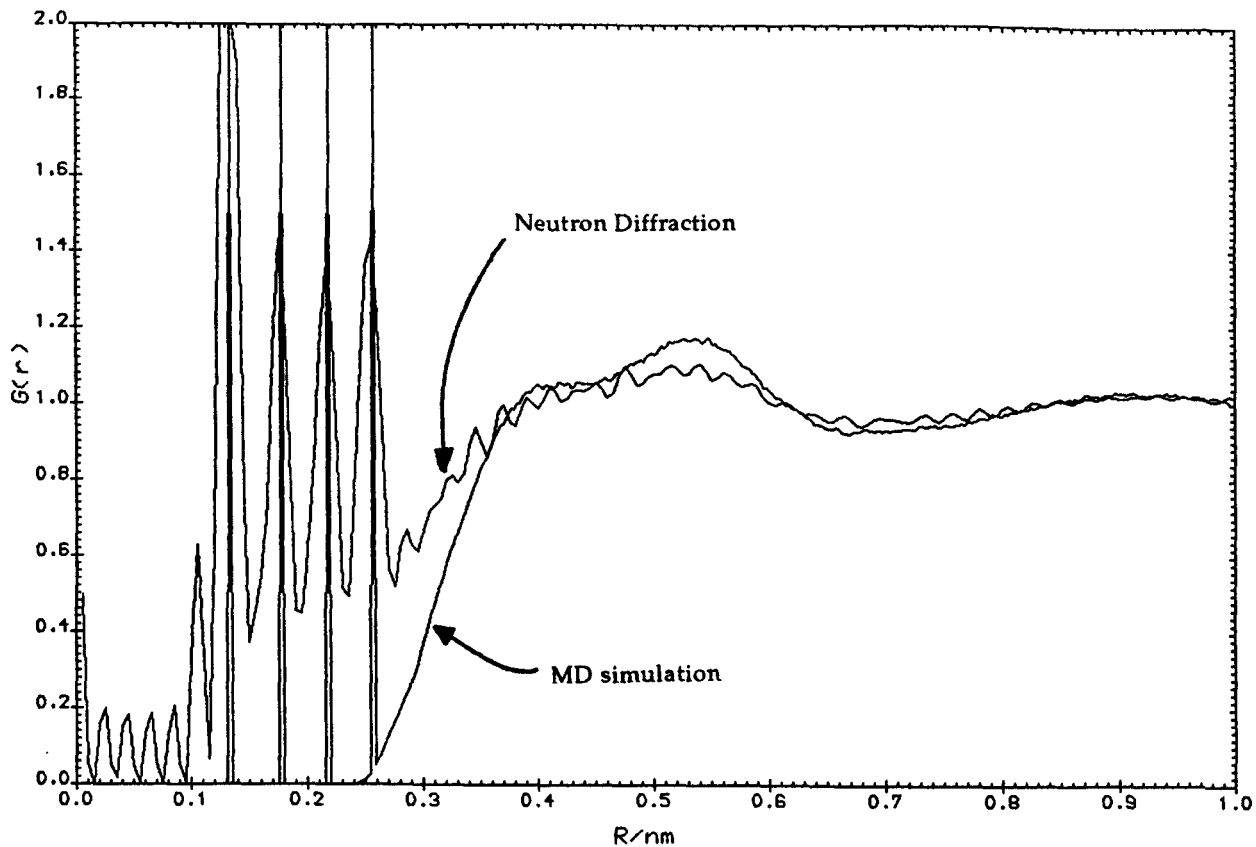


Figure 3.21 A comparison of the CClF_3 pdfs given by MD simulation and neutron diffraction

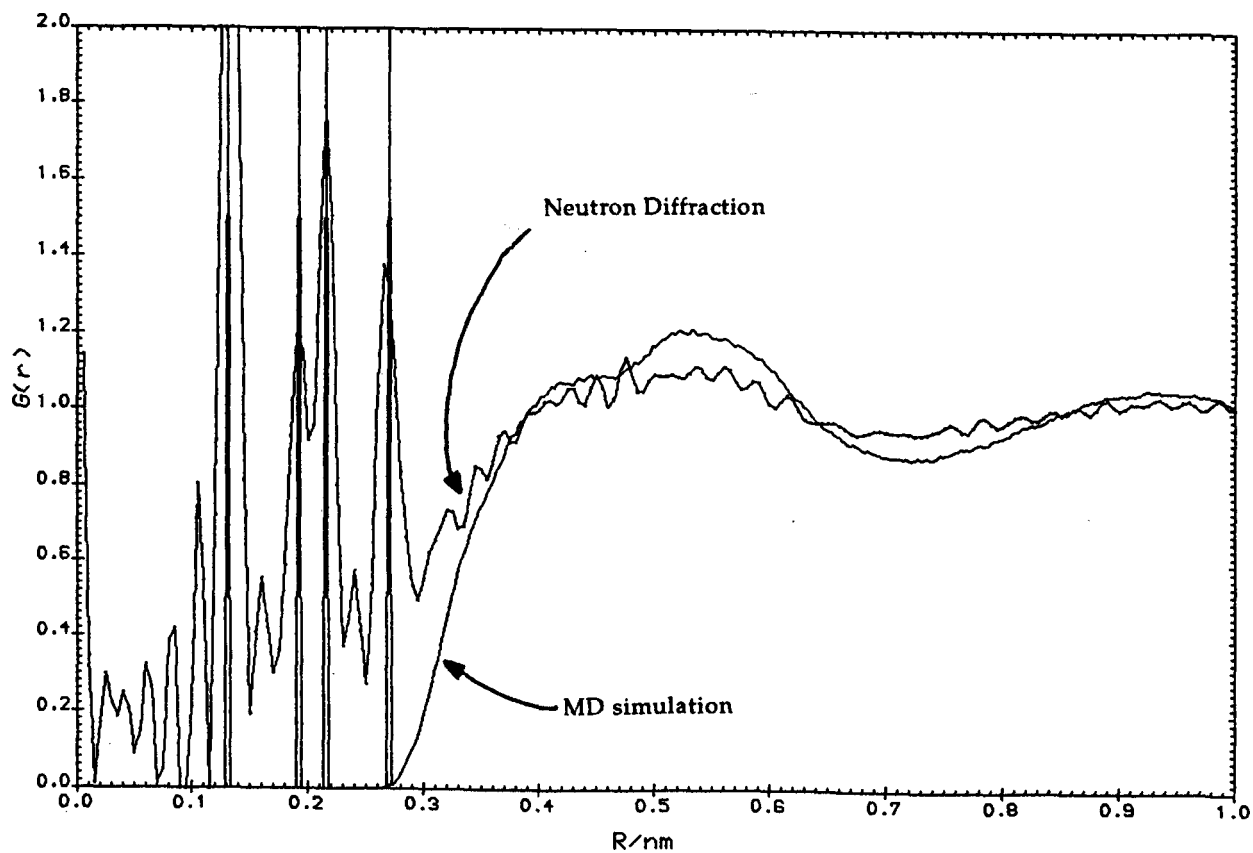


Figure 3.22 A comparison of the CBrF_3 pdfs given by MD simulation and neutron diffraction

3.5 Conclusion

The results from the simulations of dichlorodifluoromethane and fluoroform are very encouraging and show that the LJ potential equation can be a powerful tool in determining the structures of some molecules. Without the benefit of the insight that MD simulation can give, the structure of liquid CCl_2F_2 would be difficult to assess. It would be difficult to show evidence that the structure of liquid CCl_2F_2 mainly depends on just three orientations of the molecules using any other experimental technique. Even the structure of the solid derived by neutron diffraction cannot show how the molecules prefer to align in the liquid. Evidence for the close contact of H-F atoms in fluoroform, and the inference that this is caused by hydrogen bonding, can be investigated by using of neutron diffraction, as shown in Chapter Two. MD simulations, however, are the only way of showing that the negative peak in the neutron diffraction pdf of fluoroform is actually a real artifact, caused by close H-F interactions, and which orientations of molecules contribute to this peak.

The results from the other simulations, although less encouraging have, nevertheless, lead to some important information. In particular the results have shown the need for more than one set of experimental results to compare the simulations with.

Finally, the general conclusions from this study are

- (i) It is important to remember that the LJ potential is only a crude representation of the actual potential and although it may suffice in some cases it may completely fail in others.
- (ii) The larger the experimental data-base there is for a fluid, the more confident one can be that a simulation has given adequate

results. The most accurate comparison there is, however, is with the pdfs given by neutron diffraction.

(iii) Simple potentials can give an insight into the structure of fluids that can be useful in designing more powerful potentials.

REFERENCES

- [1] YARNELL, J. L., KATZ, M. J., WENZEL, R. G. and KOENIG, S. H., 1973, *Phys. Rev. A*, **7**, 2130.
- [2] ANDREANI, C., DORE, J. C. and RICCI, F. P., 1991, *Rep. Prog. Phys.*, **54**, 731.
- [3] BERMEJO, F. J., ENCISO, E., ALONSO, J., GARCIA, N. and HOWELLS, W. S., 1988, *Molec. Phys.*, **64**, 1169.
- [4] GUBBINS, K. E., GRAY, C. G., EGELSTAFF, P. A. and ANANTH, M. S., 1973, *Molec. Phys.*, **25**, 1353.
- [5] EGELSTAFF, P. A., PAGE, D. I. and POWLES, J. G., 1971, *Molec. Phys.*, **20**, 881.
- [6] LOWDEN, L. J. and CHANDLER, D., 1974, *J. Chem. Phys.*, **61**, 5228.
- [7] McDONALD, I. R., BOUNDS, D. G. and KLEIN, M. L., 1982, *Molec. Phys.*, **45**, 521.
- [8] SMITH, W. and FINCHAM, D., September 1982, *A Molecular Dynamics Programme for the Simulation of Polyatomic Molecular Liquid Mixtures Incorporating Long Range Electrostatic (Fractional Charge) Effects via the Ewald Sum*, (SERC).
- [9] ALLEN, M. P. and TILDESLEY, D. J., 1987, *Computer Simulation of Liquids*, (Clarendon Press).
- [10] HEERMANN, D. W., 1990, *Computer Simulation Methods in Theoretical Physics*, (Springer-Verlag).

- [11] BÖHM, H. J., MEISSNER, C. and AHLRICHS, R., 1984, *Molec. Phys.*, **53**, 651.
- [12] BÖHM, H. J. and AHLRICHS, R., 1985, *Molec. Phys.*, **54**, 1261.
- [13] SAGARIK, K. P. and AHLRICHS, R., 1986, *Chem. Phys. Lett.*, **131**, 74.
- [14] NOSE, S. and KLEIN, M. L., 1983, *J. Chem. Phys.*, **78**, 6928.
- [15] KNELLER, G. R. and GEIGER, A., 1989, *Molec. Phys.*, **68**, 487.
- [16] DIETZ, W. and HEINZINGER, K., 1985, *Ber. Bunsenges. Phys. Chem.*, **89**, 968.
- [17] MOUNTAIN, R. D. and MORRISON, G., 1988, *Molec. Phys.*, **64**, 91.
- [18] MURAD, S. and GUBBINS, K. E., 1978, *Computer Modelling of Matter*, ACS Symposium Series, Vol. 86, edited by P. Lykos, (American Chemical Series).
- [19] TILDESLEY, D. J. and MADDEN, P. A., 1981, *Molec. Phys.*, **42**, 1137.
- [20] SINGER, K., TAYLOR, A. and SINGER, J. V. L., 1977, *Molec. Phys.*, **33**, 1757.
- [21] COOPER, D. L., WRIGHT, S. C., ALLAN, N. L. and WINTERTON, N., 1990, *J. Fluor. Chem.*, **47**, 489, and references therein.
- [22] VERLET, L., 1968, *Phys. Rev.*, **165**, 201.
- [23] ICI REPORT, 1975, *Arcton Refrigerants, Tables of Thermodynamic Properties*, (ICI Ltd., Mond Division).

[24] HALL, C. D., JOHNSON, K. A., BURGESS, A. N., WINTERTON, N. and HOWELLS, W. S., 1991, *Molec. Phys.*, **74**, 27.

[25] HARMONY, M. D., LAURIE, V. W., KUCZKOWSKI, R. L., SCHWENDEMAN, R. H., RAMSAY, D. A., LOVAS, F. J., LAFFERTY, W. J. and MAKI, A. G., 1979, *J. Phys. Chem. Ref. Data*, **8**, 619.

[26] Eds. SKÖLD, K. and PRICE, D. L., 1986, *Methods of Experimental Physics, Volume 23; Neutron Diffraction Part A*, (Academic Press).

[27] COCKCROFT, J. K. and FITCH, A. N., 1991, *Zeit. für Kristal.*, **197**, 121.

LIVERPOOL
UNIVERSITY

